Granular flow in stirred bed reactors

Insights through radiation-based imaging techniques

van der Sande, P.C.

DOI
10.4233/uuid:95db25ba-7936-497d-9106-7cc31285bb13

Publication date
2025

Document Version
Final published version

Citation (APA)
van der Sande, P. C. (2025). *Granular flow in stirred bed reactors: Insights through radiation-based imaging techniques*. [Dissertation (TU Delft), Delft University of Technology]. https://doi.org/10.4233/uuid:95db25ba-7936-497d-9106-7cc31285bb13

Granular flow in stirred bed reactors

Insights through radiation-based imaging techniques

P.C. van der Sande

Granular flow in stirred bed reactors | P.C. van der Sande 2024

Propositions

accompanying the dissertation

Granular flow in stirred bed reactors

Insights through radiation-based imaging techniques

1. The hydrodynamics in horizontal stirred bed reactors are dominated by agitation. (Related to Chapter 2 of this thesis).
2. Single-photon emission radioactive particle tracking is inherently more robust than conventional radioactive particle tracking. (Related to Chapter 3 of this thesis).
3. Horizontal stirred bed reactors require a minimum fill level of 50% to have effective solids motion. (Related to Chapter 4 of this thesis).
4. Conventional methods to characterize the fluidization behavior, such as pressure drop and bed height, are inadequate for cohesive powders. (Related to Chapter 6 of this thesis).
5. Particle Technology should be part of both undergraduate and graduate Chemical Engineering curricula.
6. Colored figures significantly enhance the visual impact and clarity of scientific presentations.
7. Universities should continue to use research funding from fossil fuel companies, though exclusively for the purpose of advancing sustainable development.
8. A PhD degree in reactor engineering necessitates equal expertise in both fundamental fluid mechanics and image processing tools.
9. Managing individuals in a team effectively requires knowing when to reel in and when to let out the line, just as in fishing.
10. The best way to learn is to teach (*J. Robert Oppenheimer*).

These propositions are regarded as opposable and defendable, and have been approved as such by the promotor prof. dr. ir. J.R. van Ommen and co-promotor dr. ir. G.M.H. Meesters.

Granular flow in stirred bed reactors

Insights through radiation-based imaging techniques

Pieter Christian VAN DER SANDE

Granular flow in stirred bed reactors

Insights through radiation-based imaging techniques

Proefschrift

ter verkrijging van de graad van doctor
aan de Technische Universiteit Delft,
op gezag van de Rector Magnificus prof. dr. ir. T.H.J.J. van der Hagen,
voorzitter van het College voor Promoties,
in het openbaar te verdedigen op

maandag 13 januari 2025
om 15:00 uur

door

Pieter Christian VAN DER SANDE

scheikundig ingenieur
Technische Universiteit Delft, Nederland,
geboren te Delft, Nederland.

Dit proefschrift is goedgekeurd door de

promotor: prof. dr. ir. J.R. van Ommen
copromotor: dr. ir. G.M.H. Meesters

Samenstelling promotiecommissie:

Rector Magnificus	voorzitter
Prof. dr. ir. J.R. van Ommen	Technische Universiteit Delft
Dr. ir. G.M.H. Meesters	Technische Universiteit Delft
Onafhankelijke leden:	
Prof. dr. ir. R.F. Mudde	Technische Universiteit Delft
Prof. dr. ir. D.L. Schott	Technische Universiteit Delft
Prof. dr. ir. J.T. Padding	Technische Universiteit Delft
Prof. dr. ir. N.G. Deen	Technische Universiteit Eindhoven
Prof. Dr.-Ing S. Salameh	FH Münster

The research presented in this thesis was conducted in the Product and Process Engineering section of the Chemical Engineering department from the faculty of Applied Sciences (TNW) of the Delft University of Technology.

The work was carried out as part of the *Industrial Dense Granular Flows* project, which received funding from the Dutch Research Council (NWO) in the framework of the ENW PPP Fund for the top-sectors and from the Ministry of Economic Affairs in the framework of the "PPS-Toeslagregeling".

Nederlandse titel: Granulaire stroming in geroerde bedreactoren - inzichten door middel van stralingsgebasseerde beeldvormingstechnieken

Cover:	*Inside a stirred bed reactor*
Cover design:	P.C. van der Sande & B.W.M. Reijtenbagh - Adobe Firefly
ISBN:	978-94-6506-811-4
Printed by:	Ridderprint

An electronic version of this dissertation is available at http://repository.tudelft.nl/.

To Bente and my family.

Contents

Summary

Polypropylene (PP) is a versatile polymer extensively used in industries such as food packaging, automotive, healthcare, and textiles. Industrially, PP is produced via gas-phase solid-catalyzed polymerization in horizontal stirred bed, vertical stirred bed, or fluidized bed reactors. These reactors operate under controlled conditions to polymerize propylene monomers into solid PP particles. Despite their widespread application, operating these reactors is challenging due to a lack of fundamental understanding and modeling capabilities, which leads to reduced production capacity and lower quality of the final product. This gap in understanding is primarily due to the scarcity of detailed experimental data, which is difficult to obtain because of the opaqueness of the flow and the rapidly evolving gas-solids distribution, necessitating non-optical measurements with high temporal resolution.

In this dissertation, a deeper understanding of granular flow behavior in these reactors was achieved through detailed experimental measurements using radiation-based imaging. Recognizing the direct link between macro-scale flow behavior and particle-scale phenomena, this research spanned both scales. Although the primary focus of this thesis is on a horizontal stirred bed, experiments were also conducted using two additional lab-scale reactor configurations: a vertical stirred bed and a fluidized bed. High-quality data on flow patterns, phase holdup, and particle dynamics were obtained using X-ray imaging and single-photon emission radioactive particle tracking. A key novelty of this research was the use of industrial-grade powders, such as polypropylene reactor powder, as encountered in horizontal stirred bed reactors. The collected data were thoroughly analyzed to identify the key parameters influencing granular flow behavior, utilizing statistical methods and visualization tools to uncover critical insights.

First, the flow behavior of polypropylene reactor powder in a laboratory-scale horizontal stirred bed reactor (HSBR) was investigated using X-ray imaging. It was observed that agitation significantly dictates overall flow behavior and phase holdup in the HSBR. Gas injection through inlet points at the bottom resulted in spouting behavior, and the gas holdup at fixed agitator positions remained highly consistent across successive revolutions. The presence of liquid was found to deteriorate the flow behavior due to liquid bridging at particle contact points, with particle size and surface morphology influencing the powders' susceptibility to liquid.

Subsequently, a single-photon emission radioactive particle tracking method was presented, allowing the tracking of individual photon-emitting particles to evaluate the hydrodynamics of multiphase flows. This method directly utilized detected photon hit locations to reconstruct the three-dimensional position of the tracer particle, avoiding assumptions in count rate fluctuations. The tracer particle's position was determined by finding the intersection point of three two-dimensional planes from the detectors, achieving a spatial accuracy of approximately 1 mm through a subsequent calibration experimentation procedure.

Thereafter, the method was employed to characterize the particle dynamics in the HSBR. It was found that, besides the agitator rotation speed, the flow behavior is significantly influenced by the reactor fill level. At low rotation speeds and fill levels, solids motion was primarily induced by impeller blade passage, resulting in semi-static bed motion and poor solids distribution. Increased fill levels and rotation speeds led to continuous solids motion and uniform distribution. Solids circulation, quantified by a dimensionless cycle number, increased with higher fill levels and rotation speeds. The axial dispersion coefficient ranged from 10^{-6} to 10^{-5} $m^2\,s^{-1}$, increasing with rotation speed, although no conclusive relationship with fill level was observed.

Thereafter, the fluidization behavior of Geldart B particles in a vertical stirred bed reactor was investigated using X-ray imaging, pressure drop measurements, and numerical simulations via Computational Fluid Dynamics (CFD) coupled with Discrete Element Method (DEM) and Immersed Boundary Method (IBM). The experimentally obtained minimum fluidization curve and time-averaged pressure drop showed good qualitative agreement with simulations. Visual observations indicated that increasing the agitator's angular velocity reduced bubble size and improved bed homogeneity, as evidenced by reduced pressure fluctuations. Simulations revealed that while the impeller enhances solids agitation, a proper design study is essential, as static immersed bodies like the stirrer shaft can adversely impact solids motion.

Finally, the correlation between the fluidization behavior and flow properties of 10 commercially available cohesive powders was experimentally investigated. The fluidization quality of the powders in a laboratory-scale fluidized bed was assessed using a Fluidization Quality Index (FQI), computed by integrating gas holdup and its temporal variation acquired through X-ray imaging. Flowability was measured in a rotating drum operated at high speeds, which

aerated the powder bed, a critical factor in correlating fluidization behavior with flow properties. This study established a positive correlation between cohesive powders' flowability and fluidization quality, suggesting that fast and user-friendly flowability measurements in a rotating drum instrument can predict fluidization potential, aiding in process optimization and enhancing fluidization studies for cohesive powders.

In summary, the insights acquired from this thesis enhance the understanding of flow behavior and phase holdup in stirred bed reactors and cohesive fluidized beds. These findings can serve as a valuable foundation for designing, optimizing, and intensifying systems for the industrial-scale manufacturing of high-quality PP resins.

Samenvatting

Polypropyleen (PP) is een veelzijdig polymeer dat op grote schaal wordt gebruikt in de voedselverpakking, automotive, gezondheidszorg en textiel industrieën. Industrieel wordt PP geproduceerd via gasfase gekatalyseerde polymerisatie in horizontale geroerde bedreactoren, verticale geroerde bedreactoren of gefluïdiseerde bedreactoren. Deze reactoren werken onder gecontroleerde omstandigheden om propyleennmonomeren te polymeriseren tot vaste PP-deeltjes. Ondanks hun brede toepassing is het bedienen van deze reactoren uitdagend vanwege een gebrek aan fundamenteel begrip en modelleringsmogelijkheden, wat leidt tot een verminderde productiecapaciteit en lagere kwaliteit van het eindproduct. Dit gebrek aan kennis is voornamelijk te wijten aan de schaarste aan gedetailleerde experimentele gegevens, die moeilijk te verkrijgen zijn vanwege de ondoorzichtigheid van de stroming en de snel veranderende gas-vastestof verdeling, waardoor niet-optische metingen met hoge tijdsresolutie noodzakelijk zijn.

In dit proefschrift werd een dieper begrip van het granulaire stromingsgedrag in deze reactoren verkregen door gedetailleerde experimentele metingen met behulp van stralingsgebasseerde beeldvormingstechnieken. Erkennend dat er een directe link is tussen macroschaal stromingsgedrag en fenomenen op de deeltjeschaal, omvatte dit onderzoek beide schalen. Hoewel de primaire focus van dit proefschrift ligt op een horizontale roerbedreactor, werden er ook experimenten uitgevoerd met twee andere laboratoriumschaalreactorconfiguraties: een verticale roerbedreactor en een gefluïdiseerd bed. Hoogwaardige gegevens over stromingspatronen, fase-verdeling en deeltjesdynamiek werden verkregen met behulp van röntgenbeeldvorming en foton-emissie radioactieve deeltjesvolging. Een belangrijke vernieuwing van dit onderzoek was het gebruik van industriële poeders, zoals polypropyleen reactorpoeder, zoals aangetroffen in horizontale geroerde bedreactoren. De verzamelde gegevens werden grondig geanalyseerd om de sleutelparameters te identificeren die het granulaire stromingsgedrag beïnvloeden, waarbij statistische methoden en visualisatiehulpmiddelen werden gebruikt om cruciale inzichten te onthullen.

Allereerst werd het stromingsgedrag van polypropyleen reactorpoeder in een laboratoriumschaal horizontale geroerde bedreactor (HSBR) onderzocht met behulp van röntgenbeeldvorming. Er werd waargenomen dat agitatie het algehele stromingsgedrag en de fase-verdeling in de HSBR aanzienlijk bepaalt.

Gasinjectie door inlaatpunten aan de onderkant resulteerde in spuitgedrag, en de gas-verdeling op vaste roerderposities bleek zeer consistent over opeenvolgende omwentelingen. De aanwezigheid van vloeistof bleek het stromingsgedrag te verslechteren vanwege vloeistofbrugvorming bij deeltjescontactpunten, waarbij deeltjesgrootte en oppervlaktetextuur de gevoeligheid van de poeders voor vloeistof beïnvloeden.

Vervolgens werd een foton-emissie radioactieve deeltjesvolgmethode gepresenteerd waarmee de hydrodynamica van meerfasen stroming geëvalueerd kan worden door individuele foton-uitzendende deeltjes te volgen. Deze methode maakte direct gebruik van gedetecteerde fotonhits locaties om de driedimensionale positie van het tracerdeeltje te reconstrueren, waardoor aannames over fluctuaties in teltempo werden vermeden. De positie van het tracerdeeltje werd bepaald door het snijpunt van drie tweedimensionale vlakken van de detectoren te vinden, wat een ruimtelijke nauwkeurigheid van ongeveer 1 mm opleverde door middel van een kalibratie-experimentatieprocedure.

Daarna were deze methode gebruikt om de deeltjesdynamiek in de HSBR te karakteriseren. Er werd vastgesteld dat, naast de rotatiesnelheid van de roerder, het stromingsgedrag sterk wordt beïnvloed door het vulniveau van de reactor. Bij lage rotatiesnelheden en vulniveaus werd de beweging van vaste stoffen voornamelijk veroorzaakt door het passeren van de schoepen van de roerder, wat resulteerde in een semi-statische bedbeweging en een slechte verdeling van de vaste stoffen. Verhoogde vulniveaus en rotatiesnelheden leidden tot continue beweging van de vaste stoffen en een uniforme verdeling. De circulatie van de vaste stoffen, gekwantificeerd door een dimensieloze cyclusgetal, nam toe met hogere vulniveaus en rotatiesnelheden. De axiale dispersiecoëfficiënt varieerde van 10^{-6} to 10^{-5} $m^2\ s^{-1}$ en nam toe met de rotatiesnelheid, hoewel er geen duidelijk verband met het vulniveau werd gevonden.

Vervolgens werd het fluidisatiegedrag van Geldart B-deeltjes in een verticale geroerde bedreactor onderzocht met behulp van röntgenbeeldvorming, drukvalmetingen en numerieke simulaties via Computational Fluid Dynamics (CFD) in combinatie met Discrete Element Method (DEM) en Immersed Boundary Method (IBM). De experimenteel verkregen minimum fluidisatiecurve en tijdsgemiddelde drukval vertoonden goede kwalitatieve overeenstemming met simulaties. Visuele observaties gaven aan dat het verhogen van de rotatiesnelheid van de roerder de bellenomvang verminderde en de homogeniteit van het bed verbeterde, zoals ook blijkt uit verminderde drukfluctuaties. Simulaties onthulden dat hoewel de roerder de beweging van vaste stoffen verbetert, een

grondige ontwerpstudie essentieel is, omdat statische ondergedompelde lichamen zoals de roerderas een nadelige invloed kunnen hebben op de beweging van vaste stoffen.

Tenslotte werd de correlatie tussen het fluidisatiegedrag en de stromingseigenschappen van 10 commercieel verkrijgbare cohesieve poeders experimenteel onderzocht. De fluidisatiekwaliteit van de poeders in een laboratoriumschaal gefluïdiseerd bed werd beoordeeld met behulp van een Fluidization Quality Index (FQI), die werd berekend door integratie van de gasverdeling en de temporele variatie verkregen via röntgenbeeldvorming. De stromingseigenschappen werden gemeten in een roterende trommel die op hoge snelheid werd bediend, waardoor het poederbed in een beluchte toestand werd gebracht, wat een belangrijke factor bleek te zijn bij het correleren van het fluidisatiegedrag met de stromingseigenschappen. Dit onderzoek stelde een positieve correlatie vast tussen de vloeibaarheid van cohesieve poeders en de fluidisatiekwaliteit, wat suggereert dat snelle en gebruiksvriendelijke vloeibaarheidsmetingen in een roterend trommelinstrument het potentieel voor fluidisatie kunnen voorspellen, wat bijdraagt aan procesoptimalisatie en het verbeteren van fluidisatiestudies voor cohesieve poeders.

Samengevat dragen de inzichten uit dit proefschrift bij aan het begrip van stromingsgedrag en fase-verdeling in geroerde bedreactoren en cohesieve gefluïdiseerde bedden. Deze bevindingen kunnen dienen als waardevolle basis voor het ontwerpen, optimaliseren en intensiveren van systemen voor de industriële productie van hoogwaardige PP-harsen.

Nomenclature

Roman letters

ΔP	Measured pressure drop (mbar)
ΔP_0	Theoretical pressure drop (mbar)
$\Delta y_{i,j}$	Axial displacement (s)
$\mathbf{u}_g$	Gas velocity (m s^{-1})
u_{mf}	Minimum fluidization velocity (m s^{-1})
A	Area (m^2)
A	Vibration amplitude (m)
$d_{3,2}$	Area-weighted mean diameter (m)
$d_{4,3}$	Volume-weighted mean diameter (m)
$d_{p,i}$	Particle diameter (m)
D_y	Time-averaged axial dispersion coefficient (m^2 s^{-1})
e_n	Normal restitution coefficient (-)
e_t	Tangential restitution coefficient (-)
$\mathbf{F}_{contact,i}$	Particle contact force (N)
f_{vib}	Vibration frequency (Hz)
f_{x-ray}	X-ray detector trigger frequency (Hz)
$\mathbf{g}$	Gravitational acceleration (m s^{-2})
H	Bed height (cm)
H_0	Static bed height (cm)
I	X-ray intensity on the detector (-)
$\mathbf{I}$	Unit tensor (-)
I_0	X-ray intensity from the source (-)
I_i	Moment of inertia (kg m^2)
I_{empty}	X-ray intensity of empty reference (-)
I_{full}	X-ray intensity of full reference (-)
k_n	Normal stiffness (N m^{-1})
k_t	Tangential stiffness (N m^{-1})
m	Mass (kg)
m_i	Particle mass (kg)
p_g	Gas pressure (Pa)
Re	Reynolds number (-)
$\mathbf{S}$	Momentum source term (kg m^{-2} s^{-2})
t	Time (s)
$\mathbf{T}$	Particle torque (kg m s^{-2})
$\mathbf{r}_i$	Particle position (m)
$\mathbf{v}_i$	Particle velocity (m s^{-1})
V_i	Particle volume (m^3)

Greek letters

β	Interface momentum exchange coefficient (-)
τ_g	Stress tensor (N m^{-2})
δ_n	Normal overlap (m)
δ_t	Tangential overlap (m)
ϵ_g	Gas holdup (-)
η_n	Normal damping coefficient (N s m^{-1})
η_t	Tangential damping coefficient (N s m^{-1})
μ	Attenuation coefficient (-)
μ_g	Gas dynamic viscosity (kg m^{-1} s^{-1})
ω	Angular velocity (rad s^{-1})
ϕ	Solids mass flux (kg m^{-2} s^{-1})
ρ_b	Loose bulk density (kg m^{-3})
ρ_p	Particle density (kg m^{-3})
σ	Standard deviation surface position (-)
σ_y	Standard deviation of domain-averaged gas holdup (-)

Sub/superscripts

g	Gas property
i	Individual particle
p	Particle property

Abbreviations

CARPT	Computer-Aided Radioactive Particle Tracking
CFD	Computational Fluid Dynamics
CI	Cohesive Index
DEM	Discrete Element Method
FOV	Field Of View
FQI	Fluidization Quality Index
FWHM	Full Width Half Maximum
HSBR	Horizontal Stirred Bed Reactor
IBM	Immersed Boundary Method
MAE	Mean Absolute Error
PEPT	Positron Emission Particle Tracking
PMT	Photomultiplier Tubes
PP	Polypropylene
RPM	Rotations Per Minute
RPT	Radioactive Particle Tracking
SEM	Scanning Electron Microscope
SPECT	Single-Photon Emission Computed Tomography
SSIM	Structural Similarity Index
TFM	Two-Fluid Model
VSBR	Vertical Stirred Bed Reactor

1

General introduction

1.1. Granular materials

Granular materials are widely encountered in daily life and play a crucial role across various industries, including chemical, pharmaceutical, food, and mineral processing [1, 2]. In fact, over 70% of the world's manufactured products involve granular materials at some stage of their production, whether as raw materials, intermediates, or final products (see Fig. 1.1). Granular materials consist of discrete, solid macroscopic particles (typically between 1 μm and a few mm) that exhibit collective behavior due to friction and particle-particle interactions. Over the past few decades, significant advancements have been made in understanding their behavior [3]. However, the majority of research has concentrated on simplified scenarios based on natural phenomena or industrial processes with limited practical application, leaving the complex behavior of granular materials in industrial processes largely unexplored.

Figure 1.1: Granular materials find widespread applications in processing industries.

Consequently, the design and operation of equipment for handling and processing granular materials in industrial processes often fall short, hindering efficient, safe, and reliable operation. These limitations can result in significant operational and financial setbacks. Studies indicate that plants handling granular materials experience notably lower operating efficiencies compared to those dealing solely with gases or liquids [4]. Therefore, it becomes imperative to attain a deeper understanding of the complex flow behavior of granular materials encountered in industrial processes.

Granular flow is the relative movement of a bulk of particles among neighboring particles or along the equipment wall surface [5]. In dry granular flows with a particle size over 80 μm, the bulk behavior is dominated by inelastic collisions and friction, which are typically short-range and non-cohesive [6, 7], resulting in a good and consistent flow. However, industrial processes typically involve complexities at the reactor level (for example, agitation and gas flow) and particle level (for example, liquid bridging, polydispersity, and porosity). These complexities make them intrinsically hard to design and difficult to optimize. The macro-scale flow behavior, which is directly linked to the particle scale, is hard to predict: the material sometimes flows as a liquid or stops as a solid, or both phases co-exist and interfere.

1.2. Polypropylene manufacturing

An industrial process in which the flow of granular materials imposes significant operational complexities is the manufacturing of polypropylene (PP). PP is a cost-effective and versatile polyolefin resin with strong mechanical properties, thermal stability, and excellent chemical resistance. These characteristics make PP the second most produced plastic and widely used in various industries, including food packaging, automotive, healthcare, textiles, and electronics [8, 9].

One of the most important methods for the industrial manufacturing of PP is solid-catalyzed polymerization [10]. In this process, micron-sized porous catalyst particles are continuously fed into a chemical reactor vessel operating at controlled composition, temperature, and pressure. Under the influence of the catalyst, propylene monomers polymerize and form solid PP particles with a final particle size between 100 and 5000 μm [11]. Generally speaking, there can be a distinction between two types of solid-catalyzed polymerization processes (see Fig. 1.2): slurry phase and gas phase. Gas phase processes are considered superior as they do not require solid-liquid or product-catalyst separation, unlike slurry phase processes [12], and ensure excellent gas-phase

mixing and precise control of reaction parameters. The gas phase processes can be subdivided based on the type of reactor utilized: horizontal stirred bed, vertical stirred bed, or fluidized bed.

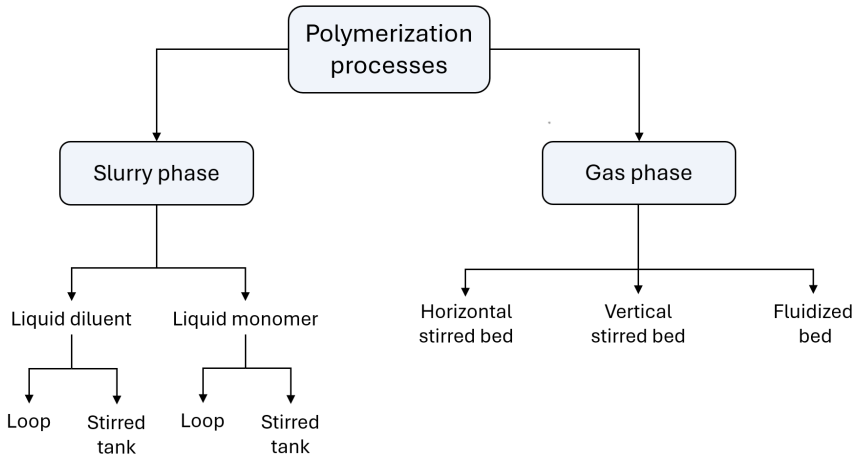

Figure 1.2: Particulate processes for the multistage polymerization of olefins. Adapted from Zacca *et al*. [10].

In these reactors, operational issues can arise from inadequate particle movement or insufficient cooling. A primary concern is the agglomeration of PP particles, which may occur if the heat from the highly exothermic polymerization reaction is insufficiently dissipated. The formed agglomerates can obstruct the discharge pipeline, disrupt the heat exchange balance, and cause deviations from the normal flow pattern, significantly impairing reactor efficiency, production capacity, and product quality [13]. In severe cases, agglomerates can occupy a large portion of the reactor volume, necessitating unscheduled plant shutdowns for cleaning, which in turn results in significant financial penalties [14].

Typically, heat removal is facilitated by spraying recycled liquid propylene onto the PP powder bed. Upon contact with the active PP, the liquid vaporizes, absorbing the heat generated by the highly exothermic polymerization reaction and thereby cooling the system. However, adequate control over the operating parameters is necessary to prevent over-wetting and achieve consistent granular flow behavior.

1.3. Imaging multiphase flows

Accurate modeling of the granular flow characteristics, such as flow pattern and phase holdup, is essential for the design of new reactors and the optimization of existing ones. However, due to the combination of a gaseous flow, mechanical agitation, and liquid quenching, these reactors are often approximated using 'black-box' type models [15]. These models comprise assumptions on the equipment scale and particle scale, which are still subject to uncertainty and debate [16].

Unfortunately, the formulated assumptions are difficult to validate due to a lack of experimental data on parameters that define the structure of the flow, such as the flow pattern, phase holdup, velocity distribution, and particle trajectories. Experimental data is lacking as it is particularly challenging to obtain due to three characteristics. Firstly, the high volume fraction of the particulate phase renders the flow opaque to visible light, which makes the current state-of-the-art flow measurement techniques used by the fluid mechanics' community (lasers, cameras, etc.) ineffective [17]. Secondly, the mechanical stress caused by the vigorous motion of the bed particles and the erosive wear from sandblasting effects pose challenges in designing probes that remain stable over extended periods of operation [18]. Finally, the gas-solids distribution changes rapidly over time, which requires measurement with a high temporal resolution [19].

An ideal experimental measurement system should not rely on optical access and must have high spatial and temporal resolutions to capture the system's fast dynamics accurately. Various diagnostic techniques have emerged to address these requirements. Particularly notable are non-invasive and non-intrusive methods, which have gained attention for their ability to observe the flow field without perturbing the medium under investigation. In this research, two radiation-based imaging techniques are employed that found their way from the medical world to fluid mechanics: X-ray imaging and radioactive particle tracking (see Fig. 1.3).

X-ray imaging is a non-intrusive radiation-based imaging technique that leverages the attenuation of X-rays as they pass through a material. This process involves X-rays traveling in a straight line from an X-ray source to a scintillation detector, allowing for the effective capture of density distribution within the system of interest. X-ray imaging has been extensively employed to investigate the behavior of granular flows in various systems, including fluidized beds [20–24], stirred beds [25], and rotating drums [26].

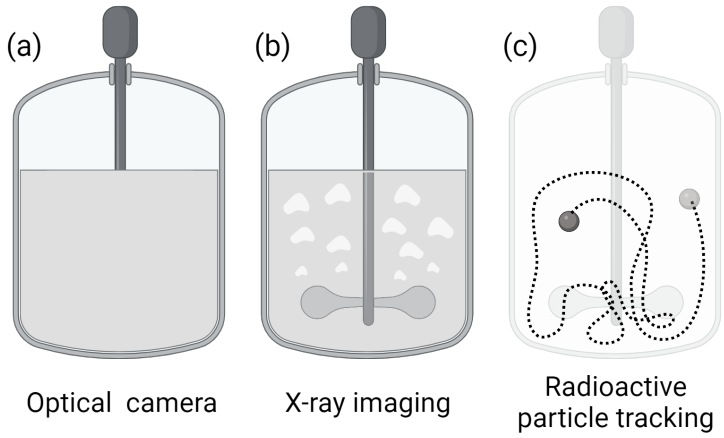

Figure 1.3: Schematic representation of imaging an opaque multiphase flow in a stirred tank reactor with (a) an optical camera, (b) X-ray imaging, and (c) radioactive particle tracking.

In contrast, radioactive particle tracking is a non-invasive measurement technique that tracks the motion of a tracer particle within a system. This method involves introducing a radioactive particle (γ-ray emitter) with properties similar to the bulk phase into the flow field [16]. The system is then operated under desired conditions while scintillation detectors placed around the system detect and monitor the position of the tracer particle over time. Radioactive particle tracking has been widely used to elucidate the flow pattern in fluidized beds [27, 28], spouted beds [29], bubble columns [30], and stirred tanks [31, 32].

By different fundamental approaches, both methods allow continuous observation of different aspects of the transient dynamics in the bed core. As such, the two methods complement each other and provide the physical basis for a better understanding of the flow behavior. Moreover, the data acquired could contribute to validating and establishing more accurate flow patterns and back-mixing models in multiphase reactors [16].

1.4. Research goal and question

Despite their widespread use, stirred bed reactors remain challenging to operate due to a lack of fundamental understanding and modeling capabilities. This knowledge gap results in reduced production capacity and lower quality of the final polymerized product. Experimental data on flow structure parameters are essential for gaining fundamental insights and validating computational models, which are crucial for optimizing industrial processes.

The primary goal of this research is to acquire a deeper understanding of granular flow behavior in stirred bed reactors through detailed experimental investigations. This thesis seeks to answer the main research question:

Main research question

How do complexities on particle and equipment level influence the granular flow behavior in stirred bed reactors?

1.5. Research approach and methodology

A comprehensive experimental approach is employed to address the research question, which involves the design and development of laboratory-scale setups, measurements with radiation-based imaging techniques, and data analysis. The experimental setups involve laboratory-scale reactors, down-scaled in close agreement with their industrial counterparts. In this research, three reactor configurations are studied: a horizontal stirred bed, a vertical stirred bed, and finally, a fluidized bed.

Recognizing the direct link between macro-scale flow behavior and complexities on the particle scale, this study encompasses both scales. Most existing studies in the literature assess the flowability of granular materials using post-processed mono-disperse, spherical particles under dry conditions (see Fig. 1.4-a). However, these studies offer limited insights into industrial processes, where granular materials exhibit higher degrees of polydispersity and irregular particle shapes and are often exposed to moisture or liquids. A key novelty of this research is the use of industrial-grade powders, such as the polypropylene reactor powder as encountered in horizontal stirred bed reactors (see Fig. 1.4-b).

High-quality data on granular flow behavior within these reactors is collected using advanced radiation-based imaging techniques, specifically X-ray imaging and single-photon emission radioactive particle tracking. These techniques allow for detailed observations of flow patterns, phase holdup, and particle dynamics under various operating conditions. The experimental investigations are conducted under various conditions, including different powders, agitation speeds, gas inlet flow rates, and fill levels. This variation is essential for capturing a wide spectrum of data, thereby providing a fundamental understanding of the system's behavior.

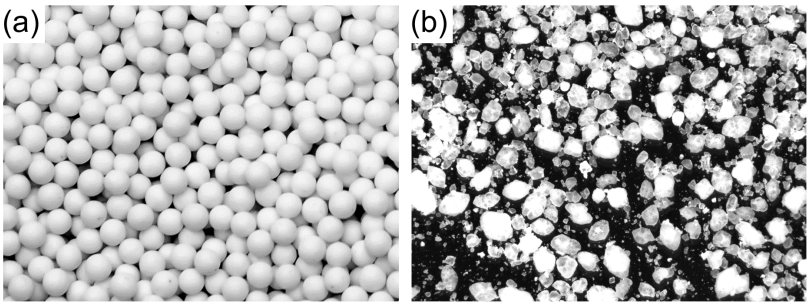

Figure 1.4: (a) Processed polypropylene particles commonly used in academic research and (b) polypropylene reactor powder.

The collected data is then thoroughly analyzed to identify the key parameters influencing the granular flow behavior. Statistical methods and visualization tools are employed to interpret the data, uncovering critical insights. These insights not only enhance the design and optimization of processes but also serve as a foundation for developing accurate computational models.

1.6. Collaborative research framework

The research that led to this thesis is part of a larger collaborative research framework, the 'Industrial Dense Granular Flows (IDGF)' consortium, which received funding from the Dutch Research Council (NWO) through the Technology Area ENW PPP funding. This funding is designed to stimulate public-private partnerships between at least two industrial partners and two knowledge institutions. The IDGF consortium is a collaborative framework between three knowledge institutions, Delft University of Technology, Eindhoven University of Technology, and University of Twente, and four industrial partners, Shell plc, SABIC, Tata Steel Ltd., and Teijin Aramid B.V.

The primary objective of the consortium is to obtain a better understanding of the complex behavior of granular flows in industrial applications, which is rarely studied in academics. The consortium's overarching objective is to develop an experimentally validated coupled Computational Fluid Dynamics (CFD) - Discrete Element Method (DEM) framework that can be used to simulate the complex features of granular flows encountered in industrial processes. The modeling framework is aimed to incorporate complexities on the particle scale, such as polydispersity, liquid bridges, heat & mass transfer, and evaporation, and the equipment scale, such as sub-fluidization and agitation. Besides the general framework, the code is accompanied by in-depth scientific case studies for calibration and validation purposes, which is crucial to ensure

the model's accuracy.

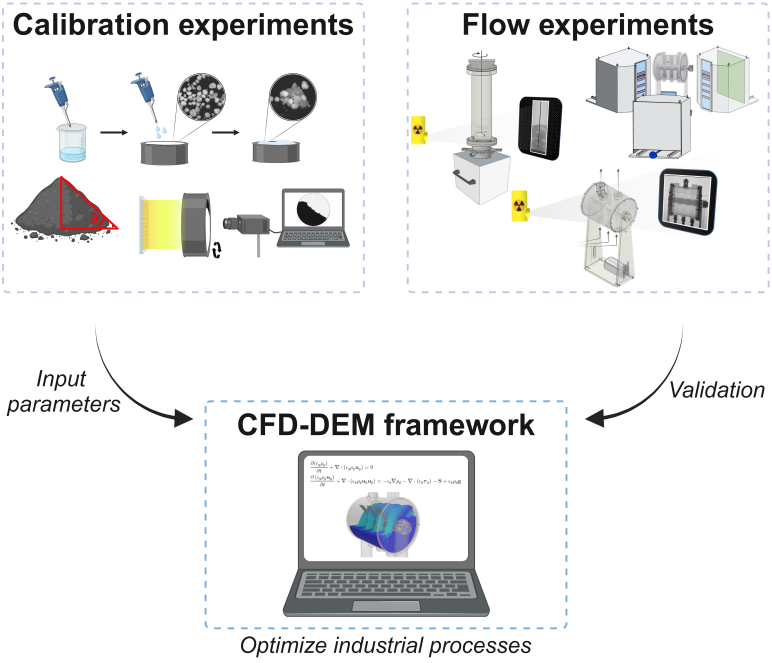

Figure 1.5: Contribution of this research work to the IDGF consortium.

This research contributes to the consortium by providing high-quality experimental datasets for the numerical calibration of industrial-grade powders and validation of the CFD-DEM models, as illustrated in Fig. 1.5. Such elaborate combined experimental and modeling studies under realistic process conditions have been found to be limited in the literature due date. If a validated CFD-DEM model of a process is developed on a laboratory scale, scaling laws can be readily applied to perform modeling of the process at a larger scale. Developing large-scale experimental processes requires significant effort and is associated with high costs. Therefore, the experimentally validated CFD-DEM framework can be an invaluable tool to reliably design processes via novel technological solutions or optimize processes to improve sustainability by reducing emissions and energy consumption. With the modeling framework developed by this consortium, the industrial partners will be directly able to evaluate the influence of changing material properties in their complex processes, aiding in improved design, scale-up, and optimization of the processes.

1.7. Thesis outline

This thesis is article-based and comprises a series of original scientific articles that have been published or have been submitted for publication. The chapters are included in their published form to facilitate easy correlation of the chapters with their respective articles, except for some minor formatting changes that we made to some of the articles to build a coherent and consistent thesis. The thesis aims to provide insight into the influence of operating parameters on the granular flow behavior in the reactors through detailed experimental investigations. Each chapter contributes to accomplishing this aim and, together, provides an answer to the main research question. The principal organization of this thesis is as follows:

In most studies reported in the literature, the flow behavior of polypropylene solids is assessed using post-processed mono-disperse, spherical particles under dry conditions, which provides limited insight into the flow behavior in industrial processes. In Chapter 2, the flow behavior and gas holdup of industrial-grade polypropylene reactor powders in a laboratory-scale horizontal stirred bed reactor are studied with X-ray imaging.

The X-ray imaging method employed in Chapter 2 can provide detailed insight into the gas holdup of a system of interest, but it does not allow the tracking of individual particles. Chapter 3 employs a novel single-photon emission radioactive particle tracking method that can be used to track individual photon-emitting particles in order to evaluate the hydrodynamics of multiphase flows.

In Chapter 4, the previously presented single-photon emission radioactive particle tracking method is employed to characterize the particle dynamics in a laboratory-scale horizontal stirred bed reactor. The influence of fill level and agitation on the particle dynamics is investigated, completing the hydrodynamic investigation of the laboratory-scale horizontal stirred bed reactor.

Besides horizontal stirred bed reactors, vertical stirred bed reactors are used for the manufacturing of polypropylene. Chapter 5 is focused on the fluidization behavior of vertical stirred bed reactors. Through a combined X-ray imaging and numerical study, the influence of agitation on the gas holdup and solids motion in a laboratory-scale gas-solid fluidized bed is elucidated.

Previous chapters were focused on powders that comprise particles with a relatively large particle size. However, in many industrial applications, powders with smaller particle sizes are used, which tend to become cohesive due

to relatively strong van der Waals forces. The fluidization of cohesive powders introduces several challenges, such as channeling and agglomeration, which even hinder some powders from being fluidized at all. In Chapter 6, the unassisted and vibro-assisted fluidization behavior of ten commercially available materials is qualitatively and quantitatively compared to the respective flow behavior. Opportunities are presented to obtain a priori insight into the expected fluidization behavior through simple powder flow testing experiments.

In Chapter 7, the conclusions are presented, and an outlook for future research is given. Preliminary results on X-ray particle velocimetry show that this method could provide information on the gas holdup and particle trajectory simultaneously as one integrated method, which opens doors to a wide array of future projects.

All articles published as part of this research are green open access and accessible through the TU Delft's repository research.tudelft.nl and are linked to their corresponding bibliography entries. Research datasets underlying the respective articles are made available at the 4.TU.ResearchData repository, aiming to make the datasets findable, accessible, interoperable, and reproducible (FAIR).

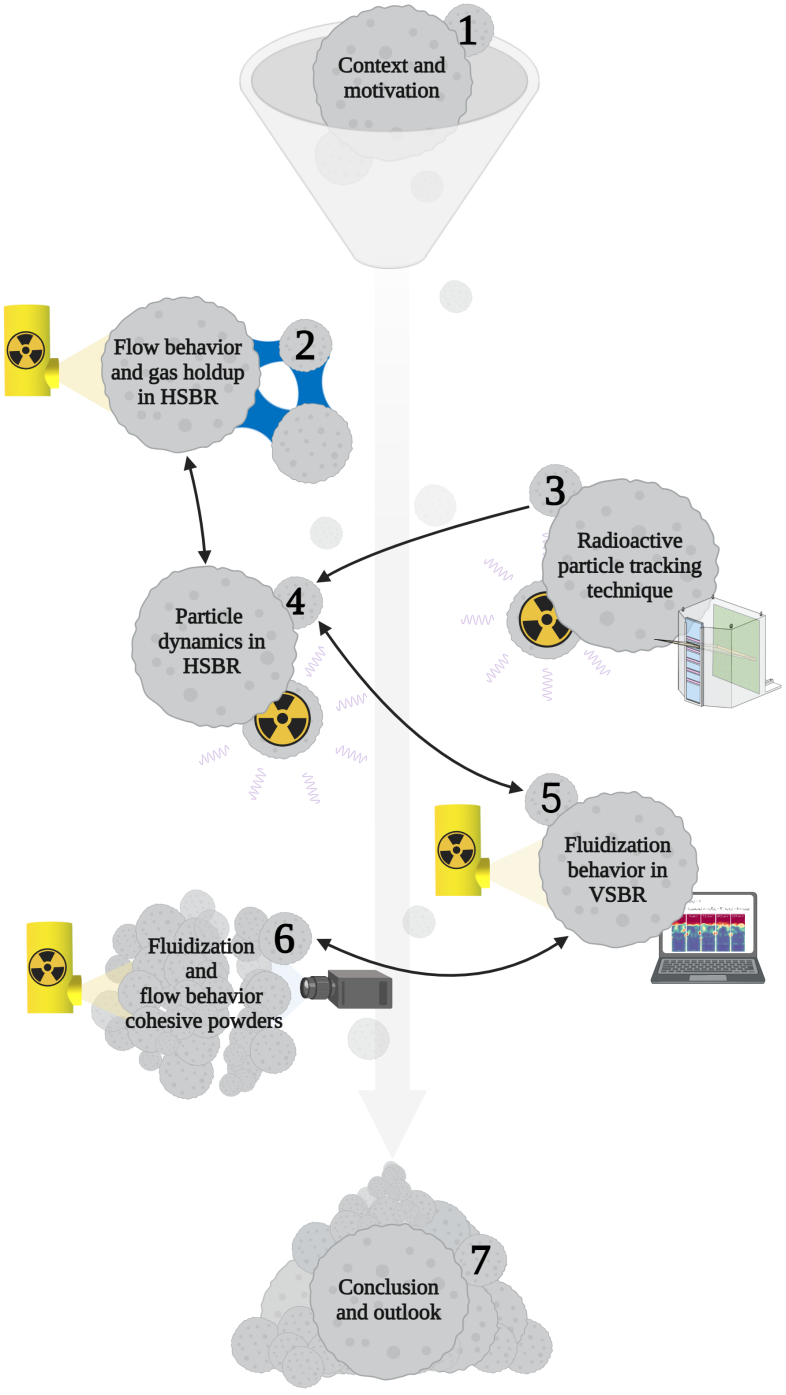
1
Context and motivation
2
Flow behavior and gas holdup in HSBR
3
Radioactive particle tracking technique
4
Particle dynamics in HSBR
5
Fluidization behavior in VSBR
6
Fluidization and flow behavior cohesive powders
7
Conclusion and outlook

1

References

[1] D. Geldart and J. Werther, *Gas fluidization technology,* Berichte der Bunsengesellschaft für physikalische Chemie **91**, 678 (1987).

[2] H. J. Herrmann, *Granular matter,* Physica A: Statistical Mechanics and its Applications **313**, 188 (2002).

[3] M. Rhodes, *Introduction to Particle Technology* (John Wiley & Sons, Ltd, 2008).

[4] E. W. Merrow, *Linking r&d to problems experienced in solids processing,* Chemical Engineering Progress **81**, 14 (1985).

[5] M. Peleg, *Flowability of food powders and methods for its evaluation — a review,* Journal of Food Process Engineering **1**, 303 (1977).

[6] H. J. Herrmann, *Granular matter,* Physica A: Statistical Mechanics and its Applications **313**, 188 (2002).

[7] N. Mitarai and F. Nori, *Wet granular materials,* Advances in Physics **55**, 1 (2006).

[8] J. Karger-Kocsis and T. Bárány, *Polypropylene Handbook Morphology, Blends and Composites: Morphology, Blends and Composites* (2019).

[9] K. Kulajanpeng, N. Sheibat-Othman, W. Tanthapanichakoon, and T. F. L. McKenna, *Multiscale modeling of multizone gas phase propylene (co)polymerization reactors—a comprehensive review,* The Canadian Journal of Chemical Engineering **100**, 2505 (2022).

[10] J. J. Zacca, J. A. Debling, and W. H. Ray, *Reactor residence time distribution effects on the multistage polymerization of olefins—i. basic principles and illustrative examples, polypropylene,* Chemical Engineering Science **51**, 4859 (1996).

[11] R. A. Hutchinson, *Modelling of particle growth in heterogeneous catalyzed olefin polymerization.*, Thesis, University of Wisconsin-Madison (1990).

[12] P. Cai, J. van Egmond, M. Fedec, J. Goad, R. Brady, and L. Chen, *Process for gas-phase polymerization having high bed bulk density,* (2013), U.S. Patent No. US 2013/0005923.

[13] C. M. van den Bleek, M.-O. Coppens, and J. Schouten, *Application of chaos analysis to multiphase reactors,* Chemical Engineering Science **57**, 4763 (2002).

[14] J. Wang, Y. Cao, X. Jiang, and Y. Yang, *Agglomeration detection by acoustic emission (ae) sensors in fluidized beds,* Industrial & Engineering Chemistry Research **48** (2009), 10.1021/ie800324m.

[15] M. Barigou, *Particle tracking in opaque mixing systems: An overview of the capabilities of PET and PEPT,* Chemical Engineering Research and Design **82**, 1258 (2004).

[16] M. Duduković, *Opaque multiphase reactors: Experimentation, modeling and troubleshooting,* Oil & Gas Science and Technology – Rev. IFP Éditions Technip Oil & Gas Science and Technology – Rev. IFP **55**, 135 (2000).

[17] C. Poelma, *Measurement in opaque flows: a review of measurement techniques for dispersed multiphase flows,* Acta Mechanica **231**, 2089 (2020).

[18] J. Werther, *Measurement techniques in fluidized beds,* Powder Technology **102**, 15 (1999).

[19] J. R. van Ommen and R. F. Mudde, *Measuring the gas-solids distribution in fluidized beds – a review,* International Journal of Chemical Reactor Engineering **6** (2008), doi:10.2202/1542-6580.1796.

[20] M. Errigo, P. Lettieri, and M. Materazzi, *X-ray imaging techniques for gas–solid fluidized beds: A technical review,* Particuology (2023).

[21] A. Helmi, E. C. Wagner, F. Gallucci, M. van Sint Annaland, J. R. van Ommen, and R. F. Mudde, *On the hydrodynamics of membrane assisted fluidized bed reactors using x-ray analysis,* Chemical Engineering and Processing: Process Intensification **122**, 508 (2017).

[22] J. Gómez-Hernández, S. Sánchez-Delgado, E. Wagner, R. F. Mudde, and J. R. van Ommen, *Characterization of tio2 nanoparticles fluidization using x-ray imaging and pressure signals,* Powder Technology **316**, 446 (2017).

[23] S. Jahangir, E. C. Wagner, R. F. Mudde, and C. Poelma, *Void fraction measurements in partial cavitation regimes by x-ray computed tomography,* International Journal of Multiphase Flow **120**, 103085 (2019).

[24] K. Wu, E. Wagner, O. Ochkin-Koenig, M. Franck, D. Weis, G. Meesters, and J. R. Van Ommen, *Time-resolved x-ray study of assisted fluidization of cohesive micron powder: On the role of mechanical vibration,* Chemical Engineering Journal **470**, 143936 (2023).

[25] K. Wu, R. Kamphorst, A. Bakker, J. Ford, E. C. Wagner, O. Ochkin-Koenig, M. Franck, D. Weis, G. M. Meesters, and J. R. van Ommen, *Stirrer design for improving fluidization of cohesive powder: A time-resolved x-ray study,* Chemical Engineering Science **294**, 120069 (2024).

[26] T. N. Papapetrou, M. Bieberle, F. Barthel, U. Hampel, and G. Lecrivain, *Investigating binary granular mixing in a rotating drum using ultrafast x-ray computed tomography,* Powder Technology **443**, 119964 (2024).

[27] F. Larachi, M. Cassanello, M. Marie, J. Chaouki, and C. Guy, *Solids circulation patterns in 3-phase fluidized-beds containing binary-mixtures of particles as inferred from rpt,* Chemical engineering research & design **73**, 263 (1995).

[28] L. Godfroy, F. Larachi, G. Kennedy, and J. Chaouki, *Simultaneous measurement of the 3-d position and velocity of a single radioactive particle in a cfb riser at high velocity,* Proceedings of CFB V, Beijing, China (1996).

[29] D. Roy, F. Larachi, R. Legros, and J. Chaouki, *A study of solid behavior in spouted beds using 3-d particle tracking,* The Canadian Journal of Chemical Engineering **72**, 945 (1994).

[30] D. Moslemian, N. Devanathan, and M. P. Dudukovic, *Radioactive particle tracking technique for investigation of phase recirculation and turbulence in multiphase systems,* Review of Scientific Instruments **63**, 4361 (1992).

[31] J. Chaouki, F. Larachi, and M. P. Dudukovic, *Noninvasive tomographic and velocimetric monitoring of multiphase flows,* Industrial and Engineering Chemistry Research **36**, 4476 (1997).

[32] A. R. Rammohan, A. Kemoun, M. H. Al-Dahhan, and M. P. Dudukovic, *Characterization of single phase flows in stirred tanks via computer automated radioactive particle tracking (carpt),* Chemical Engineering Research and Design **79**, 831 (2001).

2

Flow behavior of polypropylene reactor powder in horizontal stirred bed reactors characterized by X-ray imaging

In this chapter, we develop a laboratory-scale horizontal stirred bed reactor. Since the polypropylene reactor powders are opaque to visible light, we employ a fast X-ray imaging technique to characterize the flow behavior and gas holdup. This chapter first introduces the laboratory-scale setup and the X-ray imaging method. Then, the influence of the rotation speed, gas inlet flow rate, and liquid content on the flow behavior and gas holdup is presented and discussed.

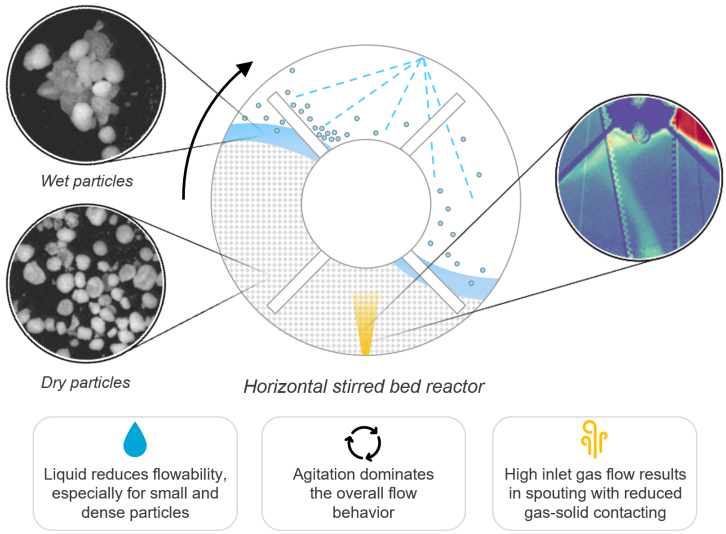

This chapter is published as P.C. van der Sande, C. de Vries, E.C. Wagner, A.C. Vögtlander G.M.H. Meesters, and J.R. van Ommen, *Flow behavior of polypropylene reactor powder in horizontal stirred bed reactors characterized by X-ray imaging*, Chemical Engineering Journal (2024).

Horizontal stirred bed reactors (HSBRs) are widely used in the commercial production of polypropylene (PP). Despite their commercial significance, a comprehensive understanding of the flow behavior in HSBRs remains elusive, primarily due to the lack of detailed experimental data. This study investigates the influence of operating parameters on the particle flow behavior of two types of PP reactor powder in a laboratory-scale HSBR using X-ray imaging. Our results indicate that the overall flow behavior and phase holdup in the HSBR are dominated by agitation. Moreover, gas injection through the inlet points at the bottom of the HSBR results in spouting behavior, which can lead to reduced gas-solid contacting and, in extreme cases, complete bypass. Finally, the presence of liquid (in this study, isopropyl alcohol) adversely affects the flow behavior of the PP reactor powder due to liquid bridging at the contact points of particles. Powders that comprise particles with relatively small sizes and dense surface morphology are particularly prone to reduced flow behavior when exposed to liquid.

2.1. Introduction

Polypropylene (PP) is a cost-effective and versatile polyolefin resin with good mechanical properties, thermal stability, and excellent chemical resistance. These characteristics make PP a preferred choice in various industries, including food packaging, automotive, healthcare, textiles, and electronics [1, 2]. In 2022, the annual global production of PP was approximately 79.1 million metric tons [3], and the global PP market is expected to see sustained growth, driven by the increased use of high-quality plastics in automotive manufacturing and the growing need for efficient packaging solutions [4].

Gas-phase catalyzed polymerization has become a crucial method in the commercial production of PP [5]. The Innovene™ PP process stands out as a particularly effective and scalable production technology [6–10]. This process typically employs two horizontal stirred bed reactors (HSBRs): the first reactor is used for forming propylene homopolymer or random copolymer, and the second downstream reactor is dedicated to producing propylene impact copolymer. HSBRs are highly valued for their ability to provide excellent gas-phase mixing and precise control over reaction parameters, which are essential for efficient PP production.

The HSBR is a cylindrical reactor comprising a series of paddles attached to a central shaft. A schematic representation of the HSBR is depicted in Fig. 4.1. At the reactor's inlet, micron-sized Ziegler-Natta catalyst particles are continuously introduced [10]. Gaseous propylene monomers are injected through inlets at the reactor's base and polymerize on the active sites of the catalyst through a coordination-insertion mechanism. To maintain a sub-fluidized state and prevent bed fluidization, the gas velocity is carefully regulated. Heat originating from the highly exothermic polymerization reaction is removed through evaporative cooling. This process involves spraying recycled liquid propylene onto the PP powder bed from various axial positions along the reactor's length. When the liquid propylene contacts the active PP, it vaporizes, absorbing the reaction heat and thereby cooling the system effectively. Throughout the polymerization process, the mildly agitated PP powder is kept at a constant inventory, allowing the PP particles to grow to sizes between 100 and 5000 µm [11]. The increasing volume of the growing particles propels the powder toward the reactor's opposite end, where it is continuously discharged.

There are significant operational challenges involved in gas-phase polymerization reactors that often arise from inadequate particle movement or insufficient cooling. A primary concern is the agglomeration of polyolefin particles,

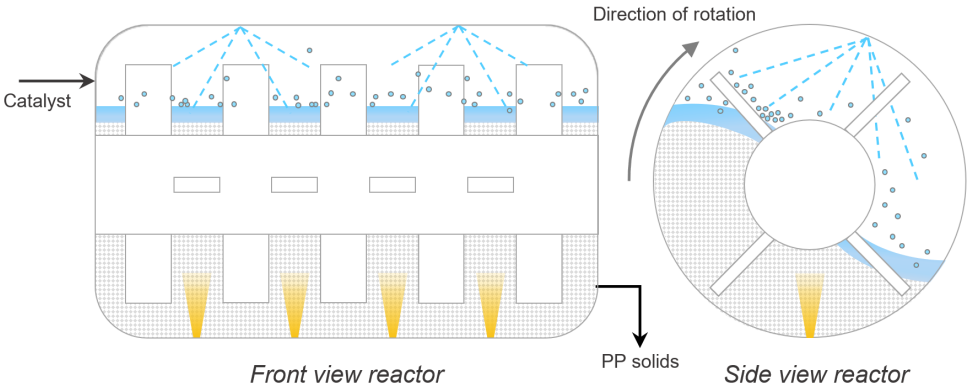

Figure 2.1: Graphical representation of the front view (left) and side view (right) of the horizontal stirred bed reactor as employed in the Innovene™ PP process. The polypropylene solids are continuously agitated, while gaseous propylene is introduced from the bottom (yellow cones), and liquid propylene quench is sprayed from the top of the reactor (blue dashed lines).

which can reduce production capacity and product quality [12]. In the Innovene™ PP process, such agglomeration is typically due to insufficient heat dissipation from inadequate quenching or poor solids circulation. Without effective and uniform heat dissipation, the temperature of polymer particles can increase, potentially reaching or exceeding their softening or melting point, leading to the formation of agglomerates or lumps. These agglomerates reduce product quality and can obstruct the discharge pipeline, disrupt the heat exchange balance, and cause deviations from the normal flow pattern, significantly impairing reactor efficiency. In severe cases, agglomerates can occupy a large portion of the reactor volume, necessitating unscheduled plant shutdowns for cleaning and resulting in significant financial penalties [13].

While a propylene quench is necessary to dissipate heat and control the reactor temperature, excess liquid propylene can create liquid bridges between particles, increasing cohesion through capillary forces [14]. This liquid bridging may lead to the formation of liquid-bound PP agglomerates, which in turn deteriorates flowability. Therefore, it is crucial to determine the optimal liquid quench rate that effectively dissipates heat while minimizing adverse effects on PP flow behavior caused by liquid bridging. Additionally, adequate solids circulation is essential to ensure uniform wetting and maintain a consistent bed temperature.

Considerable research effort has been devoted to kinetic studies of the polymerization reaction and modeling of the residence time distribution [5, 8–

10, 15–18]. The literature widely reports that the powder mixing pattern in an HSBR is influenced by two transport effects: simultaneous stirring flows with equal intensity in both the up-and downstream directions and the continuously increasing powder net flow in the downstream direction due to particle growth. Together, these effects give rise to a residence time distribution that can be effectively modeled by three to five continuous stirred tank reactors in series [8, 16].

While considerable effort has been devoted to kinetic studies and modeling, only limited studies have explored the powder flow behavior in HSBRs. The flow characteristics of biomass particles in a laboratory-scale HSBR were examined through experimental measurements [19] and computational modeling [20]. These studies reported that the axial dispersion coefficient increases with higher rotation speeds and a larger number of blades.

Additionally, the granular flow pattern in horizontal powder mixers, which shows similarities to HSBRs, has been investigated using positron emission particle tracking [21–23]. Laurent *et al*. [21] observed that radial blades in horizontal mixers create axial compartments in the bed that induce circulation loops in the bed. Subsequent research by Laurent and Bridgwater [22] demonstrated that the velocity fields and axial dispersion coefficients scale with rotation speed, aligning with the flow characteristics observed in the HSBR study by Xi *et al*. [19]. Furthermore, Laurent and Bridgwater [23] reported that at sufficiently high reactor fill levels, the agitator shaft significantly influences radial and axial particle motion.

Experimental evaluation of the powder flow behavior and phase holdup is essential for optimizing and intensifying reactor operations and validating computational models. The flow pattern and phase holdup significantly affect reactor stability and the quality and uniformity of the final polymerized product. However, the complex hydrodynamics of multiphase flow reactors pose a challenge for experimental evaluation. In the HSBR, the flow's multiphase nature, characterized by a high particulate phase fraction, results in a dense, opaque flow that hinders the use of conventional optical techniques.

In our previous work, we characterized the particle dynamics in a laboratory-scale HSBR by employing single-photon emission radioactive particle tracking. We found that the particle dynamics are highly influenced by the reactor fill level and agitator rotation speed [24, 25]. However, the particle tracking method employed did not allow for the study of the overall flow behavior and

gas holdup.

In the current study, we characterize the flow behavior of two types of PP reactor powder in a laboratory-scale HSBR under non-reactive conditions, employing an in-house X-ray imaging method. X-ray imaging has been an established non-invasive technique for assessing the phase holdup in multiphase flow systems [26–30]. We employ X-ray imaging to investigate the influence of reactor operating parameters, namely agitator rotation speed, gas inlet flow rate, and liquid content, on the flow behavior and gas holdup in the HSBR. Furthermore, we employ in-house developed software to implement X-ray imaging phase-locking, enabling local assessment of the relation between the phase holdup and the power consumption by the motor driving the agitator.

2.2. Methodology

2.2.1. Horizontal stirred bed reactor setup

The laboratory-scale HSBR used in this work consists of a 134 mm inner-diameter cylinder with a length of 150 mm. The cylinder incorporates an agitator comprising a central shaft with seven blade positions. Each position is equipped with two blades, with each blade positioned 90° apart from its neighboring blades. The inner blades have a width of 20 mm, while the end blades have a width of 15 mm. The cylinder has three gas injection inlets of 6 mm diameter at the bottom at 25, 50, and 75 % of the length. The injection points are equipped with a filter to prevent back-flow of solids. The two outlets are closed through a filter to prevent fines elutriation. Both the cylinder and the agitator are constructed from polycarbonate to mitigate X-ray radiation attenuation during the experiments. The agitator can be rotated at the desired rotation speed using an electric motor with a belt drive, which is controlled via in-house software. A schematic representation of the HSBR is illustrated in Fig. 2.2

2.2.2. Polypropylene material

This study assesses the flow behavior of two types of industrial-grade PP reactor powder. It is important to note that these powders are PP solids directly acquired from industrial HSBRs and possess significantly different properties than processed PP beads, which are typically used in academic studies. The PP powders investigated were manufactured with different catalysts and consequently possess different inherent particle properties. For ease, the powders are denoted as PP-1 and PP-3. The particle size distribution and morphology of the powders were analyzed using a particle size analyzer and microscopy, respectively. The physical properties of the materials are summarized in Table 2.1 and will be further discussed in the following paragraphs.

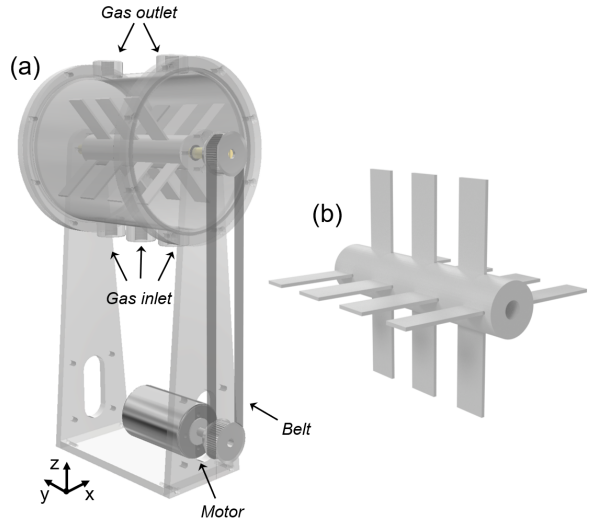

Figure 2.2: (**a**) Schematic representation of the laboratory-scale horizontal stirred bed reactor, and (**b**) the internal agitator comprising a central shaft equipped with a series of impellers.

Table 2.1: Physical properties of the powders used in this study. [a]Span = $(d_{v90}\text{-}d_{v10})/d_{v50}$.

Powder	$d_{3,2}$ (µm)	$d_{4,3}$ (µm)	Span[a] (-)	ρ_{bulk} (kg m^{-3})	u_{mf} (cm s^{-1})	Shape
PP-1	569	672	1.12	511	15	Angular
PP-3	1040	1180	0.99	368	25	Spherical

The particle size distributions of the PP materials were measured using the Malvern 3000 particle size analyzer equipped with a dry powder module and high-energy stainless steel venturi tube. The volume-based particle size distributions are represented in Fig. 2.3a. Among the two powders, PP-3 exhibits the largest particles with a Sauter mean particle size ($d_{3,2}$) of 1040 µm compared to 569 µm of PP-1. As can be observed from the cumulative distribution and the span denoted in Table 2.1, PP-1 has a slightly broader particle size distribution than PP-3.

The morphology of the materials was characterized through optical and scanning electron microscopy. A ZEISS SteREO Discovery.V8 optical microscope with manual 8x zoom was used to acquire images on the macro-scale. Figure 2.3b(1-2) shows representative optical microscope images of the powders. The images illustrate notable variations in the size and shape of the par-

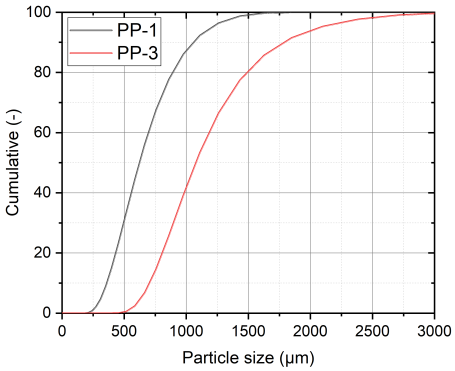

(a) Volume-based cumulative particle size distribution acquired with the Malvern 3000 particle size analyzer.

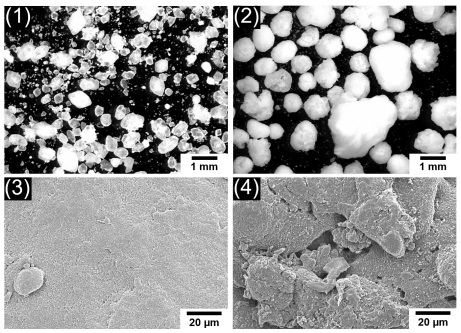

(b) Representative examples of optical microscope images of (**1**) PP-1 and (**2**) PP-3, and scanning electron microscope images of (**3**) PP-1 and (**4**) PP-3.

Figure 2.3: Properties of the PP reactor powders used in this study.

ticles, and both materials can be classified as poly-disperse in size and shape. In agreement with the particle size distribution obtained through light scattering, the images demonstrate that PP-3 exhibits the largest particles while PP-1 exhibits the smallest. Furthermore, the particles of PP-1 display angular morphology, while the particles of PP-3 possess a more spherical morphology. In addition, a JEOL JSM-6010LA scanning electron microscope was used to acquire images at the micro-scale. Before the analysis, the samples were sputter-coated with gold using a JEOL JFC-1300 auto fine coater in automatic mode to limit charging and improve image quality. From the SEM images (Fig. 2.3b(3-4)), it can be observed that the surface of PP-1 is smooth and appears to be dense. In contrast, the surface of PP-3 demonstrates a higher degree of surface roughness and the presence of macro-pores. Additional SEM images are included in Appendix A.1.

Besides the particle size distribution and morphology, the loose bulk density (ρ_b) of the powders was experimentally determined following the method of Carr [31]. PP-1 has a relatively higher bulk density (511 kg m^{-3}) compared to PP-3 (368 kg m^{-3}). Moreover, the minimum fluidization velocity (u_{mf}) of the two powders was experimentally determined through pressure drop measurements in a cylindrical fluidized bed column with an internal diameter of 5 cm. The respective pressure drop against superficial gas velocity plots are included in Appendix A.1. From the curves, the minimum fluidization velocities of PP-1 and PP-3 were determined to be 15 and 25 cm s^{-1}, respectively.

X-ray imaging

The flow behavior of the PP powders in the HSBR was experimentally assessed using an in-house fast X-ray imaging setup, schematically illustrated in Fig. 2.4a. X-ray imaging is a non-invasive imaging technique that can be used to visualize the density distribution of opaque multiphase flows. With X-ray imaging, a 2D projection of the 3D gas holdup in the HSBR was captured.

The X-ray setup consists of a standard industrial-type X-ray source (Yxlon International GmbH) with a maximum energy of 150 keV working in cone beam mode and a 2D detector (Teledyne Dalsa Xineos) with a theoretical spatial resolution of 0.20 mm placed opposite of the source. In this study, the source-detector distance was 122.5 cm, with the center of the HSBR positioned 102 cm from the source. Throughout all experiments, the setup was controlled from a workstation located outside the setup room, ensuring a safe working environment. X-ray images were acquired at a sampling rate between 35 and 70 Hz depending on the desired resolution of the acquired image. The obtained data was then stored for subsequent digital image analysis.

Each acquired image is a time-resolved projected 2D intensity map of the HSBR. A two-point calibration protocol was executed to convert the measurement intensity into a gas holdup (see Fig. 2.4b). Initially, a reference image was captured of the empty column without the shaft and impeller blades (I_{empty}). Subsequently, the column was filled with the bed material, and a full reference image was obtained (I_{full}). The X-ray measurement principle relies on the attenuation of X-rays traveling in a straight line from an X-ray source to a detector while passing through the material. The transmission of a monochromatic beam of high-energy photons with initial intensity I_0 through a material of constant density is described by the Lambert-Beer law:

$$I(x) = I_0 e^{-\mu z} \tag{2.1}$$

Here, $I(z)$ denotes the intensity measured at the detector, μ is the attenuation coefficient, and z is the thickness of the X-ray attenuating material between the source and the detector. In cases of varying attenuation, the measured intensity is the integral effect of local attenuation with the local attenuation coefficient. By applying the Lambert-Beer law, the measurement gas holdup map ($\epsilon_{measurement}$) was derived from the measurement intensity map ($I_{measurement}$) using the empty and full reference as depicted in Fig. 2.4b. The normalized gas holdup ϵ_g was calculated as follows:

$$\epsilon_g = \frac{ln(I_{measurement}/I_{full})}{ln(I_{empty}/I_{full})} \tag{2.2}$$

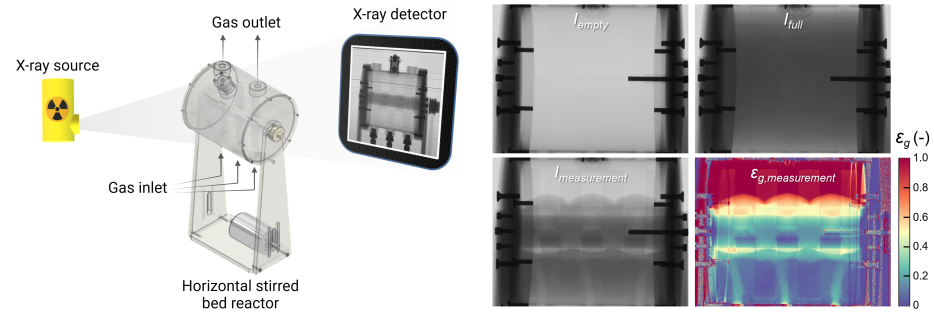

(a) Schematic representation of the experimental X-ray imaging setup.

(b) A two-point calibration procedure is employed to convert the intensity map to a gas holdup map.

Figure 2.4: X-ray imaging analysis of the horizontal stirred bed reactor hydrodynamics.

It is important to note that the normalized gas holdup in this study ranges from 0 to 1, where 1 represents pure gas and 0 dense packing of solids. Warm colors in the gas holdup map correspond to low X-ray attenuation, indicating high gas concentrations. In contrast, cold colors represent high X-ray attenuation, indicating low gas concentrations. A more detailed description of the procedure is included in our previous works [32, 33].

2.2.3. Operation and flow characterization

During the operation of the HSBR in industrial applications, the bed level is kept at constant inventory, and the rotation speed and gas inlet flow rate are kept constant. Adequate control of the operating settings is necessary to prevent operational issues, as these have a significant influence on the flow pattern in rotating systems [23, 34]. This study evaluates the impact of agitation, gas inlet, and liquid content on the flow behavior of the PP powders in the laboratory-scale HSBR.

Three different types of experiments were conducted to elucidate the flow behavior of the PP reactor powders in the HSBR. In the first set of experiments, the gas holdup was studied as a function of the rotation speed and gas inlet flow rate. The second set of experiments focused on determining how rotation speed and gas inlet flow rate affect the power consumption of the motor during agitation. Finally, the third set of experiments investigated the influence of liquid content on the flowability of the PP reactor powders.

For each experiment, the HSBR was filled to the desired level by inserting PP powder through the top opening. Depending on the specific experiment, either the gas inlet was activated, or the IPA liquid was introduced. The agitator rotation speed was then set to the desired value. After 30 s, the X-ray source and detector were switched on, and X-ray images were acquired for a measurement duration of 60 seconds at varying acquisition frequencies. For the gas holdup experiments, the gas holdup was computed from the X-ray images according to the processing workflow described in Section 2.2.1. The operational settings are summarized in Table 2.2, and the different types of experiments will be discussed in more detail in the subsequent subsections.

Table 2.2: Experimental investigations and their respective operational settings.

Parameter	Gas holdup	Power consumption	Wet flow behavior
Fill level (v%)	50	50	50
Rotation speed (RPM)	20-40-60	20-40-60	20-40-60
Total gas inlet (L min^{-1})	0-15-30-45-60	0-30-60	0
Liquid content (vol%)	0	0	0.00-1.25-2.50-5.00-10.0
Sampling frequency X-ray (Hz)	35-70	RPM dependent	35
Measurement run time (s)	60	60	60

Gas holdup

In the Innovene™ process, propylene gas is inserted through gas inlet openings at the bottom of the HSBR. In this cold model study, compressed air was supplied to the HSBR through three gas inlet points at the bottom positioned at 25, 50, and 75% of the reactor length. To assess the influence of the inlet flow rate on the gas holdup, the flow rate was incrementally increased from 0 to 60 L min^{-1} in steps of 15 L min^{-1} for various rotation speeds.

The gas holdup of the entire HSBR was acquired with an X-ray acquisition frequency of 35 Hz. To capture the fast dynamics of the gas holdup directly above the gas inlet, the gas holdup of the bottom half of the HSBR was acquired with an X-ray acquisition frequency of 70 Hz. The time-resolved X-ray images were used to compute a time-averaged gas holdup over the 60 s acquisition time:

$$\overline{\epsilon}_g(x,z) = \frac{1}{N_{\Delta t}} \sum_{t=t_0}^{t_0+\Delta t} \epsilon_g(x,y,t) \tag{2.3}$$

where x and y represent the horizontal and vertical positions, and $N_{\Delta t}$ represents the number of images between t_0 and t_0+Δt.

Power consumption

Monitoring the power consumption of the motor under the influence of varying rotation speeds (20, 40, and 60 RPM) and varying inlet flow rates (0, 30, and 60 L min^{-1}) during agitation gives valuable insight in the variation of the resistance. To monitor the power consumption, in-house integrated logging software in LabVIEW was used. During agitation, the software automatically logged the current of the motor at a specific arbitrary agitator position, ranging from 0 to 4096 during one revolution. The logged current and position were stored for further data processing. The arbitrary current was converted to power by employing a calibration protocol, and the arbitrary agitator position was converted to the angle of rotation with Equation 2.4.

$$\textit{Angle of rotation} = \frac{\textit{Position number}}{4096} \cdot 360 \tag{2.4}$$

To understand how the power consumption of the motor relates to the gas holdup, X-ray images were captured at fixed agitator positions. This was achieved by incorporating the control of the X-ray apparatus into the power consumption logging software, which allowed the triggering of the X-ray detector at fixed agitator positions. Consequently, the sampling frequency of the X-ray detector depended on the number of positions and the rotation speed of the agitator. An in-depth analysis of the correlation between phase holdup and power consumption was made possible by capturing X-ray images while simultaneously logging the power consumption at the same agitator positions.

Additionally, by capturing X-ray images at identical agitator positions over a large number of revolutions, phase-locking the position, the consistency of the phase holdup could be analyzed. An in-house MATLAB script was used to compute the structural similarity index (SSIM) of the acquired X-ray images using the image acquired during the first revolution as a reference. The SSIM represents the similarity between two images, for which a value closer to 1 indicates a better similarity [35], and thereby allows quantitative assessment of the consistency of the phase holdup.

Wet flow behavior

In the Innovene™ PP process, a liquid propylene quench is used to remove heat originating from the exothermic polymerization reaction through evaporative cooling. Excessive quench liquid may cause the formation of agglomerates or lumps due to liquid bridge formation, which can adversely affect reactor efficiency. Furthermore, ensuring sufficient solids motion is essential for achieving uniform liquid distribution. Therefore, it is crucial to quantify the influence of the liquid content and rotation speed on the flowability of PP reactor powder.

As propylene is in a gaseous state under standard temperature and pressure conditions, isopropyl alcohol (IPA) was used as a model liquid. Measurements were conducted with fixed liquid contents of 0.00, 1.25, 2.50, 5.00, and 10.0 vol% IPA by adding IPA through the top opening and agitating for 30 s to ensure a homogeneous mixture. For each liquid content, X-ray images of the flow behavior in the HSBR were captured at rotation speeds of 20, 40, and 60 RPM.

Besides a qualitative assessment of the flow behavior under various liquid contents, the deviation of the flow pattern from the normal flow pattern (0 vol% at 20 RPM) was quantitatively assessed based on the variation of the surface position. Typically, a consistent flowing surface with a low degree of variation corresponds to a good flowability, while an irregular flowing surface with a high degree of variation corresponds to a poor flowability [36]. Using this characteristic, an in-house MATLAB script was employed to compute a time-averaged X-ray image for each operational setting. Then, for each time-averaged image, the top part of the bed was extracted, and the SSIM was computed using the time-averaged X-ray image acquired under dry conditions (0 vol% IPA) at a rotation speed of 20 RPM as a reference, representing the normal flow behavior. As depicted in the previous section, the SSIM represents the similarity between two images, for which a value closer to 1 indicates a better similarity. In this way, the SSIM allows quantitative assessment of the deviation from the normal flow pattern when the bed is exposed to various liquid contents.

2.3. Results and discussion

2.3.1. Gas holdup

Gas holdup without gas inlet

A significant advantage of the employed X-ray imaging method is its ability to offer a direct projection of the gas holdup over time, enabling the visualization of both time-resolved and time-averaged flow behavior and gas holdup. Figure 2.5a presents the time-averaged gas holdup without gas inlet, facilitating

a qualitative comparison of the observed flow behavior of the two PP powders at different rotation speeds.

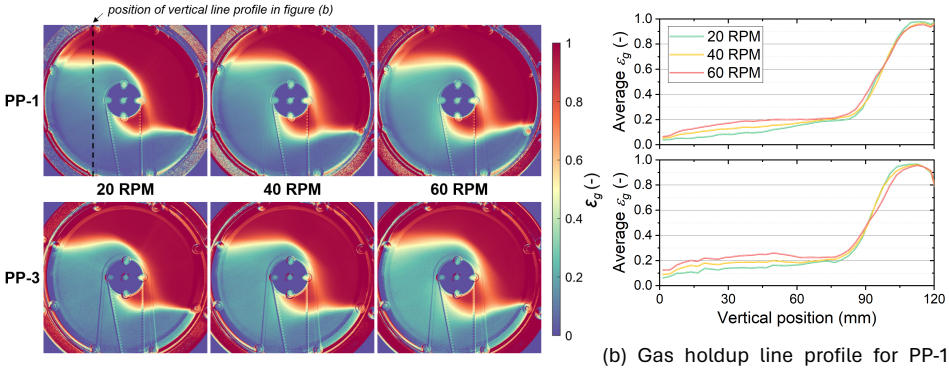

(a) Gas holdup maps.

(b) Gas holdup line profile for PP-1 (top) and PP-3 (bottom).

Figure 2.5: Time-averaged gas holdup without gas inlet for various rotation speeds. A video displaying the time-resolved flow behavior is included in the electronic appendix.

It can be observed that the clockwise impeller rotation causes the left side of the bed to rise upward and flow over the shaft. A comparison of different rotation speeds reveals that the bed expands as rotation speed increases. The expansion is attributed to the aeration of the bed due to the fast rotation of the impeller blades, which brings the bed to an aerated state. The phenomenon of aeration at elevated rotation speeds is commonly observed in rotating drums, especially for fine powders [37].

The aeration of the bed is also observed by closely evaluating the gas holdup at the different rotation speeds. As the rotation speed increases, both PP powders demonstrate a gradual increase in gas holdup. This increase is particularly noticeable at the left and upper regions of the bed, visually depicted by a lighter blue shade, indicative of a more aerated and loosely packed state. This observation is graphically reinforced by the vertical line profile in Fig. 2.5b, which shows that a higher gas holdup is attained at a higher rotation speed. Additionally, both the spatial gas holdup maps (Fig 2.5a) and the vertical profiles (Fig 2.5b) highlight that PP-3 remains a slightly higher gas holdup. Interestingly, a region with lower gas holdup, depicted by a darker blue shade, is observed at the bottom right part of the bed in all instances, indicating a denser state. The region with a dense state is most likely caused by the compaction of the bed when the particles descend after flowing over the shaft.

The agitation-induced bed aeration leads to a rise in the material flow over the shaft, as evidenced by the time-averaged gas holdup. The circumferential motion of solids, driven by the clockwise agitation that compels material to flow over the shaft, plays a crucial role in achieving a well-mixed system with a uniform particle cycle time, as was reported by Van der Sande *et al.* [25]. Comparing the gas holdup of the two PP powders across different rotation speeds reveals no significant differences. Both powders display free-flowing behavior and increased aeration with higher rotation speeds.

Gas holdup with gas inlet

In the industrial process, propylene gas is inserted through inlets spaced along the various polymerization sections of the HSBR and located underneath the surface of the polymer bed [7]. In this cold model study, compressed air was supplied to the HSBR through three gas inlet points at the bottom positioned at 25, 50, and 75% of the reactor length. Figure 2.6 illustrates the gas holdup at various gas inlet flow rates for PP-1 (Fig. 2.6a) and PP-3 (Fig. 2.6b) for a rotation speed of 20 RPM.

From both front and side views, it is evident that gas spouts, characterized by a moderate gas holdup, are formed above the gas inlet points. These spouts increase in height with higher gas flow rates. From the front view, it can be observed that the spouts are formed at each gas inlet point, at 25, 50, and 75% of the reactor length. For PP-1, gas spouts begin developing at a gas flow rate of 15 L min^{-1} and bypass the bed (i.e., reaching up to the bed surface) from 30 L min^{-1} onwards. With PP-3 having a slightly higher u_{mf} than PP-1 (25 cm s^{-1} compared to 15 cm s^{-1}), gas spouts only form at a gas flow rate of 30 L min^{-1} and bypass the bed starting from 60 L min^{-1}.

Spouting is inherently linked to reduced gas-solid contacting, particularly in cases of complete bypass. In the industrial process, both gaseous propylene and hydrogen are introduced from the bottom of the HSBR. Since the HSBR operates under a propylene atmosphere, there is readily good contact between propylene gas and the solid phase, and the bypass of propylene is not expected to significantly affect the overall process efficiency. However, hydrogen plays a crucial role in controlling chain length and terminating the polymerization reaction, which requires effective gas-solid contact. Therefore, the bypass of hydrogen gas due to spouting is undesirable. Furthermore, the formation of spouts may locally induce solids circulation, as typically observed in the annulus region of spouted beds [38]. However, characterizing the motion of individual particles in the HSBR requires particle tracking methods, which are not

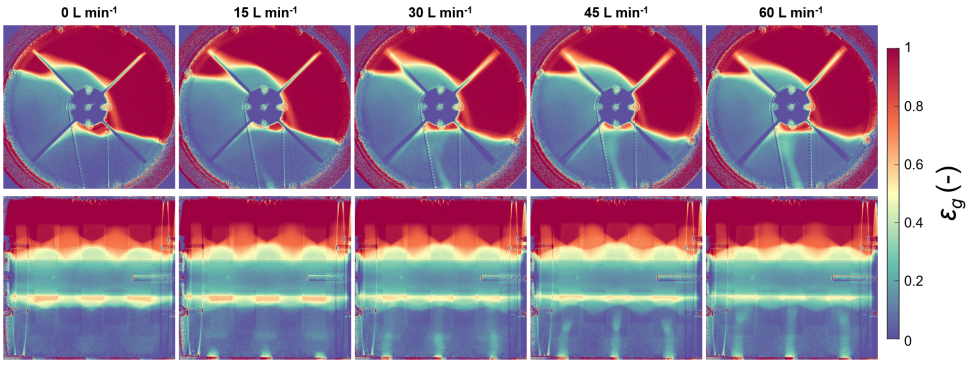

(a) Powder PP-1.

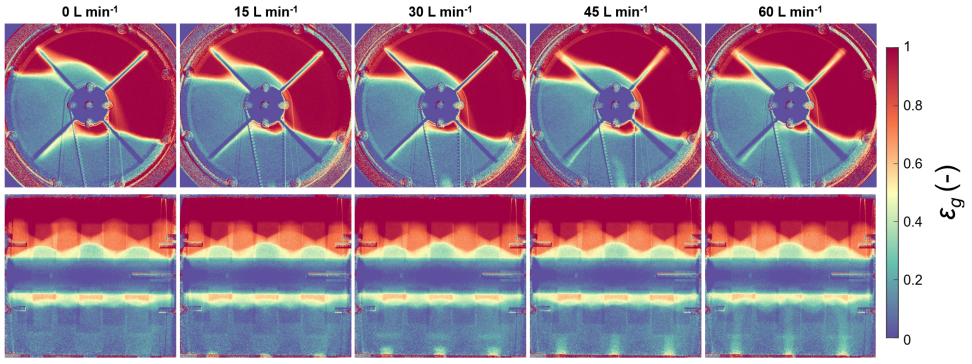

(b) Powder PP-3.

Figure 2.6: Representative gas holdup snapshots for varying gas flow rates at a rotation speed of 20 RPM displaying the side and front view of the HSBR.

the focus of this study but could serve as an extension for future investigations.

Upon close examination of the front-view gas holdup maps, the stark contrast in gas holdup between the spout and the surrounding bulk for both powders indicates limited axial mixing of gas within the solids phase. In the side-view gas holdup maps, the influence of clockwise agitation on the spout's trajectory is evident, with the spout bending toward the left side of the bed. This observation suggests tangential mixing of gas within the solids phase due to the rotational movement of the impeller blades, underscoring the significant role of agitation in the gas distribution. To further elucidate the agitation's influence on the gas inlet dynamics, Fig. 2.7 presents sequences of snapshots of the time-resolved gas holdup, acquired with an X-ray image acquisition frequency of 70 Hz, at a rotation speed of 20 RPM and gas flow rates of 15 and

60 L min^{-1} for one-quarter of the agitator revolution, corresponding to a time period of 0.75 s.

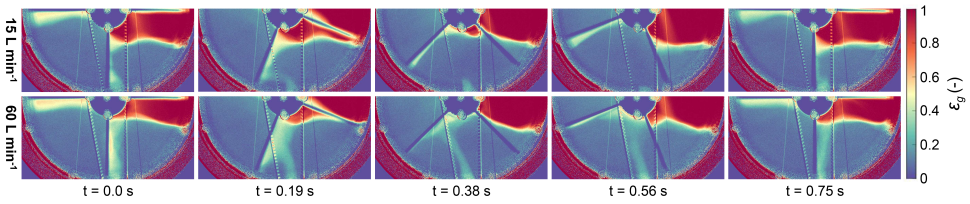

(a) Powder PP-1.

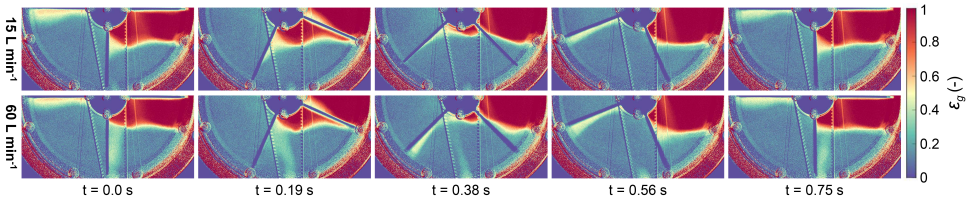

(b) Powder PP-3.

Figure 2.7: Time sequence of representative gas holdup snapshots of the bottom half of the HSBR acquired at a rotation speed of 20 RPM and a flow rate of 15 and 60 L min^{-1}. This sequence chronologically (from left to right) depicts gas holdup dynamics under the influence of the clockwise movement of the impellers through the bed during a 0.75 s time period.

The first snapshot (t=0.0 s) illustrates the gas holdup when three impeller blades (see Fig. 3.15 and the description of the HSBR geometry) align with the gas injection points. For powder PP-1, gas spouts are clearly observed right of the downward-facing impeller blades at both gas flow rates. Conversely, for PP-3, a clear gas spout is formed at a flow rate of 60 L min^{-1} while a minor gas spout is observed at a flow rate of 15 L min^{-1}, which is in agreement with previous observations made from Fig. 2.6b. From the next snapshot (t=0.19 s), it can be observed that the formed gas spouts bend toward the wakes behind the passing impeller blades, following the clockwise movement of the agitator. In the third snapshot (t=0.38 s), the gas inlet is positioned between the passing blade and the approaching blade. For both powders, it can be observed that at a flow rate of 60 L min^{-1}, the spouts remain directed toward the impeller, while at 15 L min^{-1}, it diverges from the passing impeller blades. Subsequent to this (t=0.56 s), a significant reduction of the spouts is observed for PP-1 at a flow rate of 15 L min^{-1} and PP-3 at a flow rate of 60 L min^{-1}, while it continues to be fully developed for PP-1 at a flow rate of 60 L min^{-1}. This reduction is attributed to the approaching impeller blades pushing the powder toward the

gas inlet. Finally, the last snapshot (t=0.75 s) captures the gas holdup when four impeller blades align with the gas injection points. The impeller blades offer a path of lesser resistance, leading to the reformation of spouts for PP-1 at 15 L min^{-1} and PP-3 at 60 L min^{-1}. This analysis underscores the significant influence of agitation on gas holdup dynamics.

It should be noted, however, that gas injection into the bed does not significantly impact the overall hydrodynamics of the bed. Comparing gas holdup maps obtained at flow rates of 0 L min^{-1} and 60 L min^{-1} (see Fig. 2.5), only minor bed surface restructuring due to slight bed expansion is evident. Apart from this minimal surface restructuring, the overall bed dynamics remain largely consistent across varying gas inlet flow rates. As previously mentioned, agitation appears to be the dominant factor influencing flow behavior.

2.3.2. Power consumption

In the preceding section, we explored the effects of rotation speed and gas inlet flow rate on gas holdup within the HSBR. It was demonstrated that higher rotation speeds induce mechanical aeration of the powder bed, while gas inlet can lead to spouting behavior. In this section, we broaden our investigation to include the influence of rotation speed and gas inlet flow rate on the power consumption of the motor. Utilizing an integrated phase-locking method, as described in Section 2.3.2, we obtained time-resolved power consumption data during agitator revolutions.

Figure 2.8a illustrates the power consumption within one revolution (i.e., 0 to 360°) for powder PP-3 at varying rotation speeds and gas inlet flow rates. The graphs notably depict an oscillating pattern, indicating fluctuating power consumption throughout a single agitator revolution. In the case of 0 L min^{-1} gas inlet (the gray lines in Fig. 2.8a), this oscillating pattern can be attributed to two factors. Firstly, during agitation, the powder is pushed upward in a clockwise manner until it flows freely over the shaft downward. It is evident that impellers require more power to push the powder upwards, as gravity opposes this movement, compared to moving through air. The peaks in the graph correspond to moments when an impeller blade transitions from air into the powder bed, resulting in apparent stick-slip behavior. Stick-slip behavior, extensively studied by researchers such as Albert *et al.* [39], commonly arises from external stress applied to granular media, causing an internal structure that resists the stress and leads to a jammed state. As the impeller blade motion is impeded by jammed particles ahead of it, when the applied force surpasses a critical threshold, the blade advances further into the powder bed, displacing

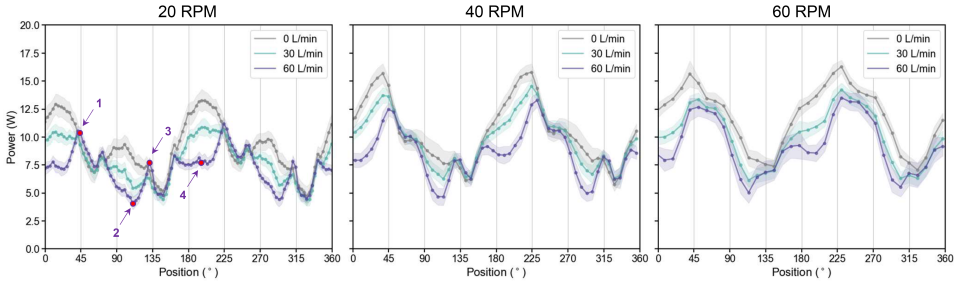

(a) Graphical representation of the power consumption fluctuations within one revolution for powder PP-3 for varying rotation speed (20, 40, and 60 RPM) and gas inlet flow rate (0, 30, and 60 L min^{-1}). The mean and standard deviation are based on 60 revolutions.

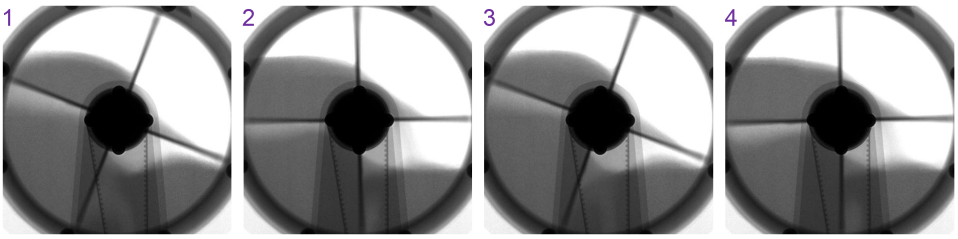

(b) X-ray images acquired at a rotation speed of 20 RPM and inlet flow rate of 60 L min^{-1} corresponding to the numbered positions indicated in Fig. (a).

Figure 2.8: The influence of the agitation and gas inlet flow rate on the power consumption within one revolution for powder PP-3.

the particles.

Figure 2.9: Video demonstrating the evolution of power consumption during a revolution.

Secondly, the geometry of the agitator contributes to the observed oscillating pattern. The agitator comprises a shaft with seven axial blade positions, each equipped with two blades positioned 90° apart from neighboring blades. This uneven distribution of blades results in a variation in total blade surface area within the bed during the clockwise rotation of the agitator, leading to

varying resistance. Consequently, this variance contributes to differences in power consumption values at the peaks. The relatively large difference is due to the limited number of blade positions in the laboratory-scale HSBR, namely 7. In industrial HSBRs, where the number of blade positions is significantly larger, the influence of uneven blade distribution is expected to be considerably smaller. Interestingly, a detailed examination of the graphs reveals that the oscillating pattern repeats every 180°, which is attributed to the system's symmetry.

When gas is introduced into the system, as indicated by the turquoise and purple lines in Fig. 2.8a, four distinct regions are observed where there is a notable deviation in power consumption compared to the 0 L min^{-1} cases. These deviations occur when the impeller blades pass over the gas inlet. As demonstrated in the previous section, gas spouts form above the gas inlet points. When impeller blades traverse the gas spout, they encounter significantly less resistance compared to moving through the bed material. The deviation begins as the blades approach the gas inlet, reaches its maximum when the blades align with the gas inlet, and diminishes as the blades move away from the gas inlet.

Within one revolution, there are two instances when four blades traverse over the gas inlet, resulting in the most significant deviation from the 0 L min^{-1} case (as indicated by Fig. 2.8 number 4). Similarly, there are two instances when three impeller blades move over the gas inlet, resulting in a smaller deviation from the 0 L min^{-1} case (as indicated by Fig. 2.8 number 2). The disparity in deviation of power consumption relative to the 0 L min^{-1} case stems from the larger total blade surface area of four blades compared to three blades. This observation underscores the influence of the gas inlet on motor power consumption. As observed for the 0 L min^{-1} cases, it can also be noted that the patterns with gas inlet repetition occur every 180° due to symmetry in the system.

Comparing the graphs obtained at different rotation speeds, it becomes evident that the 20 RPM graphs exhibit a minimum of four peaks, varying in power value due to the agitator configuration, as previously explained. Interestingly, the peaks with lower power consumption are nearly absent in the 40 RPM graphs and completely absent in the 60 RPM graphs. As established in the previous section, an increase in rotation speed leads to mechanical bed aeration. Apart from reducing local bulk density, aeration can mitigate stick-slip behavior, resulting in smoother power consumption during agitation [40].

Consequently, this reduction in stick-slip behavior leads to a decrease in the number of peaks in the graph.

The power consumption of PP-1 exhibits a comparable oscillating pattern during agitation, as shown in Appendix Fig. A.5. However, a noticeable difference between the two PP reactor powders is that PP-1 requires an overall higher power consumption, with oscillations having a larger amplitude at similar operational settings. This disparity in power consumption and amplitude between PP-1 and PP-3 can be attributed to the higher bulk density of PP-1. Since experiments were conducted using a consistent volume of PP reactor powder, the bed constituted a higher mass during experiments with PP-1 compared to PP-3. Consequently, more power is required for the agitation of PP-1. These findings align with those of Knight *et al.* [41], who investigated the impact of mass on power consumption in high-shear powder mixers and concluded that power consumption increases with higher agitated mass. Similar to PP-3, the degree of variation in power consumption is reduced with increasing rotation speed, attributed to the aeration of the bed.

Despite the system's multiphase and discrete nature, remarkably small standard deviations are observed at each agitator position in Fig. 2.8a and Appendix Fig. A.5, indicating highly consistent behavior. To further illustrate the bed's consistency, Fig. 2.10a presents a sequence of three X-ray images acquired at identical agitator positions for successive revolutions obtained through the X-ray imaging integrated phase-locking method.

Upon qualitative comparison of the images with the naked eye, no discernible differences can be observed. To further quantify their similarity, the structural similarity index (SSIM) was computed using image revolution 1 as the reference. As explained in Section 2.3.2, the SSIM represents the similarity between two images, with a value closer to 1 indicating better similarity. The SSIM index maps, depicted in Fig. 2.10b, along with the global SSIM index values of 0.99347 (image revolution 2) and 0.99346 (image revolution 3), indicate extremely high similarity. In fact, the primary difference between the images lies in the noise present in the high-intensity regions of the image (where there is no powder or flange). This suggests that the bed and gas spout exhibit remarkable consistency across successive revolutions. Since the images are acquired at identical agitator positions, it further underscores that both the bed behavior and gas spout behavior are predominantly influenced by agitation. These findings are significant, as the bed's extremely high consistency implies that the system can be reliably characterized within a short measure-

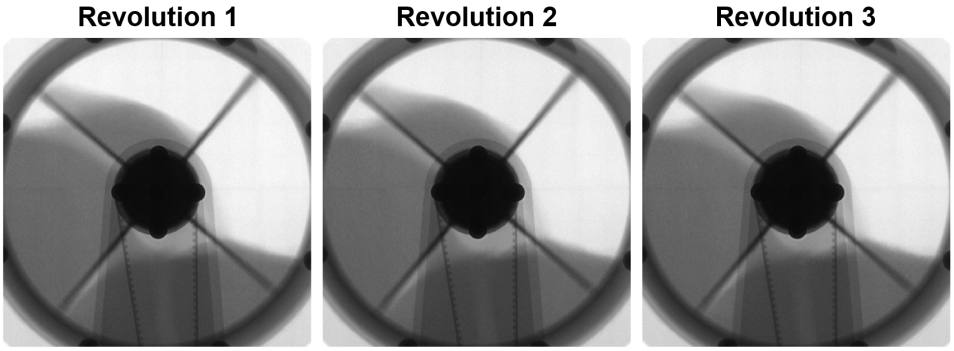

(a) Sequence of X-ray images captured at identical agitator positions for succeeding revolutions.

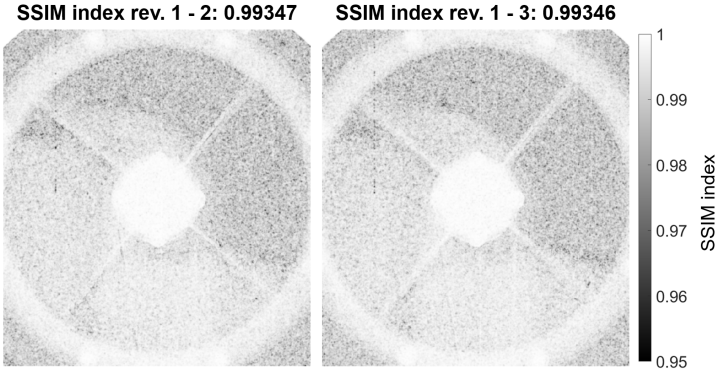

(b) Structural similarity index (SSIM) demonstrating the similarity between Fig. 2.10a images 1 and 2 (left) and images 1 and 3 (right).

Figure 2.10: Similarity between X-ray images acquired at identical agitator positions a rotation speed of 20 RPM and a gas flow rate of 60 L min^{-1}.

ment time. This is particularly relevant for computational modeling, such as Computational Fluid Dynamics - Discrete Element Modeling (CFD-DEM). Such modeling is highly CPU demanding, and investigations are therefore limited to short duration. The recurrent patterns in the HSBR open doors to employ recurrence CFD approaches [42], potentially speeding up the simulations by two orders of magnitude [43].

2.3.3. Flowability under wetted conditions

In the preceding sections, we explored the impact of rotation speed and gas inlet flow rate on gas holdup in the HSBR under dry conditions. However, in the industrial polymerization process, the bed is continuously wetted by a propy-

lene quench to dissipate heat generated by the exothermic polymerization reaction. In this section, we investigate the effect of liquid on the flow behavior in the HSBR by subjecting the PP reactor powders to various IPA contents. Figure 2.11 presents representative snapshots illustrating the flow behavior of the two PP reactor powders across IPA liquid contents ranging from 0 to 10 vol%.

Under dry conditions (0.00 vol%), both powders exhibit a smooth-flowing layer, indicative of good flowability. However, notable differences in flow behavior emerge upon exposure to IPA. While PP-3 maintains a smooth flowing layer for liquid contents up to 5.00 vol%, PP-1 demonstrates deteriorated flowability already at a liquid content of 1.25 vol%, evidenced by an irregular flowing layer. The deterioration of flowability persists with increasing liquid content. Eventually, at a liquid content of 10 vol%, cohesive forces become so pronounced that lumps of PP cycle circumferentially, rendering the powder no longer flowing. Although PP-3 also experiences a reduction in flowability at a liquid content of 10.00 vol%, it remains significantly more flowable than PP-1.

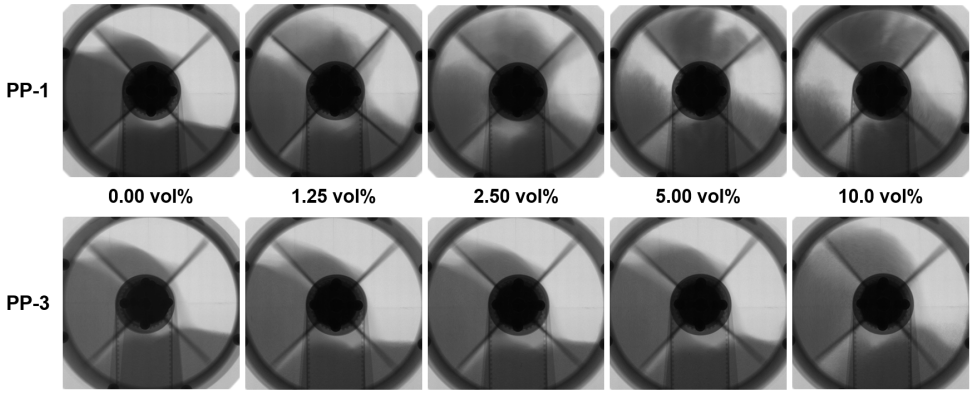

Figure 2.11: Representative X-ray images of the flow behavior of PP-1 (top) and PP-3 (bottom) at a rotation speed of 20 RPM for liquid contents of 0, 1.25, 2.50, 5.00, and 10 vol% isopropyl alcohol.

An image processing workflow was employed to quantify the deviation in flow patterns under wetted conditions. For each operational condition, the SSIM of the time-averaged flow pattern was computed with the time-averaged flow pattern acquired at 20 RPM under dry conditions serving as the reference. As previously mentioned, the SSIM represents the similarity between two images, with a value closer to 1 indicating better similarity. Utilizing the flow behavior under dry conditions at a rotation speed of 20 RPM as a reference, the value of 1-SSIM represents the deviation in the flow pattern from the normal

Figure 2.12: Video of the flow behavior at a rotation speed of 20 RPM for liquid contents of 0, 1.25, 2.50, 5.00, and 10 vol% isopropyl alcohol.

flow behavior at 20 RPM. Consequently, a larger value for 1-SSIM indicates a greater deviation. Figure 2.13 graphically illustrates the influence of liquid content and rotation speed on the deviation in flow pattern from the flow pattern under dry conditions at a rotation speed of 20 RPM.

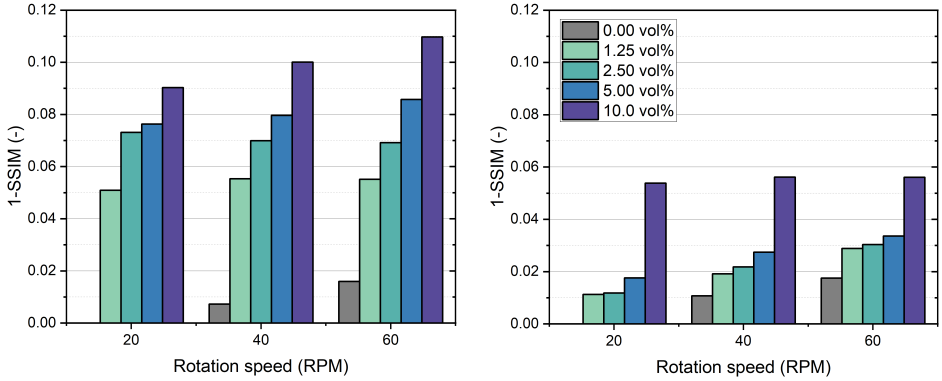

(a) PP reactor powder PP-1.

(b) PP reactor powder PP-3.

Figure 2.13: The influence of liquid content and rotation speed on the deviation in flow pattern (1-SSIM) relative to the flow pattern acquired under dry conditions at a rotation speed of 20 RPM.

In agreement with Fig. 2.5, it can be observed that increasing the rotation speed results in a small deviation in the flow pattern, which is attributed to the aeration of the bed. More interestingly, by comparing the influence of the liquid content for both powders, significant differences in the deviation of the flow pattern are observed. As qualitatively depicted in 2.5, Fig. 2.13a illustrates that the flow pattern of PP-1 already exhibits significant deviation from the normal flow pattern at a liquid content of 1.25 vol% and continues to deviate up to a 1-SSIM value of 0.11 at a liquid content of 10 vol% for a rotation speed of 60 RPM. In contrast, Fig. 2.13b demonstrates that the flow pattern of PP-3 only begins

to deviate significantly at a liquid content of 10.0 vol%. Remarkably, the deviation in the flow pattern of PP-3 at 10.0 vol% is comparable to the deviation in the flow pattern of PP-1 at 1.25 vol%, underscoring the substantial difference in susceptibility to liquid between the two PP reactor powders.

The observed differences in the apparent impact of liquid content on the flowability of the two PP reactor powders can be elucidated by their distinct particle properties. As discussed in Section 2.2, PP-1 has a Sauter mean diameter of 569 µm and comprises angular-shaped particles with a dense surface, whereas PP-3 possesses a Sauter mean diameter of 1040 µm and comprises spherical-shaped particles with a porous surface. Both differences in particle size and particle surface may contribute to the observed disparity in flowability. When liquid droplets encounter the dense surface of PP-1 (refer to Fig. 2.3b-3), the liquid is readily present at the surface, forming liquid bridges at the contact points between particles. This process enhances the cohesiveness of the powder, even at low liquid contents. Conversely, the porous surface of PP-3 (refer to Fig. 2.3b-4) allows liquid to permeate into the pores. Here, the absorbed liquid is not readily available at the surface to form liquid bridges, thereby exerting minimal influence on cohesion. Only when the pores become saturated does the IPA become available at the surface, resulting in liquid bridging that gradually enhances cohesiveness. These results underscore the importance of considering the properties of the polymerized product in the industrial HSBR when tailoring process characteristics.

2.4. Conclusion

In this study, the flow behavior of polypropylene (PP) reactor powder in a laboratory-scale horizontal stirred bed reactor (HSBR) was investigated using X-ray imaging. The influence of the agitator rotation speed, gas inlet flowrate, and liquid content on the flow behavior and phase holdup was evaluated, yielding the following conclusions:

- The overall flow behavior and phase holdup in the HSBR are strongly dictated by the agitation with the stirrer. Operation at increased rotation speed results in aeration of the bed, which in turn results in an increase in the mass flow of PP powder over the shaft.

- Gas injection through the inlet points at the bottom of the HSBR results in spouting behavior, which is more dominant for reactor powder with a smaller particle size (PP-1) compared to the powder with a larger particle size (PP-3). Spouting behavior results in reduced gas-solid contacting

and, in extreme cases, complete bypass, which will be disadvantageous for most applications.

- Agitation, as well as alternation of the impeller blade positions, influence the gas holdup and result in variations in power consumption within an agitator revolution. The degree of fluctuation in powder consumption decreases with increasing rotation speeds due to the aeration of the bed. The gas holdup at fixed agitator positions is extremely consistent for succeeding revolutions, underlining the dominance of the agitation on the overall flow behavior.

- The presence of liquid isopropyl alcohol deteriorates the flow behavior of the PP reactor powder. Liquid bridging at the contact points of particles results in a cohesive force that leads to the formation of lumps. The particle size and surface morphology highly influence the powders' susceptibility to liquid, as the flow behavior of PP powder with relatively small particle size and dense surface morphology is already strongly reduced at a liquid content of 1.25 vol%, while the flow behavior of the PP powder with larger particle size and porous surface is only reduced at a liquid content of 10 vol%.

The insights acquired from this work not only provide a further understanding of the flow behavior and phase holdup in HSBRs but can also serve as a valuable basis for optimizing, intensifying, and scaling HSBR systems for the manufacturing of high-quality PP resins on an industrial scale.

References

[1] J. Karger-Kocsis and T. Bárány, *Polypropylene Handbook Morphology, Blends and Composites: Morphology, Blends and Composites* (2019).

[2] K. Kulajanpeng, N. Sheibat-Othman, W. Tanthapanichakoon, and T. F. L. McKenna, *Multiscale modelling of multizone gas phase propylene (co)polymerization reactors—a comprehensive review,* The Canadian Journal of Chemical Engineering **100**, 2505 (2022).

[3] Statista, *Market volume of polypropylene worldwide from 2015 to 2022, with a forecast for 2023 to 2030,* (2023), accessed: 2024-5-24.

[4] F. B. Insights, *Polypropylene Market Size, Share & Trends*, Report (2020).

[5] J. J. Zacca, J. A. Debling, and W. H. Ray, *Reactor residence time distribution effects on the multistage polymerization of olefins—i. basic principles and illustrative examples, polypropylene,* Chemical Engineering Science **51**, 4859 (1996).

[6] J. Shepard, J. Jezl, E. Peters, and R. Hall, *Divided horizontal reactor for the vapor phase polymerization of monomers at different hydrogen levels,* (U.S. Patent 3 957 448, May 1976).

[7] J. Jezl, E. Peters, R. Hall, and J. Shepard, *Process for the vapor phase polymerization of monomers in a horizontal, quench-cooled, stirred-bed reactor using essentially total off-gas recycle and melt finishing,* (U.S. Patent 3 965 083, June 1976).

[8] M. Caracotsios, *Theoretical modelling of amoco's gas phase horizontal stirred bed reactor for the manufacturing of polypropylene resins,* Chemical Engineering Science **47**, 2591 (1992).

[9] A. B. Gorbach, S. D. Naik, and W. H. Ray, *Dynamics and stability analysis of solid catalyzed gas-phase polymerization of olefins in continuous stirred bed reactors,* Chemical Engineering Science **55**, 4461 (2000).

[10] C. J. Dittrich and S. M. P. Mutsers, *On the residence time distribution in reactors with non-uniform velocity profiles: The horizontal stirred bed reactor for polypropylene production,* Chemical Engineering Science **62**, 5777 (2007).

[11] R. A. Hutchinson, *Modelling of particle growth in heterogeneous catalyzed olefin polymerization.*, Thesis, University of Wisconsin-Madison (1990).

[12] C. M. van den Bleek, M.-O. Coppens, and J. C. Schouten, *Application of chaos analysis to multiphase reactors,* Chemical Engineering Science **57**, 4763 (2002), festschrift in Honour of Dr Wim van Swaaij.

[13] J. Wang, Y. Cao, X. Jiang, and Y. Yang, *Agglomeration detection by acoustic emission (ae) sensors in fluidized beds,* Industrial & Engineering Chemistry Research **48** (2009).

[14] J. N. Israelachvili, *Intermolecular and surface forces* (Academic Press, London ; San Diego, 1991).

[15] R. A. Hutchinson and W. H. Ray, *Polymerization of olefins through heterogeneous catalysis. vii. particle ignition and extinction phenomena,* Journal of Applied Polymer Science **34**, 657 (1987).

[16] N. P. Khare, B. Lucas, K. C. Seavey, Y. A. Liu, A. Sirohi, S. Ramanathan, S. Lingard, Y. Song, and C.-C. Chen, *Steady-state and dynamic modeling of gas-phase polypropylene processes using stirred-bed reactors,* Industrial & Engineering Chemistry Research **43**, 884 (2004).

[17] Z. Tian, X.-P. Gu, L. Feng, J.-P. Corriou, and G.-H. Hu, *Modeling and simulation of polypropylene particle size distribution in industrial horizontal stirred bed reactors,* Journal of Applied Polymer Science **125** (2012).

[18] M. F. Atan, M. Hussain, R. Abbasi, K. M.J.H, and M. Patah, *Advances in mathematical modeling of gas-phase olefin polymerization,* Processes **7**, 67 (2019).

[19] Y. Xi, Q. Chen, and C. You, *Flow characteristics of biomass particles in a horizontal stirred bed reactor: Part i. experimental measurements of residence time distribution,* Powder Technology **269**, 577 (2015).

[20] Y. Xi, Q. Chen, and C. You, *Flow characteristics of biomass particles in a horizontal stirred bed reactor: Part ii. modeling studies on particle residence time distribution and axial mixing,* Powder Technology **269**, 585 (2015).

[21] B. Laurent, J. Bridgwater, and D. Parker, *Convection and segregation in a horizontal mixer,* Powder Technology **123**, 9 (2002).

[22] B. Laurent and J. Bridgwater, *Performance of single and six-bladed powder mixers,* Chemical Engineering Science **57**, 1695 (2002).

[23] B. F. Laurent and J. Bridgwater, *Influence of agitator design on powder flow,* Chemical Engineering Science **57**, 3781 (2002).

[24] P. C. van der Sande, J. de Mooij, E. C. Wagner, G. M.H. Meesters, and J. R. van Ommen, *Single-photon emission radioactive particle tracking method for hydrodynamic evaluation of multi-phase flows,* Particuology , in press (2023).

[25] P. C. Van der Sande, E. C. Wagner, J. de Mooij, G. M. Meesters, and J. R. van Ommen, *Particle dynamics in horizontal stirred bed reactors characterized by single-photon emission radioactive particle tracking,* Chemical Engineering Journal **482**, 149100 (2024).

[26] M. Errigo, P. Lettieri, and M. Materazzi, *X-ray imaging techniques for gas–solid fluidized beds: A technical review,* Particuology (2023).

[27] K. Wu, E. Wagner, O. Ochkin-Koenig, M. Franck, D. Weis, G. Meesters, and J. R. Van Ommen, *Time-resolved x-ray study of assisted fluidization of cohesive micron powder: On the role of mechanical vibration,* Chemical Engineering Journal **470**, 143936 (2023).

[28] A. Helmi, E. C. Wagner, F. Gallucci, M. van Sint Annaland, J. R. van Ommen, and R. F. Mudde, *On the hydrodynamics of membrane assisted fluidized bed reactors using x-ray analysis,* Chemical Engineering and Processing: Process Intensification **122**, 508 (2017).

[29] M. Bieberle, F. Barthel, and U. Hampel, *Ultrafast x-ray computed tomography for the analysis of gas–solid fluidized beds,* Chemical Engineering Journal **189-190**, 356 (2012).

[30] J. Yates, D. Cheesman, P. Lettieri, and D. Newton, *X-ray analysis of fluidized beds and other multiphase systems,* KONA Powder and Particle Journal **20**, 133 (2002).

[31] R. L. Carr, *Evaluating flow properties of solids,* Chemical Engineering Journal **72**, 163 (1965).

[32] R. Kamphorst, P. C. van der Sande, K. Wu, E. C. Wagner, M. K. David, G. M. Meesters, and J. R. van Ommen, *The mechanism behind vibration assisted fluidization of cohesive micro-silica,* KONA Powder and Particle Journal **41**, 254 (2024).

[33] K. Wu, R. Kamphorst, A. Bakker, J. Ford, E. C. Wagner, O. Ochkin-Koenig, M. Franck, D. Weis, G. M. Meesters, and J. R. van Ommen, *Stirrer design for improving fluidization of cohesive powder: A time-resolved x-ray study,* Chemical Engineering Science **294**, 120069 (2024).

[34] P. M. Portillo, A. U. Vanarase, A. Ingram, J. K. Seville, M. G. Ierapetritou, and F. J. Muzzio, *Investigation of the effect of impeller rotation rate, powder flow rate, and cohesion on powder flow behavior in a continuous blender using PEPT,* Chemical Engineering Science **65**, 5658 (2010).

[35] D. Brunet, E. R. Vrscay, and Z. Wang, *On the mathematical properties of the structural similarity index,* IEEE Transactions on Image Processing **21**, 1488 (2012).

[36] P. Tegzes, R. Albert, M. Paskvan, A. L. Barabási, T. Vicsek, and P. Schiffer, *Liquid-induced transitions in granular media,* Physical Review E **60**, 5823 (1999).

[37] A. Castellanos, M. Sanchez, and J. Valverde, *The onset of fluidization for fine powders in rotating drums,* Materials Physics and Mechanics **3**, 57 (2001).

[38] A. Benkrid and H. S. Caram, *Solid flow in the annular region of a spouted bed,* AIChE Journal **35**, 1328 (1989).

[39] I. Albert, P. Tegzes, R. Albert, J. G. Sample, A. L. Barabási, T. Vicsek, B. Kahng, and P. Schiffer, *Stick-slip fluctuations in granular drag,* Physical Review E - Statistical Physics, Plasmas, Fluids, and Related Interdisciplinary Topics **64**, 9 (2001).

[40] C. M. Oprişan, B. Chiriac, V. Cârlescu, and D. N. Olaru, *Influence of the stiffness and the speed on the stick-slip process,* IOP Conference Series: Materials Science and Engineering **997**, 012016 (2020).

[41] P. C. Knight, J. P. K. Seville, A. B. Wellm, and T. Instone, *Prediction of impeller torque in high shear powder mixers,* Chemical Engineering Science **56**, 4457 (2001).

[42] T. Lichtenegger and S. Pirker, *Recurrence cfd – a novel approach to simulate multiphase flows with strongly separated time scales,* Chemical Engineering Science **153**, 394 – 410 (2016).

[43] T. Lichtenegger, E. Peters, J. Kuipers, and S. Pirker, *A recurrence cfd study of heat transfer in a fluidized bed,* Chemical Engineering Science **172**, 310 (2017).

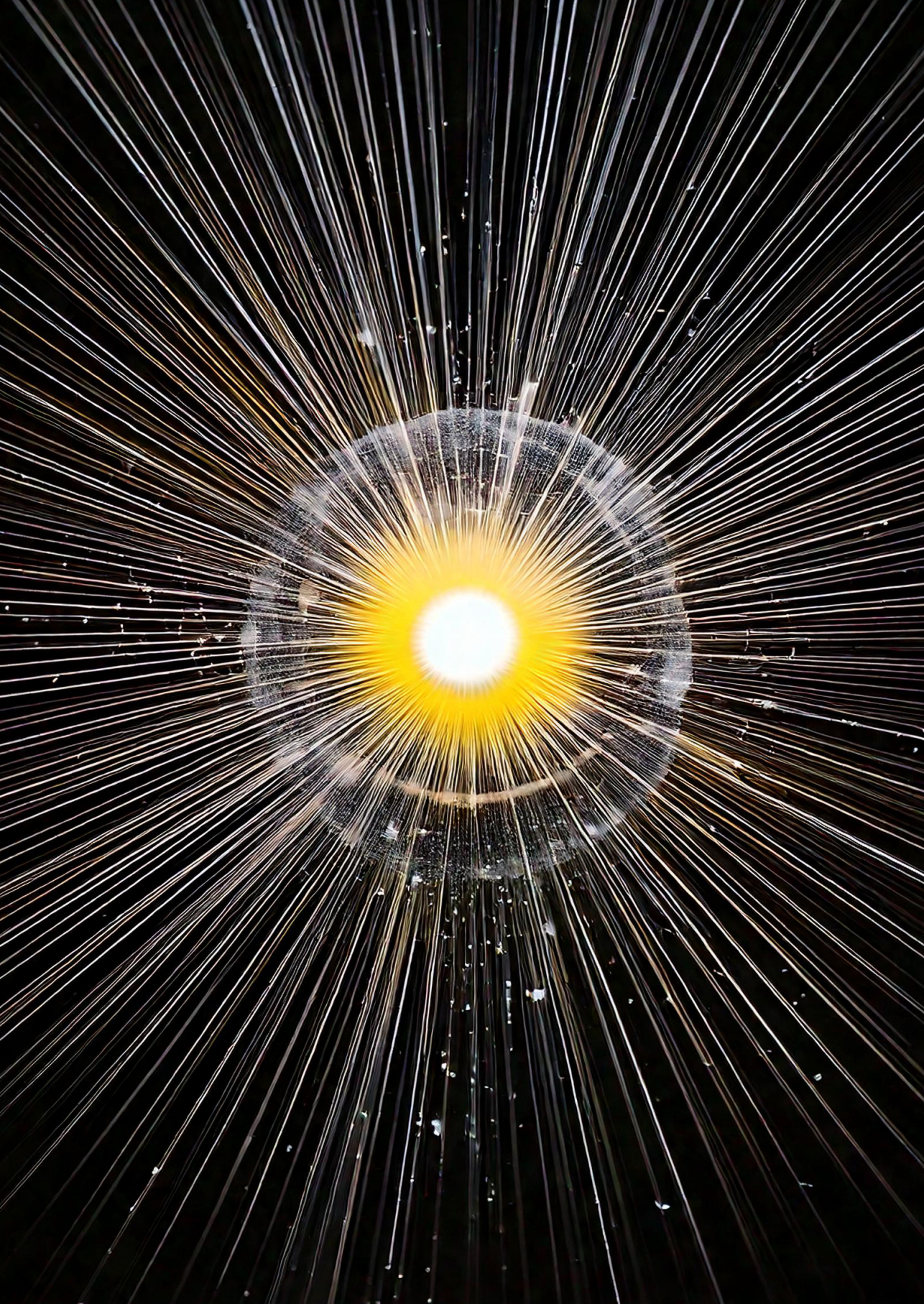

3

Single-photon emission radioactive particle tracking method for hydrodynamic evaluation of multi-phase flows

In the previous chapter, we used X-ray imaging to study the influence of the gas inlet flow rate and rotation speed on the gas holdup in the horizontal stirred bed reactor. However, X-ray imaging cannot provide insight into the behavior of individual particles. In this chapter, we employ a fundamentally novel experimental radioactive particle tracking method that allows flow field evaluation in multi-phase systems: single-photon emission radioactive particle tracking. This chapter first introduces the experimental setup of single-photon emission radioactive particle tracking and the method used to reconstruct the position. Then, the results of controlled experiments are discussed to validate the technique.

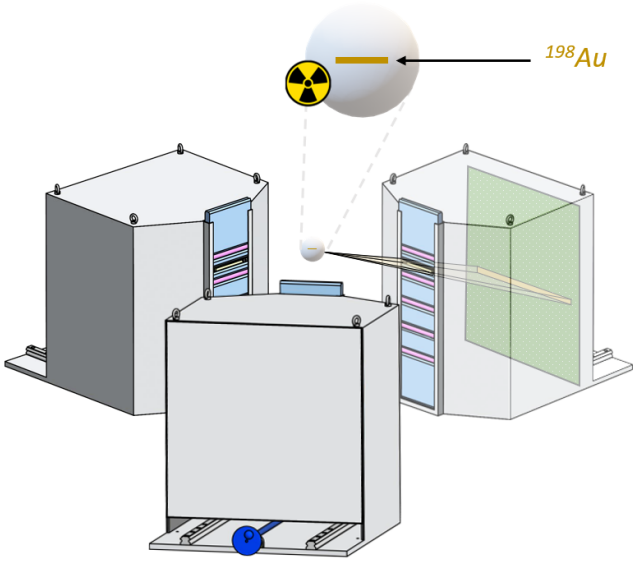

This chapter is published as P.C. van der Sande, J. de Mooij, E.C. Wagner, G.M.H. Meesters, and J.R. van Ommen, *Single-photon emission radioactive particle tracking method for hydrodynamic evaluation of multi-phase flows*, Particuology (2023).

Evaluation of the hydrodynamics of opaque multi-phase flows remains a challenging task, with implications for various industrial processes such as chemical processing, pharmaceutical, and mineral processing. Understanding how design and operational variables affect the complex behavior of multi-phase flow systems is essential for optimizing processing conditions and improving efficiency. Radioactive particle tracking (RPT) has been a proven measurement technique for evaluating hydrodynamics in multi-phase flow systems. However, a limitation of the classical RPT technique exists in the assumptions made in the simulation of the count rate received by the detectors in correcting for varying flow-induced fluctuations in the volume fraction of the dispersed phase, often encountered in industrial multi-phase flow systems. In this chapter, we employ a fundamentally novel experimental RPT method that directly uses detected incident photon hit locations for the reconstruction of the three-dimensional radioactive tracer particle position. We argue that this approach is inherently more robust as varying attenuation does not affect the reconstruction. The RPT setup consists of three identical γ-radiation slit collimator detectors that are placed equidistantly at 120° intervals. A subsequent calibration-experimentation procedure is established that allows reconstruction of the tracer particle position with spatial accuracy and precision in the order of 1 mm. We demonstrate the applications of this technique in evaluating hydrodynamics in multi-phase systems by characterizing the flow field of industrial-grade polypropylene reactor powder in a laboratory-scale horizontal stirred bed reactor.

3.1. Introduction

Multi-phase flows are widely encountered in various process industries such as chemical processing, petroleum refining, food processing, pharmaceutical, and mineral processing. Accurate modeling of hydrodynamics within multi-phase flow systems is essential for effective process design, scale-up, and optimization. However, current models include assumptions on particle and equipment scale that require experimental validation, preferably through non-invasive methods [1]. Traditional non-invasive optical techniques are not suitable for studying multi-phase flows with a large fraction of the particulate phase, often encountered in industrial applications, since the dense flows are opaque to visible light.

To overcome this limitation, non-invasive radiation-based techniques were developed to study multi-phase flow systems by tracking a single particle. These techniques, namely radioactive particle tracking (RPT), positron emission particle tracking (PEPT) [2, 3], and X-ray particle velocimetry [4, 5], were inspired by medical research. They involve introducing a single radiation-emitting or absorbing tracer particle, which is dynamically similar to the dispersed phase, into the system of interest. Detectors located around the system calculate the tracer particle's position time series through inverse reconstruction within an accuracy in the order of 1 mm [6, 7]. The acquired position time series allows for the evaluation of the hydrodynamic properties of interest.

In the case of RPT, the tracer particle contains radioactive material that emits γ-radiation of constant energy in all directions. RPT offers the advantage of using a wide selection of available tracer isotopes with characteristic photon energy, such as Sc-46, I-131, Cs-137, or Au-198 [8]. This allows for the development of tailored tracer particles that emit γ-radiation with an optimal photon energy for specific experimental conditions. This is an advantage over PEPT, which involves positron-electron annihilation photons with a fixed energy of 511 keV. X-ray particle velocimetry, on the other hand, utilizes X-ray imaging or tomography and provides simultaneous information on gas-solid distribution and single-particle dynamics. However, it requires tracer particles with a large, high-density core to induce sufficient X-ray absorption. In contrast, the mass of tracer isotope material embedded in an RPT tracer particle can be significantly lower. This characteristic facilitates the development of a tracer particle that is dynamically similar to the dispersed phase.

Generally speaking, RPT experimentation involves two successive steps: a calibration procedure and an experimental measurement. During the calibra-

tion procedure, the tracer particle is positioned at numerous known positions within the system of interest. The obtained calibration data set is then utilized to accurately reconstruct the tracer's position during the subsequent experimental measurement. In the experimental measurement phase, the tracer particle is introduced into the system, and the time-resolved tracer particle position time series is reconstructed [9].

Pioneering efforts in space-resolved three-dimensional RPT or computer-aided radioactive particle tracking (CARPT) were made by Lin *et al.* [10]. They developed photon-counting instrumentation that utilized the relationship between γ-ray intensity and the distance between the particle and the detector. The conventional setup consisted of twelve 51×51 mm sodium iodide scintillation detectors arranged in a staggered configuration. A Sc-46 ball coated with epoxy was used as the tracer particle to study re-circulation patterns in gas-fluidized beds. Before experimentation, an in situ calibration procedure was performed to establish a monotonic relationship between the count rate and the distance of the tracer to each detector. Devanathan *et al.* [11] refined the method by extending the number of detectors to sixteen and used it to investigate liquid circulation and turbulence in bubble columns. They employed a Sc-46 core embedded in a 2.4 mm polypropylene sphere with an air gap as a neutrally buoyant tracer particle. From the acquired tracer particle positions, Lagrangian auto-correlations, integral time scales, and radial and axial turbulent dispersion coefficients were computed.

In subsequent years, the established method was utilized in various studies to investigate flow fields in fluidized beds and bubble columns [12], spouted beds [13], three-phase fluidized beds [14], liquid fluidized beds [15], circulating fluidized bed risers [16], and stirred tanks [17, 18]. Efforts were made by Dudukovic [1] to further improve the spatial accuracy and precision by doubling the number of detectors to 32. They also employed a calibration procedure where the tracer was positioned at 1000 known in situ positions while recording the intensity obtained at each detector. This established approach utilizes an overabundance of detectors and employs a weighted least-squares method to calculate the tracer's position [17]. This approach uses significantly more detectors than the suggested minimum of three. Although improving the precision of the measurement, using a larger number of detectors, along with the associated electronic hardware, significantly increases the cost and complexity of RPT experimentation [19].

RPT experimentation has found various applications in chemical reactor

engineering research in recent years [6, 20–26]. Despite the growing interest in RPT, the fundamentals and design parameters for the method have not undergone significant changes [8]. Instead, efforts have been focused on improving the reconstruction methodology in terms of spatial accuracy and precision, computational time, and its ability to cope with fast fluctuations in volume fraction, which are often encountered in multi-phase flow systems. Through an analytic approach, Monte Carlo simulations have been widely used in classical RPT experimentation to analyze the accuracy and improve the reconstruction methodology [27, 28]. Several improvements have been made to the Monte Carlo method; for example, the method was extended with a Real Coded Genetic Algorithm to reduce computational time [29]. Furthermore, machine learning methods have been proposed to improve reconstruction accuracy and computation time. Godfroy *et al*. [30] demonstrated in an earlier study that a feed-forward neural network can contribute to extremely fast position calculations. Recently, Yadav *et al*. [31] showed that reconstruction algorithms based on support vector regression (SVR) and relevance vector regression (RVR) promote accurate position reconstruction.

In this work, we employ a fundamentally novel experimental radioactive particle tracking method that allows reconstruction based on the photon hit location on a two-dimensional scintillation crystal detector plate instead of classical RPT reconstruction based on the count rate. Therefore, we aim to improve RPT experimentation through a physical approach. We argue that the described method is inherently more robust, as varying attenuation caused by flow-induced fluctuations in volume fraction of the dispersed phase, such as those caused by rising bubbles between the tracer particle and detector, does not affect the reconstruction. As a result, it circumvents the need for extensive Monte Carlo dose-rate simulations or neural network optimization to cope with fast fluctuations in volume fraction. Section 3.2.1 describes the RPT setup and reconstruction methodology. Subsequently, the reconstruction results are presented and discussed in Section 3.3. To demonstrate the potential applications of the technique, an RPT case study with a horizontal stirred bed reactor is presented in Section 3.4. Finally, the work is summarized, and concluding remarks are provided in Section 3.5.

3.2. Methodology

3.2.1. Experimental setup

The RPT technique [1] employed in this work is based on the Single Photon Emission Computed Tomography (SPECT) technique, which is commonly used in the medical field [32]. The RPT setup consists of three identical γ-radiation detectors that are equidistantly placed around a field of view (FOV) at approximately 120° intervals, as depicted in Fig. 3.1.

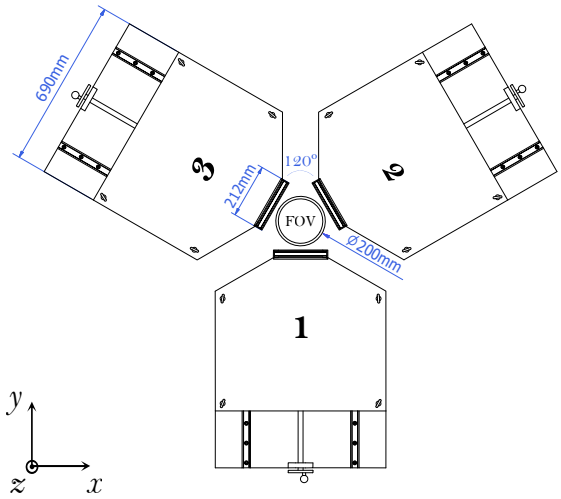

Figure 3.1: Top view representation of the RPT setup. The three detectors are placed equidistantly around a FOV at approximately 120° intervals.

Each detector comprises a casing, a slit collimator made of lead shielding plates and spacers, a scintillation crystal, and photo-multiplier tubes, as depicted in Fig. 3.2. The detector casing is constructed with 6 mm lead covered with 3 mm stainless steel. The slit collimator height, which refers to the distance between the lead shielding plates, can be adjusted using spacers of varying heights (1, 2, or 4 mm) to control the amount of γ-radiation that passes through the collimator. In this study, the detectors are equipped with a single slit positioned near the top of the lead shielding, measuring 212 mm in length and 4 mm in height, resulting in a high signal intensity at the scintillation crys-

[1] The RPT technique at the Delft University of Technology was developed by Prof. R.F. Mudde, Prof. F.J. Beekman, and E.C. Wagner. Numerous students have contributed to hardware and software development, notably R. Noordman (2014), S. van Hoesel (2015), J. de Winter (2015), S. Bechan (2016), and J. Grasmeijer (2017). In this work, the technique was first applied in a real application.

tal. The lead shielding plates have a thickness of 25 mm, effectively attenuating the γ-radiation that hits them. The scintillation crystals have a size of 550×550 mm and are coupled to an array of photomultiplier tubes (PMTs) that convert the detected γ-radiation to an amplified measurable electrical signal. The detectors are sensitive to γ-radiation with photon energies up to 600 keV.

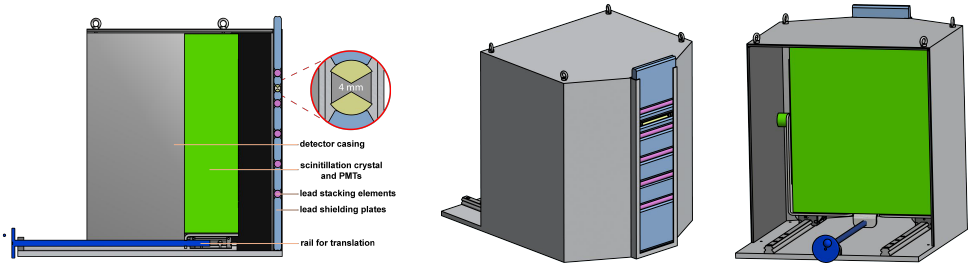

(a) Side view (b) Orthographic view (c) Back view

Figure 3.2: Schematic representation of a detector. The gray color represents the detector casing, the blue-gray color the lead shielding plates, the purple color the lead plate stacking elements, the green color the scintillation crystal and photomultiplier tubes, and the dark blue color a rail to translate the scintillation crystal. The 4 mm slit collimator is indicated in Fig. (a).

The detectors have a detection efficiency that is the result of two components. The first component is the intrinsic detector efficiency, which is the ratio of the incident γ-photons and registered photons. The detector efficiency is dependent on the energy of the incident photons and thus differs for various tracer isotopes. The second component is the geometrical efficiency. Due to the slit collimators, only a fraction of the emitted photon reaches the scintillation crystal. The geometrical efficiency is expressed as the ratio of the solid angle of the slit and the solid angle of a full sphere. The absolute detection efficiency is the multiplication of the detector and geometrical efficiency. The scintillation crystals can be translated forward or backward relative to the collimator to alter the magnification of the projection. If the crystal is moved closer to the collimator, the magnification is decreased. Conversely, if the crystal is moved farther away from the collimator, the magnification is increased. The current setup configuration has the scintillation crystal positioned at a distance of 400 mm to the slit collimator, allowing for the desired FOV to be captured.

In this work, two radioactive tracer particles were used for calibration-validation and experimentation purposes, respectively. The tracer particles were manufactured by embedding 1.6 mg gold in a 1.8 mm polystyrene bead. The in-

creased mass of the tracer by inserting the gold core was compensated for by leaving an air pocket in the particle. Following neutron irradiation at the Reactor Institute Delft, the stable gold cores were activated to the radioactive isotope Au-198 with an activity of 1 MBq for calibration-validation purposes and 27.5 MBq for experimentation purpose. Au-198 has been widely considered as a preferred tracer isotope in RPT experimentation since it emits relatively low energy photons with an energy of 412 keV and has a short half-life time of approximately 2.7 days [19].

$$^{197}_{79}\mathrm{Au} + ^{1}_{0}\mathrm{n} \rightarrow ^{198}_{79}\mathrm{Au} \xrightarrow[\gamma,\beta^-]{} ^{198}_{80}\mathrm{Hg}$$

At early stages in the design of RPT experiments, radiation safety should be considered. The tracer particle activity should be carefully considered based on the conditions and requirements of the experiment at hand, and a high activity should only be used if it can be justified. It is for this reason that a 1 MBq tracer particle is used for the static calibration and low-velocity validation measurements. The 1 MBq tracer particle activity was carefully considered to minimize the radiation dose rate for the operators during the experiments. For the reactor experiments, the tracer particle with an activity of 27.5 MBq is required to reconstruct the trajectory with a sufficiently high sampling frequency and, therefore, justified. To guarantee a safe working environment and minimize the operator radiation dose, the setup was controlled from a workstation outside the setup room.

3.2.2. Reconstruction of tracer particle position

When a γ-radiation emitting tracer particle is positioned within the FOV, radiation passing through the slit collimators hits the scintillation crystals, as schematically depicted in Appendix Fig. B.1. Each photon that hits one of the scintillation crystals is absorbed and re-emitted within the visible light spectrum. Subsequently, a photo-diode converts the re-emitted light into an electrical current corresponding to the energy of the incident photon. The energy of the incident photon can be determined from the amplitude of the electrical signal. The coordinates of the incident photon hit are determined from the distribution of the signals coming from the PMTs. The data acquired with the detectors is processed by an in-house LabVIEW program, which produces a list containing the xz-coordinates of the activated pixels of each detector, the photon energies, and times of detection.

The coordinates of all photon hits detected by a scintillation crystal can be combined to create a two-dimensional projection of the incoming radiation consisting of 512×512 pixels with a pixel size of 1.072 mm. To reconstruct the position of the radioactive tracer particle from its projections on the three detectors, a backward projection method is employed. The workflow for reconstructing the tracer particle position from the detector output data is schematically depicted in Fig. 3.3.

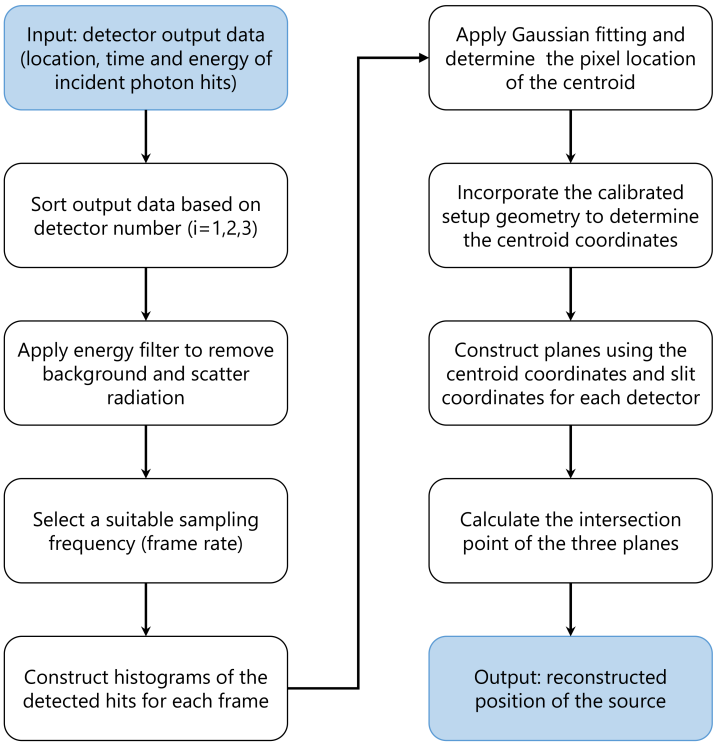

Figure 3.3: The reconstruction data processing workflow: from detector output data to the reconstructed position.

First, the raw data is sorted for the detector where the photon hit was detected. Then, an energy filter is applied to remove hits originating from the background and scatter radiation. The energy filter bandwidth is determined by taking into consideration the characteristic photon energy of the tracer isotope that is used in the experiments. In this work, an energy filter bandwidth of 400 - 600 keV is used. Next, the reconstruction sampling frequency is selected, i.e., the number of reconstructions performed per second. The maximum sampling

frequency achievable for reconstruction is directly related to the count rate detected by the detector, which in turn is a function of the source activity and distance to the detector [33]. Due to the slit collimator detector configuration, the projection of the tracer particle on each scintillation crystal appears as a horizontal line at a specific height. Only the height of the projected line is required to reconstruct the tracer particle position, and therefore, the two-dimensional detector image is reduced to a one-dimensional image. For each frame, the number of detected photons is counted at each detector z-coordinate pixel value. An example of a histogram of detected photons originating from a static tracer particle is plotted in Fig. 3.4. The detector configuration and stochastic nature of radiation result in a Poisson distribution. The Poisson distribution can be approximated with a Gaussian model for sufficiently large data sets. Therefore, a Gaussian model is fitted to the distribution, represented by the red line in Fig. 3.4. The centroid of the Gaussian fit best represents the height of the line projection, and therefore, the pixel value of the centroid is utilized in the position reconstruction.

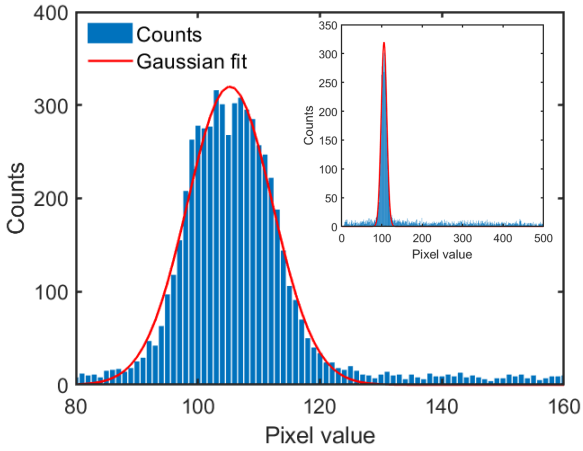

Figure 3.4: The distribution of detected photons and corresponding Gaussian fit for a static grid point. The Gaussian fit centroid pixel value is used as input in the reconstruction algorithm.

To incorporate the output from the three detectors, a geometric origin is defined as the midpoint of the FOV. The locations of the scintillation crystals and slit collimators relative to the origin are calculated. For each detector ($i = 1, 2, 3$), a plane is reconstructed using a set of three points indicated in Fig. 3.5a: P_i represents the Gaussian fit centroid pixel value in the center of the detector, while L_i and R_i correspond to the middle points on the left and right side of the slit, respectively. By constructing a plane through these points for

all three detectors simultaneously, a unique intersection point is formed. The coordinates of this intersection point represent the reconstructed position of the radioactive tracer particle, as shown in Fig. 3.5b. Each set of points, $\mathbf{P}_i$, $\mathbf{L}_i$ and $\mathbf{R}_i$ results in the plane equation:

$$d_i = \mathbf{n}_i \cdot \mathbf{x} \tag{3.1}$$

where $\mathbf{x}$ is the general xyz-position vector.

$$\mathbf{a}_i = \mathbf{L}_i - \mathbf{R}_i \tag{3.2}$$
$$\mathbf{b}_i = \mathbf{L}_i - \mathbf{P}_i \tag{3.3}$$
$$\mathbf{n}_i = \mathbf{a}_i \times \mathbf{b}_i \tag{3.4}$$
$$d_i = \mathbf{L}_i \cdot \mathbf{n}_i \tag{3.5}$$

The system of equations can be written in matrix representation which provides a straightforward manner of solving for the plane intersection point $\dot{x}$

$$\boldsymbol{N}\dot{\boldsymbol{x}} = \mathbf{D} \tag{3.6}$$
$$\begin{pmatrix} \mathbf{n_1}^T \\ \mathbf{n_2}^T \\ \mathbf{n_3}^T \end{pmatrix} \begin{pmatrix} \dot{x} \\ \dot{y} \\ \dot{z} \end{pmatrix} = \begin{pmatrix} d_1 \\ d_2 \\ d_3 \end{pmatrix} \tag{3.7}$$

The intersection point of the planes, i.e., the reconstructed position of the tracer particle, is then computed from

$$\dot{\boldsymbol{x}} = \mathbf{N^{-1}D} \tag{3.8}$$

3.2.3. Setup calibration

The coordinates of the reconstructed position are calculated using System of Equations 3.7. However, these calculations can be affected by potential inaccuracies in the hand-measured positions of $\mathbf{L}_i$ and $\mathbf{R}_i$. To ensure reconstruction with high spatial accuracy and precision, calibration of the RPT setup geometry is required. The calibration process aims to correct for errors in the spatial geometry of the setup caused by manual measurements. This is achieved by minimizing the sum of the squares of the residuals for a large number of true tracer particle positions and the corresponding reconstructed tracer particle positions using a constrained non-linear least-squares optimization algorithm

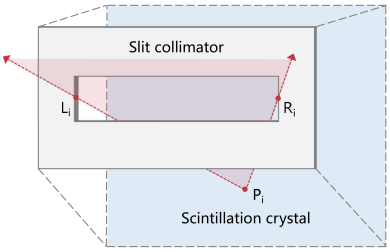

(a) The points used to construct a plane: (P_i) location of the hit on the detector; (L_i) left side; and (R_i) right side of the slit.

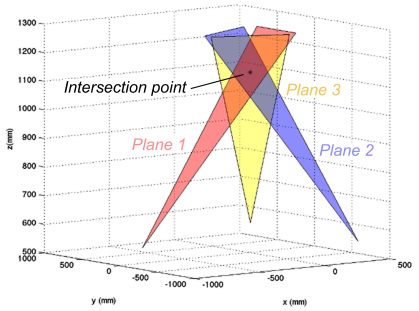

(b) Intersection point of the planes constructed from the three detectors. Adapted from [2].

Figure 3.5: The tracer particle position is reconstructed by constructing a plane from each detector and computing the unique intersection point of these planes.

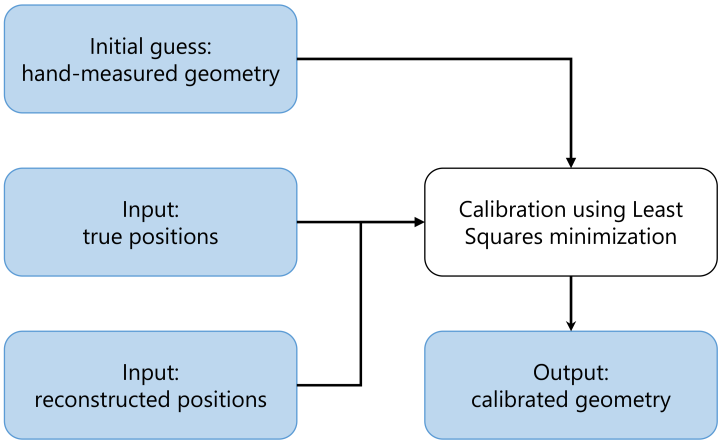

Figure 3.6: The calibration processing workflow. Calibration requires an initial guess geometry and true and reconstructed tracer particle locations as input. The algorithm returns a calibrated geometry.

in MATLAB. The calibration workflow is illustrated in Fig. 3.6.

A three-dimensional cylindrical grid of 95 predefined tracer particle positions and reconstructed positions was constructed. For this purpose, a 300 mm circular solid aluminum optical breadboard with holes spaced 25 mm apart on the diagonal was mounted on a rotation table, which was then mounted on a lifting table. The 1 MBq Au-198 tracer particle (see Section 3.2.1) was placed

[2] R. Noordman, Setting up SPECT measurements – tracking particles inside fluidized beds, M.Sc. thesis (2014).

in a plastic shielding and mounted on top of a 300 mm aluminum bar with a screw thread, as shown in Fig. 3.7.

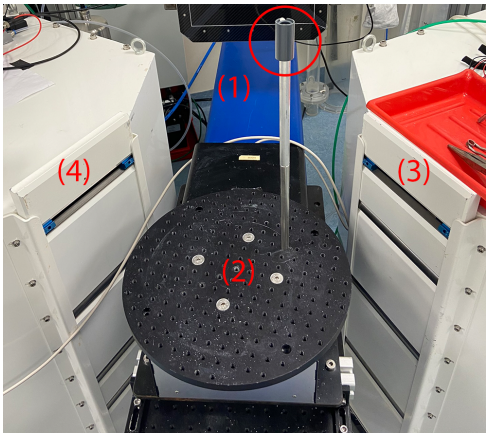

Figure 3.7: The experimental calibration setup: (1) plastic container containing the tracer particle; (2) rotation table; (3) slit of detector 1 and; (4) slit of detector 3.

The cylindrical grid was constructed by incrementally translating the tracer particle in the xy and xz-planes and successively rotating the tracer particle in the xy-plane. The coordinates of the known tracer particle positions are denoted as the true positions. At each grid position, the emitted γ-radiation was detected for a duration of 21 s to allow accurate Gaussian fitting and centroid determination. The position was reconstructed using the workflow described in Section 3.2.2. A selection of 35 true and reconstructed positions was used as input for the optimization algorithm. As described later in Section 3.2.4, the full grid consisting of all the true positions and reconstructed positions was used for the validation of the method.

Finally, an initial guess of the hand-measured setup geometry is required. The geometry is described by six (x,y,z) coordinates, representing the left and right sides of the slit collimators (see Fig. 3.5a), as well as three (x,y) coordinates corresponding to the middle points of the detectors. A constrained nonlinear least squares optimization method in MATLAB is used to minimize the sum of the squares of the residuals by varying the hand-measured geometry parameters with upper and lower bound values of 50 mm. The output of the algorithm is a calibrated set of geometry values encompassing the spatial orientation of the detectors. These calibrated geometry values substitute the initial guess hand-measured values and are utilized in subsequent processing steps.

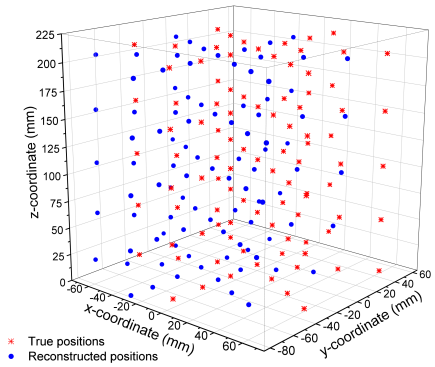

(a) Three-dimensional scatter of the true grid positions and reconstructed grid positions before calibration.

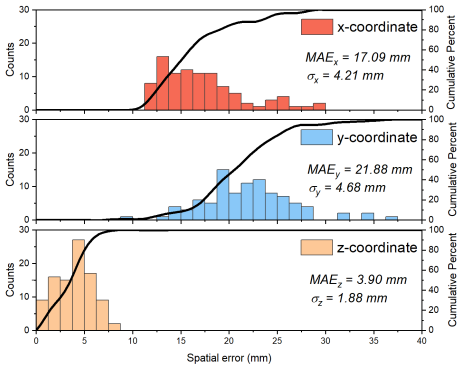

(b) Absolute spatial error of the true position relative to the reconstructed position before calibration.

Figure 3.8: Reconstruction of the 95 grid positions before calibration.

3.2.4. Method validation

The performance of the setup is validated using both static and dynamic experiments, utilizing the calibrated geometry. The validation process consists of two parts. Firstly, the spatial accuracy and precision of the calibrated setup are assessed under static conditions using the complete cylindrical grid. As outlined in Section 3.2.3, the grid comprises 95 positions distributed within a volume of 75 mm radius and 200 mm height. For each grid point, the absolute error between the coordinates of the true position and the reconstructed position is calculated, allowing evaluation of the spatial accuracy and precision of the reconstruction.

Secondly, dynamic validation experiments are conducted. Employing the same experimental setup as the static validation experiments (see Fig. 3.7), the tracer particle is horizontally rotated at varying radii and angular velocities while maintaining a fixed height in the middle of the FOV. The acquired data from both static and dynamic validation experiments is processed at different reconstruction sampling frequencies to examine the relationship between spatial precision and sampling frequency.

3.3. Results and discussion

3.3.1. Non-calibrated reconstruction

To emphasize the importance of calibrating the RPT setup geometry, reconstruction of the grid positions (see Section 3.2.3) was performed using the hand-measured geometry. The reconstruction processing workflow was applied,

with the hand measured geometry as input, to reconstruct the tracer particle positions. The true positions and the reconstructed positions before calibration are plotted in Fig. 3.8a.

It can be observed that the reconstructed positions (in blue) deviate significantly from the true positions (in red). Notably, the spatial error becomes more pronounced for lower z-coordinate values. During the reconstruction, the intersection point of three planes originating from the three detectors is determined. The spatial error becomes infinitely large if the three planes are parallel to each other. When the planes are nearly parallel, as is the case for z-coordinate values close to the slit height, even slight deviations in the plane angles result in substantial variations in the coordinates of the intersection point. Consequently, the reconstruction exhibits poor spatial accuracy and precision for lower z-coordinate positions. The spatial error, represented by the absolute distance between the true grid point and the corresponding reconstructed grid point, is illustrated for the x, y, and z coordinates in Fig. 3.8b. It can be observed that the mean absolute errors (MAE) are 17.09, 21.88, and 3.90 mm for the x, y, and z-coordinate, respectively. Moreover, the standard deviations (σ) are 4.21, 4.68 and 1.88 mm for the x, y and z-coordinate, respectively. The cumulative percentage curve shows that 90 percent of the grid points have a spatial error smaller than 24 mm, 26 mm, and 6 mm in x, y, and z, respectively. The MAE and standard deviation in x and y exceed the acceptable range for the desired particle tracking applications in lab-scale systems. Thus, reconstruction of the tracer particle position using the hand-measured setup geometry does not yield satisfactory spatial accuracy and precision.

3.3.2. Setup calibration

To improve the spatial accuracy and precision of the reconstruction, a calibration workflow was implemented as detailed in Section 3.2.3. By minimizing the absolute error between the true position and the reconstructed position for the selected 35 grid points, the constrained optimization algorithm returns calibrated geometry values. The hand-measured and calibrated spatial orientation of the three detectors is illustrated in Appendix Fig. B.2. It can be observed that the optimization algorithm yields a geometry in which each detector undergoes slight translation and rotation relative to its orientation in the hand-measured geometry, effectively correcting for measurement inaccuracies.

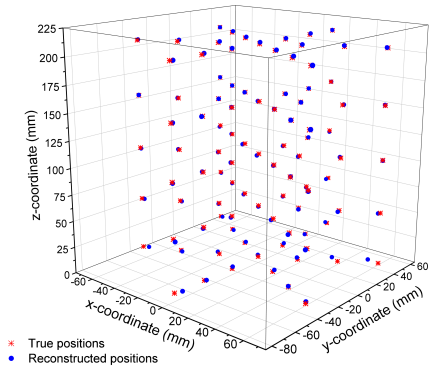

(a) Three-dimensional scatter of the true grid positions and reconstructed grid positions after calibration.

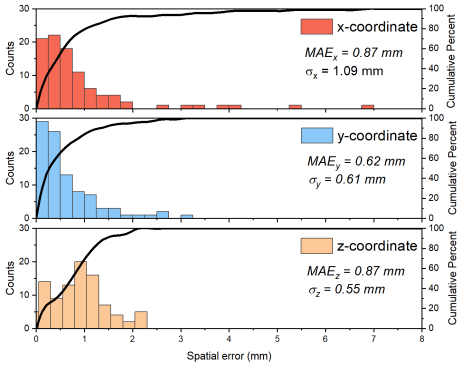

(b) Absolute spatial error of the true position relative to the reconstructed position after calibration.

Figure 3.9: Reconstruction of the 95 grid positions after calibration.

3.3.3. Method validation

Static validation

In the implemented method, the calibrated geometry is utilized for the reconstruction of the tracer particle positions. As explained in Section 3.2.4, the tracer particle was positioned at 95 known locations to validate the static reconstruction. The true positions and the reconstructed positions after calibration are depicted in Fig. 3.9a. It can be observed that for a large number of the grid points, the reconstructed positions (in blue) overlap with the true positions (in red), which is in sharp contrast to the reconstruction before calibration (Fig. 3.8a), in which the positions deviate significantly. This qualitative observation demonstrates substantial improvement in spatial accuracy achieved through calibration.

To assess the spatial accuracy quantitatively, the absolute spatial error between the reconstructed position and the true position is presented for the x, y, and z-coordinate in Fig. 3.9b. It can be observed that the mean absolute errors (MAE) are significantly reduced to 0.87, 0.62, and 0.87 mm for the x, y, and z-coordinate, respectively. Consequently, calibration has reduced the MAE by a factor of 20, 35, and 4 in x, y, and z, respectively, compared to the reconstruction before calibration. Similarly, the standard deviations (σ) after calibration are reduced to 1.09, 0.61 and 0.55 mm for the x, y and z-coordinate, respectively. This demonstrates that calibration improves both the spatial accuracy and the spatial precision of the reconstruction. The cumulative percentage curve shows that 90 percent of the grid points exhibit a spatial error smaller

than 1.5 mm in x and z and smaller than 1.3 mm in y. Fig. 3.9a also illustrates that lower z-coordinate grid points are associated with higher spatial errors in x and y, similar to the reconstruction before calibration. Therefore the desired volume of interest must be placed above the detector slits. Yet, the calibration yields satisfactory spatial accuracy and precision.

The aforementioned reconstruction process involves determining the tracer particle position based on the counts acquired over a sampling time of 21 s. Consequently, the sampling frequency of this reconstruction is approximately 0.05 frames per second (fps). In this case, all the counts detected during the measurement time window are collectively utilized to calculate a single reconstructed position. However, since many applications involve dynamic scenarios, it is desirable to increase the sampling frequency to be able to reconstruct the trajectory of a dynamic tracer particle with sufficient accuracy and precision. Thus, the entire grid is reconstructed at sampling frequencies of 0.125 fps, 0.5 fps, 2 fps, and 4 fps. Fig. 3.10 presents a two-dimensional top-view of the full grid, showcasing the true positions (in red) and the reconstructed positions (in blue) for the different sampling frequencies.

It can be observed that the sampling frequency has a significant impact on the spatial precision of the reconstruction. When the sampling frequency increases from 0.05 fps to 0.125 fps, the 285 reconstructed positions (3 for each of the 95 grid points) are closely clustered around their respective true positions, resulting in a low MAE (1.45 mm) and standard deviation (1.45 mm). This demonstrates that a high level of spatial precision is achieved. However, as the sampling frequency further increases to 0.5 fps, 2 fps, and 4 fps, the number of reconstructed positions increases while the spatial precision decreases. This results in the reconstructed positions being loosely scattered around the true positions, leading to a higher MAE and standard deviation. The decrease in spatial precision is attributed to the reduction in the number of counts (i.e., detected γ-ray photons) available for each frame during the reconstruction. With a higher sampling frequency, the same number of counts is now distributed over a larger number of successive frames, leading to the availability of fewer counts per frame. Consequently, the Gaussian model is fitted to a smaller data set, negatively influencing the accuracy of the fit. This effect is observable by comparing the reconstruction of a single grid point for a sampling frequency of 0.125 fps and 2 fps, as depicted in Fig. 3.11.

At a sampling frequency of 0.125 fps, the large number of counts allows the Poisson distribution to be approximated accurately with a Gaussian model. In

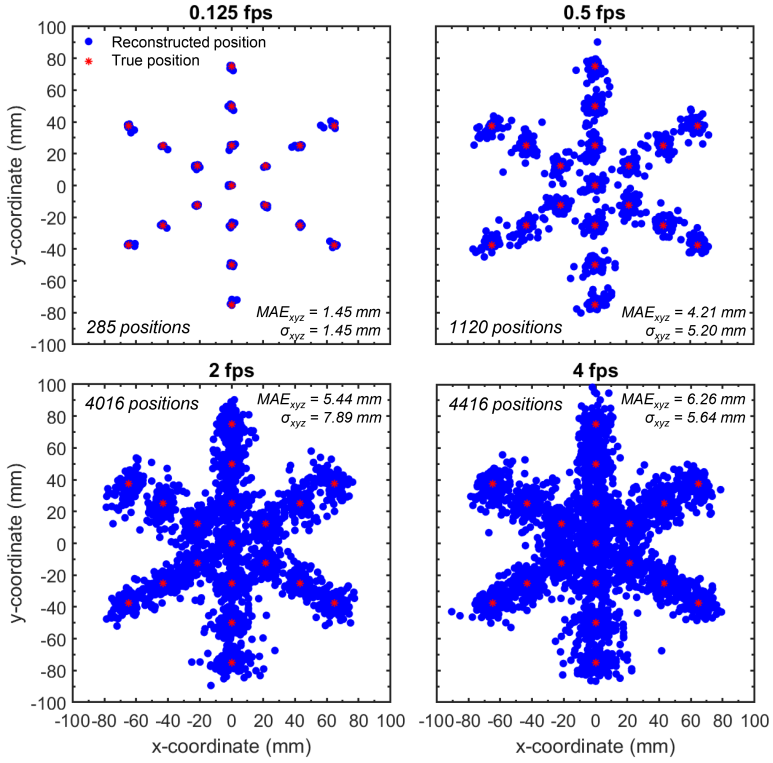

Figure 3.10: Reconstruction of true positions and reconstructed positions of the 1 MBq tracer particle with a sampling frequency of 0.125, 0.5, 2, and 4 fps. The number of reconstructed positions, Pythagorean mean absolute error (MAE$_{xyz}$), and standard deviation σ_{xyz} are indicated in each sub-figure.

contrast, when the sampling frequency is increased to 2 fps, the underlying distribution is poorly sampled, resulting in a Gaussian fit with reduced confidence. Mostoufi *et al.* [33] showed that the number of recorded incident photon hits is directly proportional to the sampling time of the reconstruction. Furthermore, they demonstrated that the spatial precision is inversely proportional to the square root of the sampling time. The same fundamental relationship between the spatial precision and reconstruction sampling time is observed here by comparing the standard deviation for the sampling frequencies of 0.125 fps and 0.5 fps.

As the sampling frequency is further increased, the number of counts in some segments becomes insufficient for reliable Gaussian fitting and reconstruction of the tracer particle's position. This phenomenon is evident when

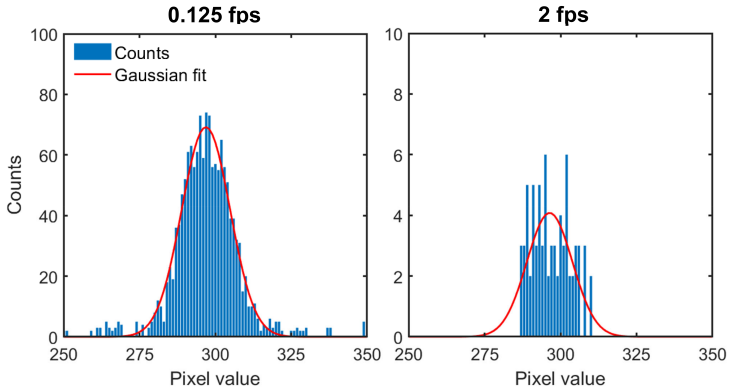

Figure 3.11: Example of the histogram and Gaussian fit for a single grid point reconstructed with a sampling frequency of 0.125 fps (left) and 2 fps (right).

comparing the reconstructions at 2 fps and 4 fps in Fig. 3.10. Increasing the sampling frequency by a factor of two should also lead to a proportional increase in the number of reconstructed positions. However, as can be observed, the number of reconstructed positions only increases by 10%, indicating that a large number of attempted reconstructions do not result in a reconstructed position due to unsuccessful Gaussian fitting. Interestingly, the standard deviation of the error decreases from 7.89 mm to 5.64 mm. This is attributed to the large number of failed reconstructions at a sampling frequency of 4 fps. The frames that have an extremely low number of counts at a sampling frequency of 2 fps result in a reconstructed position with poor spatial precision, essentially becoming an outlier in the data set. When trying to reconstruct these positions at an even higher sampling frequency, they can no longer be reconstructed, resulting in the outliers being discarded from the data set and thereby improving the overall spatial precision. Notably, further increasing the sampling frequency would result in a further decrease in the number of reconstructed positions, which is highly undesirable if one would like to reconstruct the trajectory of a moving tracer particle.

However, the above is not necessarily a limitation of the RPT method. As described earlier, the spatial precision is inversely proportional to the square root of the sampling time. To improve the spatial precision, or conversely, the sampling frequency, with a factor of 2, an increase in the number of detected incident photons with a factor of 4 is required. As the number of detected photons is directly proportional to the source's activity, improved precision can be accomplished by increasing the activity of the tracer particle. This can be

achieved by either increasing the mass of the radionuclide or extending the activation time of the tracer.

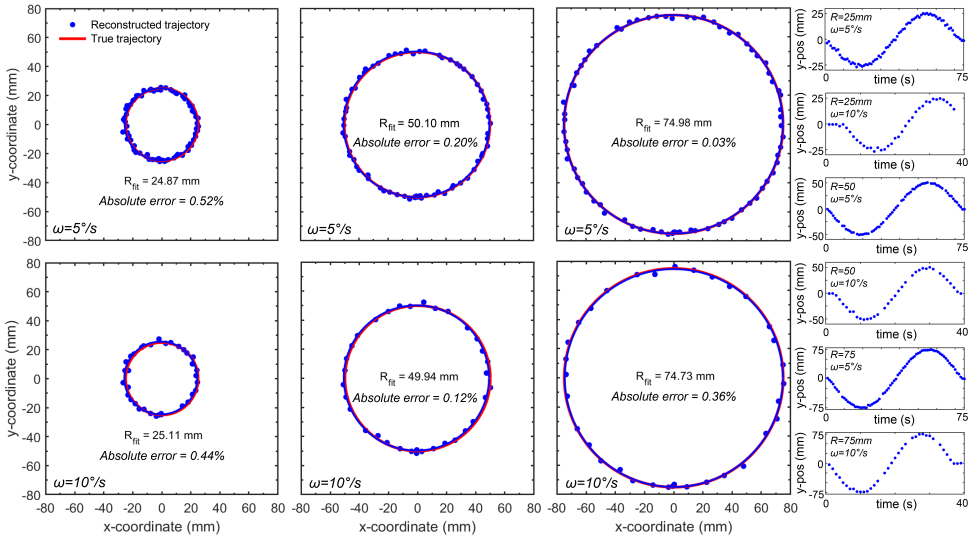

Figure 3.12: Reconstruction of the true and reconstructed trajectory for horizontal rotation at 25, 50 and 75 mm radii and angular velocity of 5° and 10° per second with a sampling frequency of 1 fps. At the right, the temporal evolution of the y-position is shown for one rotation for each measurement.

Dynamic validation

The aforementioned reconstructions focused on a static tracer particle. However, since most applications are dynamic, it is crucial to validate the technique's performance in reconstructing the trajectory of a moving tracer particle. Therefore, a series of dynamic experiments were conducted in which the 1 MBq tracer particle was horizontally rotated at radii of 25, 50, and 75 mm, with angular velocities of 5 and 10 degrees per second. The true trajectories and the corresponding reconstructed trajectories are presented in Fig. 3.12 for the different radii and angular velocities.

The true trajectory of the tracer particle is represented by a red circle, while the reconstructed positions are depicted as blue scatter dots in Fig. 3.12. To evaluate the spatial precision of the reconstruction, the reconstructed positions were fitted to a circle, indicated by the blue circles in the figure, with their corresponding radii displayed. The close alignment between the true trajectory and the reconstructed trajectory indicates a high level of spatial precision. No instances of poorly reconstructed positions were observed across all cases.

To quantify the spatial precision, the absolute percentage errors between the true radii and the fitted radii were computed. The error values range from 0.03% (R = 75 mm, ω = 5° per second) to 0.52% (R = 25 mm, ω = 5° per second), emphasizing reconstruction with excellent spatial precision. Moreover, from the temporal evolution of the y-coordinate, it can be observed that the reconstruction correctly captures the trajectory in time.

During the reconstruction time window, the movement of the tracer particle introduces a spread of radiation over a larger area of the detector, resulting in a Gaussian fit with a lower peak and increased Full Width Half Maximum (FWHM). This phenomenon shares similarities with motion blur observed in optical cameras. Consequently, the reconstructed position of a moving tracer particle represents an average position rather than an instantaneous one. Fig. 3.13 depicts the obtained distribution of counts and the corresponding Gaussian fit for a relatively low and high linear velocity.

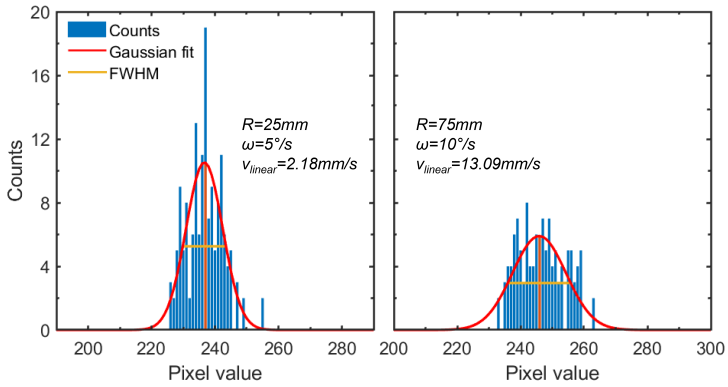

Figure 3.13: Influence of linear velocity on the distribution of counts and Gaussian fit for the horizontal rotation experiments with a 1 MBq tracer particle. Reconstruction is performed with a sampling frequency of 1 fps.

When comparing the two cases, it can be observed that the count distribution is narrower (FWHM = 13 px) and exhibits a higher peak when the linear velocity is low, which is the case for a small radius (25 mm) and low angular velocity (5° per second). Conversely, when the linear velocity is increased, as in the case of a large radius (75 mm) and high angular velocity (10° per second), the particle covers a greater distance within a single reconstruction frame. This leads to a broader distribution of the counts (FWHM = 20 px) with a lower peak. Yet, as demonstrated in Fig. 3.12, the reconstruction accurately captures the tracer particle trajectory with sufficient spatial precision in both scenarios.

The horizontal rotation trajectory of the 1 MBq tracer particle at a radius of 50 mm and angular velocity of 5° per second was reconstructed with a sampling frequency of 0.125, 0.5, 2 and 4 fps to examine the impact of the sampling frequency on the spatial precision under dynamic conditions. Fig. 3.14 displays the reconstructed trajectories for each sampling frequency.

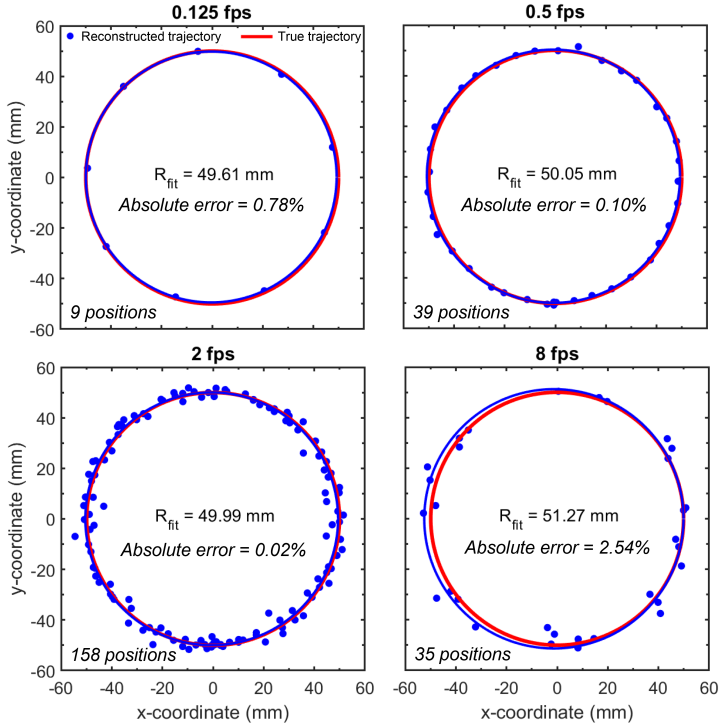

Figure 3.14: Reconstruction of the true and reconstructed trajectory for horizontal rotation at 50 mm radius and angular velocity of 5° per second, reconstructed with a sampling frequency of 0.125, 0.5, 2 and 4 fps

From the figure, it can be observed that the true trajectory closely follows the reconstructed trajectory (in red) at sampling frequencies of 0.125 and 0.5 fps, indicating high spatial precision. However, at a sampling frequency of 2 fps, the reconstructed positions scatter more loosely around the true trajectory, suggesting reduced spatial precision compared to the low sampling frequencies. Despite the random scattering around the true trajectory, the fit remains accurate, with a spatial absolute percentage error of only 0.02% relative to the true radius. This demonstrates that the trajectory can still be accurately

reconstructed even at the reduced sampling frequency. However, further increasing the sampling frequency to 8 fps results in the inability to accurately reconstruct the tracer particle's trajectory. This is indicated by the poor spatial precision and the decrease in the number of reconstructed positions. Similar to the reconstruction of the static tracer particle at 4 fps, a larger number of frames contain too few counts to perform Gaussian fitting and reconstruct the tracer particle's position. As described earlier, it should be noted that increasing the activity of the tracer particle would lead to trajectory reconstruction with improved spatial precision at high sampling frequencies.

3.4. Case study: flow field in a horizontal stirred bed reactor

3.4.1. Setup description

Through static and dynamic validation, the presented RPT method has been demonstrated to be able to reconstruct the three-dimensional position of a tracer particle with high spatial accuracy and precision. To showcase the technique's applicability in characterizing hydrodynamics in multi-phase systems, a hydrodynamic study was conducted using a 27.5 MBq radioactive tracer particle within a laboratory-scale horizontal stirred bed reactor (HSBR). HSBRs play an important role in the processing of granular materials and find applications in various fields, such as biomass pyrolysis [34] and polyolefin manufacturing [35, 36]. The HSBR generally contains a granular bed that is mildly stirred by a series of blades attached to a center shaft, resulting in a well-mixed system.

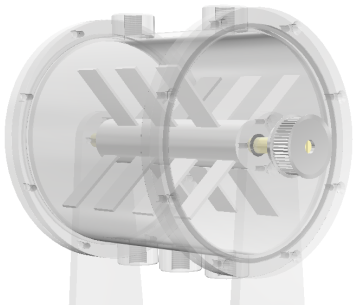

Figure 3.15: Schematic representation of the laboratory-scale horizontal stirred bed reactor used in the case study.

In this work, a laboratory-scale HSBR was developed to investigate the hydrodynamics in non-reactive environments, aiming to enhance the understanding of granular motion in HSBRs in polypropylene manufacturing applications. The HSBR, presented in Fig. 3.15, consists of a 140 mm outer-diameter cylin-

der with a length of 150 mm. The cylinder incorporates an agitator comprising a central shaft with seven blade positions. Each position is equipped with two blades, with each blade positioned 90° apart from its neighboring blades. Both the cylinder and the agitator are constructed from polycarbonate to reduce attenuation during the experiments.

3.4.2. Radioactive particle tracking experiments

To conduct RPT experiments, the RPT setup was first calibrated following the workflow outlined in Section 3.2.3. Subsequently, the HSBR was positioned in the center of the FOV of the RPT setup. A mass of 410 g industrial-grade polypropylene reactor powder, with a bulk density of ρ_b=368 kg m^{-3} and a median diameter of d_{v50}=985 µm, was loaded into the reactor, resulting in a 60% volume fill grade. The 27.5 MBq Au-198 radioactive tracer particle, composed of 1.6 mg Au-198 embedded in a 1.8 mm polystyrene bead with an air gap (see Section 3.2.1), was added to the HSBR. The agitator was then rotated at a rotation speed of 20 rpm using an electric motor with a belt drive. The tracer particle's trajectory was recorded for a duration of 10 min, equivalent to 200 impeller rotations. To ensure a safe working environment and minimize radiation exposure to the operators, the experimental procedure was controlled from a workstation situated outside the setup room. The three-dimensional trajectory was reconstructed based on the workflow described in Section 3.2.2. The reconstruction was performed with a sampling frequency of 10 fps, i.e., a sampling time of 100 ms.

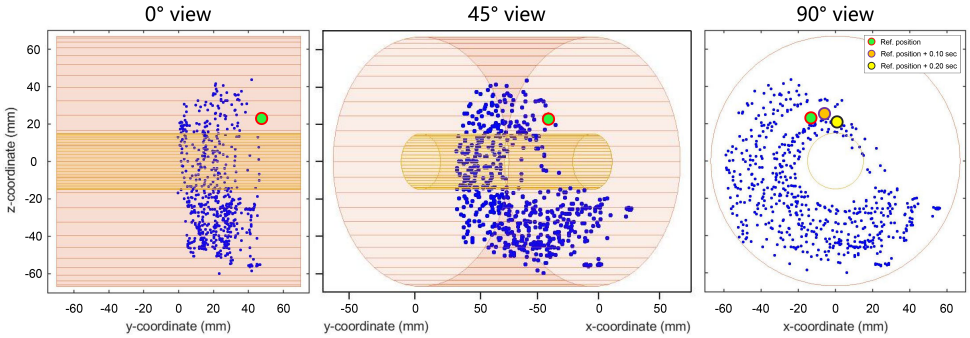

Figure 3.16: Reconstructed positions of the tracer particle in the HSBR accumulated for a time period of 1 min. The instantaneous position is referenced by the red-outlined green dot. Two consecutive reconstructed positions are indicated in the 90° view. The reactor wall and stirrer shaft are indicated with a red and yellow color, respectively.

3.4.3. Results and discussion

Fig. 3.16 displays the time-resolved trajectory for a 1 min time interval, providing 0°, 45°, and 90° angle views to illustrate the three-dimensional nature of the reconstruction. Each blue scatter marker represents a unique reconstructed position accumulated during the 1 min time interval. The 90° angle view exhibits three consecutive reconstructed positions: the instantaneous reference position, the reference position after 100 ms, and the reference position after 200 ms. The small spatial step observed between these consecutive reconstructed positions shows that a sampling frequency of 10 fps is sufficient to track the trajectory of the tracer particle within the HSBR when operated at a rotation speed of 20 rpm.

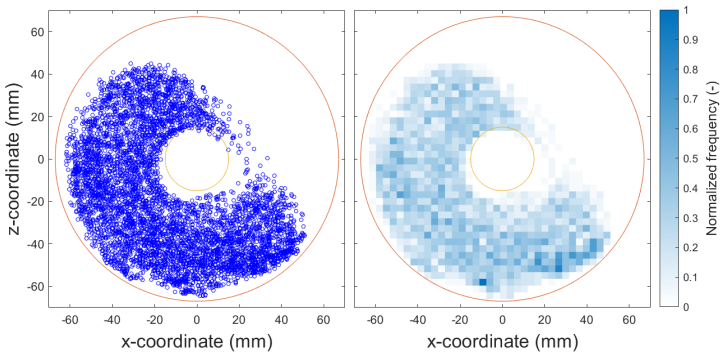

Figure 3.17: Reconstructed spatial distribution (left) and normalized spatial frequency distribution (right) measured for a time period of 10 min shown for the x-z plane.

The time-averaged flow behavior of the tracer particle can be characterized from the acquired positions data set. Fig. 3.17 shows the particle positions in the xz-plane accumulated during the 10 min measurement time, allowing visualization of the particle circumferential and radial motion. Since the agitator rotates in a clockwise direction, the granular bed undergoes clockwise mixing, causing the left side of the bed to move upward and flow freely over the shaft. From the scatter plot, Fig. 3.17-left, it can be observed that the tracer particle exhibits good radial dispersion throughout the bed. During the 10 min measurement, the particle follows clockwise trajectories near the reactor wall, through the center of the granular bed, and close to the shaft. This is an important observation, as any tracer particle used to evaluate flow behavior in a particular medium should exhibit similar dynamics to the medium itself. A mesh-grid function in MATLAB was used to compute the normalized frequency, representing the solids hold-up, for a rectangular grid of the HSBR

xz-plane. The solids hold-up map, depicted in Fig. 3.17-right, reveals the absence of dead zones, which would be indicated by dark blue coloration, and demonstrates a uniform radial solids hold-up throughout the bed.

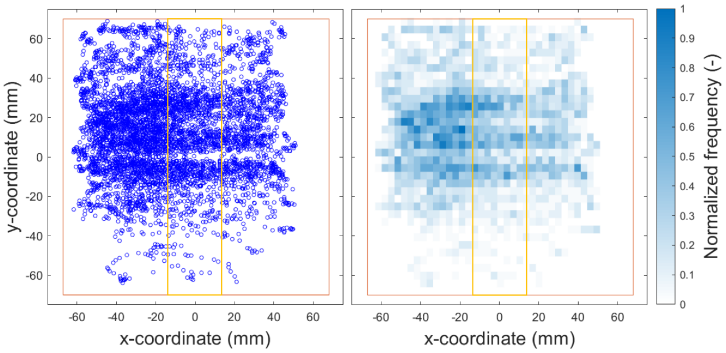

Figure 3.18: Reconstructed spatial distribution (left) and normalized spatial frequency distribution (right) measured for a time period of 10 min shown for the x-y plane.

Fig. 3.18 depicts the particle positions in the xy-plane accumulated during the 10 min measurement time, providing insight into the axial motion of the tracer within the reactor. It can be observed from the scatter plot, depicted in Fig. 3.18-left, that the tracer particle exhibits significant axial movement throughout the HSBR, with reconstructed positions at nearly every coordinate value along the y-axis during the 10 min measurement period. The solids hold-up map, depicted in Fig. 3.18-right, demonstrates a heterogeneous distribution. From the figure, distinct zones with a dark blue coloration (i.e., high solids hold-up) and light blue to white coloration (i.e., low solids hold-up) can be identified.

Finally, the velocity field of the tracer particle is computed from the time-resolved positions using a center-difference approach

$$v_{i,j}(t) = \frac{x_i(t_j+\Delta t) - x_i(t_j)}{\Delta t} \tag{3.9}$$

The velocity vectors, $v(t)$, at their corresponding position, $x(t)$ are plotted in Fig. 3.19 for a time interval of 3 min. From the velocity field, two distinct regions can be distinguished. On the one hand, a low-velocity region at the bottom and left side of the bed is recognized when the agitator is the driving force for the motion of the bed. On the other hand, a high-velocity region at the top right side of the bed is recognized when the bed flows freely over the shaft, and

gravity becomes the dominant driving force, resulting in significantly higher velocities.

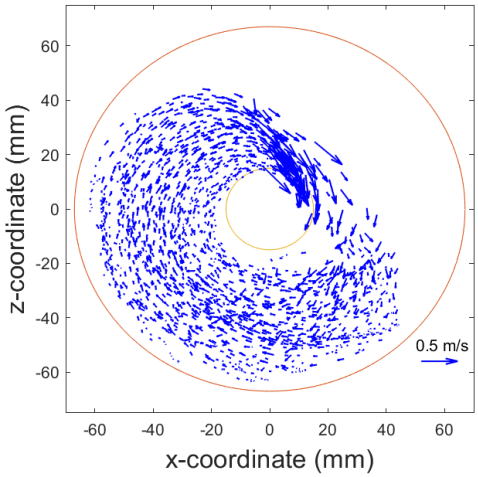

Figure 3.19: Reconstructed tracer particle velocity flow field map shown for the x-z plane. The velocity vectors are computed from the time-resolved tracer trajectory measured for a time period of 3 min.

The significant variation within the velocity flow field is also clear from the computed velocity statistics. Table 3.1 presents the median, mean, and maximum velocity of the tracer particle, as well as the velocity at the tip of the impeller blades for a rotation speed of 20 RPM. It is interesting to compare the computed tracer velocity statistics to the tip speed. When the HSBR is operated at a rotation speed of 20 RPM, the mean velocity of the tracer particle is approximately 0.52 times the tip speed. In contrast, the maximum observed velocity is found to be approximately 4.4 times the tip speed. As described above, the high velocity is likely attributed to the gravity experienced by the tracer particle during the flow over the reactor shaft.

The time-resolved tracer particle trajectory, time-averaged solids hold-up profiles, and velocity field acquired with single-photon emission RPT can aid in a better understanding of the nature of the flow field in horizontal stirred bed reactors. Moreover, the experimental data sets can contribute to the validation of computational models of the reactors.

Table 3.1: Velocity statistics for the velocity quiver plot presented in Fig. 3.19.

v_{median} (mm/s)	v_{mean} (mm/s)	v_{max} (mm/s)	v_{tip} (mm/s)
60.5	73.6	623.5	140.3

3.5. Conclusions

Radioactive particle tracking is a valuable technique for visualizing flow fields in multi-phase systems, offering potential benefits in process optimization and intensification. However, traditional approaches rely on assumptions in simulating the count rate received by detectors for reconstructing the position of the radioactive tracer particle.

In this paper, we employ a novel radioactive particle tracking approach based on a fundamentally different reconstruction method. The detected photon hit locations are directly utilized for reconstructing the three-dimensional position of the tracer particle, thereby circumventing the need for assumptions in count rate fluctuations. The setup includes three identical γ-radiation slit collimator detectors positioned equidistantly at 120°. The tracer particle's three-dimensional position is reconstructed by determining the intersection point of three two-dimensional planes originating from the detectors. Through a calibration-experimentation procedure, we achieved a spatial accuracy of approximately 1 mm for tracer particle position reconstruction. In a case study, we demonstrated the application of the method in evaluating the hydrodynamics in a horizontal stirred bed reactor system. The trajectory of a 27.5 MBq tracer particle in the reactor was reconstructed over a 10 min time period with a sampling frequency of 10 fps. Using the reconstructed positions, we analyzed the radial, circumferential, and axial spatial distributions, as well as the velocity flow field. The hydrodynamic insights that can be obtained from radioactive particle experimentation provide valuable information for validating computational models and can contribute to the optimization and intensification of multi-phase flow systems.

References

[1] M. Dudukovic, *Opaque multiphase reactors: Experimentation, modeling and troubleshooting,* Oil & Gas Science and Technology – Rev. IFP Éditions Technip Oil & Gas Science and Technology – Rev. IFP **55**, 135 (2000).

[2] D. J. Parker, M. R. Hawkesworth, and T. D. Beynon, *Process applications of emission tomography,* The Chemical Engineering Journal and the Biochemical Engineering Journal **56**, 109 (1995).

[3] C. S. Stellema, J. Vlek, R. F. Mudde, J. J. M. de Goeij, and C. M. van den Bleek, *Development of an improved positron emission particle tracking system,* Nuclear Instruments and Methods in Physics Research Section A: Accelerators, Spectrometers, Detectors and Associated Equipment **404**, 334 (1998).

[4] A. Seeger, U. Kertzscher, K. Affeld, and E. Wellnhofer, *Measurement of the local velocity of the solid phase and the local solid hold-up in a three-phase flow by x-ray based particle tracking velocimetry (xptv),* Chemical Engineering Science **58**, 1721 (2003).

[5] U. Kertzscher, A. Seeger, K. Affeld, L. Goubergrits, and E. Wellnhofer, *X-ray based particle tracking velocimetry–a measurement technique for multi-phase flows and flows without optical access,* Flow Measurement and Instrumentation **15**, 199 (2004).

[6] M. Rasouli, F. Bertrand, and J. Chaouki, *A multiple radioactive particle tracking technique to investigate particulate flows,* AIChE Journal **61**, 384 (2015).

[7] C. Windows-Yule, J. Seville, A. Ingram, and D. Parker, *Positron emission particle tracking of granular flows,* Annual Review of Chemical and Biomolecular Engineering **11**, 367 (2020).

[8] R. K. Upadhyay, H. J. Pant, and S. Roy, *Experimental validation of design and performance parameters of radioactive particle tracking (rpt) experimentation,* Applied Radiation and Isotopes **153**, 108814 (2019).

[9] S. Roy, *Radiotracer and particle tracking methods, modeling and scale-up,* AIChE Journal **63**, 314 (2017).

[10] J. S. Lin, M. M. Chen, and B. T. Chao, *A novel radioactive particle tracking facility for measurement of solids motion in gas fluidized beds,* AIChE Journal **31**, 465 (1985).

[11] N. Devanathan, D. Moslemian, and M. P. Dudukovic, *Flow mapping in bubble columns using carpt,* Chemical Engineering Science **45**, 2285 (1990).

[12] D. Moslemian, N. Devanathan, and M. P. Dudukovic, *Radioactive particle tracking technique for investigation of phase recirculation and turbulence in multiphase systems,* Review of Scientific Instruments **63**, 4361 (1992).

[13] D. Roy, F. Larachi, R. Legros, and J. Chaouki, *A study of solid behavior in spouted beds using 3-d particle tracking,* The Canadian Journal of Chemical Engineering **72**, 945 (1994).

[14] F. Larachi, M. Cassanello, M. Marie, J. Chaouki, and C. Guy, *Solids circulation patterns in 3-phase fluidized-beds containing binary-mixtures of particles as inferred from rpt,* Chemical engineering research & design **73**, 263 (1995).

[15] F. Larachi, E. Lord, J. Chaouki, C. Chavarie, and L. Behie, *Phenomenological study of solids mixing in a binary liquid fluidized bed,* Prep Fluidization VIII, Tours, France , 385 (1995).

[16] L. Godfroy, F. Larachi, G. Kennedy, and J. Chaouki, *Simultaneous measurement of the 3-d position and velocity of a single radioactive particle in a cfb riser at high velocity,* Proceedings of CFB V, Beijing, China (1996).

[17] J. Chaouki, F. Larachi, and M. P. Dudukovic, *Noninvasive tomographic and velocimetric monitoring of multiphase flows,* Industrial and Engineering Chemistry Research **36**, 4476 (1997).

[18] A. R. Rammohan, A. Kemoun, M. H. Al-Dahhan, and M. P. Dudukovic, *Characterization of single phase flows in stirred tanks via computer automated radioactive particle tracking (carpt),* Chemical Engineering Research and Design **79**, 831 (2001).

[19] S. Roy, F. Larachi, M. H. Al-Dahhan, and M. P. Dudukovic, *Optimal design of radioactive particle tracking experiments for flow mapping in opaque multiphase reactors,* Applied Radiation and Isotopes **56**, 485 (2002).

[20] S. Roy, A. Kemoun, M. H. Al-Dahhan, and M. P. Dudukovic, *Experimental investigation of the hydrodynamics in a liquid–solid riser,* AIChE Journal **51**, 802 (2005).

[21] M. S. Fraguío, M. C. Cassanello, F. Larachi, S. Limtrakul, and M. Dudukovic, *Classifying flow regimes in three-phase fluidized beds from carpt experiments,* Chemical Engineering Science **62**, 7523 (2007).

[22] D. Guha, P. A. Ramachandran, and M. P. Dudukovic, *Flow field of suspended solids in a stirred tank reactor by lagrangian tracking,* Chemical Engineering Science **62**, 6143 (2007).

[23] E. Alizadeh, O. Dubé, F. Bertrand, and J. Chaouki, *Characterization of mixing and size segregation in a rotating drum by a particle tracking method,* AIChE Journal **59**, 1894 (2013).

[24] O. Dubé, D. Dubé, J. Chaouki, and F. Bertrand, *Optimization of detector positioning in the radioactive particle tracking technique,* Applied Radiation and Isotopes **89**, 109 (2014).

[25] V. Jain, L. Kalo, D. Kumar, H. J. Pant, and R. K. Upadhyay, *Experimental and numerical investigation of liquid–solid binary fluidized beds: Radioactive particle tracking technique and dense discrete phase model simulations,* Particuology **33**, 112 (2017).

[26] L. Kalo, H. J. Pant, M. C. Cassanello, and R. K. Upadhyay, *Time series analysis of a binary gas-solid conical fluidized bed using radioactive particle tracking (rpt) technique data,* Chemical Engineering Journal **377** (2019), 10.1016/j.cej.2018.08.193.

[27] F. Larachi, J. Chaouki, and G. D. Kennedy, *3d mapping of solids flow fields in multiphase reactors with rpt,* AIChE Journal **41**, 439 (1995).

[28] F. Larachi, G. Kennedy, and J. Chaouki, *A γ-ray detection system for 3-d particle tracking in multiphase reactors,* Nuclear Instruments and Methods in Physics Research Section A: Accelerators, Spectrometers, Detectors and Associated Equipment **338**, 568 (1994).

[29] A. Yadav, M. Ramteke, H. J. Pant, and S. Roy, *Monte carlo real coded genetic algorithm (mcrga) for radioactive particle tracking (rpt) experimentation,* AIChE Journal **63**, 2850 (2017).

[30] L. Godfroy, F. Larachi, G. Kennedy, B. Grandjean, and J. Chaouki, *On-line flow visualization in multiphase reactors using neural networks,* Applied Radiation and Isotopes **48**, 225 (1997).

[31] A. Yadav, T. K. Gaurav, H. J. Pant, and S. Roy, *Machine learning based position-rendering algorithms for radioactive particle tracking experimentation,* AIChE Journal **66** (2020), 10.1002/aic.16954.

[32] B. L. Holman and S. S. Tumeh, *Single-Photon Emission Computed Tomography (SPECT): Applications and Potential,* JAMA **263**, 561 (1990).

[33] N. Mostoufi, G. Kenned, and J. Chaouki, *Decreasing the sampling time interval in radioactive particle tracking,* Canadian Journal of Chemical Engineering **81**, 129 (2003).

[34] Y. Xi, Q. Chen, and C. You, *Flow characteristics of biomass particles in a horizontal stirred bed reactor: Part ii. modeling studies on particle residence time distribution and axial mixing,* Powder Technology **269**, 585 (2015).

[35] M. Caracotsios, *Theoretical modelling of amoco's gas phase horizontal stirred bed reactor for the manufacturing of polypropylene resins,* Chemical Engineering Science **47**, 2591 (1992).

[36] C. J. Dittrich and S. M. P. Mutsers, *On the residence time distribution in reactors with non-uniform velocity profiles: The horizontal stirred bed reactor for polypropylene production,* Chemical Engineering Science **62**, 5777 (2007).

4

Particle dynamics in horizontal stirred bed reactors characterized by single-photon emission radioactive particle tracking

In the previous chapter, we demonstrated the operation of a novel single-photon emission radioactive particle tracking method. By employing a designated calibration-experimentation procedure, we demonstrated reconstruction with a spatial accuracy of approximately 1 mm in controlled experiments. In this chapter, we employ single-photon radioactive particle tracking to investigate the influence of reactor operating parameters on the polypropylene reactor powder particle dynamics in the laboratory-scale horizontal stirred bed reactor. This chapter first reintroduces the laboratory-scale horizontal stirred bed reactor and the radioactive particle tracking method. Then, the influence of reactor fill level and agitator rotation speed on the flow field, solids circulation, and axial dispersion are presented and discussed.

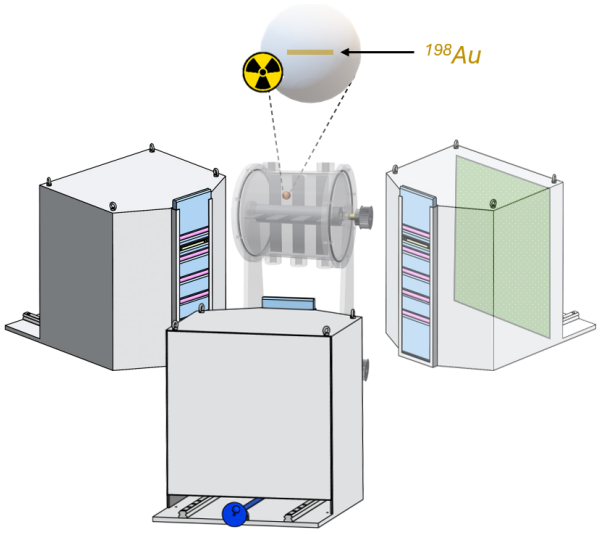

This chapter is published as P.C. van der Sande, E.C. Wagner, J. de Mooij, G.M.H. Meesters, and J.R. van Ommen, *Particle dynamics in horizontal stirred bed reactors characterized by single-photon emission radioactive particle tracking*, Chemical Engineering Journal 482 (2024).

Horizontal stirred bed reactors are widely used in the commercial manufacturing of polypropylene. However, a comprehensive understanding of the particle dynamics in horizontal stirred bed reactors remains elusive, primarily due to the lack of detailed experimental data. In this work, we studied the influence of operating parameters on the particle flow dynamics in a laboratory-scale horizontal stirred bed reactor using single-photon emission radioactive particle tracking. The results show that the general solids flow behavior is strongly affected by both the agitator rotation speed and reactor fill level. Operation at low rotation speed and low fill level results in solids flow with poor radial and circumferential distribution due to internal bed circulation. On the contrary, at increased rotation speeds and fill levels, solids motion throughout the bed is continuous, resulting in excellent solids distribution. The solids circulation was found to increase for both an increase in rotation speed and reactor fill level. The axial dispersion coefficient, on the other hand, shows a linear relation with the rotation speed, but no conclusive relation between the axial dispersion coefficient and the reactor fill level was found.

4.1. Introduction

Polypropylene (PP) is the second-most produced polyolefin resin globally, trailing only polyethylene. PP is recognized as a versatile material with robust mechanical properties, thermal stability, and excellent chemical resistance and therefore widely used in food packaging, automotive, healthcare, textile, and electronics industries [1, 2]. The global PP market is projected to experience sustained growth due to the increasing demand for efficient food packaging solutions and the incorporation of high-quality plastics in automotive manufacturing [3].

Among various PP manufacturing methods, gas-phase catalyzed polymerization has gained significant commercial importance [4]. In particular, the utilization of horizontal stirred bed reactors (HSBRs) in the gas-phase Innovene PP process has proven to be a successful approach for efficient and scalable PP production [5–9]. The HSBR offers distinct advantages for propylene polymerization, ensuring excellent gas-phase mixing and precise control of reaction parameters.

The HSBR is a cylindrical reactor with a series of paddles attached to a central shaft, as illustrated in Fig. 4.1. At the front end of the HSBR micron-sized Ziegler-Natta supported catalyst particles are continuously introduced. Gaseous propylene monomers are injected at the bottom of the reactor and polymerize on the active sites of the catalyst surface via a coordination-insertion mechanism. The gas velocity is carefully controlled to prevent fluidization of the bed and maintain a sub-fluidized state. The mildly agitated PP powder is maintained at a constant inventory while the polymerization progresses, and the particles grow to a final size ranging from 100 to 5000 µm [10]. The volume increase due to particle growth pushes the powder toward the opposite end of the reactor, where it is continuously discharged.

In gas-phase polymerization reactors, operational issues can arise if the process is not adequately operated with respect to particle movement. Besides reduced production capacity and product quality, a significant issue encountered in the reactors is the agglomeration of polyolefin particles [11]. In the Innovene PP process, agglomeration may arise due to insufficient heat dissipation as a result of poor solids circulation. Insufficient heat dissipation during the process can lead to elevated surface temperatures of polymer particles, potentially reaching the softening temperature or even surpassing the melting temperature of the polymer, resulting in the local formation of agglomerates or lumps. Agglomeration can significantly impair reactor efficiency by

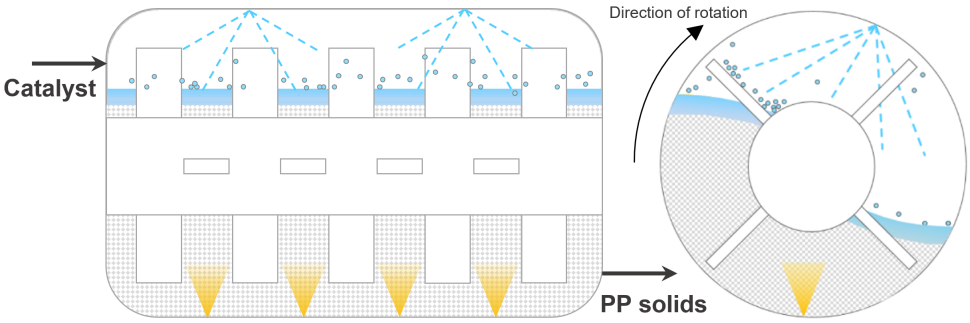

Figure 4.1: Schematic representation of the front view (left) and side view (right) of the horizontal stirred bed reactor as employed in the Innovene PP process. The PP solids are continuously agitated, while gaseous propylene is introduced from the bottom of the reactor and liquid propylene quench is sprayed from the top.

obstructing the discharging pipeline, disrupting the heat exchange balance, causing deviations from the normal flow pattern, and, in severe cases, occupying a substantial portion of the reactor volume, leading to an unscheduled shutdown of the plant and incurring substantial financial penalties [12].

In the Innovene process, heat removal is facilitated by spraying recycled liquid propylene onto the PP powder bed from several axial positions along the length of the reactor. Upon contact with the active PP, the liquid vaporizes, absorbing the heat generated by the highly exothermic polymerization reaction and thereby cooling the system. Adequate solids circulation is necessary to achieve uniform wetting to attain a uniform bed temperature.

Significant research effort has been dedicated to kinetic studies of the polymerization reaction and theoretical modeling of the residence time distribution [4, 7–9, 13–16]. It is commonly accepted that the powder mixing pattern in an HSBR results from two transport effects: the continuously increasing powder net flow in the downstream direction caused by the particle growth, and the simultaneous stirring flows with equal intensity in the up- and downstream directions. Both together lead to a residence time distribution that can be described by three to five continuous stirred tank reactors in series [7, 14].

Apart from computational modeling and residence time distribution experiments, experimental studies evaluating the hydrodynamics, or particle dynamics, in the HSBR have been very scarce in the current literature. The flow characteristics of biomass particles in a laboratory-scale HSBR were studied by experimental measurements [17] and computational modeling [18]. The axial

dispersion coefficient was reported to increase with increasing rotation speed and number of blades, which was confirmed through experimentation and modeling. The granular flow patterns in a horizontal powder mixer, a system that shows similarities to an HSBR, were investigated by positron emission particle tracking in a collection of studies [19–21]. Laurent *et al*. [19] observed that the radial blades in horizontal mixers define axial compartments in the bed, in which loops of circulation were formed. In consecutive work, Laurent and Bridgwater [20] demonstrated that the velocity fields and axial dispersion coefficients scaled with the rotation speed, which is in good agreement with the aforementioned flow characteristics of biomass particles in a laboratory-scale HSBR [17]. Moreover, at sufficiently high reactor fill levels, the agitator shaft was reported to have a dominant effect on the radial and axial particle motion Laurent and Bridgwater [21]. Evaluating the particle dynamics is crucial for optimizing and intensifying reactor operation, as well as validating computational models. The extent of solids circulation and axial dispersion significantly influences the stability of reactor operation and the quality and uniformity of the final polymerized product. However, the hydrodynamics of multiphase flow reactors are well-known for their complexity, making their evaluation challenging. The multiphase nature of the flow in the HSBR, characterized by a large fraction of the particulate phase, makes the dense flow opaque to visible light. Consequently, the use of well-established optical techniques is hindered.

In this study, we characterize the particle dynamics in a laboratory-scale HSBR under non-reactive conditions, employing an in-house single-photon emission radioactive particle tracking (RPT) method previously introduced by Van der Sande *et al*. [22]. Traditional RPT has emerged as a proven non-invasive technique for assessing hydrodynamic phenomena in multiphase flow systems [23–29]. It generally involves the introduction of a γ-radiation emitting tracer particle, possessing similar physical properties as the dispersed phase, into the system of interest. Subsequently, strategically positioned detectors surrounding the system enable precise reconstruction of the tracer particle's positional trajectory over time, thereby facilitating a comprehensive evaluation of hydrodynamic properties. In comparison to traditional methods, single-photon emission RPT involves reconstruction based on the photon hit location on a two-dimensional detector, mitigating the effect of varying attenuation on the reconstruction. By employing a designated calibration-experimentation procedure, Van der Sande *et al*. [22] demonstrated reconstruction with a spatial accuracy of approximately 1 mm in controlled experiments. Moreover, the ability to study hydrodynamics in a real system was demonstrated with a case study. In the present experimental work, we employ single-photon RPT to in-

vestigate the influence of reactor operating parameters, namely reactor fill level and agitator rotation speed, on the flow field, solids circulation, and axial dispersion in a laboratory-scale HSBR.

4.2. Methodology

4.2.1. Horizontal stirred bed reactor setup

The laboratory-scale HSBR used in this work consists of a 134 mm inner-diameter cylinder with a length of 150 mm. The cylinder incorporates an agitator comprising a central shaft with seven blade positions. Each position is equipped with two blades, with each blade positioned 90° apart from its neighboring blades. The inner blades have a width of 20 mm, while the end blades have a width of 15 mm. Both the cylinder and the agitator are constructed from polycarbonate to mitigate γ-radiation attenuation during the RPT experiments. The agitator can be rotated at the desired rotation speed using an electric motor with a belt drive, which is controlled via in-house software. A schematic illustration of the HSBR can be found in Appendix C.1.

To closely resemble industrial conditions, industrial-grade PP reactor powder was used in the experiments. The powder was characterized using a ZEISS SteREO Discovery.V8 optical microscope with manual 8x zoom. ImageJ software was utilized to determine the particle size distribution based on a large number of captured optical microscope images. Figure 4.2 presents the number-based particle size distribution, the corresponding cumulative curve, and a typical optical microscope image of the PP powder. From the cumulative curve, it can be observed that the powder has a median diameter (d_{n50}) of 1050 µm. Additionally, the loose bulk density ($\rho_{b,loose}$) of the powder was experimentally determined following the method of Carr [30] to be 368 kg m^{-3}.

4.2.2. Radioactive particle tracking

Experimental setup

The single-photon emission RPT technique utilized in this work is based on the single-photon emission computed tomography (SPECT) technique, commonly used in the medical field [31]. The RPT setup, recently introduced by Van der Sande *et al.* [22], consists of three identical γ-radiation detectors that are equidistantly placed around a field of view at approximately 120° intervals, as shown schematically in Fig. 4.3. Each detector is composed of a casing, a slit collimator made of lead shielding plates and spacers, a scintillation crystal, and photo-multiplier tubes. The setup configuration in the current experimental work has the scintillation crystal positioned at a distance of 400 mm from the collimator, allowing for the entire volume of the lab-scale HSBR to be

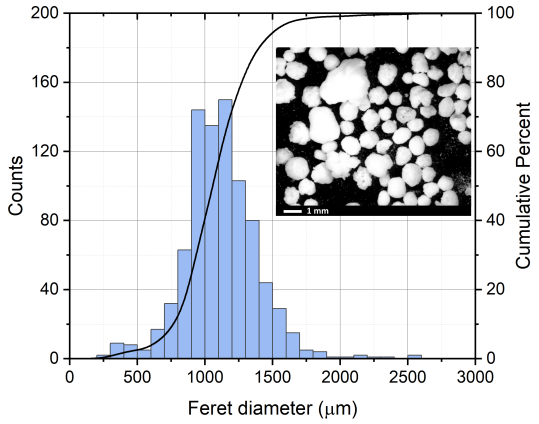

Figure 4.2: Number-based particle size distribution and optical microscope image of the PP powder acquired with the ZEISS SteREO Discovery.V8 optical microscope.

captured. Fig. 4.4 shows the experimental setup with the HSBR positioned in the center of the field of view.

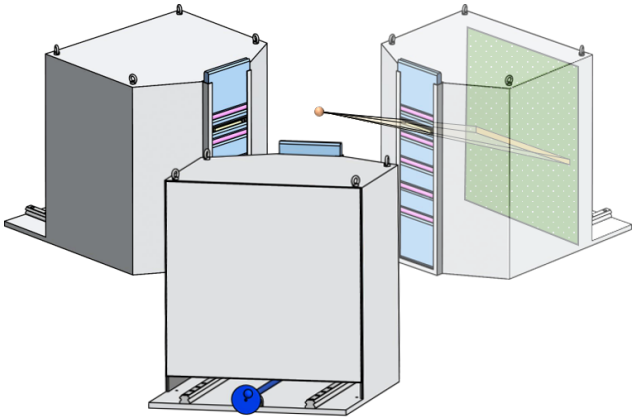

Figure 4.3: Schematic of the RPT setup showcasing the three detectors placed equidistant with a 120° angle. The γ-radiation emitted by a radioactive tracer particle passes through the slit collimators and hits the scintillation crystals.

Radioactive tracer particles

In this work, two radioactive tracer particles were manufactured for calibration and experimentation purposes, respectively. The manufacturing process involved embedding 1.6 mg gold within 1.8 mm polystyrene beads. To compensate for the increased mass due to the gold core, air pockets were intentionally left within the particles. Consequently, the resulting core-shell particles had

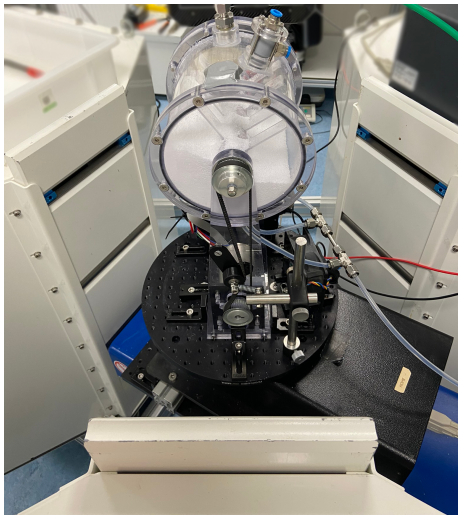

Figure 4.4: Photograph of the experimental setup. The HSBR loaded with PP powder is positioned in the center of the RPT setup, comprising three γ-radiation detectors.

a diameter of 1.8 mm and a density of 1.65 mg cm^{-3}. With a particle diameter of 1.8 mm, the tracer particle is near the upper bound of, but still within, the particle size distribution, as evident from Fig. 4.2, and is therefore assumed to show representative dynamics. Neutron irradiation at the TU Delft Reactor Institute was employed to activate the stable gold cores to the radioactive isotope ^{198}Au, providing an activity of 1 MBq for calibration and 27.5 MBq for experimentation purpose.

$$^{197}_{79}\mathrm{Au} + ^{1}_{0}\mathrm{n} \rightarrow ^{198}_{79}\mathrm{Au} \xrightarrow[\gamma,\beta^-]{} ^{198}_{80}\mathrm{Hg}$$

Since the isotope ^{198}Au has a relatively short half-life of approximately 2.7 days and emits 412 keV photons in its decay to ^{198}Hg, it is a preferred tracer isotope for RPT experimentation [29].

Reconstruction tracer particle position

When a γ-radiation emitting tracer particle is placed within the field of view, radiation that passes through the slit collimators hits the scintillation crystals. Each photon hit is recorded as an event, which has an associated xz-position, energy, and time of detection. Combining the positions of all events detected by a scintillation crystal allows for the creation of a two-dimensional projection of the incoming γ-radiation. A backward projection method is employed to

reconstruct the position of the radioactive tracer particle based on its projections on the three detectors. For each detector, a plane is reconstructed using the location of the detected photon hit on the scintillation crystal and the position of the slit collimator, as schematically represented for one detector in Fig. 4.3. By simultaneously constructing planes for all three detectors, a unique intersection point is obtained. The coordinates of this intersection point represent the position of the radioactive tracer particle. The detector configuration and stochastic nature of radiation result in a Poisson distribution of detection events. The standard deviation of the calculated tracer particle coordinates is inversely proportional to the square root of the sampling time, which is directly proportional to the number of detected events [32]. Increasing the activity of the tracer particle increases the number of detected events and thus decreases the standard deviation of the calculated coordinates.

The single-photon emission RPT experimental procedure involves two successive steps (Fig. 4.5): (1) setup calibration using the 1 MBq tracer; and (2) trajectory reconstruction using the 27.5 MBq tracer. The calibration of the setup's geometry is performed to ensure accurate reconstruction of the tracer particle position. The calibration process aims to correct errors in the spatial geometry of the setup arising from manual measurements. This is achieved by minimizing the sum of residuals squared for a large number of known tracer particle positions and their corresponding reconstructed positions, utilizing a constrained non-linear least-squares optimization algorithm in MATLAB. The output of this algorithm provides calibrated geometry values, encompassing the spatial orientation of the detectors. The calibrated geometry values replace the initial hand-measured values and are employed in the subsequent trajectory reconstruction step. In the trajectory reconstruction step, the tracer particle is added to the HSBR, and its trajectory is monitored.

The reconstruction sampling time, i.e., the time between consecutive reconstructions, is directly related to the count rate detected by the detector, which in turn is a function of the source activity and distance to the detector. With the current tracer activity of 27.5 MBq, a sampling time of 100 ms was attained throughout the experiments. A sampling time of 100 ms, which equates to 10 reconstructions each second, was proven sufficient to capture small spatial steps in the trajectory of the tracer particle [22]. Relating the number of detected events used in each reconstruction at a sampling time of 100 ms to the controlled validation experiments reported by Van der Sande *et al.* [22], a spatial accuracy of approximately 5 mm is expected. A more detailed description of the experimental procedure and discussion on the recon-

struction is described in our previous work [22].

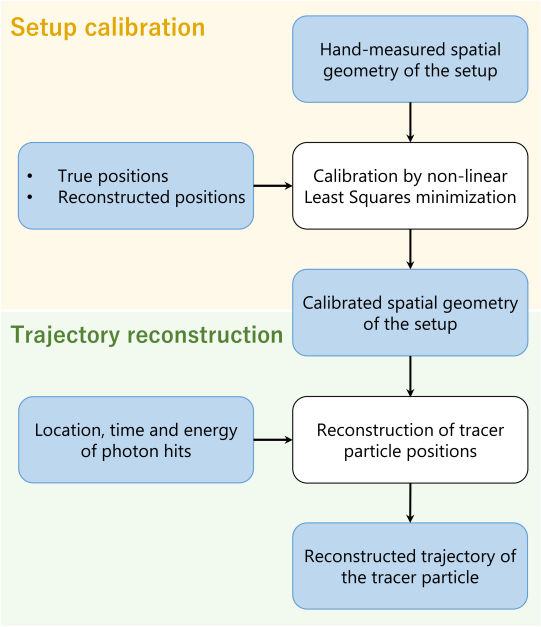

Figure 4.5: Graphical representation of the experimental and data processing workflow to reconstruct the trajectory of the tracer particle, following a subsequent calibration and experimentation step.

4.2.3. Operation and flow characterization

During the operation of the HSBR in industrial applications, the bed level is kept at constant inventory, and the rotation speed is kept constant. Adequate control of the fill level and rotation speed is necessary to prevent operational issues, as these have a significant influence on the particle dynamics in rotating systems [21, 33]. An experimental parameter study was performed to comprehend the influence of both aforementioned parameters on particle dynamics in the HSBR. The set of operating conditions is denoted in Table 4.1.

For each experiment, the HSBR was loaded with the desired fill level by inserting PP powder through the top opening. Subsequently, the 27.5 MBq tracer was added to the HSBR. The agitator rotation speed was then set to the desired value using in-house software. After 10 s, the RPT detectors were switched on, and the trajectory of the tracer particle was monitored for a duration of 20 min. Since the rotation speeds used in this study vary between 20 RPM to

60 RPM, the reactor agitator has made between 400 to 1200 rotations during a 20 min measurement, which is assumed sufficient for reliable data interpretation. From the obtained data set, the particle dynamics in the HSBR were characterized and analyzed.

Solids flow field

The obtained particle trajectory was used to evaluate the solids flow field in the xz-plane (see Fig. 4.7 for a definition of the coordinate system). The particle velocity was computed from the time-resolved tracer particle positions by

$$v_{i,j}(t) = \frac{x_i(t_j+\Delta t) - x_i(t_j)}{\Delta t} \tag{4.1}$$

To compute the velocity heat map, a mesh-grid function in MATLAB was used to create a rectangular grid of the HSBR xz-plane. The flow velocity at each grid cell was computed by triangulation-based natural neighbor interpolation. Following a similar procedure, the velocity vectors were normalized and interpolated to compute the direction of the flow.

Solids circulation

The particle dynamics in an HSBR are dominated by continuous agitation, which induces particle circulation. Slow and irregular particle circulation is undesirable in industrial operation, as it may lead to the formation of hot spots due to insufficient and irregular heat dissipation, potentially causing agglomeration and impairing reactor efficiency. In contrast, fast particle circulation allows for more frequent particle wetting, thereby improving the uniformity of the bed.

The particle circulation behavior in the experimental HSBR can be directly characterized by the obtained trajectory of the tracer particle. To quantify the particle circulation behavior, a cycle time is defined as the time it takes for a particle to make a full circumferential cycle. An in-house MATLAB script was used to determine the number of cycles and respective cycle times for each experiment.

Table 4.1: Experimental operating conditions investigated. Each possible combination of the fill level and rotation speed is studied.

Parameter	Value		
Fill level (v%)	40	50	60
Rotation speed (RPM)	20	40	60

Solids axial dispersion

Since RPT allows the trajectory of a tracer particle to be obtained, the axial dispersion can be evaluated from Einstein's expression [34]. The local particle dispersion (D_y) coefficient is calculated with a method derived from Mostoufi and Chaouki [26] and Pallarès and Johnsson [35]. The axial displacement during a time interval Δt is:

$$\Delta y_{i,j} = y_i(t_{j+1}) - y_i(t_j) \tag{4.2}$$

$$t_j = t_0 + j\Delta t \tag{4.3}$$

The mean displacement can then be defined as:

$$\bar{\Delta y} = \frac{1}{N_t}\frac{1}{N_p}\sum_{j=1}^{N_t}\sum_{i=1}^{N_p}\Delta y_{i,j} \tag{4.4}$$

where N_t is the number of time steps and N_p is the number of particles. The axial dispersion coefficient, $D_{y,i,j}$, of a single particle at a certain time-step is then computed as:

$$D_{y,i,j} = \frac{(\Delta y_{i,j} - \bar{\Delta y})^2}{2\Delta t} \tag{4.5}$$

Finally, the coefficients are averaged over the experiment duration to obtain the time-averaged axial dispersion coefficient:

$$D_y = \frac{1}{N_t}\sum_{j=1}^{N_t} D_{y,j} \tag{4.6}$$

As emphasized by Pallarès and Johnsson [35], careful consideration of the time interval value (Δt) holds significant importance when computing the axial dispersion coefficient. Setting Δt at a very low scale (around 10^{-1} s or even lower) results in the dispersion coefficient not aligning well with the observed trajectory [35]. Conversely, when opting for considerably high Δt values, there is a risk of exceeding the characteristic time for axial transport, resulting in a loss of valuable information. To determine the most suitable Δt to be used in this work, the influence of the Δt on the calculated value of the axial dispersion coefficient was studied by calculating the axial dispersion coefficient values

using a wide range of Δt values. The results are presented in Appendix C.2. It can be observed that at a very low scale, the axial dispersion quickly decreases until a plateau is reached for a Δt larger than 5 s. Moreover, for a Δt of 30 s or larger, the calculated axial dispersion coefficients for different experimental conditions approach each other, hinting that valuable information that allows distinction between experimental conditions might be lost. Therefore, a Δt of 10 s was considered suitable and was consequently employed in the evaluation of the axial dispersion.

4.3. Results and discussion

4.3.1. Time-resolved trajectory

For each set of operating conditions, the trajectory of the 27.5 MBq tracer particle within the HSBR was reconstructed over a time period of 20 min with a sampling time of 100 ms. Fig. 4.7 presents the particle trajectory for a 1 min time period for a reactor fill level of 50% and a rotation speed of 40 RPM, providing 0°, 45°, and 90° angle views to show the three-dimensional nature of the reconstruction. The blue scatter markers represent distinct reconstructed positions accumulated during the specified time interval. A video showing the time-resolved trajectory can be viewed by scanning the QR code in Fig. 4.6. In the 90° angle view, three consecutive reconstructed positions of the tracer particle are exhibited: the instantaneous reference position, the reference position after 0.1 s, and the reference position after 0.2 s. The relatively small spatial step between these consecutive reconstructed positions underscores the adequacy of the 100 ms sampling time for accurately tracing the tracer particle's path within the HSBR at a rotation speed of 40 RPM.

Figure 4.6: Video of the tracer particle trajectory for a fill level of 50% and rotation speed of 40 RPM. The instantaneous position is indicated by the red-outlined green dot, and the blue scatter markers represent distinct reconstructed positions that have accumulated during the time interval.

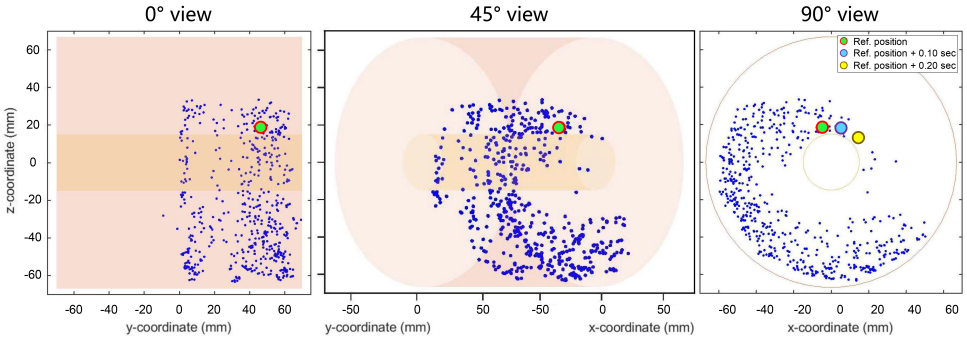

Figure 4.7: Reconstructed positions of the tracer particle accumulated for a time period of 1 min for a fill level of 50% and rotation speed of 40 RPM. The instantaneous position is referenced by the red-outlined green dot. Two consecutive reconstructed positions are indicated in the 90° view. The reactor wall and agitator shaft are indicated in red and orange.

4.3.2. Solids flow field

The solids flow fields were computed via the aforementioned grid interpolation procedure and are shown for the xz-plane in Fig. 4.8. When considering the flow velocity, two regions can be distinguished in each plot, namely a low velocity (cold color) region at the bottom and left side of the bed and a high velocity (warm color) region at the top and right side of the bed. At the bottom and left side of the bed, the agitator is the driving force for the motion of the bed material, yielding uniform solids dynamics with a low velocity. In the current work, the rotation speed was varied from 20 to 60 RPM, which corresponds to a Froude number varying from 0.03 to 0.28. A Froude number below 1 means that the gravitational force is dominant over the inertia force, indicating that the flow behavior of the bed is influenced by the force exerted by the impeller blades, frictional forces on the wall, shear forces, and gravity [36]. In contrast to the bottom and left side of the bed, at the top and right of the bed, the bed material flows freely over the shaft, and gravity is the driving force for the downward motion of the bed material. This region is characterized by higher flow velocities. As expected, it can be observed that the flow velocity increases in both regions with increasing agitator rotation speed.

Notable observations are made when comparing the solids flow field for the various experimental conditions. From the flow fields, local circulation under the shaft can be observed for the cases of 40% fill level with a rotation speed of 20 and 40 RPM. The particles that experience local circulation are less likely to reach the top of the bed. This behavior would be highly undesirable from an application point of view, as it may result in large temperature

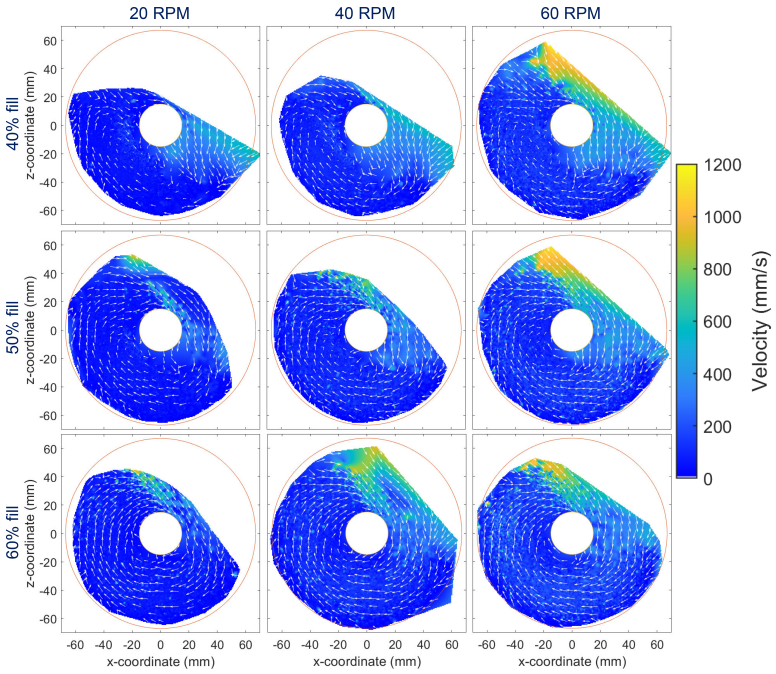

Figure 4.8: Projection of the time-averaged tracer velocity heat maps and flow direction quiver plots in the xz-plane averaged over the y-axis.

gradients in the bed due to poor heat dissipation. However, a further increase in rotation speed to 60 RPM results in the expansion of the bed. Such expansion or aeration at increased rotation speeds is commonly encountered in rotating drum reactors [37], and in this case, allows a significant part of the bed to flow over the shaft, thereby significantly improving the circumferential motion. Nonetheless, internal circulation under the shaft can still be observed. Increasing the reactor fill level from 40% to 50% improves the circumferential motion and reduces the internal circulation. Notably, no internal circulation is observed at a reactor fill level of 50% and a rotation speed of 60 RPM, indicative of excellent circumferential solids motion. Consistent findings are evident across various rotation speeds when the fill level is maintained at 60%.

These findings align closely with the observations documented by Laurent *et al.* [36], who noted the presence of a circulation loop beneath the agitator shaft in a horizontal powder mixer operated at low fill levels. This phenomenon was attributed to a substantial portion of the bed flowing underneath the shaft. Conversely, at higher fill levels, the shaft compelled the powder to flow over it, preventing the formation of a circulation loop. Laurent *et al.* [36] observed the

most notable change in flow behavior between fill levels of 40% and 50%, correlating with the splitting of material by the shaft. Some material was found to flow over the shaft, while the rest was found to flow beneath it, forming a circulation loop. As discussed, the same phenomenon is also visible for distinct cases in Figure 4.8. Interestingly, despite the difference in design and configuration of the agitator among horizontal powder mixers and an HSBR, the most notable change in flow behavior was also observed to occur between 40% and 50% fill level in this work, which is attributed to the flow over the shaft.

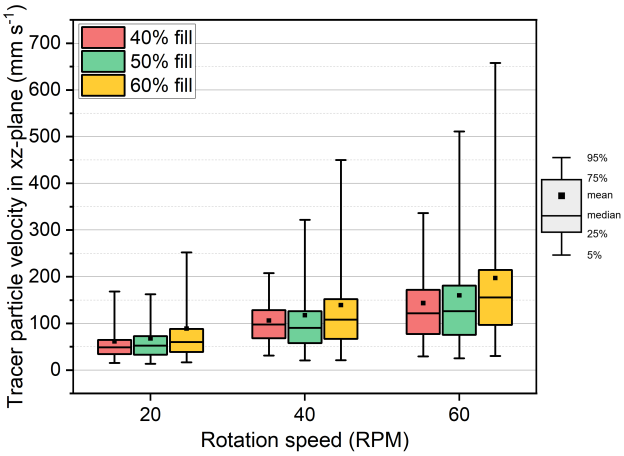

Figure 4.9: Influence of the fill level and rotation speed on the flow velocity distribution of the tracer particle in the xz-plane.

Figure 4.9 quantitatively presents the solids velocity as a box plot for the various operating conditions. In agreement with the flow field profiles (Fig. 4.8), the solids velocity shows an increase for both an increase in rotation speed and reactor fill level. More specifically, it can be observed that the mean velocity has a linear relationship with the rotation speed. In addition, it is interesting to relate the solids velocity directly to the tip speed of the impeller blades by dividing the mean velocity, shown in Fig. 4.9, by the respective impeller tip speed, shown in Table 4.2. The obtained results are plotted in Fig. 4.10.

Table 4.2: Impeller tip speed at the various rotation speeds.

Rotation speed (RPM)	Tip speed (mm s^{-1})
20	140.3
40	280.6
60	421.0

It can be observed that the ratio of the mean tracer particle velocity to the tip speed decreases with an increasing rotation speed for all tested reactor fill levels. It is evident that, across all rotation speeds, the highest value is obtained for a reactor fill level of 60%. For a fill level of 60% and a rotation speed of 20 RPM, the mean speed of the tracer particle is approximately 0.63 times the tip speed of the impeller blades. When increasing the rotation speed, the ratio decreases quickly at first but then appears to stabilize at higher rotation speeds. The 40 and 50% fill levels show a similar decreasing trend with increasing rotation speed. This observation is further supported by additional experiments for a larger set of experimental conditions presented in Appendix C.4. Overall, the results show that increasing the rotation speed of the impellers has diminishing returns on the mean velocity of the tracer particle. Increasing the rotation speed increases the mean tracer particle velocity by a fraction, which in turn decreases with increasing rotation speed.

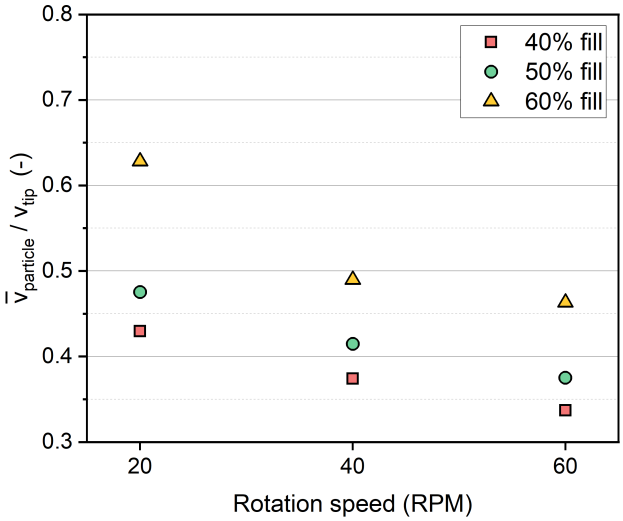

Figure 4.10: Influence of the fill level and rotation speed on the ratio of the mean particle velocity to the impeller blade tip speed.

4.3.3. Solids circulation

The normalized radial occupancy over a time period of 20 min is presented in Fig. 4.11. From the xz-plane, the circumferential and radial dispersion of the tracer particle in the reactor is visualized. Due to the clockwise rotation of the agitator, the granular bed is mixed in a clockwise manner, resulting in the left side of the bed being pushed upward and flowing over the shaft. A clear distinction can be made between cases with poor distribution and good distribu-

tion. Notably, when the reactor is operated with a fill level of 40% at rotation speeds of 20 and 40 RPM, the radial distribution of the tracer particle throughout the bed is poor, indicated by the presence of zones with high normalized occupancy (dark blue color) and low normalized occupancy (light blue to white color). It is important to note that the plots concern normalized occupancy. If the particle resides at a certain preferred radial position for a longer duration, which is the case for operation at 40% fill level at 20 and 40 RPM, it results in a dark blue-colored region. Operation with a low fill level and low rotation speed results in a flowing regime that is characterized as a semi-static bed, in which solids motion is induced only by the passage of an impeller blade. In agreement with the flow fields presented in Fig. 4.8, it appears that under these operating conditions, the tracer particle experiences predominantly internal circulation in a region under the shaft. As mentioned earlier, the tracer particle size is near the upper bound of the particle size distribution of the PP powder. It can be observed that with the aforementioned operating conditions, the flow behavior results in poor radial solids dispersion of solids in the bed and potentially results in size segregation, which is highly undesirable from an industrial application point of view.

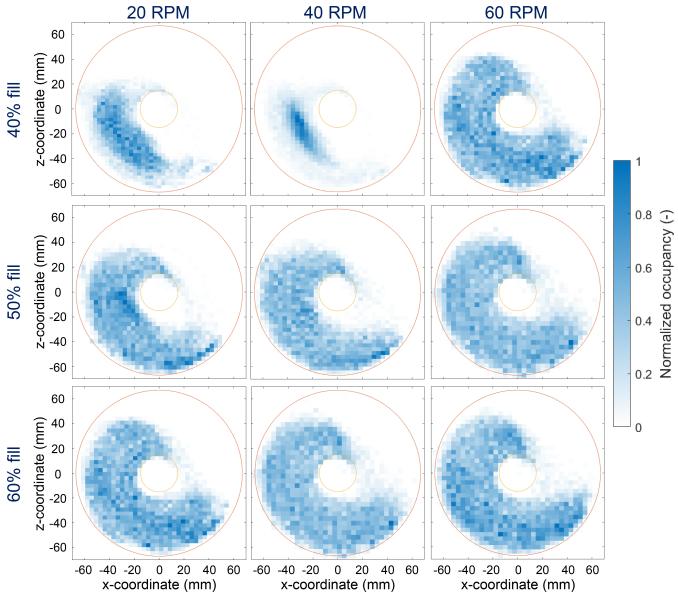

Figure 4.11: Influence of the fill level and rotation speed on the tracer particle normalized radial occupancy. In each plot, the HSBR shaft is indicated by the yellow outlined circle.

On the contrary, when the reactor is operated with a higher fill level and/or

higher rotation speed, it can be observed that the normalized occupancy is uniform throughout the bed, indicative of improved solids distribution and a well-mixed bed. A clear transition is notable when the rotation speed is increased from 40 RPM to 60 RPM at a reactor fill level of 40%. In contrast to the rotation speed of 20 and 40 RPM, at a rotation speed of 60 RPM, the bed is aerated and thereby expanded. The expansion of the bed facilitates free powder flow over the shaft, improving the circumferential motion and radial dispersion. A similar observation is made when only the reactor fill level is increased from 40% to 50%, which results in improved powder flow. The bed is in a regime that can be characterized as a dynamic bed, where solids motion throughout the bed is continuous, resulting in a more uniform solids distribution. The impeller blades no longer induce motion only by passing through the bed but rather continuously transport the bed with a clockwise motion. This observation is in line with results obtained by Laurent *et al.* [36] and Laurent and Bridgwater [20], who studied the performance of single and six-blade powder mixers for various fill levels. They found that at a low fill level, the flow is directed only by the passage of the impeller blade through the bed, allowing the material to flow on the free surface and forming a circulation loop below the shaft. At a higher fill level, the presence of the shaft influences the flow behavior, and the bed is pushed continuously in a clockwise manner by an impeller blade as a solid plug.

To quantify the circumferential motion of the solids, a particle cycle time is defined as the time it takes for the tracer particle to flow over the shaft and complete a full circumferential cycle. In the industrial manufacturing of PP in an HSBR, a low cycle time would mean that the particle frequently passes the top of the reactor, where it is wetted by the quenching liquid and thus cooled down through evaporative cooling. Frequent wetting allows better control of the temperature of the polymerized solids and, therefore, a uniform temperature distribution throughout the bed. The cycle time is presented as a box plot for the various operating conditions in Fig. 4.12.

In agreement with previous observations made from the flow field and the normalized radial occupancy, the increase in reactor fill level leads to improved powder flow, enhancing the circumferential motion of solids. To further elucidate the relation between rotation speed and cycle time, a dimensionless cycle number is proposed. The cycle number is defined as the ratio of the number of particle cycles per unit time to the number of agitator rotations per unit time, as denoted in Equation 4.7. The cycle number for the various operating conditions is plotted in Fig. 4.13.

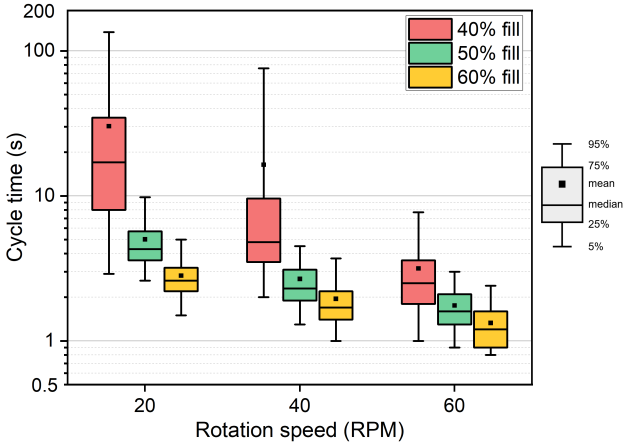

Figure 4.12: Influence of the fill level and rotation speed on the cycle time distribution of the tracer particle.

$$Cycle\ number = \frac{\#\ particle\ cycles\ per\ unit\ time}{\#\ agitator\ rotations\ per\ unit\ time} \tag{4.7}$$

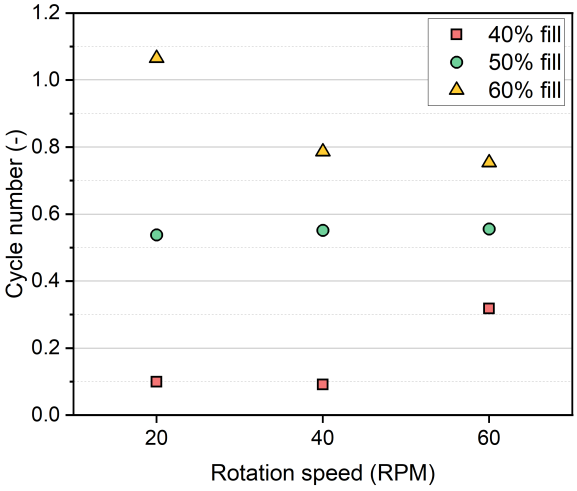

Figure 4.13: Influence of the reactor fill level and rotation speed on the dimensionless cycle number, representing the number of particle cycles per full revolution of the agitator.

It can be observed that a reactor fill level of 40% results in a cycle number that remains constant at a value of 0.1 for a rotation speed of 20 and 40 rpm, meaning that a tracer particle makes 0.1 cycles for each revolution of the agitator. In line with earlier observations, a clear jump is observed when the rotation

speed is increased to 60 RPM. At a fill level of 50%, the cycle number remains constant for the various rotation speeds at a value of approximately 0.55, indicating a linear relationship between the cycle time and the rotation speed. When further increasing the fill level to 60%, the cycle number is increased. Interestingly, the cycle number has a maximum value of approximately 1.1 at a rotation speed of 20 RPM, indicative of solid circulation faster than the agitator rotation. In this case, the particle moves with the same angular velocity as the impellers in a large part of the bed and is likely to overtake an impeller blade during the free flow over the shaft, as expected from the velocity profile in Fig. 4.8. The finding is in agreement with observations made from the presented particle velocity results in Fig. 4.10.

4.3.4. Solids axial dispersion

The normalized axial occupancy over a time period of 20 min is presented in Fig. 4.14. From the xy-plane, the axial dispersion of the tracer particle in the reactor is visualized. Since the impellers are straight, and there is no external driving force for axial transport, the axial motion of the tracer particle is considered to be random, meaning that when a particle is lifted by an impeller blade, it has an equal chance to flow to the left or right of the impeller.

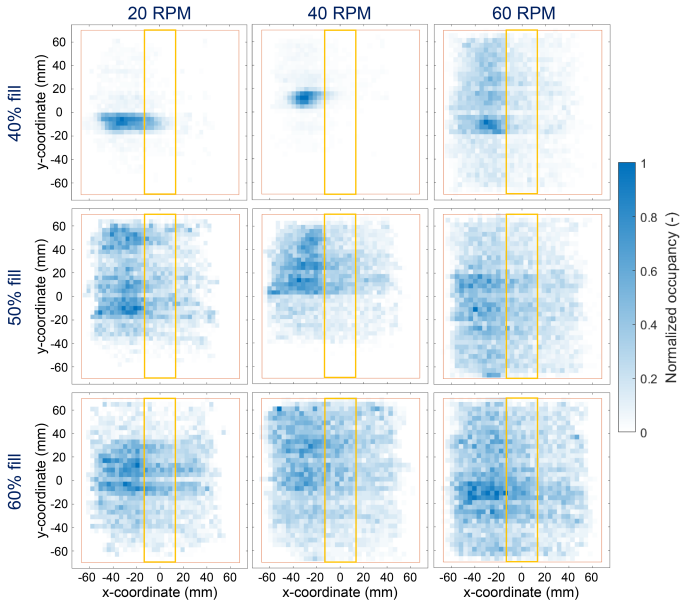

Figure 4.14: Influence of the fill level and rotation speed on the tracer particle normalized axial occupancy. In each plot, the reactor shaft is indicated by the yellow-outlined rectangle.

In the figure, a clear distinction can be made between cases with low and high axial distribution. When the reactor is operated with a fill level of 40% at rotation speeds of 20 and 40 RPM, the axial dispersion of the tracer particle throughout the bed is low, indicated by small areas with a high normalized occupancy (dark blue color). As described earlier, with the aforementioned operating conditions, there is significant internal bed circulation and poor circumferential solids motion. It is evident from Fig. 4.14 that this behavior results in a low degree of axial dispersion. On the other hand, when the powder flow is improved due to an increase in rotation speed and reactor fill level, the axial dispersion throughout the reactor is increased. The latter observation is evident from the significant axial movement the tracer particle shows through the HSBR, as it is reconstructed at nearly each coordinate value along the y-axis. In addition, the normalized occupancy is increasingly more uniform and has a higher coverage with increasing reactor fill level and rotation speed.

Next to the solids hold-up, it is interesting to study the dynamics of the axial dispersion. The temporal evolution of the axial position of the tracer particle is illustrated in Fig. 4.15 for the various operating conditions. In agreement with previously discussed results, a clear distinction can be observed between the experiments with a 40% fill level operated at 20 and 40 RPM and the rest of the measurements. When the HSBR is operated at the former operating conditions, the tracer particle shows significantly less axial motion compared to the other operating conditions.

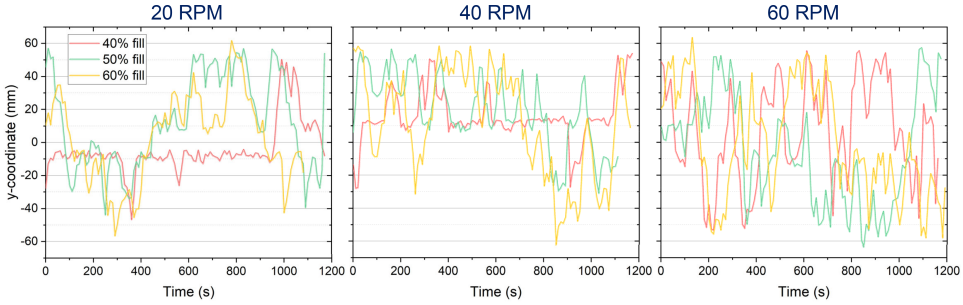

Figure 4.15: The temporal evolution of the axial position of the tracer particle as a function of the reactor fill level and rotation speed.

As described in Section 4.2.1, the HSBR incorporates an agitator comprising a central shaft with seven blade positions. Each position is equipped with two blades, with each blade positioned 90° apart from its neighboring blades. The blade configuration in the HSBR appears to induce ‘conveyor belt’ com-

partments in the bed at low reactor fill levels and rotation speeds, in which particles circulate at a fixed axial position for a certain residence time. A particle, or cluster of particles, may reside for tens of seconds up to several minutes within one compartment before it moves to another compartment. The compartments are not recognized for higher reactor fill levels and/or rotation speeds, as visible in Fig. 4.15. Although a zone with high normalized occupancy is visible in the solids hold-up profile for a fill level of 40% and rotation speed of 60 RPM at the y-coordinate −20 mm, it is evident from the temporal evolution that this is not caused by the particle residing in a 'conveyer-belt' compartment over a long time period. Rather, the particle frequently resides at, or passes, this axial position for a short time period. When accumulating a large number of short time periods at a certain axial position, it results in a high normalized occupancy. In contrast to our findings, Laurent and Bridgwater [20] observed axial compartments defined by the radial supports on which the blades are fixed at all fill levels, ranging from 20% to 60%, in horizontal powder mixers. However, the difference is likely attributed to the difference in the system design, in particular the configuration of the agitator.

The time-averaged axial dispersion coefficient is plotted in Fig. 4.16. It can be observed that the axial dispersion coefficient ranges from 10^{-6} to 10^{-5} $m^2\ s^{-1}$. Moreover, the results clearly show that the axial dispersion coefficient increases with increasing rotation speed, which is in line with findings of Laurent and Bridgwater [21], Portillo *et al.* [33] and Xi *et al.* [17], who studied the axial dispersion in comparable powder agitating systems. In this work, the lowest values are found for the measurements with 40% fill level operated at 20 and 40 RPM. Interestingly, the highest extent of axial dispersion is obtained for a reactor fill level of 40% and a rotation speed of 60 RPM. Under these operation conditions, significant bed expansion is observed, which in turn increases the circumferential motion of the solids, as is evident from the solids' hold-up profile and cycle time. At low fill levels, the solids have more free physical space to move freely during the flow over the shaft, potentially increasing their axial reach. The latter would explain the obtained higher value for the axial dispersion coefficient under these operating conditions. By comparing the observed trend with the temporal changes in the axial position of the tracer particle (depicted in Fig. 4.15) and the axial solids hold-up (shown in Fig. 4.14), it can be concluded that the trend aligns well across the obtained results.

While the literature on axial dispersion in laboratory-scale HSBRs is very scarce, significant attention has been given to studying axial dispersion in rotating drums through numerical simulations and experimental investigations.

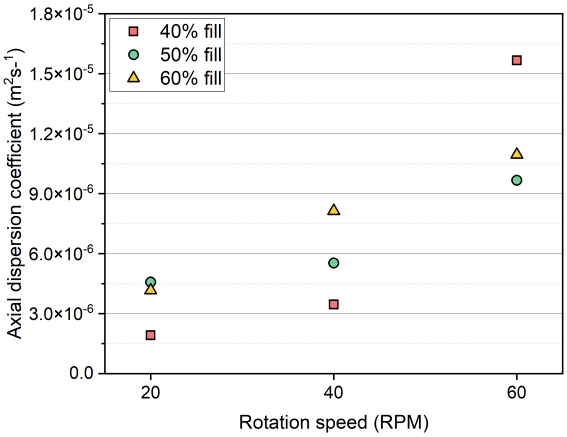

Figure 4.16: The influence of the reactor fill level and rotation speed on the axial dispersion coefficient.

Notably, axial dispersion coefficients have been documented for rotating drums at approximately 10^{-6} $m^2\,s^{-1}$ [38], a value that corresponds well with or is slightly below the coefficients showcased in Fig. 4.16. The minor difference between the values in a rotating drum and the HSBR could be attributed to their different configurations. The HSBR comprises an agitator, which potentially leads to increased axial movement when compared to a rotating drum.

An additional common observation concerning rotating drums is the linear correlation between the axial dispersion coefficient and the rotation speed. It is important to note that drawing a direct comparison to this work was challenging due to the narrower range of rotating speeds in rotating drums typically encountered in the literature, usually spanning from 5 to 15 RPM [38, 39]. Studies showed that the axial dispersion coefficient in rotating drums is influenced by the fill level. Namely, it was demonstrated that a higher fill level corresponds to a lower axial dispersion coefficient [38]. This particular effect is not discernible across all operating conditions for the laboratory-scale HSBR, as evident from Fig. 4.16. In this work, it was demonstrated that an increase in fill level results in increased powder flow, which in turn results in a lower particle cycle time. When the bed material flows over the shaft more frequently, it could potentially facilitate increased axial transport in the process. However, an increased fill level also reduces the free space in the reactor, potentially decreasing the flowing path length of the particles and thereby limiting axial transport. These two conflicting mechanisms result in an inconclusive relationship between the fill level and the axial dispersion coefficient in the HSBR.

4.4. Conclusions

In the current work, a quantification of the particle flow dynamics in a non-reactive laboratory-scale horizontal stirred bed reactor (HSBR) is provided using single-photon emission radioactive particle tracking (RPT). The technique has been used to reconstruct the trajectory of a 27.5 MBq tracer particle in the HSBR over a time period of 20 min with a sampling time of 100 ms under various operating conditions. From the obtained reconstructed positions data set the particle dynamics were studied. The influence of two operating parameters, namely the reactor fill level and agitator rotation speed, on the flow field, solids circulation behavior, and axial dispersion has been evaluated, and the following conclusions can be drawn:

- The general particle flow behavior in the HSBR is strongly affected by the reactor fill level and agitator rotation speed. At low rotation speed and low fill level, solids motion is induced only by the passing of an impeller blade, resulting in semi-static bed motion characterized by poor solids distribution. At increased fill levels and rotation speeds, continuous solids motion throughout the bed results in a uniform solids distribution.

- The solids circulation, quantified by a dimensionless cycle number, is faster with increasing reactor fill level and rotation speed.

- The axial dispersion coefficient ranges from 10^{-6} to 10^{-5} $m^2\,s^{-1}$, which is similar to or somewhat higher than values reported for rotating drums. The axial dispersion coefficient increases with increasing rotation speed. The highest extent of axial dispersion is obtained for a reactor fill level of 40% when operated at 60 RPM, but no conclusive relation between the axial dispersion coefficient and the reactor fill level was found.

The knowledge acquired from this work not only provides a further understanding of the particle dynamics in HSBRs but can also serve as a valuable basis for optimizing, intensifying, and scaling HSBR systems for the manufacturing of high-quality polypropylene resins on an industrial scale.

References

[1] J. Karger-Kocsis and T. Bárány, *Polypropylene Handbook Morphology, Blends and Composites: Morphology, Blends and Composites* (2019).

[2] K. Kulajanpeng, N. Sheibat-Othman, W. Tanthapanichakoon, and T. F. L. McKenna, *Multiscale modelling of multizone gas phase propylene (co)polymerization reactors—a comprehensive review,* The Canadian Journal of Chemical Engineering **100**, 2505 (2022).

[3] F. B. Insights, *Polypropylene Market Size, Share & Trends*, Report (2020).

[4] J. J. Zacca, J. A. Debling, and W. H. Ray, *Reactor residence time distribution effects on the multistage polymerization of olefins—i. basic principles and illustrative examples, polypropylene,* Chemical Engineering Science **51**, 4859 (1996).

[5] J. Shepard, J. Jezl, E. Peters, and R. Hall, *Divided horizontal reactor for the vapor phase polymerization of monomers at different hydrogen levels,* (U.S. Patent 3 957 448, May 1976).

[6] J. Jezl, E. Peters, R. Hall, and J. Shepard, *Process for the vapor phase polymerization of monomers in a horizontal, quench-cooled, stirred-bed reactor using essentially total off-gas recycle and melt finishing,* (U.S. Patent 3 965 083, June 1976).

[7] M. Caracotsios, *Theoretical modelling of amoco's gas phase horizontal stirred bed reactor for the manufacturing of polypropylene resins,* Chemical Engineering Science **47**, 2591 (1992).

[8] A. B. Gorbach, S. D. Naik, and W. H. Ray, *Dynamics and stability analysis of solid catalyzed gas-phase polymerization of olefins in continuous stirred bed reactors,* Chemical Engineering Science **55**, 4461 (2000).

[9] C. J. Dittrich and S. M. P. Mutsers, *On the residence time distribution in reactors with non-uniform velocity profiles: The horizontal stirred bed reactor for polypropylene production,* Chemical Engineering Science **62**, 5777 (2007).

[10] R. A. Hutchinson, *Modelling of particle growth in heterogeneous catalyzed olefin polymerization*, Thesis (1990).

[11] C. M. van den Bleek, M.-O. Coppens, and J. Schouten, *Application of chaos analysis to multiphase reactors,* Chemical Engineering Science **57**, 4763 (2002).

[12] J. Wang, Y. Cao, X. Jiang, and Y. Yang, *Agglomeration detection by acoustic emission (ae) sensors in fluidized beds,* Industrial & Engineering Chemistry Research **48** (2009).

[13] R. A. Hutchinson and W. H. Ray, *Polymerization of olefins through heterogeneous catalysis. vii. particle ignition and extinction phenomena,* Journal of Applied Polymer Science **34**, 657 (1987).

[14] N. P. Khare, B. Lucas, K. C. Seavey, Y. A. Liu, A. Sirohi, S. Ramanathan, S. Lingard, Y. Song, and C.-C. Chen, *Steady-state and dynamic modeling of gas-phase polypropylene processes using stirred-bed reactors,* Industrial & Engineering Chemistry Research **43**, 884 (2004).

[15] Z. Tian, X.-P. Gu, L. Feng, J.-P. Corriou, and G.-H. Hu, *Modeling and simulation of polypropylene particle size distribution in industrial horizontal stirred bed reactors,* Journal of Applied Polymer Science **125** (2012).

[16] M. F. Atan, M. Hussain, R. Abbasi, K. M.J.H, and M. Patah, *Advances in mathematical modeling of gas-phase olefin polymerization,* Processes **7**, 67 (2019).

[17] Y. Xi, Q. Chen, and C. You, *Flow characteristics of biomass particles in a horizontal stirred bed reactor: Part i. experimental measurements of residence time distribution,* Powder Technology **269**, 577 (2015).

[18] Y. Xi, Q. Chen, and C. You, *Flow characteristics of biomass particles in a horizontal stirred bed reactor: Part ii. modeling studies on particle residence time distribution and axial mixing,* Powder Technology **269**, 585 (2015).

[19] B. Laurent, J. Bridgwater, and D. Parker, *Convection and segregation in a horizontal mixer,* Powder Technology **123**, 9 (2002).

[20] B. Laurent and J. Bridgwater, *Performance of single and six-bladed powder mixers,* Chemical Engineering Science **57**, 1695 (2002).

[21] B. F. Laurent and J. Bridgwater, *Influence of agitator design on powder flow,* Chemical Engineering Science **57**, 3781 (2002).

[22] P. C. Van der Sande, J. de Mooij, E. C. Wagner, G. M.H. Meesters, and J. R. van Ommen, *Single-photon emission radioactive particle tracking method for hydrodynamic evaluation of multi-phase flows,* Particuology , , in press (2023).

[23] J. S. Lin, M. M. Chen, and B. T. Chao, *A novel radioactive particle tracking facility for measurement of solids motion in gas fluidized beds,* AIChE Journal **31**, 465 (1985).

[24] M. Duduković, *Opaque multiphase reactors: Experimentation, modeling and troubleshooting,* Oil & Gas Science and Technology – Rev. IFP Éditions Technip Oil & Gas Science and Technology – Rev. IFP **55**, 135 (2000).

[25] D. Moslemian, N. Devanathan, and M. P. Dudukovic, *Radioactive particle tracking technique for investigation of phase recirculation and turbulence in multiphase systems,* Review of Scientific Instruments **63**, 4361 (1992).

[26] N. Mostoufi and J. Chaouki, *Local solid mixing in gas–solid fluidized beds,* Powder Technology **114**, 23 (2001).

[27] S. Roy, *Radiotracer and particle tracking methods, modeling and scale-up,* AIChE Journal **63**, 314 (2017).

[28] S. Roy, A. Kemoun, M. H. Al-Dahhan, and M. P. Dudukovic, *Experimental investigation of the hydrodynamics in a liquid–solid riser,* AIChE Journal **51**, 802 (2005).

[29] S. Roy, F. Larachi, M. H. Al-Dahhan, and M. P. Duduković, *Optimal design of radioactive particle tracking experiments for flow mapping in opaque multiphase reactors,* Applied Radiation and Isotopes **56**, 485 (2002).

[30] R. L. Carr, *Evaluating flow properties of solids,* Chemical Engineering Journal **72**, 163 (1965).

[31] B. L. Holman and S. S. Tumeh, *Single-photon emission computed tomography (spect). applications and potential,* Jama **263**, 561 (1990).

[32] N. Mostoufi, G. Kennedy, and J. Chaouki, *Decreasing the sampling time interval in radioactive particle tracking,* The Canadian Journal of Chemical Engineering **81**, 129 (2003), https://onlinelibrary.wiley.com/doi/pdf/10.1002/cjce.5450810116 .

[33] P. M. Portillo, A. U. Vanarase, A. Ingram, J. K. Seville, M. G. Ierapetritou, and F. J. Muzzio, *Investigation of the effect of impeller rotation rate, powder flow rate, and cohesion on powder flow behavior in a continuous blender using PEPT,* Chemical Engineering Science **65**, 5658 (2010).

[34] A. Einstein, *Investigations on the Theory of the Brownian Movement* (Courier Corporation, 1956).

[35] D. Pallarès and F. Johnsson, *A novel technique for particle tracking in cold 2-dimensional fluidized beds—simulating fuel dispersion,* Chemical Engineering Science **61**, 2710 (2006).

[36] B. Laurent, J. Bridgwater, and D. Parker, *Motion in a particle bed agitated by a single blade,* AIChE journal **46**, 1723 (2000).

[37] Q. Huang, H. Zhang, and J. Zhu, *Experimental study on fluidization of fine powders in rotating drums with various wall friction and baffled rotating drums,* Chemical Engineering Science **64**, 2234 (2009).

[38] S. Yang, K. Luo, and J. W. Chew, *Three-dimensional axial dispersion dynamics of granular flow in the rolling-regime rotating drum,* Powder Technology **332**, 131 (2018).

[39] S. Yang, L. Zhang, K. Luo, and J. Wei, *DEM investigation of the axial dispersion behavior of a binary mixture in the rotating drum,* Powder Technology **330**, 93 (2018).

5

Granular flow in stirred gas-solid fluidized bed reactors: a combined X-ray and numerical study

The previous chapters were focused on the flow behavior and particle dynamics in a horizontal stirred bed reactor. Besides horizontal stirred bed reactors, vertical stirred gas-solid fluidized bed reactors are employed in gas-solid polymerization of propylene. However, the complex gas-solid contacting dynamics pose challenges in the design, scale-up, and operation of these reactors. In this chapter, a combined experimental by X-ray imaging and pressure drop measurements and numerical Computational Fluid Dynamics (CFD) - Discrete Element Method (DEM) - Immersed Boundary Method (IBM) approach is conducted to study the influence of agitation on the fluidization performance of Geldart B particles.

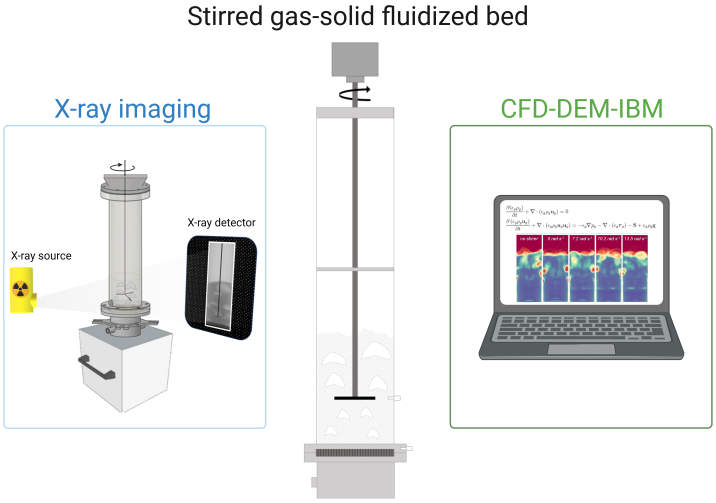

This chapter is published as P.C. van der Sande, M.J.A. de Munck, K. Wu, D.R. Rieder, D.E.A. van den Eertwegh, E.C. Wagner, G.M.H. Meesters, E.A.J.F. Peters, J.A.M. Kuipers, and J.R. van Ommen, *Fluidization behavior of stirred gas-solid fluidized beds: a combined X-ray and CFD-DEM-IBM study*, Chemical Engineering Journal 499 (2024).

Stirred gas-solid fluidized bed reactors are commercially employed in polyolefin manufacturing, but the complex gas-solid contacting dynamics pose challenges in design, scale-up, and operation. In this study, the influence of agitation on the fluidization performance of Geldart B particles was investigated experimentally by X-ray imaging and pressure drop measurements and numerically by Computational Fluid Dynamics (CFD) - Discrete Element Method (DEM) - Immersed Boundary Method (IBM). The experimentally obtained minimum fluidization curve and time-averaged pressure drop show good qualitative agreement with the simulation results. Visual observations underscore that an increase in the angular velocity of the agitator results in reduced bubble size and improved bed homogeneity, as further evidenced by reduced pressure fluctuations. Furthermore, the simulations reveal that while the impeller enhances solids agitation, a proper design study is imperative, considering that static immersed bodies, such as the stirrer shaft, can adversely impact solids motion.

5.1. Introduction

Gas-solid fluidized beds, in which a gas is passed upward through a bed of settled particles to suspend the particles in a fluid-like state, find widespread applications across various industries requiring good solids mixing, as well as efficient heat and mass transfer [1]. However, for many practical applications, the design, scale-up, and operation of gas-solid fluidized beds remain challenging due to the inherently complex and scale-dependent hydrodynamics. Over time, several methods have been suggested to enhance the performance of fluidized beds by introducing an additional source of energy to the bed, such as gas pulsation, sound, vibration, or agitation [2].

Stirred gas-solid fluidized bed reactors, also referred to as vertical stirred bed reactors (VSBRs), utilize mechanical agitation to introduce external energy into the system. Agitation facilitates improved solids mixing, a high degree of bed homogeneity, improved heat transfer, intensive gas-solid contact, and allows fluidization of cohesive materials [3, 4]. Due to these advantageous characteristics, stirred gas-solid fluidized beds are widely applied in industrial processes. One of their most significant applications is in solid-catalyzed gas-phase polymerization [5]. BASF pioneered stirred gas-solid fluidized bed polymerization processes with the introduction of the Novolen vertical stirred bed process for the manufacture of polypropylene in 1969 [6, 7]. In this reactor, the gas phase monomer undergoes polymerization with a co-monomer and hydrogen under the influence of a solid catalyst. Effective heat management in these exothermic polymerization reactions is crucial to prevent runaway process conditions that could lead to polymer melting. Heat management is intricately linked to gas-solid contact, but the complex gas-solid contacting principles in these reactors present challenges in design, scale-up, and operation and, therefore, require detailed investigation.

Early studies, such as those by [3], conducted in the 1950s, explored the effects of agitation in gas-solid fluidized beds. Through pressure drop measurements, they showed that immersed oscillating stirring elements can improve the fluidization quality and increase heat transfer between air and the extended surface in a rectangular vessel. [8] correlated the pressure drop and power requirements in gas-solid fluidized beds agitated by a blade-type agitator. Moreover, [4] experimentally investigated the bed expansion and fluctuation in a cylindrical gas-solid fluidized bed with stirred promoters. It was reported that the agitation promotes the fluidization quality by improving particle mixing. Furthermore, [9] studied the influence of agitation of a frame impeller on the fluidization performance of Geldart type D particles through experimen-

tation and numerical simulation. They found that agitation facilitates homogeneous fluidization with increased uniformity of particle velocities. More recently, [10] performed a numerical simulation of the fluidization behavior of cohesive powders in stirred gas-solid fluidized beds with a frame impeller. Employing a Two-Fluid Model (TFM), they found that increasing the strength of the mechanical agitation intensifies the movements of the particles, especially in the lateral direction.

Sophisticated computer models, such as Computational Fluid Dynamics (CFD) - Discrete Element Method (DEM), offer a means to gain fundamental insights into the hydrodynamics of stirred gas-solid fluidized beds. It is commonly accepted in the scientific community that CFD-DEM simulations are more accurate, allow more detailed analysis, and have, among others, advantages with respect to polydispersity and non-spherical particles compared to TFM simulations, which tend to be faster and less computationally expensive [11–13]. With the current increase in computational power, CFD-DEM simulations of complex gas-solid systems are becoming more feasible. However, such simulations are very CPU demanding, and therefore, several approaches, such as coarse-graining or application of recurrence CFD (r-CFD), have been developed [14–16].

In this study, we extend a CFD-DEM model with an Immersed Boundary Method (IBM) in order to conduct a fundamental investigation into the fluidization behavior of Geldart B particles in a non-reactive stirred gas-solid fluidized bed reactor. A crucial aspect of using computer models is model verification to ensure its accuracy. To experimentally verify the CFD-DEM-IBM model, a laboratory-scale experimental and a one-on-one computational stirred gas-solid fluidized bed reactor have been developed. This paper focuses on the thorough comparison of the simulations with detailed hydrodynamic features obtained through experimental investigation. Since gas-solid fluidized beds are opaque to visible light, we employed X-ray imaging to visualize the fluidization behavior of the experimental stirred gas-solid fluidized bed. This paper first describes the experimental and simulation methods. Then, the experimental conditions and simulation parameters employed in the study are elaborated on. Subsequently, the results are presented and discussed. Finally, the results are summarized, and conclusions are drawn.

5.2. Methodology

5.2.1. Experimental methods

Stirred gas-solid fluidized bed setup

The experimental stirred gas-solid fluidized bed reactor consists of a fluidized bed column and an agitating system, as illustrated in Fig. 5.1a. The fluidized bed column is comprised of a 90 mm inner-diameter perspex cylinder with a length of 700 mm fitted with a 3 mm thick sintered stainless steel distributor plate. The agitating system comprises a 800 mm long stainless steel shaft with a three-blade PLA rectangular impeller at the bottom, positioned at the height of 50 mm above the distributor plate. The stirrer is mechanically agitated by a motor positioned atop the column. The column contains pressure ports through which the pressure can be measured at a height of 6 mm and 65 mm above the distributor plate.

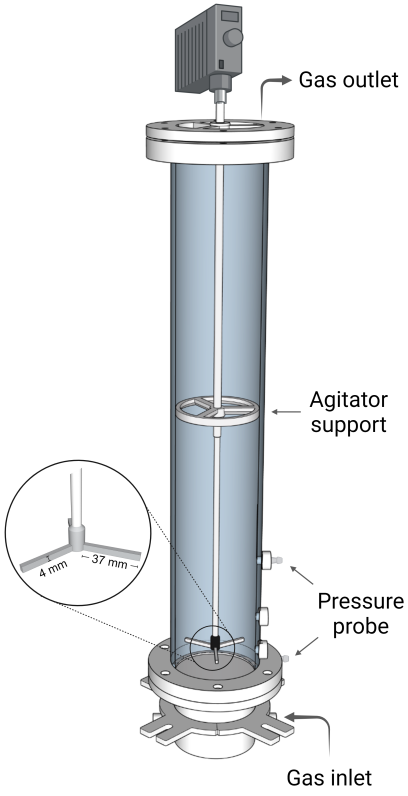

(a) Schematic of the stirred gas-solid fluidized bed reactor, which consists of a fluidized bed column and an agitating system.

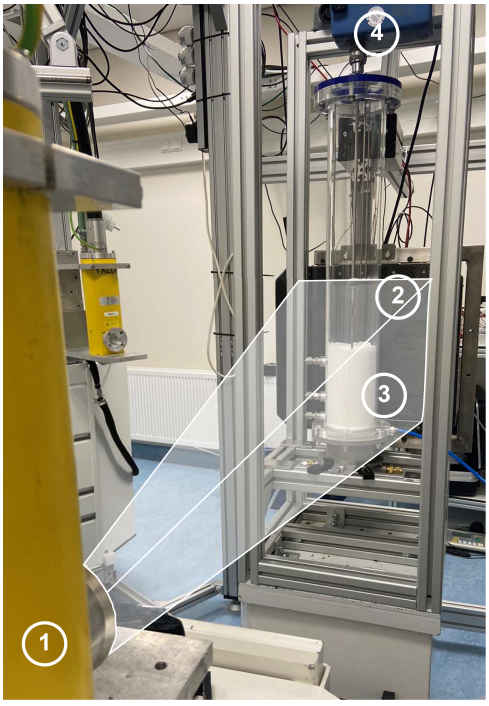

(b) Optical camera photo of the stirred gas-solid fluidized bed reactor comprising the particle bed (3) positioned in between the X-ray source (1) and the X-ray detector (2), with a schematic representation of the X-ray beam. The motor (4) used to agitate the stirrer is positioned atop the column.

Figure 5.1: Experimental setup used in this study.

X-ray imaging

The hydrodynamics of the stirred gas-solid fluidized bed were experimentally assessed using an in-house fast X-ray imaging setup, as depicted in Fig. 5.1b. X-ray imaging is a non-invasive imaging technique that can be used to visualize the hydrodynamics of opaque multiphase flows effectively [17, 18]. Through X-ray imaging, a 2D projection of the spatial gas-solids distribution in the stirred gas-solid fluidized bed reactor was captured.

The X-ray setup consists of a standard medical-use X-ray source (Yxlon International GmbH) with a maximum energy of 150 keV working in cone beam mode and a 2D detector (Teledyne Dalsa Xineos) with a theoretical spatial resolution of 0.20 mm placed opposite of the source. X-ray images were acquired at a sampling rate of 50 Hz over a measurement period of 60 s, equating to the acquisition of 3000 images per experiment. The obtained data were then stored for subsequent digital image analysis.

The X-ray measurement principle relies on the attenuation of X-rays traveling in a straight line from an X-ray source to a detector while passing through the material. The transmission of a monochromatic beam of high-energy photons with initial intensity I_0 through a material of constant density is described by the Lambert-Beer law:

$$I(L) = I_0 e^{-\mu z} \tag{5.1}$$

Here, $I(z)$ denotes the intensity measured at the detector, μ is the attenuation coefficient, and z is the thickness of the X-ray attenuating material between the source and the detector. For varying attenuation, the measured intensity is the integral effect of local attenuation with the local attenuation coefficient.

Each acquired image is a time-resolved projected 2D intensity map of the stirred gas-solid fluidized bed reactor. A calibration protocol was executed to convert the measurement intensity into a gas holdup. Initially, a reference image of the empty column was captured without the agitating system. Subsequently, the column was filled with the bed material, and a full reference image was obtained. By applying the Lambert-Beer law, the measurement gas holdup map was derived from the measurement intensity map using the empty and full reference, as depicted in Fig. 5.2. The normalized gas holdup ϵ_g was calculated as follows:

$$\epsilon_g = \frac{\ln(I_{\text{measurement}}/I_{\text{full}})}{\ln(I_{\text{empty}}/I_{\text{full}})} \tag{5.2}$$

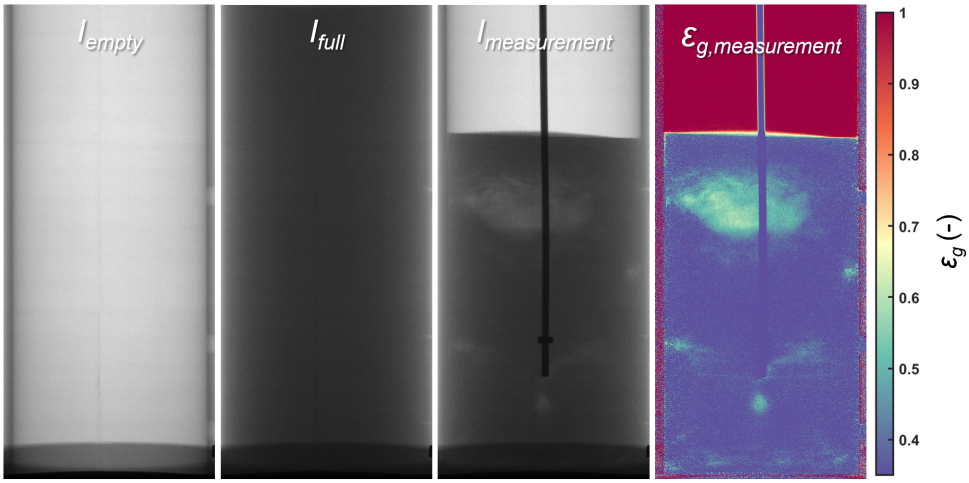

Figure 5.2: The measurement gas holdup (ϵ_g) map is computed from the measurement intensity map by employing Lambert-Beer law with an empty and full reference.

The calibration protocol is discussed in more detail and validated in the work by Wu *et al.* [19]. It is important to note that the normalized gas holdup in this study ranges from 0.37 to 1, where 1 represents pure gas and 0.37 close packing of solids. Warm colors in the gas holdup map correspond to low X-ray attenuation, indicating high gas concentrations. In contrast, cold colors represent high X-ray attenuation, indicating low gas concentrations.

Pressure measurements

To experimentally determine the minimum fluidization velocity and quantitatively evaluate the quality of fluidization during the measurements, the pressure drop was measured over the powder bed. The gas pressure was probed with a sampling frequency of 1000 Hz using OMEGA PX409-10WG5V pressure transducer positioned at heights of 6 mm and 65 mm above the distributor plate.

The time-averaged pressure drop and standard deviation of the pressure drop are common indicators for assessing fluidization quality. The acquired pressure data was multiplied with the column's cross-sectional area (A) and divided by the mass of the solids (m) and the gravitational acceleration (g) to give the normalized pressure drop ($\Delta PA/(mg)$).

5.2.2. Simulations

In this work, the CFD-DEM-IBM combination of the CFD framework FoxBerry [20] and the DEM code MercuryDPM [21] is used. The code has been utilized and validated in previous works [13, 22]. The gas phase is described by the continuity equation and the volume-averaged Navier-Stokes equations, respectively given by:

$$\frac{\partial(\epsilon_g \rho_g)}{\partial t} + \nabla \cdot \left(\epsilon_g \rho_g \mathbf{u}_g\right) = 0 \tag{5.3}$$

$$\frac{\partial\left(\epsilon_g \rho_g \mathbf{u}_g\right)}{\partial t} + \nabla \cdot \left(\epsilon_g \rho_g \mathbf{u}_g \mathbf{u}_g\right) = -\epsilon_g \nabla p_g - \nabla \cdot \left(\epsilon_g \tau_g\right) - \mathbf{S} + \epsilon_g \rho_g \mathbf{g} \tag{5.4}$$

τ_g is the gas phase stress tensor using the general Newtonian form. **S** represents the momentum source term for the gas-solids interaction, given by:

$$\mathbf{S} = \sum_i 3\pi \mu_g \epsilon_g d_{p,i} \beta \left(\mathbf{u}_g - \mathbf{v}_i\right) D\left(\mathbf{r} - \mathbf{r}_i\right) \tag{5.5}$$

The momentum source term uses the polynomial distribution function of Deen *et al.* [23] using a mapping width of $3d_p$. The drag correlation of Beetstra *et al.* [24] is employed:

$$\beta = 10\frac{(1-\epsilon_g)}{\epsilon_g^2} + \epsilon_g^2\left(1 + 1.5\sqrt{1-\epsilon_g}\right) + \frac{0.413 Re_p}{24\epsilon_g^2}\frac{\left[\epsilon_g^{-1} + 3\epsilon_g(1-\epsilon_g) + 8.4 Re_p^{-0.343}\right]}{\left[1 + 10^{3(1-\epsilon_g)} Re_p^{-0.5-2(1-\epsilon_g)}\right]} \tag{5.6}$$

Where the Reynolds number is computed via:

$$Re_p = \frac{\epsilon_g \rho_g \left|\mathbf{u}_g - \mathbf{v}_p\right| d_p}{\mu_g} \tag{5.7}$$

The translational and rotational movement of each individual particle is calculated by solving Newton's equations:

$$m_i \frac{d\mathbf{v}_i}{dt} = -V_i \nabla p_g + 3\pi \mu_g \epsilon_g d_{p,i} \beta \left(\mathbf{u}_g - \mathbf{v}_i\right) + m_i \mathbf{g} + \sum \mathbf{F}_{contact,i} \tag{5.8}$$

$$I_i \frac{\omega_i}{dt} = \mathbf{T}_i \tag{5.9}$$

where $\mathbf{v}_i$ is the particle velocity. The forces on the right-hand side for the translational motion (equation 5.8) are respectively due to the far-field pressure gradient, drag, gravity, and contact forces due to particle-particle or particle-wall collisions. The contact forces are captured by a soft-sphere model originally developed by Cundall and Strack [25]. $\mathbf{T}_i$ is the torque which changes due to the tangential component of the individual contact forces resulting from the linear-spring dashpot model, I_i the moment of inertia and ω_i the rotational velocity (1/s).

Stirrer and cylinder geometry

Neither the geometry of the column wall nor of the stirrer aligns with the underlying 3D Cartesian grid of the continuous phase. To represent both, a second-order implicit ghost cell Immersed Boundary Method (IBM) is employed [26]. In this method, the coefficients of the discretized momentum equations of the continuous fluid are adapted if the surface of an object intersects with the discretization stencil. This manipulation utilizes a directional, second-order extrapolation to compute the velocity in the immersed cell under the assumption of a no-slip boundary condition at the object's surface. Additionally, if a cell center is located inside the object, the local velocity corresponding to the solid body motion of the object is imposed on the solution.

The cylinder geometry is approximated by a tube with radius R. All required values for the application of the IBM, such as intersection points of grid lines with the cylinder, are determined analytically [27]. In contrast, a mesh in the Standard Tesselation Language format is employed for the complex geometry of the stirrer. There, the surface of the object is approximated by a set of interconnected triangles. To determine the required intersections to apply the IBM, the triangles are first associated with the intersecting Cartesian cells via a triangle/axis-aligned-bounding-box intersection algorithm, and subsequently, ray/triangle intersection calculations are carried out to determine the relevant intersect [28]. The required information is recomputed for each fluid time step, following the rotation of the stirrer mesh. The particle contact with the stirrer and cylinder is covered in the DEM code MercuryDPM as reported by Weinhart *et al.* [21].

5.3. Setup

5.3.1. Experiments

Commercially available Geldart B-type high-purity alumina powder (SASOL) is used as bed material in this study. The powder has a Sauter mean particle diameter of 0.94 mm and a particle density of 1300 kg m^{-3}. For the fluidiza-

tion experiments, the column was loaded with 774 g of material, constituting a settled bed height of approximately 150 mm. Through pressure drop measurements, of which the results are presented in Section 5.4.1, the minimum fluidization velocity (u_{mf}) was experimentally determined to be 32.5 cm s^{-1}.

Throughout all experiments, the inlet gas velocity was controlled at 39.3 cm s^{-1}, corresponding to 1.2u_{mf}. The influence of agitation on the hydrodynamics was systematically assessed by evaluating the hydrodynamics of a bed without an agitator, a bed with a static agitator, and a bed with an agitator while stirring at angular velocities of 7.2, 10.2, and 13.5 rad s^{-1}. An overview of the experimental parameters is provided in Table 5.1.

Table 5.1: Experimental parameters used in this study.

Parameter	Symbol	Value	Unit
Particle diameter	d_p	$9.4{\cdot}10^{-4}$	m
Particle density	ρ_p	1300	kg m^{-3}
Inlet velocity air	u_o	0.393	m s^{-1}
Angular velocity stirrer	ω	7.2 - 10.2 - 13.5	rad s^{-1}
Sampling frequency X-ray	f_{xray}	50	Hz
Measurement run time	t_{meas}	60	s

5.3.2. Simulations

The CFD-DEM-IBM simulations were carried out using a 3D rectangular column with dimensions 0.1×0.1×0.4 m (width ×depth × height) wherein the cylindrical tube with 90 mm inner-diameter is positioned. The main simulation parameters are listed in Table 5.2. The DEM collision parameters for γ-Al_2O_3 are previously reported by Sutkar *et al.* [29]. In order to improve the gas phase resolution and the corresponding IBM method, the grid size is chosen to be smaller than the particle diameter. This is allowed by making use of the continuous two-way smoothing function of Deen *et al.* [23] for the Lagrangian-Eulerian mapping as studied by de Munck *et al.* [13]. This smoothing function is also subsequently used and validated in previous works, see de Munck *et al.* [22, 30, 31]. The boundary conditions for the continuous phase were set as a uniform superficial air velocity equal to 39.3 cm s^{-1} at the bottom and a fixed pressure boundary condition of 1 atm at the top of the domain.

5.4. Results and discussion

5.4.1. Minimum fluidization curve

The pressure drop as a function of the superficial gas velocity was acquired through experimentation and simulation using a column without an agitator. It

Table 5.2: Simulation parameters used in this study.

Parameter	Symbol	Value	Unit
Number of particles	N_p	1 369 215	-
Particle diameter	d_p	$9.4{\cdot}10^{-4}$	m
Particle density	ρ_p	1300	kg m^{-3}
Inlet velocity air	u_0	0.393	m s^{-1}
Angular velocity stirrer	ω	7.2 - 10.2 - 13.5	rad s^{-1}
Friction coefficient	μ_0	0.1	-
Normal coefficient of restitution	e_n	0.74	-
Tangential coefficient of restitution	e_t	0.1	-
Normal stiffness	k_n	3000	N m^{-1}
Tangential stiffness	k_t	1305.6	N m^{-1}
Normal dampening coefficient	η_n	0.0056	N s m^{-1}
Tangential dampening coefficient	η_t	0.012	N s m^{-1}
CFD time step	t_{flow}	$2.5{\cdot}10^{-5}$	s
DEM time step	t_{DEM}	$2.5{\cdot}10^{-6}$	s
Time simulated	t	11	s
Number of grid cells (width)	N_x	100	-
Number of grid cells (depth)	N_y	100	-
Number of grid cells (height)	N_z	400	-

is important to establish that the model can accurately capture the fluidization behavior of the granular bed and thus gives a correct representation of pressure drop. Fig. 5.3 presents the time-averaged normalized pressure drop ($\Delta PA/(mg)$) as a function of the superficial gas velocity.

At gas velocities below 30 cm s^{-1}, a difference between the simulated and the experimentally obtained time-averaged normalized pressure drop can be observed. Although both curves show a characteristic linear increase in the pressure drop in a fixed bed regime, the simulated pressure drop is slightly higher than the experimentally obtained one. Moreover, by closely evaluating the points at which the plateaus are reached, the minimum fluidization velocity for the alumina powder is found to be approximately 27.5 cm s^{-1} in the simulation and 32.5 cm s^{-1} in the experiment.

Two root causes are discerned for these differences. First, the superficial gas velocity is step-wise increased in the simulation, whereafter, the pressure drop data is averaged over a 0.5 s time period. A 0.5 s time period could be insufficient to give a stable averaging pressure, but longer simulation times are very computationally expensive, and therefore a compromise has to be found. In contrast, in the experiment, averaging was performed for a 30 s period after stabilizing the system.

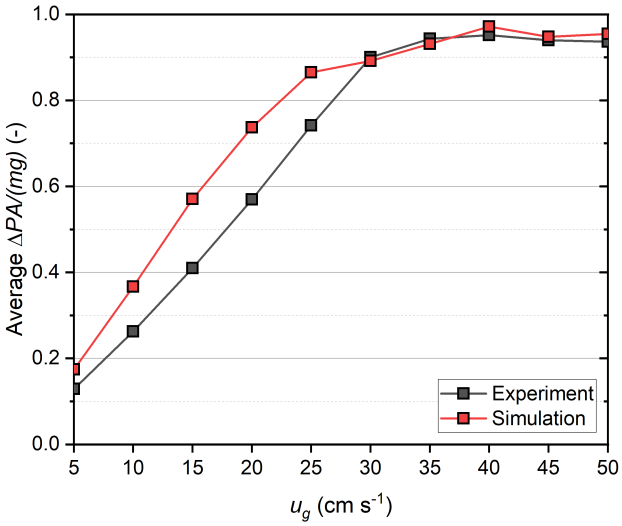

Figure 5.3: The time-averaged normalized pressure drop measured at the height of 6 mm above the distributor plate as a function of the superficial gas velocity, u_g.

Second, the measured pressure drop in a fixed bed regime is highly susceptible to the packing of solids and meso-structure of the bed. Manual filling in the experimental procedure could give rise to a heterogeneous solids packing, which in turn results in a lower pressure drop as the gas finds a path with lower resistance. Moreover, in the simulation, the meso-structure is less resolved, which increases the tendency of the gas to form bubbles. At higher gas velocities (from 30 cm s^{-1} onward), there is a good agreement between the simulated and the experimentally obtained time-averaged normalized pressure drop, as both curves approach a plateau at an average normalized pressure drop of approximately 0.95 when fluidization is attained. This is in agreement with the theory that pressure drop differences due to different packing vanish, which increases the likelihood that the differences in observed pressure drop are caused by the heterogeneous solids packing in the experiment and the challenges in resolving the meso-structure of the bed in the simulation. Notably, at gas velocities higher than the minimum fluidization velocity, a good agreement is observed, demonstrating that the model can accurately describe the pressure drop over the bed under fluidized conditions, which is key to this work.

5.4.2. Visualization of the fluidization behavior

A significant advantage of time-resolved X-ray imaging is that it can provide a direct projection of the gas holdup over time, which allows visualization of the fluidization behavior. Similarly, a 2D projection presenting the gas holdup over time can be obtained from the CFD-DEM-IBM simulations. Through displaying representative snapshots, Fig. 5.4 presents a qualitative comparison of the experimentally observed fluidization behavior and the simulated fluidization behavior for various stirrer settings.

From the experiment-simulation comparison, it becomes evident that the upper part of the bed in the simulations displays more disorderly behavior, especially visible in the splash zone, caused by the formation of larger bubbles. In contrast, the experimental bed shows less frequent and smaller bubbles, thereby displaying less disorderly behavior. The difference could be attributed to differences in the meso-structure of the bed and a slightly different fluidization regime, which can be better understood by the presented data on the minimum fluidization velocity determination.

Here, a discrepancy in the obtained pressure drop at low gas velocities was attributed to a difference in minimum fluidization velocity and the meso-structure of the beds. The same can contribute to the observed difference in fluidization behavior. At, or close to, the point of minimum fluidization, the bed is in a loosely packed state, which allows gas to flow through the meso-structure of the bed. In the experiment, this results in the gas flowing well-distributed through the bed. Therefore, the fluidization behavior observed in the experiment is more homogeneous, and a slightly lower gas holdup is obtained in the snapshots.

In the simulation, a lower minimum fluidization velocity was found, which means that the simulations are performed at a higher u_g/u_{mf} ratio when compared to the experiments. To elucidate this effect, the experiments were also performed at a superficial gas velocity of 45 cm s^{-1}. The corresponding X-ray images are included in Appendix Fig. D.1. It can be observed that at a velocity of 45 cm s^{-1}, the bed displays significantly more chaotic behavior compared to the behavior at the velocity of 39.3 cm s^{-1}, despite it only being a 15% increase. Interestingly, now the flow pattern shows stronger similarities to the simulation, suggesting that, indeed, the difference in u_g/u_{mf} ratio could play an important role.

In addition, the meso-structure of the bed is less resolved. This difference in behavior is shown by displaying the temporal evolution of the flow pattern over a time window of 0.4 s for a rotation speed of 10.2 rad s^{-1} (see Appendix Fig. D.2). When comparing the bottom zone of the experimental and simulated flow patterns in Appendix Fig. D.2, it can be observed that both display the presence of horizontal gas structures directly above the distributor plate. These structures rise up before being dispersed into bubbles by the stirrer. As the meso-structure of the bed is less resolved for the simulation, the gas has the tendency to form bubbles more rapidly in the simulations than in the experiments, as observable in the figure. In turn, the coalescence of the bubbles leads to the formation of larger bubbles that contribute to the disorderly splash zone observed in the simulations. On the contrary, in the experiments, a significantly smaller number of bubbles are formed that display more structured behavior.

Moreover, another reason contributing to the more disorderly behavior could be that the simulated beds have more energy dissipation when compared to the experiments, as was also shown by Li and Kuipers [32], Verma *et al.* [33]. This would require a more detailed investigation of the effect of the collision parameters on the fluidization characteristics, which is outside the scope of the present paper.

5.4.3. Time-averaged gas holdup

With the time-resolved gas holdup ϵ_g acquired through X-ray imaging and simulation, a time-averaged gas holdup was computed:

$$\overline{\epsilon}_g(x,z) = \frac{1}{N_{\Delta t}} \sum_{t=t_0}^{t_0+\Delta t} \epsilon_g(x,z,t) \tag{5.10}$$

where x and z represent the horizontal and vertical positions, and $N_{\Delta t}$ represents the number of images between t_0 and t_0+Δt. From the time-averaged gas holdup, a line-averaged gas holdup is computed alongside the vertical direction to display the gas holdup over the bed height:

$$\overline{\epsilon}_{g,x}(z) = \frac{1}{N} \sum_{x=1}^{N} \overline{\epsilon}_g(x,z) \tag{5.11}$$

where N is the number of pixels in the horizontal direction at the height z.

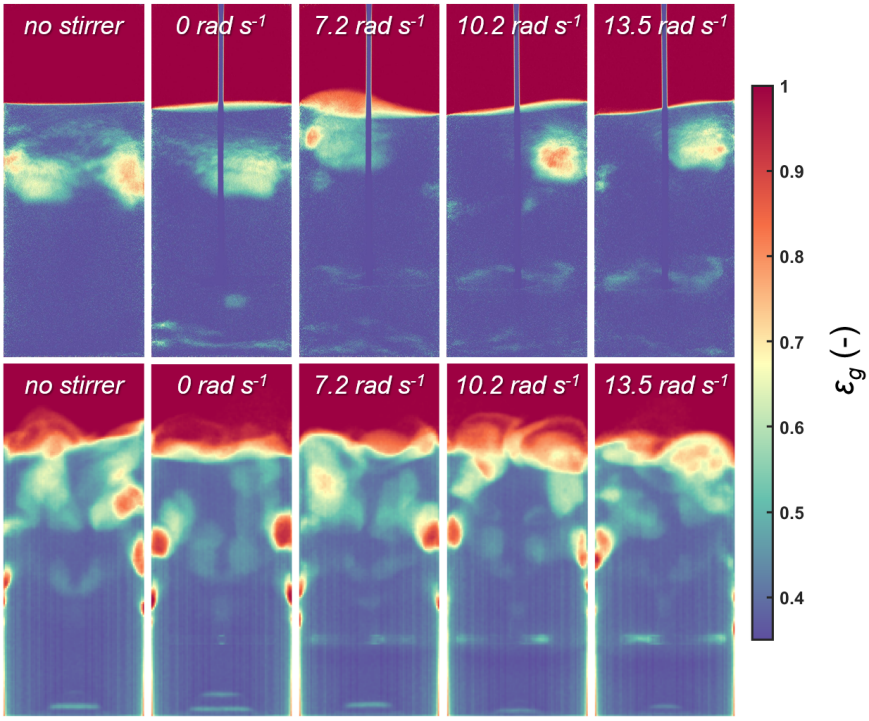

Figure 5.4: Typical snapshots of the fluidization behavior at a superficial gas velocity of 39.3 cm s^{-1} for various stirrer settings obtained through experimental X-ray imaging (top) and simulation (bottom).

Fig. 5.5 depicts the time-averaged gas holdup profiles obtained through X-ray imaging (Fig. 5.5a) and simulation (Fig. 5.5b). In both cases, a local increase in gas holdup is visible at an axial position of 50 mm. This increase in gas holdup is attributed to the wakes formed behind the impeller blades. In agreement with the time-resolved snapshots of the fluidization behavior (Figure 5.4), it is evident that the wakes, and thereby the local time-averaged gas holdup, increases with increasing angular velocity. The good agreement in wake formation between the experiment and simulation demonstrates that the simulation adequately captures the fluid dynamics in the stirring zone.

At higher axial positions, some deviation between the experiment and the simulation can be observed. The simulation displays a steady increase in the average gas holdup for an increase in the axial position, attributed to the coalescence of bubbles, while in the experiments, less frequent and smaller bubbles appear, resulting in a more uniform system with a lower gas holdup. In

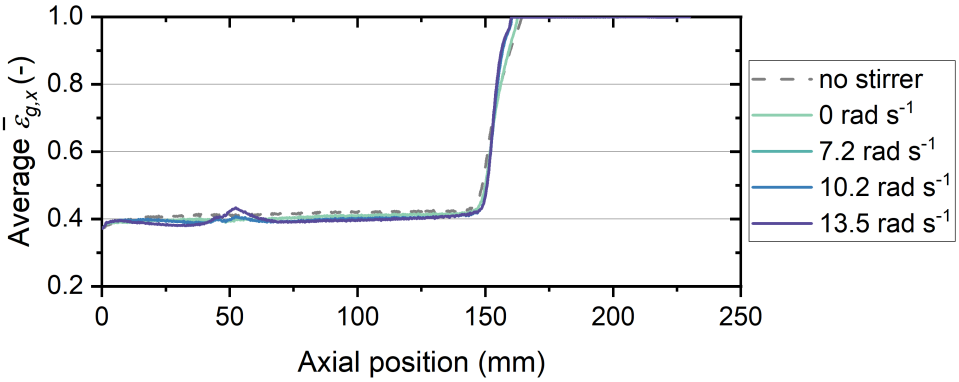

(a) Time-averaged gas holdup over the axial position acquired through X-ray imaging experiments.

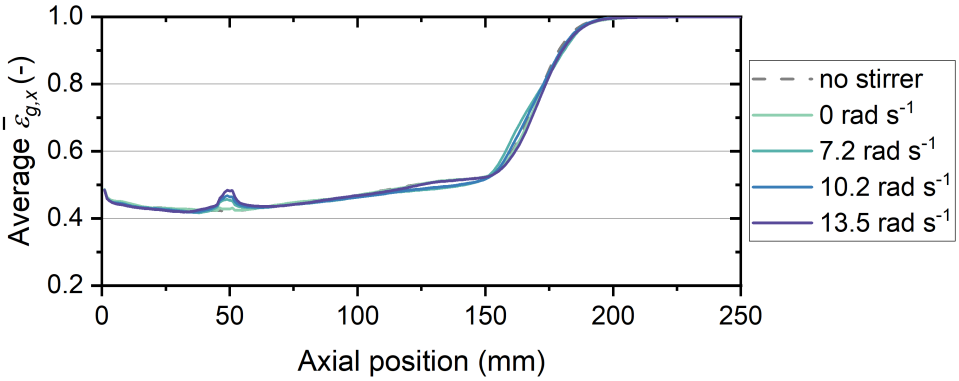

(b) Time-averaged gas holdup over the axial position acquired through simulation.

Figure 5.5: Influence of the angular velocity on the time-averaged gas holdup over the axial position.

the simulations, a clear difference in the top and bottom regions is observed, which is attributed to the rapid coalescence of bubbles. The more disorderly behavior observed in the simulation results in a smooth increase in the time-averaged gas holdup in the splash zone, identifiable at heights between 150 and 200 mm. On the contrary, the more homogeneous bed observed in the experimental results in a sharp increase in gas holdup in the splash zone, identifiable at an axial position of 150 mm. Besides, an increase in the wake volume and the homogeneity of the bed, caused by increasing the angular velocity of the stirrer, was not found to have a significant effect on the time-averaged line-averaged gas holdup.

5.4.4. Pressure analysis

The gas pressure was measured at the height of 6 mm and 65 mm above the distributor plate experimentally and through simulation. Fig 5.6 presents the time-averaged normalized pressure drop. It can be observed that the experimentally obtained normalized pressure drop is accurately captured by the simulation at both heights for all agitator settings. At a height of 6 mm, a normalized pressure drop of approximately 0.95 is observed, indicative of high-quality fluidization both in the experiment and simulation.

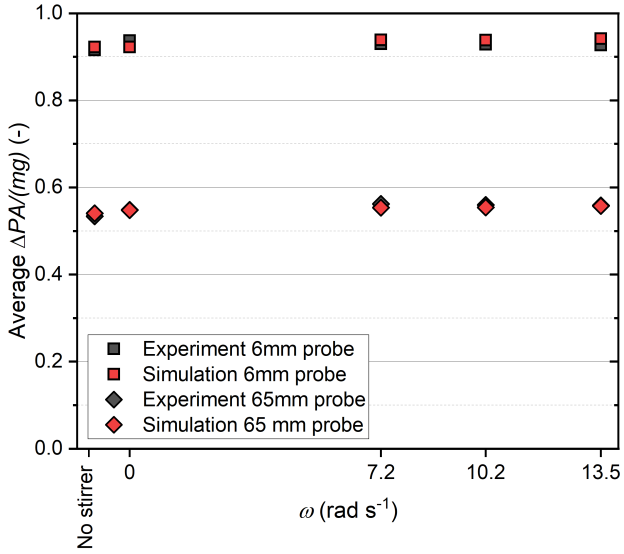

Figure 5.6: The influence of agitation on the time-averaged normalized pressure drop.

Figure 5.7 presents the standard deviation of the normalized pressure drop. The standard deviation of the pressure drop in a fluidized bed is correlated with the bubbling dynamics caused by the energy dissipation due to particle collisions and fluid-particle/stirrer-particle interactions. Typically, an increase in fluid-particle/stirrer-particle interactions leads to a higher bed homogeneity and thus a lower pressure drop standard deviation [32, 33]. Both the experimentally measured and simulated standard deviations of the pressure drop decrease with increasing angular velocity, suggesting greater bed homogeneity. When increasing the angular velocity, the bubble size is reduced, resulting in a more homogeneous fluidized bed due to the stirring motion. This is in close agreement with reported literature (see Section 5.1) and visual observations of the hydrodynamic behavior, as discussed in the previous section.

By comparing the experiment and the simulation, it can be observed that the standard deviation of the pressure drop in the simulation results is larger. This is attributed to the more disorderly nature of the bed (see Fig. 5.4), which in turn is caused by a lower minimum fluidization velocity and a less resolved meso-structure in the simulation, which resulted in more rapid bubble formation and coalescence in the simulations compared to the experiments. Yet, both the experiment and simulation clearly depict that the enhanced particle-stirrer interaction by means of mechanical agitation improves bed homogeneity, which is desirable in applications that require excellent gas-solid contacting.

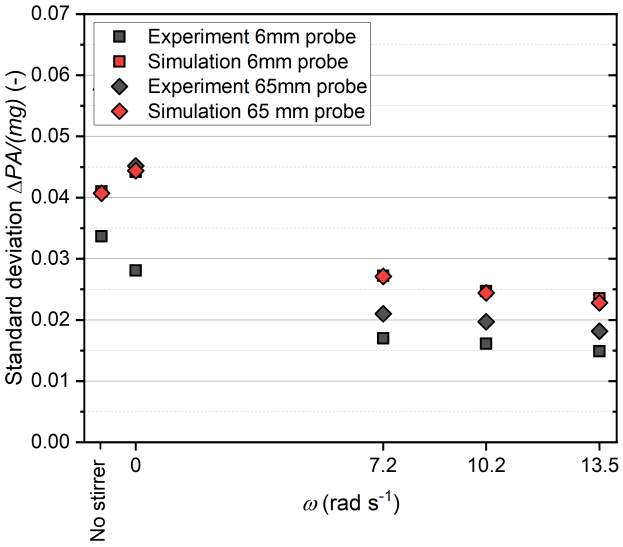

Figure 5.7: The influence of agitation on the standard deviation of the pressure drop.

5.4.5. Solids mass flux

The CFD-DEM-IBM simulations allow one to study the solids motion and mass flux in more detail, which is not attainable via the currently applied experimental measurements. Experimental techniques such as positron emission particle tracking (PEPT), radioactive particle tracking (RPT), and X-ray particle velocimetry (XPTV) can be used for comparing the solids mass flux obtained from experiments and simulation [34, 35], which is not pursued in this work but can serve as an extension of this study. The time-averaged solids mass fluxes for the x- and z-directions are obtained by multiplying the local solids holdup with the obtained average particle velocities of all particles in the cell of interest. This is captured by:

$$\langle \phi_m \rangle = \langle \mathbf{v}_p \rho_p \left(1 - \epsilon_g\right) \rangle \tag{5.12}$$

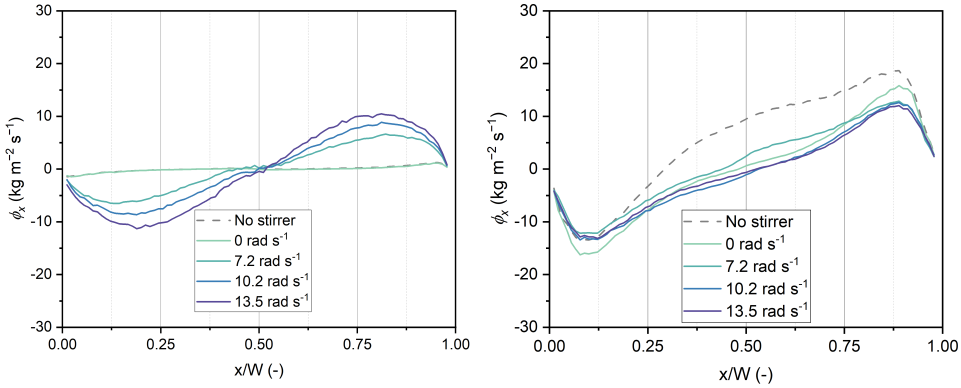

(a) x-component mass flux at a height of 5 cm.

(b) x-component mass flux at a height of 7.5 cm.

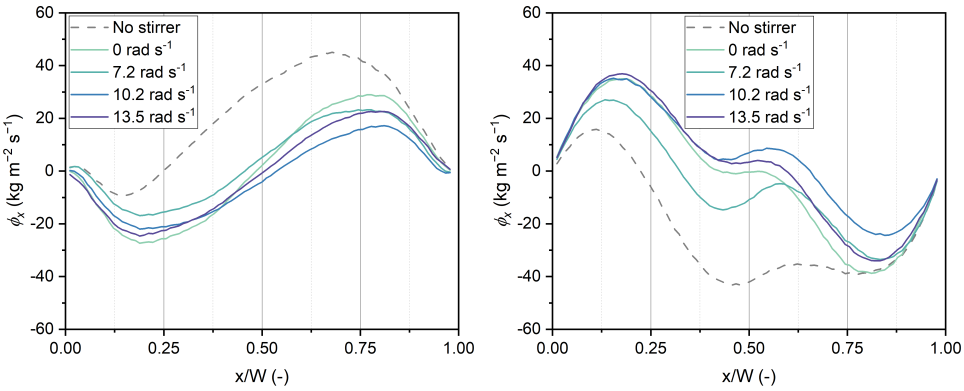

(c) x-component mass flux at a height of 10 cm.

(d) x-component mass flux at a height of 15 cm.

Figure 5.8: The x-component mass flux at various heights in the bed as for various stirrer settings. Note that the vertical axes have different limits for visibility purposes.

First, the time-averaged solids mass flux for the x-direction is discussed at heights equal to 5, 7.5, 10, and 15 cm. Fig. 5.8 shows the altered time-averaged x-component of the solids mass flux for the normalized column diameter (x/W) under the influence of agitation. It can be noticed that at a height of 5 cm, where the stirrer is located, the x-component of the solids mass flux is significantly altered due to the rotating stirrer (Fig. 5.8a). Following the stirrer rotation speed, the magnitude of the solids mass flux is increased as the solids are agitated by the stirrer motion. On the contrary, the effect of the stirrer rotational motion is less pronounced at higher axial positions. It can even be concluded

that the stirrer shaft acts as a static immersed body, reducing the flowability of the solids material, clearly observed in Fig. 5.8b, Fig. 5.8c and Fig. 5.8d where the case without the stirrer results in a higher x-component of the solids mass flux. Besides, it should be noted that at these heights, the stirrer blades are less influential as they are placed lower inside the bed. Therefore, solids motion is mainly dominated by the gas-solid interaction, as evident from the mass flux in Fig. 5.8d caused by the splash zone.

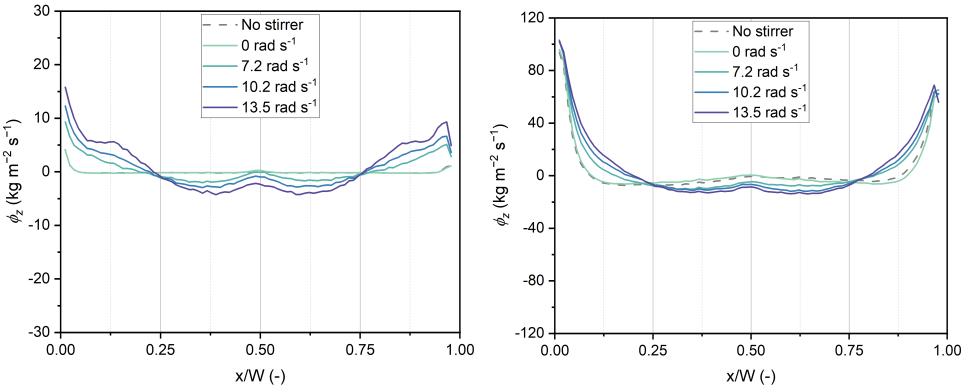

(a) z-component mass flux at a height of 5 cm.

(b) z-component mass flux at a height of 7.5 cm.

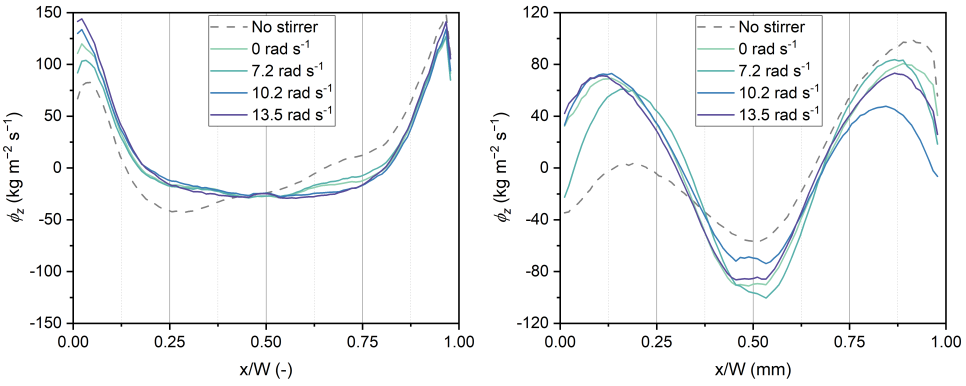

(c) z-component mass flux at a height of 10 cm.

(d) z-component mass flux at a height of 15 cm.

Figure 5.9: The z-component mass flux at various heights in the bed as for various stirrer settings. Note that the vertical axes have different limits for visibility purposes.

Fig. 5.9 represents the solids mass flux z-component at heights equal to 5, 7.5, 10, and 15 cm for the normalized column diameter (x/W). Complementary to the x-component, the stirrer blade rotation alters the solids mass flux directly at the vertical position of the stirrer, as observed in Fig. 5.9a. At higher

angular velocities, the solids mass flux is increased, especially in the region of 0.25 and 0.75 of the normalized column diameter (x/W). Based on the gas holdup data, this can be better understood by the fact that bubbles are created by the stirrer rotation. The bubble wake provides a transport mechanism for the solids. Subsequently, at h = 7.5 cm (Fig. 5.9b), this rising mechanism results in a symmetrical solids mass flux, which is higher at the sides of the column for the higher stirrer rotations, while being lower in the column center. This pattern is further evolving due to the preferential bubble pathway, resulting in a symmetrical solids mass flux at h = 10 cm and 15 cm. This symmetrical solids mass flux is influenced by the immersed object in the center of the column, which becomes clear by comparing the 0 rad s^{-1} and the case without a stirrer. By a detailed comparison between these cases, it is observed that the immersed static shaft object gives rise to a symmetrical flow pattern, which is not discerned in the case without the stirrer.

Based on the discussions both on the x- and z-components of the solids mass flux, it becomes evident that the solids agitation is improved directly near the stirrer blades, while further up in the bed, the solids agitation is reduced due to the shaft, which acts as a static immersed body. This highlights that assisted fluidization through a vertically placed stirrer can improve the solids agitation. Still, a proper design study needs to be performed as static immersed bodies (e.g. the stirrer shaft) negatively influence the solids motion [19].

5.5. Conclusion

In this study, the influence of agitation of a vertical three-blade agitator on the fluidization performance of Geldart B particles in a laboratory-scale column is experimentally investigated through X-ray imaging and pressure drop measurements and numerically through CFD-DEM-IBM simulation. The influence of agitation was systematically assessed by evaluating the fluidization behavior of a bed without an agitator, a bed with a static agitator, and a bed with an agitator while stirring at angular velocities of 7.2, 10.2, and 13.5 rad s^{-1}, at $1.2u_{mf}$.

The simulated minimum fluidization curve and time-averaged pressure drop are in qualitative agreement with the experimentally obtained ones, which validates the numerical model. Direct visualization of the fluidization behavior shows that an increase in the angular velocity of the agitator results in reduced bubble size, improved bed homogeneity, and the formation of wakes behind the impeller blades. The reduced bubble size and improved bed homogeneity are further substantiated by the observed decreasing standard deviation of the

pressure drop for an increasing angular velocity. Moreover, the agreement between the experiment and simulation in wake formation is good, demonstrating that the simulation adequately captures the fluid dynamics in the stirring zone. Deviations between the simulations and experiments in the gas holdup at the top of the bed were attributed to a slightly lower minimum fluidization velocity and less-resolved meso-structure of the bed in the simulations, which results in more intense bubbling and a more disorderly splash zone. An in-depth analysis of the solids flow field through simulation shows that the solids agitation is improved directly near the stirrer blades, while higher up in the bed, the solids agitation is reduced due to the shaft, which acts as a static immersed body. This emphasizes that while assisted fluidization through a vertically placed stirrer can improve the solids agitation, a proper design study is crucial as static immersed bodies, such as the stirrer shaft, negatively influence the solids motion.

Besides contributing to a further understanding of the hydrodynamics of stirred gas-solid fluidized beds, this work provides a validated CFD-DEM-IBM simulation method that can be used to simulate fluidized beds with moving internals, such as stirrers. By implementing approaches that speed up the simulation run time, such as coarse-graining and r-CFD, future investigations could aid in optimizing, intensifying, and scaling the systems for industrial applications, such as polyolefin manufacturing.

References

[1] L.-S. Fan and C. Zhu, *Principles of gas-solid flows* (Cambridge University Press, Port Chester, NY, United States, 1999).

[2] V. Francia, K. Wu, and M.-O. Coppens, *Dynamically structured fluidization: Oscillating the gas flow and other opportunities to intensify gas-solid fluidized bed operation,* Chemical Engineering and Processing - Process Intensification **159**, 108143 (2021).

[3] I. Reed, T. M. and M. R. Fenske, *Effects of agitation on gas fluidization of solids,* Industrial & Engineering Chemistry **47**, 275 (1955).

[4] A. Sahoo, *Bed expansion and fluctuation in cylindrical gas solid fluidized beds with stirred promoters,* Advanced Powder Technology **22**, 753 (2011).

[5] A. B. Gorbach, S. D. Naik, and W. H. Ray, *Dynamics and stability analysis of solid catalyzed gas-phase polymerization of olefins in continuous stirred bed reactors,* Chemical Engineering Science **55**, 4461 (2000).

[6] H. Trieschmann, W. Rau, T. Jacobsen, and H. Pfannmueller, *Polymerization of propylene with ziegler catalysts in a stirred gas phase reactor,* (1972).

[7] W. Rau, H. G. Trieschmann, and K. Wisseroth, *Methods of removing heat from polymerization reactions of monomers in the gas phase,* (1977).

[8] M. Leva, *Pressure drop and power requirements in a stirred fluidized bed,* AIChE Journal **6**, 688 (1960).

[9] Y. Han, J.-J. Wang, X.-P. Gu, L.-F. Feng, and G.-H. Hu, *Homogeneous fluidization of geldart d particles in a gas–solid fluidized bed with a frame impeller,* Industrial & Engineering Chemistry Research **51**, 16482 (2012).

[10] S. Wang, Y. Chen, Y. Jia, R. Tian, Q. Sun, J. Fan, and Y. Ma, *Numerical simulation of flow behavior of particles in a gas-solid stirred fluidized bed,* Powder Technology **338**, 119 (2018).

[11] M. van Sint Annaland, G. Bokkers, M. Goldschmidt, O. Olaofe, M. van der Hoef, and J. Kuipers, *Development of a multi-fluid model for poly-disperse dense gas-solid fluidized beds part i: model derivation and numerical implementation,* Chemical Engineering Science **64**, 4222 (2009).

[12] V. Verma and J. T. Padding, *A novel approach to mp-pic: Continuum particle model for dense particle flows in fluidized beds,* Chemical Engineering Science: X **6**, 100053 (2020).

[13] M. J. A. de Munck, J. B. van Gelder, E. A. J. F. Peters, and J. A. M. Kuipers, *A detailed gas-solid fluidized bed comparison study on CFD-DEM coarse-graining techniques,* Chemical Engineering Science **269**, 118441 (2023).

[14] M. Sakai and S. Koshizuka, *Large-scale discrete element modeling in pneumatic conveying,* Chemical Engineering Science **64**, 533 (2009).

[15] T. Lichtenegger and S. Pirker, *Recurrence cfd – a novel approach to simulate multiphase flows with strongly separated time scales,* Chemical Engineering Science **153**, 394 – 410 (2016).

[16] T. Lichtenegger, E. Peters, J. Kuipers, and S. Pirker, *A recurrence cfd study of heat transfer in a fluidized bed,* Chemical Engineering Science **172**, 310 (2017).

[17] K. Wu, E. C. Wagner, O. Ochkin-Koenig, M. Franck, D. Weis, G. M. H. Meesters, and J. R. van Ommen, *Time-resolved x-ray study of assisted fluidization of cohesive micron powder: On the role of mechanical vibration,* Chemical Engineering Journal **470**, 143936 (2023).

[18] M. Errigo, P. Lettieri, and M. Materazzi, *X-ray imaging techniques for gas–solid fluidized beds: A technical review,* Particuology (2023).

[19] K. Wu, R. Kamphorst, A. Bakker, J. Ford, E. C. Wagner, O. Ochkin-Koenig, M. Franck, D. Weis, G. M. Meesters, and J. R. van Ommen, *Stirrer design for improving fluidization of cohesive powder: A time-resolved x-ray study,* Chemical Engineering Science **294**, 120069 (2024).

[20] S. Kamath, M. V. Masterov, J. T. Padding, K. A. Buist, M. W. Baltussen, and J. A. M. Kuipers, *Parallelization of a stochastic Euler-Lagrange model applied to large scale dense bubbly flows,* Journal of Computational Physics: X **8**, 100058 (2020).

[21] T. Weinhart, L. Orefice, M. Post, M. P. van Schrojenstein Lantman, I. F. Denissen, D. R. Tunuguntla, J. M. Tsang, H. Cheng, M. Y. Shaheen, H. Shi, P. Rapino, E. Grannonio, N. Losacco, J. Barbosa, L. Jing, J. E. Alvarez Naranjo, S. Roy, W. K. den Otter, and A. R. Thornton, *Fast, flexible particle simulations — An introduction to MercuryDPM,* Computer Physics Communications **249**, 107129 (2020).

[22] M. J. A. de Munck, E. A. J. F. Peters, and J. A. M. Kuipers, *Fluidized bed gas-solid heat transfer using a CFD-DEM coarse-graining technique,* Chemical Engineering Science **280**, 119048 (2023).

[23] N. G. Deen, M. van Sint Annaland, and J. A. M. Kuipers, *Multi-scale modeling of dispersed gas-liquid two-phase flow,* Chemical Engineering Science **59**, 1853 (2004).

[24] R. Beetstra, M. A. van der Hoef, and J. A. M. Kuipers, *Drag Force of Intermediate Reynolds Number Flow Past Mono- and Bidisperse Arrays of Spheres,* AIChE Journal **53**, 489 (2007).

[25] P. A. Cundall and O. D. L. Strack, *A discrete numerical model for granular assemblies,* Geotechnique **29**, 47 (1979).

[26] N. G. Deen, S. H. L. Kriebitzsch, M. A. van der Hoef, and J. A. M. Kuipers, *Direct numerical simulation of flow and heat transfer in dense fluid–particle systems,* Chemical Engineering Science **81**, 329 (2012).

[27] A. Eghbalmanesh, A. Fathiganjehlou, D. R. Rieder, M. Hoogendoorn, M. Miloshevska, M. W. Baltussen, E. A. J. F. Peters, K. A. Buist, and J. A. M. Kuipers, *CFD-validated pore network modeling of packed beds of non-spherical particle,* Chemical Engineering Science **283**, 119396 (2024).

[28] T. Akenine-Möller, E. Haines, N. Hoffman, A. Pesce, M. Iwanicki, and S. Hillaire, *Real-Time Rendering, Fourth Edition* (CRC Press, 2018) p. 1 – 1178.

[29] V. S. Sutkar, N. G. Deen, B. Mohan, V. Salikov, S. Antonyuk, S. Heinrich, and J. A. M. Kuipers, *Numerical investigations of a pseudo-2D spout fluidized bed with draft plates using a scaled discrete particle model,* Chemical Engineering Science **104**, 790 (2013).

[30] M. J. A. de Munck, E. A. J. F. Peters, and J. A. M. Kuipers, *CFD-DEM Fluidized Bed Drying Study Using a Coarse-Graining Technique,* Industrial & Engineering Chemistry Research **62**, 20911 (2023).

[31] M. J. A. de Munck, E. A. J. F. Peters, and J. A. M. Kuipers, *CFD-DEM modeling and validation of solids drying in a gas-fluidized bed,* Chemical Engineering Science **291**, 119922 (2024).

[32] J. Li and J. A. M. Kuipers, *Effect of competition between particle-particle and gas-particle interactions on flow patterns in dense gas-fluidized beds,* Chemical Engineering Science **62**, 3429 (2007).

[33] V. Verma, N. G. Deen, J. T. Padding, and J. A. M. Kuipers, *Two-fluid modeling of three-dimensional cylindrical gas-solid fluidized beds using the kinetic theory of granular flow,* Chemical Engineering Science **102**, 227 (2013).

[34] P. C. Van der Sande, J. de Mooij, E. C. Wagner, G. M. H. Meesters, and J. R. van Ommen, *Single-photon emission radioactive particle tracking method for hydrodynamic evaluation of multi-phase flows,* Particuology (2024).

[35] M. Errigo, C. Windows-Yule, M. Materazzi, D. Werner, and P. Lettieri, *Non-invasive and non-intrusive diagnostic techniques for gas-solid fluidized beds – a review,* Powder Technology **431**, 119098 (2024).

6

On the inherent correlation between the fluidization and flow properties of cohesive powders

In the previous chapters, we dealt with particles that have a mean particle size larger than 500 µm. In many industrial applications, powders with smaller particle sizes are utilized due to their high surface-to-volume ratio. However, the relative magnitude of the attractive van der Waals forces acting on these particles starts out-weighting the gravitational force, making the powders cohesive. Challenges associated with this cohesiveness limit the applicability of conventional processing methods like gas-solid fluidization. In this chapter, we study the fluidization and flow properties of a range of commercially available cohesive powders with the objective of finding to what extent the two properties show a quantitative correlation.

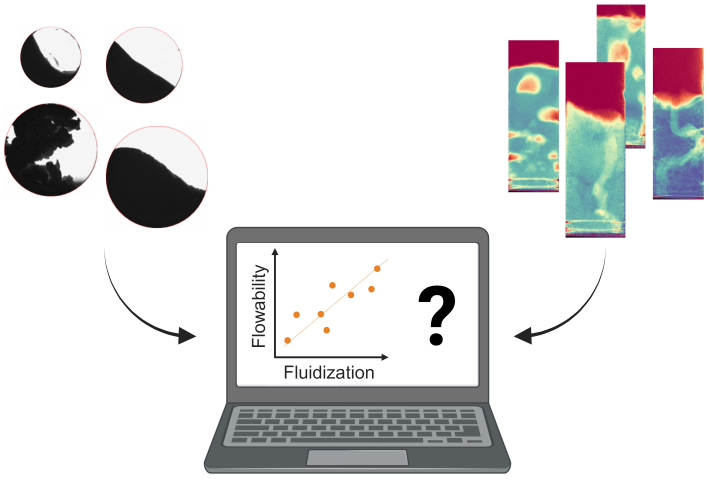

This chapter is based on P.C. van der Sande, K. Wu, R. Kamphorst, E.C. Wagner, G.M.H. Meesters, and J.R. van Ommen, *On the inherent correlation between the fluidization and flow properties of cohesive powders*, Accepted for publication in AIChE Journal (2024).

In this study, we examine the correlation between the fluidization behavior and flow properties of 10 commercially available cohesive powders by fluidization and rotating drum experiments. The rotating drum was operated at high rotation speeds to bring the powder bed into an aerated state, characterized by comparable flow fields and stress conditions as encountered in a gas-solid fluidized bed. We propose a Fluidization Quality Index (FQI) computed based on X-ray imaging that overcomes the limitations of conventional analyses for assessing fluidization quality when applied to cohesive powders. By analyzing flow patterns through X-ray imaging, FQI integrates the gas holdup and its temporal variation to offer a reliable indicator of the fluidization quality. The study establishes a positive correlation between the flowability and fluidization quality of cohesive powders, highlighting their inherent relationship. Furthermore, we show how flowability measurements can aid in predicting whether mechanical vibration may improve fluidization characteristics. These findings suggest that fast and user-friendly flowability measurements in a rotating drum instrument can predict fluidization potential, aiding in process optimization and enhancing fluidization studies for cohesive powders.

6.1. Introduction

Solid particles are used in fields such as catalysis and the pharmaceutical, chemical, and environmental industries. In recent years, a gradual shift has taken place towards the use of powders with smaller particle sizes due to the beneficial properties of their high surface-to-volume ratio, for example, in the fields of medicine [1], catalysis [2], and composite development [3]. Therefore, handling such solids is becoming a more important component of many industrial processes. The smaller particle sizes introduce complications, however, as the attractive van der Waals forces start dominating over other forces at smaller particle sizes, making the powders cohesive and impeding flow and aeration [4]. Challenges associated with this cohesiveness limit the applicability of conventional processing methods like gas-solid fluidization.

Gas-solid fluidization is realized by passing a gas upward through a bed of settled particles to suspend them in a fluid-like state, which results in homogeneous solids mixing and efficient heat and mass transfer between the two phases [5]. In the context of fluidization, several classification systems exist in which cohesiveness plays an essential role, most prominently the Geldart classification and Bond number[6]. The use of the Geldart classification is widespread in particular, as its prediction of fluidization behavior is solely based on particle size and density, which are typically easy to obtain [7]. Generally, coarse powders, such as Geldart group A and B, can be well fluidized. Cohesive powders, such as Geldart group A/C and C, however, tend to form agglomerates such that, upon fluidization, both primary particles and particle agglomerates are present in the bed, while the fundamental description of agglomerate formation and breakup - either it is force or energy based - is largely debatable, making it challenging to predict fluidization behavior [6]. Additionally, agglomerates are fragile by nature, making it difficult to assess their properties [8]. Associated with this complexity, Geldart group A/C powders within the Geldart classification, which are typically recognized as cohesive (or mildly cohesive), have been observed to occasionally form agglomerates as well [9, 10]. It should also be pointed out that the boundary between type A and C powders is poorly defined, in part due to the fact that density and primary particle size are not the sole parameters determining powder behavior.

Adding to the complexity of predicting fluidization behavior based on particle properties is that cohesive powders typically do not fluidize upon utilizing unassisted fluidization techniques, showing channeling and plugging instead [7]. The latter challenges the design and operation of conventional fluidized beds of cohesive powders, thereby limiting practical applications. Over time,

methods have been developed that aid the fluidization of cohesive powders by introducing an additional source of energy to the bed that disrupts channeling [11]. These assistance methods include mechanical stirring [12, 13], gas pulsation [14, 15], acoustic waves [16, 17], and mechanical vibration [18, 19]. In particular, mechanical vibration has been recognized as an effective method of aiding the fluidization behavior of cohesive powders and, therefore, readily finds practical applications. However, despite the significant progress in aiding the fluidization of cohesive powders, there is still a missing ability to predict whether a particular fine powder will be fluidized with or without the implementation of an assistance method, and which assistance method is optimal and effective remains a challenging task. Moreover, carrying out fluidization experiments is time-consuming and requires substantial infrastructure to regulate gas supply and ensure safe gas outlet handling, particularly when dealing with fine particles that are highly prone to entrainment. For practical applications, direct visualization of fluidization behavior is challenging. Therefore, the assessment largely relies on indirect measurements, such as pressure drop and bed expansion. Furthermore, the observed phenomena can be scale-dependent and are susceptible to initial conditions, which are, in turn, influenced by user-dependent factors. Consequently, there is a pressing need for fast, user-friendly, and user-independent powder flow testing methods.

For cohesive powder, the degree of cohesion significantly affects flowability, therefore, a wide array of powder flow testing methods has been developed to characterize the flow properties of powders [20–24].For mildly cohesive powders, quantitative indicators, including angle of repose [25], angle of avalanche [26], powder discharge flow [27], torques in aerated powder bed [28], were measured to assist the interpretation of powder cohesion. For adequate characterization in relation to a unit operation, the flow field and stress state of the powder should be comparable in the powder flow tester and the respective unit operation [21, 29]. In a fluidized bed, the powder bed can be considered to be in a highly dispersed and low consolidation state. Rotating drums have been widely used to characterize the flowability of powders in the dynamic flowing regime in a state of low consolidation [26, 30–34]. The rotating drum powder characterization instrument comprises a cylinder typically half-filled with powder that is rotated around its axis at desired rotation speed. Interestingly, several studies have shown that a cohesive powder bed can transition from a quasi-periodic avalanche mode to a fluidized mode as the rotation speed increases [35–39]. At low speeds, the powders initially undergo periodic avalanches. These avalanches result in mixing with the surrounding gas, which can lead to partial fluidization by entraining gas. As the rotation speed in-

creases, the time it takes for the entrained gas to be evacuated becomes comparable to the interval between avalanches. This leads to the establishment of a permanent fluidized region [36]. The presence of this fluidized region is evident from the expansion of the bed and the flattened free surface, which exhibits fluid-like behavior similar to that observed in a fluidized bed. It remains, however, unclear to what extent the flow behavior observed in a rotating drum can be linked to the fluidization behavior in unassisted and assisted fluidized beds.

In this work, we study the fluidization and flow properties of a range of commercially available cohesive powders with the objective of finding to what extent they are correlated. In the first part of the present work, the flowability properties are studied by employing a rotating drum powder flow analysis instrument. By performing measurements at different drum rotation speeds, we elucidate how the flow behavior of the various powders is influenced by the rotation speed. The second part of the present work presents an analysis of the fluidization properties in the absence and presence of mechanical vibration. We show that conventional methods to monitor the fluidization quality, namely total pressure drop and bed height, have significant shortcomings for cohesive powders. Instead, we argue that the directly observed flow pattern better represents the fluidization quality, and therefore, an advanced method that quantifies the fluidization quality based on the observed flow pattern is introduced in this work. The final part of the present work consists of a detailed cross-comparison of the flow and fluidization properties to assess their inherent correlation. We argue that a good correlation implies that data obtained through flowability studies in a user-friendly rotating drum instrument could quickly and reliably indicate whether a certain cohesive powder is likely to be fluidized, with or without the implementation of an assistance method. Such insights hold promise for enhancing fluidization studies by providing a more efficient and reliable means of predicting powder fluidization behavior, thereby potentially optimizing fluidization processes.

6.2. Methodology

6.2.1. Materials

Ten commercially available materials were evaluated for their flowability and fluidization behavior. These materials included polystyrene, egg white, bentonite, silica, lactose, four types of starches, and sorbitol. Sorbitol, a non-cohesive poly alcohol, was chosen as a reference material due to its excellent flowability. The particle size and morphology of the powders were analyzed using a particle size analyzer and scanning electron microscopy, respectively.

The physical properties of the materials are summarized in Table 6.1 and will be further discussed in the following paragraphs.

Table 6.1: Physical properties of the powders used in this study. [a]Volume-weighted mean particle size. [b]Area-weighted mean particle size. [c]Span = $(d_{v90}\text{-}d_{v10})/d_{v50}$.

Powder	$d_{4,3}$ (µm)[a]	$d_{3,2}$ (µm)[b]	Span (-)[c]	Shape	Geldart group [7]
Sorbitol	201.0	74.5	1.75	Angular	A
Potato starch	45.5	36.1	1.23	Spherical	C
Modified corn starch	42.3	19.4	1.98	Angular	C
Polystyrene	40.6	40.4	0.21	Spherical	C
Bentonite	29.8	10.3	2.49	Angular	C
Egg white	28.9	9.6	2.50	Spherical	C
Corn starch	14.7	13.2	0.89	Spherical	C
Tapioca starch	14.6	13.0	0.91	Spherical	C
Silica	6.6	4.1	2.05	Angular	C
Lactose	5.1	2.1	1.84	Angular	C

The particle size distribution was measured using the Malvern 3000 particle size analyzer, equipped with a dry powder module and high-energy stainless steel venturi tube. Measurements were taken in an obscure range of 0.5–8.0%. The volume-based particle size distributions of the materials are represented in Fig. 6.1 by depicting respective d_{v10}, d_{v50}, and d_{v90} values. It can be observed that the d_{v50} ranges from 5.0 µm (Lactose) to 190 µm (Sorbitol), illustrating a significant spread in particle size across the materials studied. Based on their median (d_{v50}), volume-weighted mean ($d_{4,3}$), and area-weighted mean particle size ($d_{3,2}$), all powders can be classified as Geldart C type, except sorbitol, which is classified as a Geldart A type. However, as commonly encountered in real applications, the powders consist of a collection of particles that display a distribution in particle sizes. The width of the particle size distribution is quantified by computing the span as $(d_{v90}\text{-}d_{v10})/d_{v50}$. It can be observed that corn starch, tapioca starch, and polystyrene have a small span value, indicating a narrow particle size distribution. On the contrary, modified corn starch, bentonite, and egg white have a large span value, representing a wide particle size distribution.

The morphology of the powders was analyzed employing a JEOL JSM 7500F field emission scanning electron microscope with an acceleration voltage of 5 kV. The imaging was performed at magnifications between 100 and 1000.

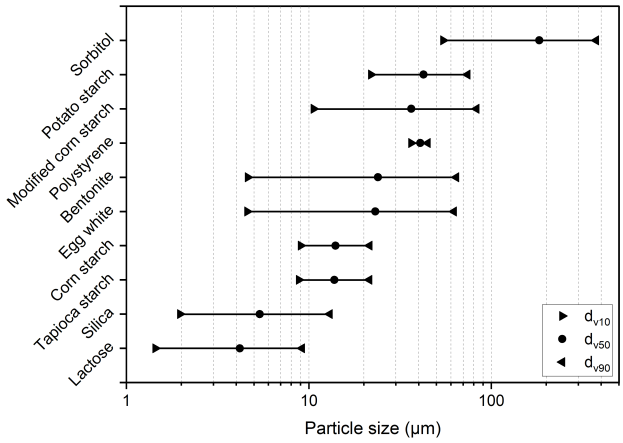

Figure 6.1: Volume-based particle size distribution of the powders included in this study.

Before imaging, the samples were sputter-coated with gold to reduce sample charging and improve the image quality using a JEOL JFC-1300 auto fine coater in automatic mode for a gold sputtering duration of 30 s. Typical acquired scanning electron microscope images of the powders are depicted in Fig. 6.2.

In agreement with the measured particle size shown in Fig. 6.1, it can be observed that the powders display a significant spread in particle sizes (see Appendix Fig. E.1 for the complete particle size distribution). Moreover, notable differences are observed considering the morphology of the particles. On the one hand, potato starch, polystyrene, egg white, tapioca starch, and corn starch display a spherical shape with relatively smooth surfaces. On the other hand, sorbitol, modified corn starch, bentonite, silica, and lactose are characterized by an angular shape.

6.2.2. Flowability experiments

Rotating drum setup

The flowability of the materials was analyzed using the GranuDrum® rotating drum instrument [33]. This automated powder flowability analysis instrument is designed to characterize the flowability of materials in the dynamic flowing regime. The GranuDrum® comprises a rotating drum cylinder, an LED panel inducing contrast between powder and air, and a digital camera (5MP Monochrome CMOS). These components are positioned within a case to maintain consistent light conditions, as illustrated in Fig. 6.3. The drum cylinder is made of stainless steel with sidewalls of transparent coated glass to allow visualization of the powder bed. The drum has a inner diameter of 84 mm and a depth of

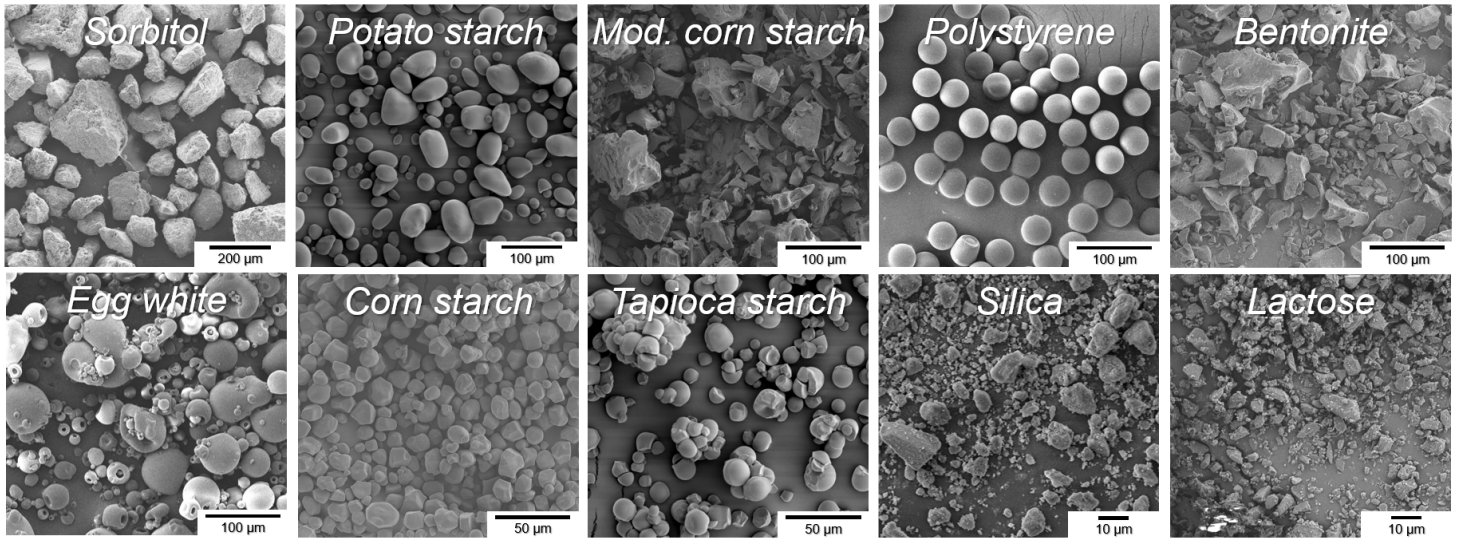

Figure 6.2: Scanning electron microscope images of the powders. It should be noted that images are acquired at magnifications between 100 and 1000. Therefore, the lengths of the scale bars presented in the respective images differ.

20 mm, corresponding to a total volume of 110 mL. The depth of the drum significantly exceeds 6.4 times the mean particle radius of all powders, such that front and back wall friction effects on the flow characteristics are mitigated according to Jain et al. [40]. The instrument was connected to a computer for operation and image acquisition. The environmental temperature was maintained at 20 °C, with humidity in a range of 30% - 50%.

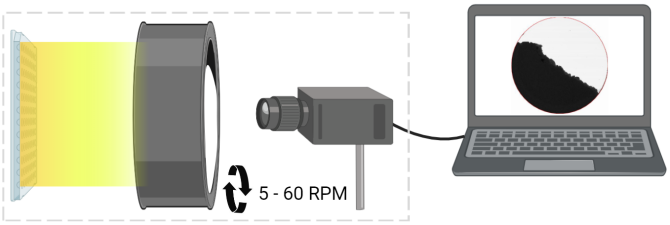

Figure 6.3: Schematic representation of the rotating drum setup. The GranuDrum® instrument consists of a rotating drum, digital camera, and LED panel. The instrument is connected to a computer for operation and image acquisition.

Image acquisition and analysis

For each experiment, a volume of 55 cm^3 of the designated material was loaded in the drum cylinder, resulting in a 50% fill level. The drum was then placed in the instrument and rotated around its horizontal axis at rotation speeds of 5, 10, 30, and 60 RPM. The rotation speed was varied to elucidate how bed expansion, as the result of high angular velocities, influenced the flowability of the materials. At each rotation speed, the digital camera acquired a snapshot every 600 ms for a duration of 60 s, giving a total of 100 images. The camera was operated at a shutter speed of 0.85 ms to capture the bed dynamics at high rotation speeds accurately.

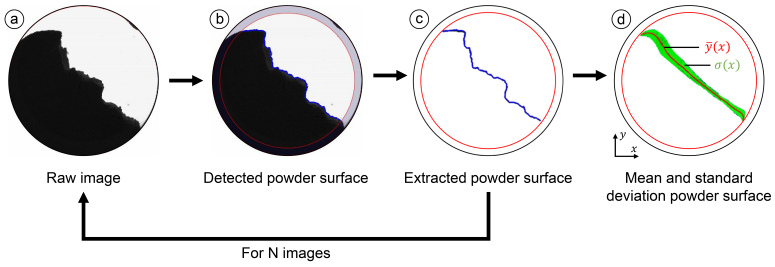

Figure 6.4: Image processing workflow to compute the cohesive index.

The acquired images were processed through a digital image analysis workflow introduced by Neveu et al. [34], illustrated in Fig. 6.4. For each image, the interface between the powder and air in the raw image (Fig. 6.4-a) was detected by an edge detection algorithm (Fig. 6.4-b). Subsequently, the detected powder surface is extracted (Fig. 6.4-c). This procedure is executed for all the images acquired during a measurement. From the extracted powder surface positions, a mean powder surface position and standard deviation are computed (Fig. 6.4-d) through Equation 6.1 [34]:

$$\sigma(x) = \sqrt{\frac{\sum_{i=1}^{N_y(x)} (\bar{y}(x) - y_i(x))^2}{N_y(x)}} \tag{6.1}$$

where $\sigma(x)$ is the standard deviation, $N_y(x)$ the number of images, $\overline{y}(x)$ the mean surface position, and $y_i(x)$ is the surface position for image i. The standard deviation of the surface position represents the temporal fluctuations of the powder surface and is correlated to the cohesive index (CI), a quantitative interpretable powder flowability descriptor, as:

$$CI = \frac{1}{D_{crop}} \sum_{x} \sigma(x) \tag{6.2}$$

where D_{crop} is the diameter of the cropped image [41, 42]. The CI is related to powder flowability as depicted in Table 6.2. A low CI value, representing low temporal fluctuations of the powder surface, corresponds to excellent flowability, while a high CI value, representing significant temporal fluctuations of the powder surface, corresponds to poor flowability [42].

Table 6.2: Classification of powder flowability based on the cohesive index.

Flowability	Cohesive index
Excellent	< 5
Good	≤ 5 < CI < 10
Fair	≤ 10 < CI < 20
Passable	≤ 20 < CI < 30
Poor	≤ 30 < CI < 40
Very poor	≤ 40 < CI < 50
Very, very poor	≥ 50

6.2.3. Fluidization experiments

Many challenges are associated with fluidizing cohesive powders, such as agglomeration, channeling, and plugging [7]. In this study, mechanical vertical vibration is employed as an assistance method to initiate or improve the fluidization of the powders. The influence of vertical vibration on the fluidization behavior of the powders was systematically assessed by evaluating the pressure drop, bed height, flow pattern, and gas holdup without mechanical vibration (referred to as unassisted fluidization) and with vertical vibration employed (referred to as vibro-assisted fluidization).

Fluidized bed column

A laboratory-scale fluidized bed setup was used to assess the fluidization behavior of the powders. The fluidized bed column was comprised of a 50 mm inner-diameter perspex cylinder with a length of 400 mm coupled to a plenum-chamber beneath using a 3 mm thick sintered stainless steel distributor plate to allow even gas distribution. The distributor plate was cleaned using an ultrasound bath before use. For each experiment, a volume of 200 cm^3 of fresh powder was gently dosed and loaded into the column, corresponding to an initial bed height of 10 cm. This procedure was consistently followed to ensure comparable initial conditions for all experiments. An expansion breakout box was installed atop the column to recycle entrained powder. The gas vent was directed through a wash bottle and solids HEPA filter to collect escaped particles before releasing the fluidizing gas into the atmosphere. Compressed air, dried and filtered to remove oil and dust, was directed into the column through a mass flow controller (Bronkhorst F-202AV). The flow rate was set to achieve a superficial gas velocity of 6 cm s^{-1} at 20 °C. This velocity is sufficiently high to fully fluidize Sorbitol powder, which has the highest theoretical minimum fluidization velocity (u_{mf}) among the powders studied. The column was mounted on a vibration table to facilitate vibro-assisted fluidization with vertical oscillation. In this study, the vibro-assisted fluidization experiments were performed through vertical vibration with a frequency of 30 Hz and an amplitude of 1 mm. This condition has been shown to effectively enhance the fluidization of cohesive powders [18].

X-ray imaging method

The fluidization behavior of the various powders was experimentally assessed using an in-house fast X-ray imaging setup. X-ray imaging is a non-invasive imaging method that allows visualization of opaque multiphase flows. Through X-ray imaging, a 2-dimensional projection of the three-dimensional gas holdup in the fluidized bed was captured. The X-ray setup consists of a standard industrial-type X-ray source (Yxlon International GmbH) with a maximum energy of 150 keV

working in cone beam mode and a 2D detector (Teledyne Dalsa Xineos) with a theoretical spatial resolution of 0.15 mm placed opposite of the source. To ensure a safe working environment, the setup was controlled from a workstation located outside the setup room during the measurements. X-ray images were acquired at a sampling rate of 50 Hz over a measurement period of 120 s, equating to the acquisition of 6000 images per experiment. The obtained data was then stored for subsequent digital image analysis.

Each acquired image is a time-resolved projected 2D intensity map of the fluidized bed. A two-point calibration protocol was performed to compute a gas holdup from the measurement intensity. This requires two reference images: an image of the empty column and an image of the full column. The X-ray measurement principle is based on the attenuation of X-rays traveling in a straight line from an X-ray source to a detector while passing through matter. The transmission of a monochromatic beam of high-energy photons with initial intensity I_0 through matter of constant density is described by the Lambert-Beer law:

$$I(x) = I_0 e^{-\mu z} \tag{6.3}$$

Here, $I(z)$ denotes the intensity measured at the detector, μ is the attenuation coefficient, and z is the material thickness. In cases of varying attenuation, the measured intensity is the integral effect of local attenuation with the local attenuation coefficient. By applying the Lambert-Beer law, the measurement gas holdup map was derived from the measurement intensity map using the empty and full reference as depicted in Fig. 6.5. The normalized gas holdup ε_g was calculated as follows:

$$\epsilon_g = \frac{ln(I_{measurement}/I_{full)}}{ln(I_{empty}/I_{full})} \tag{6.4}$$

It should be noted that the normalized gas holdup in this study ranges from 0 to 1, where 1 represents pure gas and 0 dense packing of solids. Warm colors in the gas holdup map correspond to low X-ray attenuation, indicating high gas concentrations. In contrast, cold colors represent high X-ray attenuation, indicating low gas concentrations. A detailed validation of the method is presented in the work by Wu et al. [13]

Fluidization quality index

The acquired X-ray images provide a qualitative description of the fluidization behavior. To allow a direct quantitative comparison to the quantitative cohesive index, we developed a method to quantify the fluidization quality based on

(a) Schematic representation of the experimental setup.

(b) A two-point calibration procedure is employed to convert the intensity map to a gas holdup map.

Figure 6.5: X-ray imaging analysis of the fluidized bed hydrodynamics.

the acquired X-ray images. With the gas holdup ε derived from X-ray imaging, a time-averaged gas holdup profile $\overline{\varepsilon}_g$ can be calculated as follows:

$$\overline{\varepsilon}_g(x,y) = \frac{1}{N_{\Delta t}} \sum_{t=t_0}^{t_0+\Delta t} \varepsilon_g(x,y,t) \tag{6.5}$$

where $N_{\Delta t}$ is the number of X-ray imaging frames between t_0 and $t_0 + \Delta t$, x is the horizontal pixel position, and y is the vertical pixel position.

Moreover, the standard deviation of the gas holdup serves as an indicator of the flow pattern's variability over time. This metric allows for the assessment of how dynamic the system is, providing valuable insights into the flow patterns. For each pixel position (x, y) the time-based standard deviation of the gas holdup σ is computed as:

$$\sigma(x,y) = \sqrt{\frac{\sum_{t=t_0}^{t_0+\Delta t} [\varepsilon_g(x,y,t) - \overline{\varepsilon}_g(x,y)]^2}{N_{\Delta t} - 1}} \tag{6.6}$$

A low σ represents regions with less or no bubbling or other changes in density. On the contrary, regions with frequent bubbles and solid motion give rise to a large σ. Therefore, σ can be considered a quantitative indication of the system variability within a time interval.

Either the time-averaged gas holdup or its standard deviation solely cannot provide a fair quantitative description of the fluidization behavior. For instance,

a channeling bed and a very homogeneously fluidized bed can exhibit similarly low standard deviation values. Furthermore, a bed of fine powder can have a loosely packed state with a high time-averaged gas holdup, yet is not possible to be fluidized. Therefore, incorporating both, we propose a quantitative description of the fluidization behavior that is the product of the time-averaged gas holdup and the temporal standard deviation of the domain-averaged gas holdup:

$$\textit{Fluidization quality index (FQI)} = \overline{\epsilon}(x, y) \cdot \sigma_y(y) \tag{6.7}$$

Pressure analysis

Pressure drop measurements are commonly carried out in order to monitor and evaluate the fluidization quality. To assess the fluidization quality, the pressure drop across the powder bed was monitored with an OMEGA PX409-10WG5V differential pressure transducer. The gas pressure was probed at two positions: one located in the bed flange, approximately 6 mm above the distributor plate, and the other at the gas outlet of the bed. The pressure measurements were synchronized with the X-ray imaging system to ensure simultaneous data acquisition. The pressure drop was sampled at 1000 Hz, with a measurement error of 2% of the full scale (14 mbar), as specified by the manufacturer. The pressure drop across the bed was then obtained as the difference between the pressure measured at these two taps.

The evaluation of fluidization quality relies on the time-averaged pressure drop and the standard deviation of the pressure drop. The acquired pressure values (ΔP) were divided by the static pressure exerted by the powder, (ΔP_0), to yield a normalized pressure drop, a commonly used indicator of fluidization quality. Values of the normalized pressure drop correspond to the fraction of powder that is being fluidized.

$$\Delta P_0 = \frac{mg}{A} \tag{6.8}$$

where A is the column cross-sectional area, m is the mass of the powder and g is the gravitational acceleration.

Bed expansion

The time-averaged bed height H is measured according to time-averaged gas fraction profiles obtained from X-ray imaging. The bed surface is identified

based on the time-averaged series of radial-averaged gas fraction $\overline{\overline{\varepsilon}}_{g,y}$:

$$\overline{\overline{\varepsilon}}_{g,y}(y) = \frac{1}{N_x N_{\Delta t}} \sum_{t=t_0}^{t_0+\Delta t} \sum_{x=1}^{N} \varepsilon_g(x, y, t) \tag{6.9}$$

where $N_{\Delta t}$ is the number of X-ray imaging frames between t_0 and $t_0 + \Delta t$, N_x is the pixel number over the horizontal line at height y. The time-averaged bed height H is determined to height y where $\overline{\overline{\varepsilon}}_{g,y}$, counting from the freeboard to the bottom, first falls below 0.9. The bed expansion ratio H/H_0 is determined as the ratio of the time-averaged bed height H over the initial bed height H_0.

6.3. Results and discussion

6.3.1. Flow properties

Flow pattern

The powder flowability was analyzed using the GranuDrum® rotating drum instrument for a range of rotation speeds varying from 5 to 60 RPM. Figure 6.6 depicts typical snapshots of the granular flow behavior for a rotation speed of 5 RPM, 10 RPM, 30 RPM, and 60 RPM. Notably, for free-flowing powders, such as sorbitol, the observed flow behavior is intrinsically linked to the drum rotation speed. As mentioned earlier, free-flowing powders transit through six flow modes upon an increasing rotation speed: slipping, slumping, rolling, cascading, and finally centrifuging [43].

This behavior can be observed for sorbitol, which is free-flowing and non-cohesive, and depicts a flat surface at a rotation speed of 5 RPM, while cascading motion, characterized by an S-shape surface [44], is observed when inertial effects become more pronounced at a rotation speed of 60 RPM. For all other powders, however, the cohesive nature gives rise to a more complex flow structure, as already observed by Rietema [35]. At a rotation speed of 5 RPM, the cohesive powders show intermittent quasiperiodic avalanches of lumps. The bed is characterized by large values of the dynamic angle of repose and rough powder surfaces due to the formation of lumps.

On the contrary, at a rotation speed of 60 RPM, four different types of behavior can be distinguished. The first behavior is cascading motion, characterized by an S-shape powder surface. As mentioned earlier, this behavior is typical for free-flowing powders when exposed to elevated rotation speeds, such as sorbitol in this study. The second type of flow behavior is associated with intermittent quasiperiodic avalanches, which is similar to the behavior most

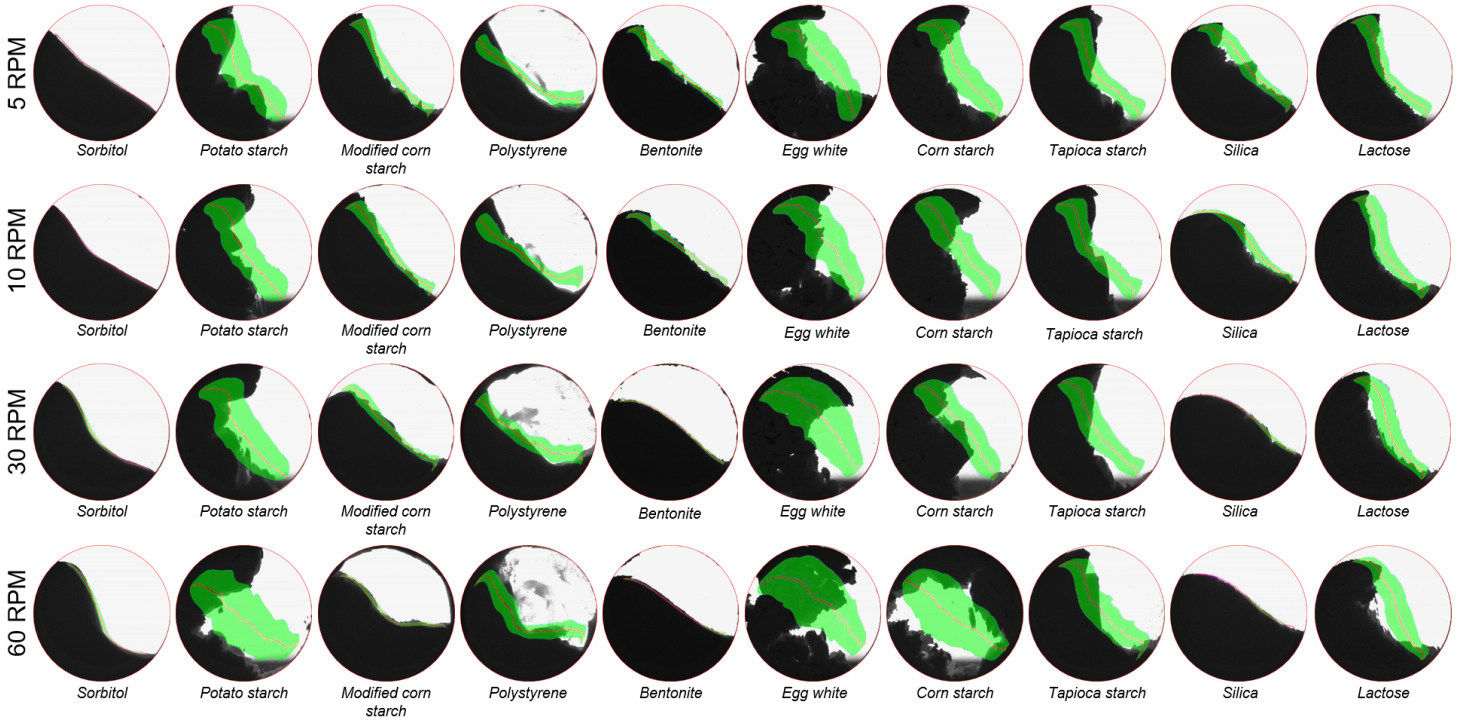

Figure 6.6: Representative snapshots of the flow pattern of the powders at rotation speeds of 5, 10, 30, and 60 RPM, ordered from top to bottom. The mean (red line) and standard deviation (green area) of the powder surface position are superimposed with transparency over the flow pattern images. Video S1 displaying the flow behavior is included in the electronic supplementary of the article.

(mildly) cohesive powders display at low rotation speeds. This behavior is observed for the powders polystyrene, tapioca starch, and lactose, which continue to show intermittent quasiperiodic avalanche flow behavior similar to their respective 5 RPM behavior. A third type of flow behavior is distinguishable from its 5 RPM counterpart by a flattened, aerated powder bed, as ambient gas is entrained in the bulk due to the fast mixing. This results in an expanded state in which the free surface flattens [37]. Due to the aeration, the flowability of these powders is significantly improved. From Fig. 6.6, it becomes evident that the powders modified corn starch, bentonite, and silica show this type of behavior. The observation that a bed of these powders is prone to become aerated is promising when considering their fluidization potential. Finally, the last type of behavior is associated with powder adherence to the walls of the drum. When subjected to high rotation speed, highly cohesive powders undergo frequent revolutions along the perimeter of the drum without displaying typical avalanche behavior. This type of behavior can be observed for potato starch, egg white, and corn starch. The irregular position of the powder surface also shows that the angle of repose would be inadequate in characterizing the flowability of powder of high cohesiveness.

Cohesive index

While the flow pattern can give qualitative insight into the flowability of the powders, it is yet difficult to compare the flowability among different powders. Therefore, the flow behavior was quantified with the CI using a digital image analysis workflow. As mentioned earlier, the CI is a standardized quantitative interpretable powder flowability descriptor based on the temporal fluctuations of the powder surface. The mean and standard deviation of the powder surface position are superimposed with transparency over the flow pattern images in Fig. 6.6. The CI is plotted against the rotation speed in Fig. 6.7.

The powders identified with similar types of flow behavior can be further distinguished according to the cohesive index. In line with the qualitative flow behavior, the free-flowing nature of sorbitol consequently results in a low cohesive index for all tested rotation speeds. By referring to Table 6.2 the flowability can be classified as excellent to good. The powders modified corn starch, bentonite, and silica experienced significant aeration upon an increasing rotation speed, improving their flowability [45]. In agreement with the observed flow behavior, this is clearly observed by the downward trend in the cohesive index for an increase in rotation speed. The flowability ranges from passable and poor at a rotation speed of 5 RPM to good and excellent at a rotation speed of 60 RPM. Polystyrene, tapioca starch, and lactose depict a higher cohesive

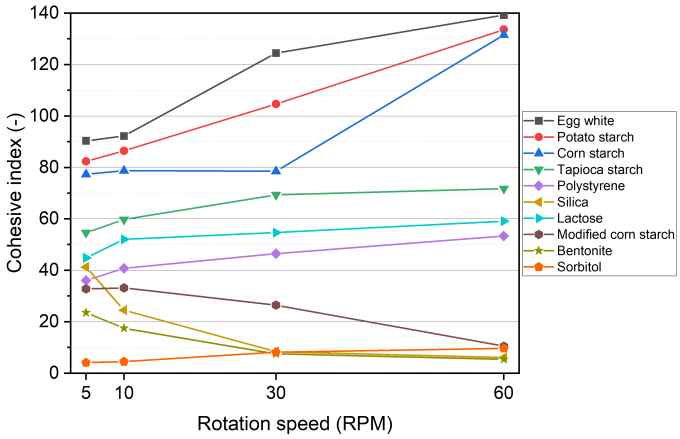

Figure 6.7: The flow behavior quantified by the cohesive index.

index and show a minor increase in the cohesive index for an increase in rotation speed, indicating that their flowability is not significantly affected. Their flowability can be considered poor to very, very poor. Finally, potato starch, egg white, and corn starch depict an even higher cohesive index and demonstrate a significant increase upon an increase in rotation speed. According to their CI, the flowability is classified as very, very poor. This is in agreement with the observed behavior, which was characterized by adherence to the walls of the drum. Interestingly, when relating the qualitative and quantitative flow behavior to the mean particle size, span, and shape of the powders (see Table 6.1), it becomes evident that there is no relation, underscoring the complexity associated with the flow of cohesive powders. Overall, the quantitative CI is found to be in good agreement with the qualitative description of the flow pattern.

6.3.2. Fluidization properties

Flow pattern

Figure 6.8 demonstrates the comparison between the time-resolved flow patterns of unassisted and vibro-assisted fluidization. Without any external assistance, the intrinsic cohesiveness of most powders leads to the formation of gas channels of varying sizes, which allows the inlet gas to bypass the bed, thereby resulting in poor gas-solid interactions and a largely stationary bed. This effect is particularly pronounced in powders characterized by a high cohesive index. Within this context, the nature of fluidization behavior is further distinguished by the morphology of the gas channels; for instance, potato starch, egg white, and tapioca starch exhibit the formation of curved macro-channels

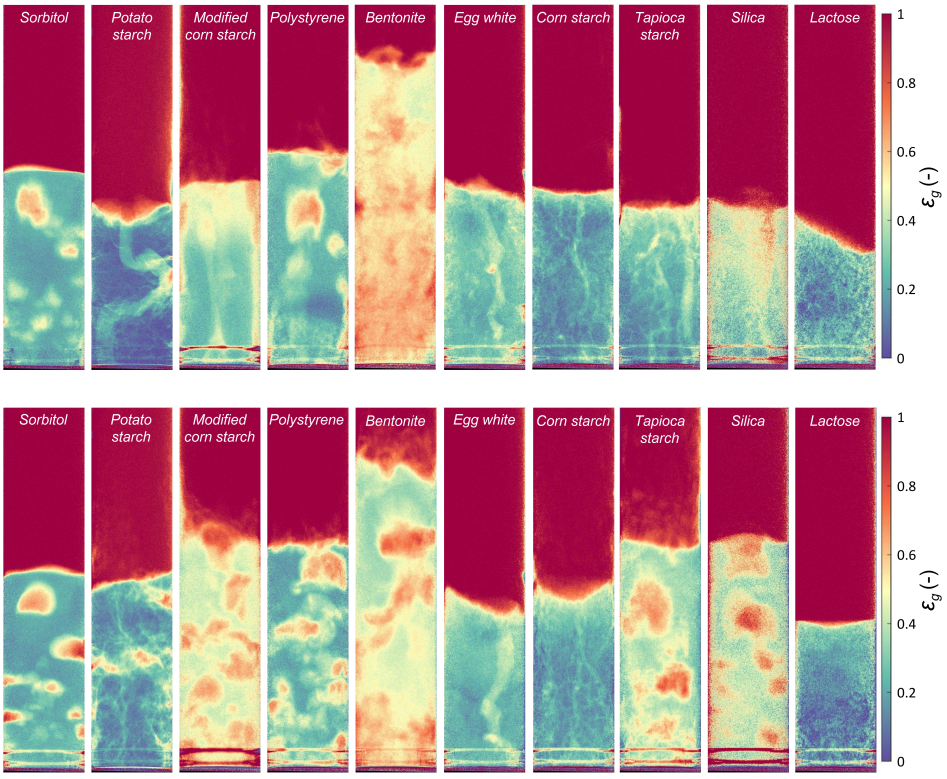

Figure 6.8: Representative still images of the flow patterns of the unassisted (top) and vibro-assisted beds (bottom). Videos S2 and S3, displaying the evolution of the flow patterns, are included in the electronic supplementary of the article.

(also known as rat holes), whereas corn starch and lactose powder beds present branched micro-channels.

When comparing the flow patterns between unassisted and assisted fluidization, it becomes clear that the introduction of mechanical vibration generally modifies the dynamics of powder fluidization, especially in powders with high cohesive indexes, enhancing particle mobility significantly. It disrupts macro channels in modified corn starch, silica, and tapioca starch, although it is less effective against micro channels [18]. Notably, except for highly cohesive materials such as egg white, corn starch, potato starch, and lactose, other powders transition from micro-channeling fluidization behavior to a bubbling state, therefore remarkably enhancing fluidization. It should, however, be noted that potato starch displays fluidization of large agglomerates upon the introduction of mechanical vibration, as can be observed in a video included in the elec-

tronic supplementary of the article.

A comprehensive analysis of visual results allows for systematic categorization of fluidization behavior, ranging from a highly turbulent bubbling state to a relatively stationary sub-fluidized state. Figure 6.9 presents a comparison of the time-averaged flow patterns attained for unassisted fluidization and vibro-assisted fluidization. The time-averaged flow patterns demonstrate that powders prone to forming micro or macro channels tend to remain static (i.e., little difference between the pattern in Fig. 6.8 and Fig. 6.9), leading to an uneven distribution of gas and solids, as illustrated in Fig. 6.9. Additionally, the formation of gas-channeling structures is notably stable, while mechanical vibrations enhance the overall mobility of particles. However, it is observed that powders forming micro-channels still exhibit limited mobility, while those forming large channels or bubbles show a significantly improved homogeneity in gas-solids mixing.

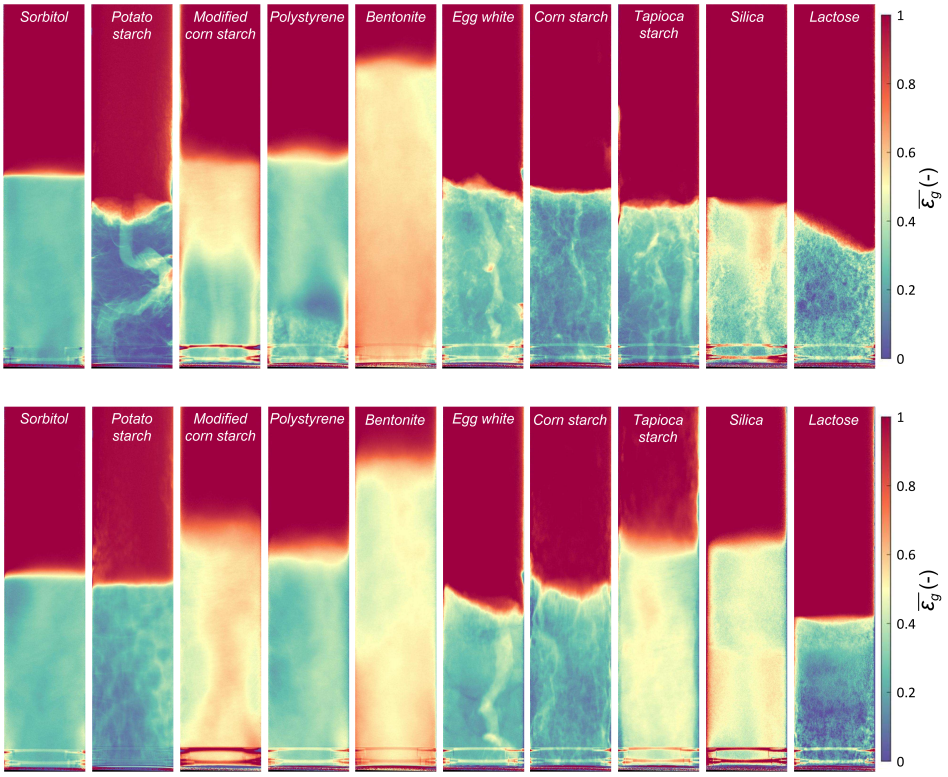

Figure 6.9: Time-averaged flow pattern of the unassisted (top) and vibro-assisted hydrodynamics (bottom).

Bed expansion

Figure 6.10 compares the bed expansion in both unassisted and assisted beds across the various powder types. Notably, the application of mechanical vibrations contributes to an increased bed expansion, except for egg white and lactose powders. Bentonite displays the most significant bed expansion, approximately doubling its static height ($H/H_0 = 2$), which corresponds to the observed intensive bubbling fluidization behavior. Under vibration assistance, the fluidization of these powders is further enhanced, which is particularly notable with silica, tapioca, and potato starch powders, as the disruption of microchannels significantly elevates powder expansion. In contrast, for Geldart Group A Sorbitol powder, a high degree of fluidization was already attained in the absence of mechanical vibration. Therefore, the assistance did not add to any significant bed expansion. This indicates that, while vibration enhances bubbling behavior, that is creating more bubbles of small sizes, while it is not necessary to further enhance the dilation of emulsion phase. In addition, this level of bed expansion is not inherently superior to those powders under sub-fluidized conditions, such as egg white and modified corn starch. Therefore, these results demonstrate that, due to the cohesive nature, a higher bed expansion is indicative of a fluidized state, while it cannot be used to compare across different powders to determine the fluidization quality directly. This finding aligns with our prior research as it suggests that an elevated bed expansion does not necessarily provide direct insights into the internal arrangement of powder particles [18, 19].

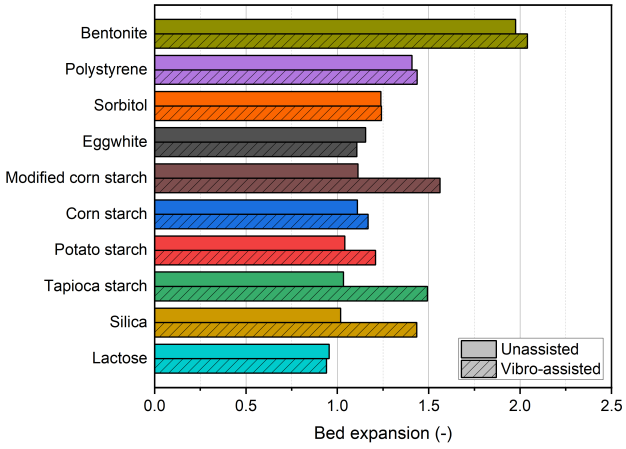

Figure 6.10: Time-averaged the bed expansion ratio. The expansion ratio is computed by dividing the time-averaged bed height (Fig. 6.9) by the settled bed height.

Pressure analysis

Figure 6.11 shows the normalized pressure drop of the unassisted and vibro-assisted beds. It can be observed that the normalized pressure drop increases and becomes more stable upon the introduction of mechanical vibrations. In light of the X-ray images presented in Fig. 6.8 and Fig. 6.9, the pressure drop graphs do, however, also highlight the shortcomings of using the total pressure drop as the sole indicator of fluidization quality, as pointed out in earlier work [19]. The normalized pressure drop only serves as a useful tool when the measured pressure drop indeed stems from fluidized particles, which is typically the case for non-cohesive powders. In contrast, the obtained pressure drop measured over beds of cohesive powders is potentially influenced by multiple phenomena, including spouting, plugging, arching, and fluidization.

Whereas the presence of one or more of these phenomena can be deduced from the otherwise nonphysical results of unassisted lactose and vibro-assisted fluidized egg white, as the normalized pressure drop exceeded unity, in the case of corn starch, the X-ray images demonstrate the presence of semi-stable structures in the bed. Normalized pressure drops are a strong indicator of fluidization quality for well-fluidizing powders (sorbitol, bentonite, silica), but on the boundary of Geldart group C and A, powders may experience channeling and plugging behavior, rendering the pressure data misleading if not interpreted with the utmost care.

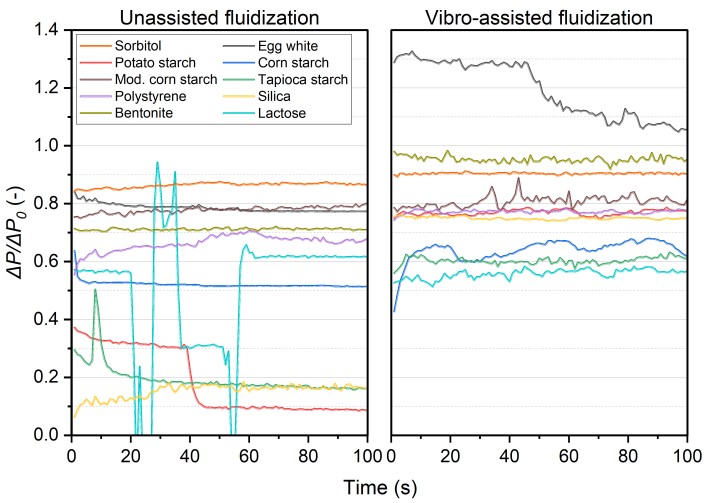

Figure 6.11: Temporal evaluation of the normalized pressure drop for unassisted fluidization (left) and vibro-assisted fluidization (right).

Fluidization quality index

Figure 6.12 illustrates the computed FQI based on the flow patterns discussed in Section 6.3.2. By comparing FQI to the flow patterns shown in Fig. 6.8, it is concluded that FQI can effectively classify different fluidization states, ranging from homogeneous bubbling and partial bubbling to micro- and macro-channeling (also known as rat-holes) to complete stationary, and is found to proportionally increases in this order. Such quantification is independent of the expanded bed height and highlights the dynamic elements in the bed, which is the key to evaluating fluidization behavior.

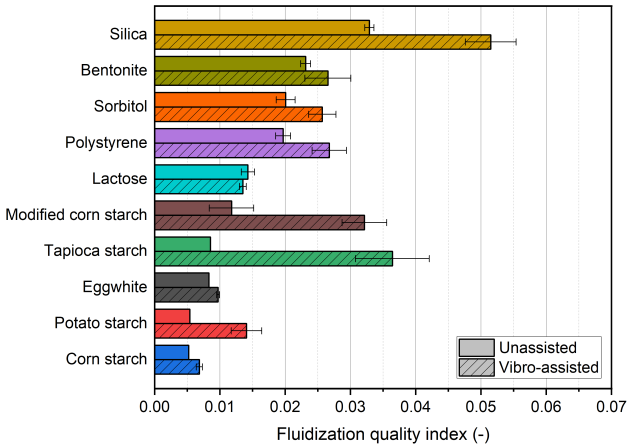

Figure 6.12: The fluidization behavior quantified by the fluidization quality index.

Generally, it is observed that FQI increases with the application of mechanical vibration, with notable exceptions such as lactose powder, which predominantly forms micro-channels. Significant improvements are found with tapioca, silica, and modified corn starch when the vibration is applied. Their flow patterns also show that existing channels have been disrupted, transitioning into a bubbling stage - a change quantitatively described by doubling the FQI. In comparison to the pressure drop and bed expansion ratio, FQI appears to be an effective indicator for describing the fluidization state of cohesive powders.

It becomes clear that the fluidization behavior cannot be simply governed by the mean particle size, size distribution span, and shape factor solely (see Table 6.1), but as a collective behavior of the particle properties. This underscores the limitations of traditional methods that aim to predict fluidization behavior.

6.3.3. Comparison fluidization and flow property

The flowability characterization measurements demonstrated that the rotation speed has a significant impact on the apparent flowability of the powders. According to the literature mentioned above, when the rotation speed is high, such as the 60 RPM used in this study, the powder bed expands and achieves an aerated state comparable to that of a gas-solid fluidized bed. Therefore, the flow characteristics observed in an aerated state in a rotating drum instrument are likely correlated with the associated fluidization behavior.

As discussed above, unlike Geldart A and B particles, cohesive fine powder exhibits more complex and in-homogeneous flow patterns subjected to fluidization. It is evident that the normalized total pressure drop and bed expansion, which are commonly used to monitor fluidization quality for Geldart A and B particles, have limitations in accurately characterizing the fluidization quality of cohesive powders. As an alternative, the flow pattern based fluidization quality index (FQI) is adopted here to evaluate the observed fluidization behavior. The results show that the FQI quantifies and distinguishes various fluidization states, as shown in Table 6.3.

Table 6.3: Comparison fluidization and flow property. ^{a}As measured at a rotation speed of 60 RPM.

Powder	Flow descriptor (CI)^{a}	Fluidization descriptor (FQI^{-1})	Fluidization descriptor (FQI^{-1})
	60 RPM	Unassisted	Vibro-assisted
Bentonite	Good (5.5)	Bubbling (43.2)	Bubbling (37.7)
Silica	Good (6.1)	Mild bubbling (30.4)	Bubbling (19.4)
Sorbitol	Good (9.7)	Bubbling (49.8)	Bubbling (38.9)
Modified corn starch	Fair (10.5)	Mild bubbling (84.9)	Bubbling (31.1)
Polystyrene	Very, very poor (53.4)	Mild bubbling (50.8)	Bubbling (37.4)
Lactose	Very, very poor (59.2)	Channelling (70.0)	Mild bubbling (74.0)
Tapioca starch	Very, very poor (71.8)	Channelling (116.8)	Bubbling (27.4)
Corn starch	Very, very poor (131.5)	Rat-hole (191.9)	Channelling (146.0)
Potato starch	Very, very poor (133.6)	Rat-hole (185.2)	Channeling (71.1)
Egg white	Very, very poor (139.3)	Rat-hole (120.2)	Rat-hole (103.0)

By analyzing the flowability at different rotation speeds, we found that a flowability test with a rotation speed of 60 RPM is best correlated to the fluidization descriptor. A summary of the acquired flow and fluidization properties is presented in Table 6.3, where we provide the reciprocal of the FQI, denoted as FQI^{-1}, for ease of comparison with the CI. A low FQI^{-1} indicates good fluidization property, while a high FQI^{-1} indicates poor fluidization property. Specifically, powders with good and fair flowability (CI < 20) tend to exhibit bubbling

or partial bubbling behavior during fluidization. An interesting observation is that this group includes bentonite, silica, and modified corn starch. These powders exhibited significant aeration and improved flowability as the rotation speed increased (see Fig. 6.6 and Appendix Fig. E.2). On the other hand, powders with very poor flowability (CI > 40) tend to demonstrate macro-channeling (also known as rate-hole) and static powder behavior. Moreover, for very cohesive powders in the regime of very, very poor flowability, the fluidization behavior can be further distinguished. The transition from micro-channeling (CI between 50-75) to macro-channeling (CI > 140) indicates that the fluidization phenomena are connected to quantitative measurements of the CI.

With the assistance of mechanical vibration, the fluidization quality can be improved for certain powders. The table indicates that powders with a CI lower than 75 are effectively facilitated, showing a transition from channeling to bubbling. For powders that originally exhibit bubbling behavior, mechanical vibration improves bubbling with the observation of an increased number of smaller bubbles in the bed and a lower FQI^{-1} value, indicating higher gas holdup and/or more intense gas-solids mixing. Powders with a CI higher than 75 (specifically corn starch, potato starch, and egg white) show some improvement with the assistance of mechanical vibration. However, it is evident that these powders cannot be fluidized under these conditions, despite corn starch and potato starch transitioning from rat-hole to channeling.

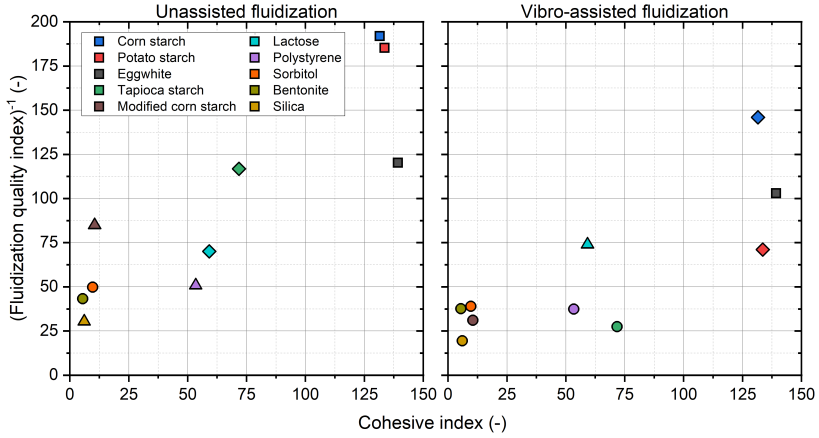

Figure 6.13: Cohesive index against the reciprocal of the fluidization quality index for unassisted fluidization (left) and vibro-assisted fluidization (right). The cohesive index values are measured at a rotation speed of 60 RPM. The symbols correspond to the qualitative fluidization descriptor: rat-hole □, channeling ◇, mild bubbling △, and bubbling ○.

To visualize the relation, the FQI^{-1} is plotted against the CI in Fig. 6.13. In accordance with the above, powders with a high CI value (tapioca starch, egg white, potato starch, and corn starch) display a high FQI^{-1} value. Conversely, powders with a low CI value (silica, bentonite, sorbitol) display a low FQI^{-1} value. Although the data is loosely scattered, a positive correlation between the CI and the FQI^{-1} is clearly observed, further supporting the intrinsic connection between the flowability and fluidization property. In addition, the designated CI value is shown to be capable of predicting the corresponding fluidization behavior of the cohesive powders. When comparing unassisted fluidization with vibro-assisted fluidization, it is evident that mechanical vibration leads to a decrease in the FQI^{-1} across all powder types, indicating an improvement in fluidization quality. However, the powders with a CI exceeding 100 are still challenging to be fluidized, even with vibration assistance. This highlights the CI's potential as a predictive indicator of the associated fluidization quality in practical applications. Based on these observations, it is clear that flowability and fluidization properties are inherently correlated.

6.4. Conclusion

In this study, a comprehensive examination of the fluidization and flow properties of 10 commercially available materials was conducted through rotating drum and fluidization experiments. Operating the rotating drum instrument at a rotation speed of 60 RPM generates an aerated state within the powder bed, which allows for comparable flow field and stress conditions as in a fluidized bed. By analyzing the fluidization behavior, it was observed that widely applied analyses based on normalized pressure drop and bed expansion, which are typically used for assessing the fluidization quality of Geldart A and B powders, have limitations when applied to cohesive powders. Therefore, the fluidization behavior was quantified based on the observed flow pattern, which was studied using X-ray imaging. A novel fluidization quality index (FQI) was introduced, which combines the time-averaged gas holdup and the temporal standard deviation of the domain-averaged gas holdup, thereby offering a reliable indicator of fluidization quality.

By carefully comparing powder flowability and fluidization properties, a positive correlation between flowability (quantified by the cohesive index, CI) and fluidization quality (quantified by the inverse of the FQI) was established, underscoring their inherent relationship. This finding holds significance as it indicates that simple flowability measurements conducted in a rotating drum instrument can provide valuable insights into the expected fluidization quality of cohesive powders. Consequently, these insights offer a reliable means of

predicting whether a cohesive powder is likely to fluidize, with or without assistance methods applied. This understanding holds promise for enhancing fluidization studies and optimizing industrial processes reliant on fluidization techniques.

References

[1] L. Feng and Z. Liu, *Graphene in biomedicine: Opportunities and challenges,* Nanomedicine **6**, 317 (2011).

[2] L. Qu, Y. Liu, J.-B. Baek, and L. Dai, *Nitrogen-doped graphene as efficient metal-free electrocatalyst for oxygen reduction in fuel cells,* ACS Nano **4**, 1321 (2010), https://doi.org/10.1021/nn901850u .

[3] X. Zhu, Q. Zhang, C. Huang, Y. Wang, C. Yang, and F. Wei, *Validation of surface coating with nanoparticles to improve the flowability of fine cohesive powders,* Particuology **30**, 53 (2017).

[4] R. Kamphorst, K. Wu, S. Salameh, G. M. H. Meesters, and J. R. van Ommen, *On the fluidization of cohesive powders: Differences and similarities between micro- and nano-sized particle gas-solid fluidization,* The Canadian Journal of Chemical Engineering **101**, 227 (2023).

[5] L.-S. Fan and C. Zhu, *Principles of Gas-Solid Flows* (Cambridge University Press, 1998).

[6] W. C. Q. LaMarche, P. Liu, K. M. Kellogg, A. M. Lattanzi, and C. M. Hrenya, *Toward general regime maps for cohesive-particle flows: Force versus energy-based descriptions and relevant dimensionless groups,* AIChE Journal **67**, e17337 (2021), https://aiche.onlinelibrary.wiley.com/doi/pdf/10.1002/aic.17337 .

[7] D. Geldart, *Types of gas fluidization,* Powder Technology **7**, 285 (1973).

[8] A. Teleki, R. Wengeler, L. Wengeler, H. Nirschl, and S. Pratsinis, *Distinguishing between aggregates and agglomerates of flame-made TiO_2 by high-pressure dispersion,* Powder Technology **181**, 292 (2008).

[9] L. Niu, Z. Chu, M. Cai, and M. Liu, *Modified force balance model of estimating agglomerate sizes in a gas-solid fluidized bed,* Industrial and Engineering Chemistry Research **58**, 8472 (2019).

[10] A. A. Motlagh, J. R. Grace, M. Salcudean, and C. Hrenya, *New structure-based model for eulerian simulation of hydrodynamics in gas–solid fluidized beds of Geldart group A particles,* Chemical Engineering Science **120**, 22 (2014).

[11] R. Kamphorst, P. C. van der Sande, K. Wu, E. C. Wagner, M. K. David, G. M. Meesters, and J. R. van Ommen, *The mechanism behind vibration assisted fluidization of cohesive microsilica,* KONA Powder and Particle Journal **41**, 254 (2024).

[12] S. Alavi and B. Caussat, *Experimental study on fluidization of micronic powders,* Powder Technology **157**, 114 (2005).

[13] K. Wu, R. Kamphorst, A. Bakker, J. Ford, E. C. Wagner, O. Ochkin-Koenig, M. Franck, D. Weis, G. M. Meesters, and J. R. van Ommen, *Stirrer design for improving fluidization of cohesive powder: A time-resolved X-ray study,* Chemical Engineering Science **294**, 120069 (2024).

[14] E. Al-Ghurabi, M. Shahabuddin, N. Siva Kumar, and M. Asif, *Deagglomeration of ultrafine hydrophilic nanopowder using low-frequency pulsed fluidization,* Nanomaterials **10**, 388 (2020).

[15] S. Ali, E. AL-Ghurabi, A. Ajbar, Y. Mohammed, M. Boumaza, and M. Asif, *Effect of frequency on pulsed fluidized beds of ultrafine powders,* Journal of Nanomaterials **2016**, 1 (2016).

[16] R. Chirone, F. Raganati, P. Ammendola, D. Barletta, P. Lettieri, and M. Poletto, *A comparison between interparticle forces estimated with direct powder shear testing and with sound assisted fluidization,* Powder Technology **323**, 1 (2018).

[17] P. Ammendola and R. Chirone, *Aeration and mixing behaviours of nano-sized powders under sound vibration,* Powder Technology **201**, 49 (2010).

[18] K. Wu, E. Wagner, O. Ochkin-Koenig, M. Franck, D. Weis, G. Meesters, and J. R. Van Ommen, *Time-resolved X-ray study of assisted fluidization of cohesive micron powder: On the role of mechanical vibration,* Chemical Engineering Journal **470**, 143936 (2023).

[19] R. Kamphorst, K. Wu, M. van Baarlen, G. M. Meesters, and J. R. van Ommen, *Effect of vibrational modes on fluidization characteristics and solid distribution of cohesive micro- and nano-silica powders,* Chemical Engineering Science **291**, 119911 (2024).

[20] R. L. Carr, *Evaluating flow properties of solids,* Chemical Engineering **72**, 163 (1965).

[21] J. Schwedes, *Review on testers for measuring flow properties of bulk solids,* Granular matter **5**, 1 (2003).

[22] K. Thalberg, D. Lindholm, and A. Axelsson, *Comparison of different flowability tests for powders for inhalation,* Powder Technology **146**, 206 (2004).

[23] M. Leturia, M. Benali, S. Lagarde, I. Ronga, and K. Saleh, *Characterization of flow properties of cohesive powders: A comparative study of traditional and new testing methods,* Powder Technology **253**, 406 (2014).

[24] S. Z. Ajabshir, D. Barletta, and M. Poletto, *The effect of process conditions on powder flow properties for slow flow regimes,* KONA Powder and Particle Journal **advpub**, 2025006 (2024).

[25] I. Mishra, M. J. Molnar, M. Y. Hwang, A. Shetty, and C. M. Hrenya, *Experimental validation of the extraction of a particle-particle cohesion model (square-force) from simple bulk measurements (defluidization in a rheometer),* Chemical Engineering Science **259**, 117782 (2022).

[26] M. Krantz, H. Zhang, and J. Zhu, *Characterization of powder flow: Static and dynamic testing,* Powder Technology **194**, 239 (2009).

[27] L. Zhu, H. Lu, M. Poletto, H. Liu, and Z. Deng, *Hopper discharge of cohesive powders using pulsated airflow,* AIChE Journal **66**, 16240 (2020), https://aiche.onlinelibrary.wiley.com/doi/pdf/10.1002/aic.16240 .

[28] I. Mishra, P. Liu, A. Shetty, and C. M. Hrenya, *On the use of a powder rheometer to probe defluidization of cohesive particles,* Chemical Engineering Science **214**, 115422 (2020).

[29] J. K. Prescott and R. A. Barnum, *On powder flowability,* Pharmaceutical technology **24**, 60 (2000).

[30] A. Castellanos, J. M. Valverde, A. T. Pérez, A. Ramos, and P. K. Watson, *Flow regimes in fine cohesive powders,* Physical review letters **82**, 1156 (1999).

[31] X. Y. Liu, E. Specht, and J. Mellmann, *Experimental study of the lower and upper angles of repose of granular materials in rotating drums,* Powder Technology **154**, 125 (2005).

[32] S. L. Pirard, G. Lumay, N. Vandewalle, and J.-P. Pirard, *Motion of carbon nanotubes in a rotating drum: The dynamic angle of repose and a bed behavior diagram,* Chemical Engineering Journal **146**, 143 (2009).

[33] H. Shi, G. Lumay, and S. Luding, *Stretching the limits of dynamic and quasi-static flow testing on cohesive limestone powders,* Powder Technology **367**, 183 (2020).

[34] A. Neveu, F. Francqui, and G. Lumay, *Measuring powder flow properties in a rotating drum,* Measurement **200**, 111548 (2022).

[35] K. Rietema, *The Dynamics of Fine Powders* (Springer Dordrecht, Dordrecht, 1991).

[36] A. Castellanos, M. Sanchez, and J. Valverde, *The onset of fluidization for fine powders in rotating drums,* Materials Physics and Mechanics **3**, 57 (2001).

[37] A. Castellanos, J. M. Valverde, and M. A. S. Quintanilla, *Fine cohesive powders in rotating drums: Transition from rigid-plastic flow to gas-fluidized regime,* Physical Review E **65**, 061301 (2002).

[38] Q. Huang, H. Zhang, and J. Zhu, *Experimental study on fluidization of fine powders in rotating drums with various wall friction and baffled rotating drums,* Chemical Engineering Science **64**, 2234 (2009).

[39] Q. Huang, H. Zhang, and J. Zhu, *Onset of an innovative gasless fluidized bed—comparative study on the fluidization of fine powders in a rotating drum and a traditional fluidized bed,* Chemical Engineering Science **65**, 1261 (2010).

[40] N. Jain, J. M. Ottino, and R. M. Lueptow, *Regimes of segregation and mixing in combined size and density granular systems: an experimental study,* Granular Matter **7**, 69 (2005).

[41] L. Orefice, J. Remmelgas, A. Neveu, F. Francqui, and J. G. Khinast, *A novel methodology for data analysis of dynamic angle of repose tests and powder flow classification,* Powder Technology **435**, 119425 (2024).

[42] V. N. Tondare, J. G. Whiting, A. L. Pintar, S. P. Moylan, A. Neveu, and F. Francqui, *An interlaboratory study for assessing repeatability and reproducibility of the data generated by rotating drum powder rheometers (Part 1: Granudrum),* Powder Technology **441**, 119810 (2024).

[43] H. Henein, J. K. Brimacombe, and A. P. Watkinson, *Experimental study of transverse bed motion in rotary kilns,* Metallurgical Transactions B **14**, 191 (1983).

[44] N. Taberlet, P. Richard, and E. John Hinch, *S shape of a granular pile in a rotating drum,* Physical Review E **73**, 050301 (2006).

[45] R. Freeman, *Powder testing - dealing with the daily challenges,* Powder Handling and Processing **17**, 294 – 296 (2005).

7

Epilogue

7.1. Conclusions

The research presented in this thesis is aimed at acquiring a deeper understanding of the complex granular flow behavior in stirred and fluidized bed reactors. A deeper understanding of granular flow behavior in these reactors was achieved through detailed experimental measurements using advanced nuclear techniques. Experiments were conducted in three laboratory-scale systems: a horizontal stirred bed, a vertical stirred bed, and a fluidized bed. High-quality data on flow patterns, phase holdup, and particle dynamics were obtained using X-ray imaging and single-photon emission radioactive particle tracking. The collected data were thoroughly analyzed to identify the key parameters influencing granular flow behavior, utilizing statistical methods and visualization tools to uncover critical insights.

Horizontal stirred bed reactor

First, the flow behavior of polypropylene reactor powder in a laboratory-scale horizontal stirred bed reactor (HSBR) was investigated using X-ray imaging. It was found that the overall flow behavior and phase holdup in the HSBR are strongly influenced by agitation. Gas injection through the inlet points at the bottom of the HSBR resulted in spouting behavior, which was more pronounced for powder with a smaller particle size (PP-1) compared to powder with a larger particle size (PP-3). Additionally, agitation, as well as alternation of the impeller blade positions, influence the gas holdup and result in variations in power consumption within an agitator revolution. The fluctuation in powder consumption decreased with increasing rotation speeds due to bed aeration. The gas holdup at fixed agitator positions was extremely consistent across successive revolutions, underlining the dominance of agitation on the overall flow behavior. The presence of liquid isopropyl alcohol was observed to deteriorate the flow behavior of the PP reactor powder. This deterioration was caused by liquid bridging at particle contact points, creating cohesive forces that led to lump formation. The particle size and surface morphology significantly influenced the powders' susceptibility to liquid.

X-ray imaging provided detailed insight into the flow behavior and phase holdup in the HSBR, but it did not allow the tracking of individual particles. Therefore, a novel single-photon emission radioactive particle tracking method was developed to obtain insight into the particle dynamics in the HSBR. This method tracks individual photon-emitting particles, using detected photon-hit locations to directly reconstruct the tracer particle's three-dimensional position. This approach eliminates the need for assumptions in count rate fluctuations, which is a limitation in conventional radioactive particle tracking. The three-dimensional position of the tracer particle was determined by finding the intersection point of three two-dimensional planes originating from the detectors. Through a calibration-experimentation procedure, a spatial accuracy of approximately 1 millimeter was achieved, which was found sufficient to study particle trajectories in the laboratory-scale HSBR.

Single-photon emission radioactive particle tracking was employed to characterize the particle dynamics in the laboratory-scale HSBR. The results revealed that particle flow behavior in the HSBR is significantly influenced by the reactor fill level and agitator rotation speed. At low rotation speeds and fill levels, solids motion is primarily induced by the passing impeller blade, resulting in semi-static bed motion with poor solids distribution. As fill levels and rotation speeds increase, continuous solids motion throughout the bed leads to uniform solids distribution. Additionally, the solids circulation, quantified by a dimensionless cycle number, was found to be faster with increasing reactor fill level and rotation speed. The axial dispersion coefficient was found to range from 10^{-6} to 10^{-5} $m^2\,s^{-1}$ and increased with increasing rotation speed, while no conclusive relation between the axial dispersion coefficient and the reactor fill level was found.

Vertical stirred bed reactor

Besides HSBRs, vertical stirred bed reactors (VSBRs) are used to manufacture polypropylene. The influence of agitation on the fluidization performance of Geldart B particles was investigated using X-ray imaging, pressure drop measurements, and Computational Fluid Dynamics (CFD) coupled with the Discrete Element Method (DEM) and Immersed Boundary Method (IBM). The experimentally obtained minimum fluidization curve and time-averaged pressure drop showed good qualitative agreement with the simulation results. Visual observations indicated that increasing the agitator's angular velocity reduces bubble size and improves bed homogeneity, which was also indicated by decreased pressure fluctuations. Furthermore, simulations revealed that while the impeller enhances solids agitation, a careful design study is imperative,

considering that static immersed bodies, such as the stirrer shaft, can adversely impact solids motion.

Fluidized bed of cohesive powders
In previous works, the focus was on powders with a particle size > 100 µm. However, in many industrial applications, powders with smaller particle sizes are used, which tend to become cohesive due to relatively strong van der Waals forces. The fluidization of cohesive powders introduces several challenges, such as channeling and agglomeration, which even hinder some powders from being fluidized at all. In Chapter 6, the correlation between the fluidization behavior in a fluidized bed and flow properties in a rotating drum of ten commercially available cohesive powders was investigated. It was found that operating the drum at high rotation speeds creates a fluidized state, similar to a fluidized bed. A Fluidization Quality Index (FQI) was computed using X-ray imaging, which integrated gas holdup and its temporal variation to assess fluidization quality. This study established a positive correlation between cohesive powders' flowability and fluidization quality, suggesting that fast and user-friendly flowability measurements in a rotating drum instrument can predict fluidization potential, aiding in process optimization and enhancing fluidization studies for cohesive powders.

In perspective
In conclusion, the insights gained from this thesis enhance the understanding of flow behavior and phase holdup in stirred bed reactors and cohesive fluidized beds. This knowledge can serve as a valuable basis for optimizing, intensifying, and scaling systems for the industrial manufacturing of high-quality PP resins in particular, but it can also be widely applied to other granular flow applications.

7.2. Opportunities for future work

Although this research has advanced the experimental understanding of stirred bed reactors, it has also raised several intriguing questions, creating opportunities for further study.

In this research, X-ray imaging and single-photon emission radioactive particle tracking were employed to study the behavior of stirred bed reactors (see Fig. 7.1). X-ray imaging provided detailed insights into the gas holdup of a system but did not allow the tracking of individual particles. Conversely, single-photon emission radioactive particle tracking enabled the tracking of individual particles but did not provide insights into gas holdup. Both methods have

proven invaluable and complement each other, offering comprehensive hydrodynamic insight into the system.

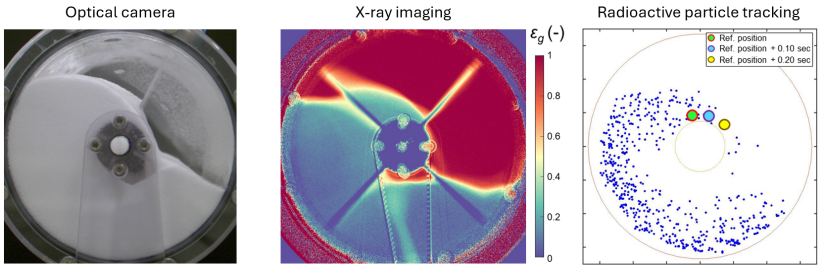

Figure 7.1: Overview of the experimental methods employed in this research.

Although both methods complement each other when used separately, the simultaneous acquisition of bulk and single-particle behavior would be a great step forward, as the particle scale dynamics could be directly linked to the reactor scale behavior. In fact, the nuclear measurement platform at the Delft University of Technology was originally designed to integrate X-ray imaging and single-photon emission radioactive particle tracking into a single advanced acquisition system. However, achieving simultaneous operation has been challenging due to significant differences in detector sensitivity. The detectors for radioactive particle tracking are developed to detect individual photons, whereas the X-ray sources generate significant X-ray radiation. Simultaneous operation would quickly overexpose the single-photon emission radioactive particle tracking detectors, rendering particle tracking problematic. Advanced shielding with high-density materials may offer potential solutions, but exploring alternative approaches is also warranted.

A possible method that could provide simultaneous insight into the bulk and single particle behavior is X-ray particle tracking, often referred to as X-ray particle velocimetry (XPTV) [1–6]. In the final stages of this research, a preliminary investigation into the feasibility of XPTV at the Delft University of Technology was conducted. This technique utilizes X-ray imaging while a radiation-absorbing tracer particle is present within the equipment under study, thereby providing simultaneous information on gas-solids distribution and single-particle behavior. However, a critical consideration is ensuring that the tracer particle exhibits sufficient X-ray absorption to enable tracking while also accurately representing the flow properties of the bulk particles. To induce sufficient contrast, many studies employing X-ray velocimetry typically use tracer particles ranging from several millimeters to centimeters in size [5, 6]. However, these

particle sizes are significantly larger than the bed material of interest in this work and would, therefore, result in size segregation.

Inspired by a manufacturing process by Parker and Mäkiharju [7], we developed a method to synthesize tracer particles by soaking a 1.8 mm high-purity porous alumina bead (SASOL) in a 58wt% aqueous KI solution for 24 h. After a subsequent drying step, the attenuation of the tracer particle was notably increased when compared to an untreated alumina particle, as can be observed in Fig. 7.2-c. The tracer particle was inserted in the horizontal stirred bed reactor to characterize the influence of the fill level and rotation speed on the cycle time distribution, following a workflow based on Chapter 3 in this thesis.

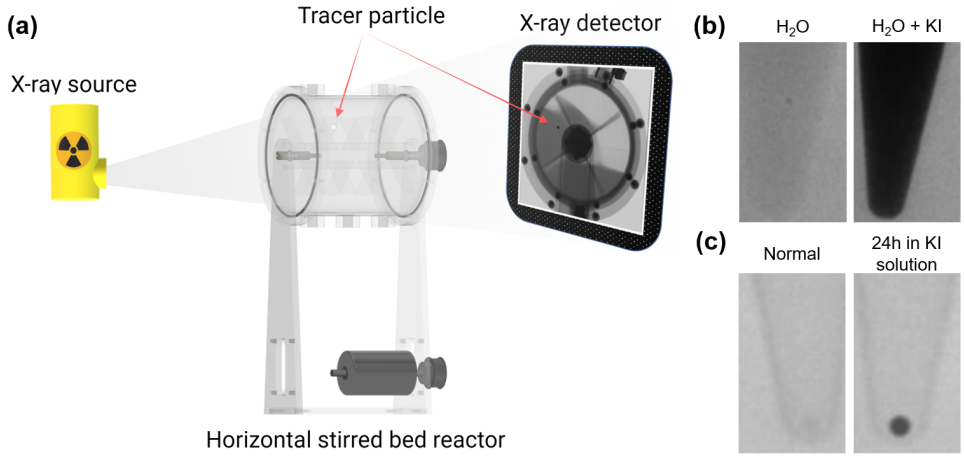

Figure 7.2: Preliminary investigation of X-ray particle velocimetry. (a) Schematic representation of X-ray particle velocimetry in the laboratory-scale horizontal stirred bed reactor, (b) X-ray images of Eppendorf tubes filled with water and a 58wt% aqueous KI solution, and (c) X-ray images of a normal 1.8 mm alumina bead and a 1.8 mm alumina bead soaked in a 58wt% aqueous KI solution for 24 h.

Figure 7.3 shows a sequence of X-ray images illustrating the bulk flow of polypropylene reactor powder and the trajectory of the 1.8 mm alumina tracer particle in the laboratory-scale HSBR. It is evident that the 1.8 mm alumina particle after a KI solution treatment step provides sufficient X-ray attenuation, such that the circumferential trajectory can be clearly monitored in a polypropylene bed with a depth of 14 cm. An image processing workflow was employed to extract the particle cycle time distribution for each operational condition. Figure 7.4 graphically compares the cycle time distribution acquired with XPTV to the cycle time distribution acquired with single-photon emission as presented

in Chapter 4.

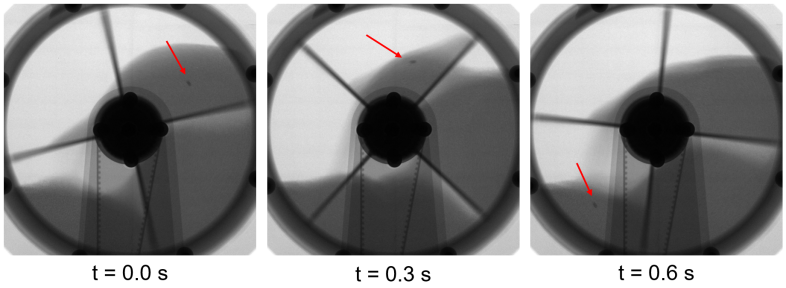

Figure 7.3: Sequence of X-ray images illustrating the bulk flow of polypropylene reactor powder and the trajectory of the 1.8 mm alumina tracer particle in the laboratory-scale horizontal stirred bed reactor operated at a fill level of 50% and rotation speed of 20 RPM.

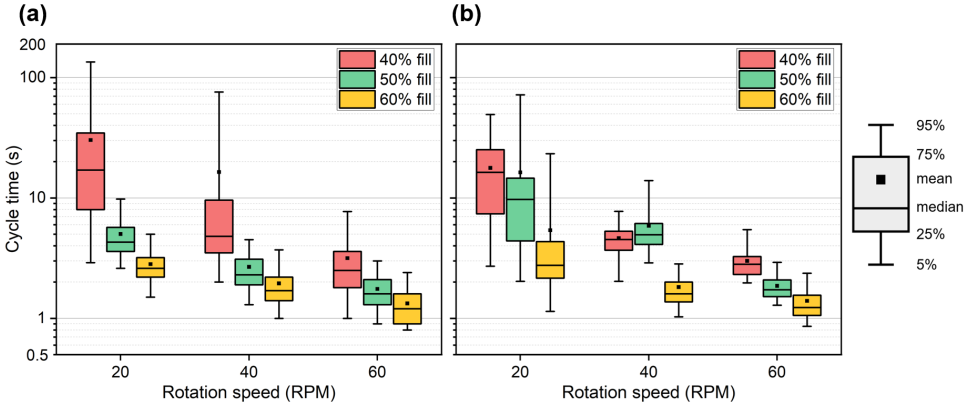

Figure 7.4: Cycle time distribution of the tracer particle in the laboratory-scale horizontal stirred bed reactor obtained by (a) single-photon emission radioactive particle tracking and (b) X-ray particle velocimetry.

It can be observed that the overall trend is similar, demonstrating that both an increase in fill level and rotation speed results in a decrease in the cycle time. However, it should be noted that the preliminary presented data acquired with XPTV is based on a measurement time of 5 min, compared to 20 min for single-photon emission radioactive particle tracking, and therefore has lower confidence. Nevertheless, the preliminary results show that XPTV can provide information on the gas holdup and particle trajectory simultaneously as one integrated method, which opens doors to a wide array of opportunities. However, proper design and development of the tracer particle is imperative, as a

too-strong deviation from the bulk particles may result in segregation.

Throughout this research, experiments were conducted using laboratory-scale stirred and fluidized beds, typically sized in the order of centimeters to decimeters. In contrast, industrial horizontal stirred bed reactors for PP manufacturing can reach lengths of approximately 20 m. Given the dimensional constraints for characterization using advanced nuclear measurement techniques at the Delft University of Technology, our study pushed the limits of the setup's dimensions. Therefore, an important next step would be to utilize the experimental datasets to validate computational fluid dynamics (CFD) - discrete element method (DEM) models. Once a CFD-DEM model is properly calibrated and validated at the laboratory scale, computational studies can then be extended to larger industrial scales, provided sufficient computational resources are available. This approach ensures that insights gained from the laboratory-scale experiments are robustly applied and extrapolated to industrial settings.

Moreover, the experiments in this thesis were conducted under controlled, non-reactive conditions at room temperature and atmospheric pressure to provide a clear understanding of how operating parameters influence complex flow characteristics. Additionally, the impact of liquid on flow behavior was assessed under fixed liquid contents. In contrast, industrial polymerization reactors typically operate at temperatures ranging from 50 to 70 °C, while liquid is quenched from the top and subsequently evaporates. Despite these differences, this research has established a robust foundation for studying complex features in laboratory-scale reactors using nuclear measurement techniques. Future research can expand upon this foundation by adapting experimental setups to operate at elevated temperatures and pressures, including continuous wetting using X-ray attenuating liquids. These advancements will further contribute to effectively bridging the gap between laboratory findings and industrial processes.

References

[1] J. B. Drake, N. P. Franka, and T. J. Heindel, *Developing x-ray particle tracking velocimetry for applications in fluidized beds,* in *ASME International Mechanical Engineering Congress and Exposition*, Vol. 48715 (2008) pp. 379–386.

[2] J. B. Drake, L. Tang, and T. J. Heindel, *X-ray particle tracking velocimetry in fluidized beds,* in *Fluids Engineering Division Summer Meeting*, Vol. 43727 (2009) pp. 1733–1742.

[3] T. Lappan, D. Herting, M. Ziauddin, J. Stenzel, N. Shevchenko, S. Eckert, K. Eckert, and S. Heitkam, *X-ray particle tracking velocimetry in an overflowing foam,* Applied Sciences **13** (2023), 10.3390/app13031765.

[4] X. Chen, W. Zhong, and T. J. Heindel, *Orientation of cylindrical particles in a fluidized bed based on stereo x-ray particle tracking velocimetry (xptv),* Chemical Engineering Science **203**, 104 (2019).

[5] S. Iannello, P. U. Foscolo, and M. Materazzi, *Investigation of single particle devolatilization in fluidized bed reactors by x-ray imaging techniques,* Chemical Engineering Journal **431**, 133807 (2022).

[6] M. Errigo, A. Sebastiani, S. Iannello, M. Materazzi, and P. Lettieri, *Application of imaging techniques for the characterization of lumps behaviour in gas–solid fluidized-bed reactors,* Fuel **349**, 128634 (2023).

[7] J. T. Parker and S. A. Mäkiharju, *Experimentally validated x-ray image simulations of 50 µm x-ray piv tracer particles,* Measurement Science and Technology **33**, 055301 (2022).

A

Appendix A

A.1. Supplementary information on polypropylene material

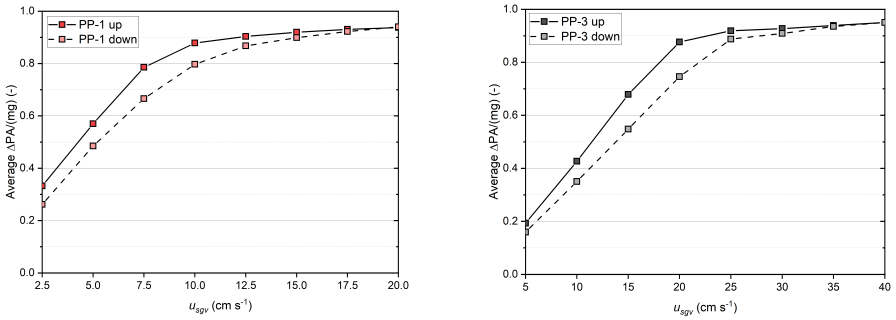

(a) PP reactor powder PP-1.

(b) PP reactor powder PP-3.

Figure A.1: Normalized pressure drop against superficial gas velocity curves for PP-1 and PP-3 measured in a cylindrical fluidized bed column with an internal diameter of 5 cm. From the curves, the minimum fluidization velocities were determined to be 15 cm s^{-1} for PP-1 and 25 cm s^{-1} for PP-3.

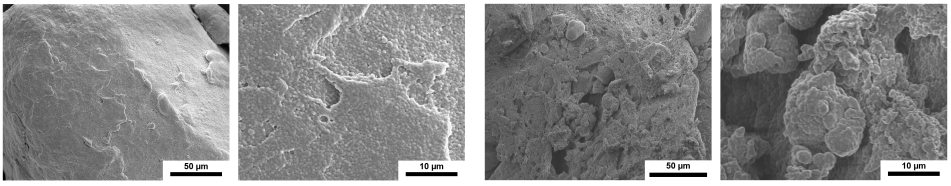

(a) PP reactor powder PP-1.

(b) PP reactor powder PP-3.

Figure A.2: Representative scanning electron microscope images of polypropylene reactor powder PP-1 and PP-3 acquired with a JSM-6010LA scanning electron microscope.

A

A.2. Gas holdup

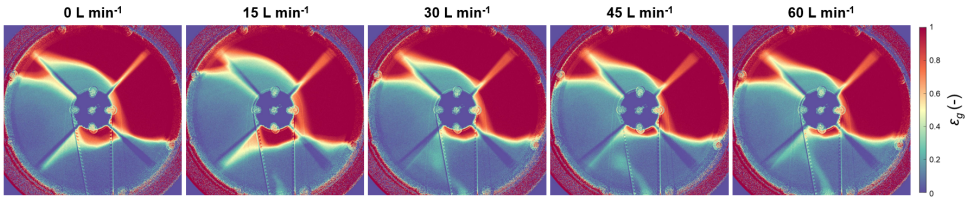

(a) PP reactor powder PP-1.

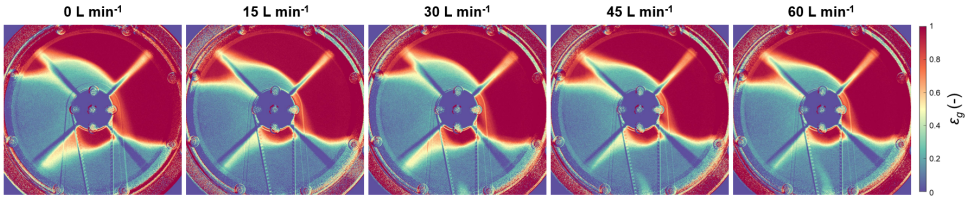

(b) PP reactor powder PP-3.

Figure A.3: Representative snapshots of the gas holdup for varying gas flow rates at a rotation speed of 40 RPM displaying the side view of the HSBR.

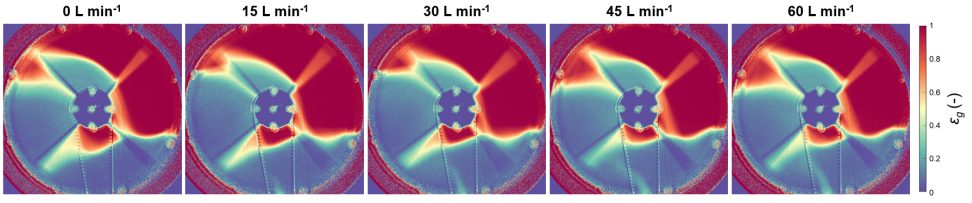

(a) PP reactor powder PP-1.

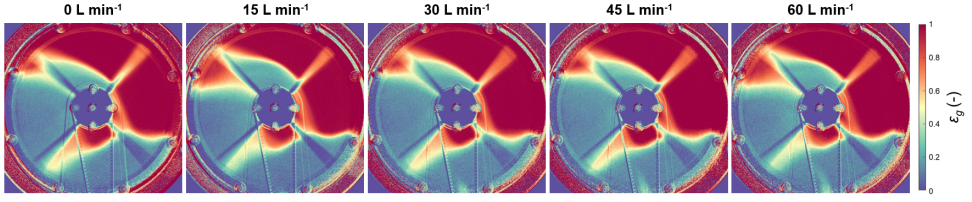

(b) PP reactor powder PP-3.

Figure A.4: Representative snapshots of the gas holdup for varying gas flow rates at a rotation speed of 60 RPM displaying the side view of the HSBR.

A.3. Power consumption

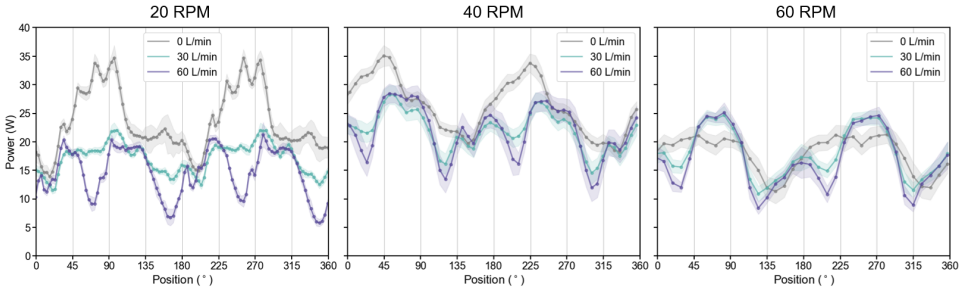

Figure A.5: Graphical representation of the power consumption fluctuations within one revolution for powder PP-1 for varying rotation speed (20, 40, and 60 RPM) and gas inlet flow rate (0, 30, and 60 L min^{-1}). The mean and standard deviation are based on 60 revolutions.

B

Appendix B

B.1. Gamma-radiation detection

The γ-radiation emitted by the tracer particle passes through the slit collimator and reaches the scintillation crystal. The distribution of hits on the scintillation crystal follows a Poisson distribution, as depicted in Fig. B.1. The Poisson distribution is approached with a Gaussian for sufficiently large data sets. The pixel value corresponding to the centroid of the Gaussian fit is considered the most accurate representation of the tracer particle's projected position and is used for the reconstruction. The distance between the slit collimator and the scintillation crystal can be adjusted to control the magnification of the projection.

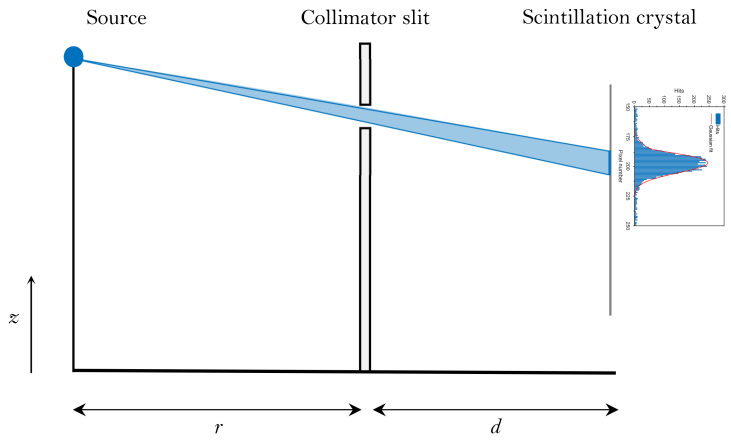

Figure B.1: Schematic representation of the γ-radiation pathway from the radioactive tracer particle, through the slit collimator to the scintillation crystal. The letter 'r' and 'd' represent the tracer particle to slit collimator and slit collimator to scintillation crystal distance, respectively.

B.2. Calibration setup

To calibrate the spatial geometry of the RPT setup, a constrained non-linear least squares optimization algorithm was employed. This algorithm aims to minimize the spatial error between the true position of the tracer particle and

the reconstructed position obtained from the RPT system. The algorithm adjusts the geometry values within specified upper and lower bounds (set at 50 mm) and returns the calibrated geometry. The calibrated spatial orientation of the three detectors is shown in Fig. B.2. A comparison with the hand-measured geometry reveals that each detector in the calibrated setup has undergone a slight translation and rotation, effectively correcting for measurement inaccuracies. The calibration process leads to significantly improved accuracy and precision in the reconstruction of the tracer particle position.

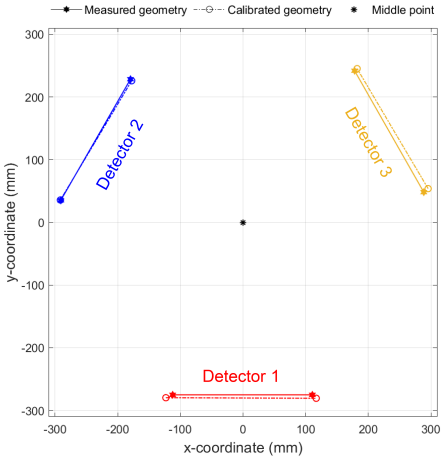

Figure B.2: Spatial orientation of the three detectors relative to the middle point in the hand-measured geometry and calibrated geometry.

C

Appendix C

C.1. Schematic of the horizontal stirred bed reactor

Fig. C.1 shows a schematic representation of the laboratory-scale horizontal stirred bed reactor used in this work. The reactor consists of a 134 mm outer-diameter cylinder with a length of 140 mm and incorporates an agitator comprising a central shaft with seven blade positions. Each position is equipped with two blades, with each blade positioned 90° apart from its neighboring blades. The inner blades have a width of 20 mm, while the end blades have a width of 15 mm. The agitator can be rotated at the desired rotation speed using an electric motor with a belt drive, which is controlled via in-house software.

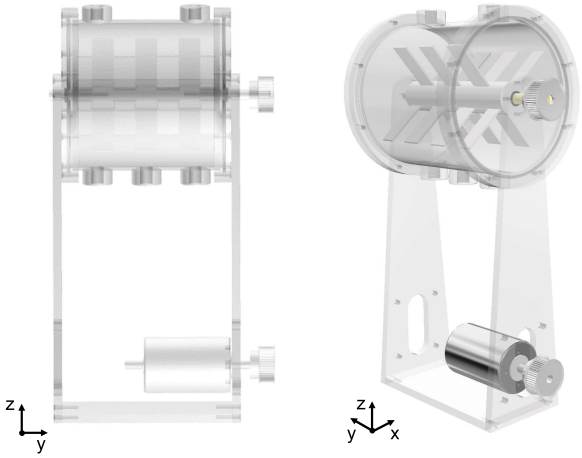

Figure C.1: Schematic representation of the laboratory-scale horizontal stirred bed reactor. The x-y-z origin is defined in the center of the HSBR cylinder.

C.2. Axial dispersion time-step

As elaborated on in Section 4.2.3, the axial dispersion coefficient, $D_{y,i,j}$, of a single particle at a certain time-step, is computed as:

$$D_{y,i,j} = \frac{(\Delta y_{i,j} - \bar{\Delta y})^2}{2\Delta t} \tag{C.1}$$

Fig. C.2 demonstrates how the time-step, Δt, influences the computed value of the axial dispersion coefficient for a wide range of time-step values. At low time-step values, the axial dispersion decreases rapidly until a plateau is reached beyond a Δt of 5 seconds. When Δt exceeds 30 seconds, dispersion coefficients for various experimental conditions converge, indicating a loss of potential information that is unique to a specific experimental condition. Considering both extremes, a Δt of 10 s was deemed appropriate and was therefore used in the calculations of the axial dispersion coefficient in this work.

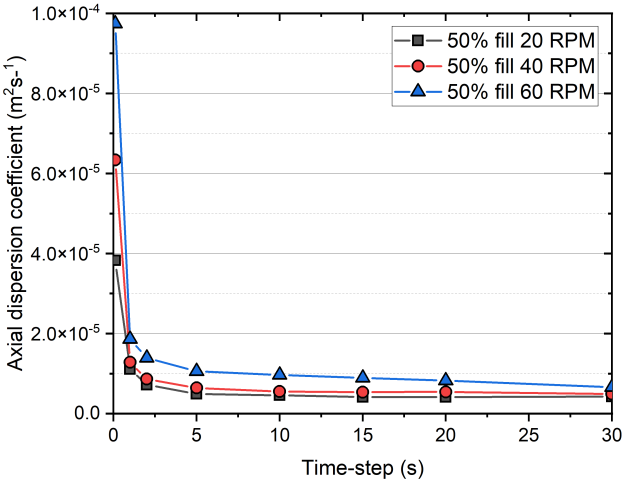

Figure C.2: Supporting information for Section 4.2.3 demonstrating the influence of the time-step, varied from 0.1 to 30 s, on the computed value of the axial dispersion coefficient for operating conditions with a fill level of 50% and rotation speed of 20, 40, and 60 RPM. Based on the plots, a time-step of 10 s was deemed appropriate in the calculations since the axial dispersion coefficient is at a plateau, and the coefficients for various experimental conditions have not converged.

C.3. Video reconstructed trajectory

Video C.3 presents the trajectory of the 27.5 MBq tracer particle through the HSBR operated at a fill level of 50% and a rotation speed of 40 RPM for a 1 min time period. The reconstruction is performed with a sampling time of 100 ms. The projected area is rotating to demonstrate the three-dimensional nature of the reconstruction.

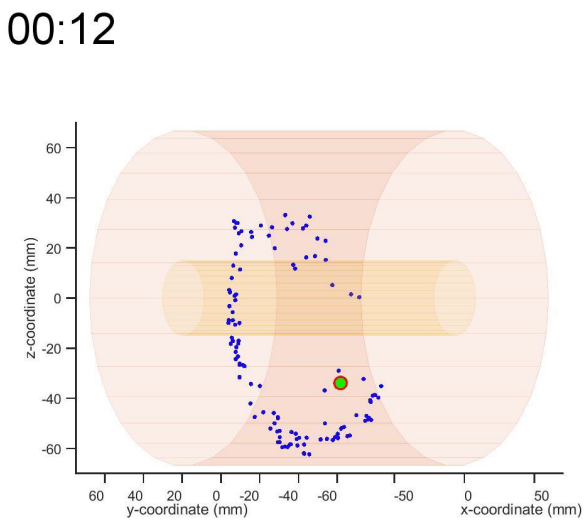

Figure C.3: Trajectory of the tracer particle for a fill level of 50% and rotation speed of 40 RPM. The instantaneous position is indicated by the red-outlined green dot, and the blue scatter markers represent distinct reconstructed positions that have accumulated during the specified time interval.

C.4. Tracer particle velocity

Fig. C.4 presents supporting experimental results that show the influence of the fill level and rotation speed on the ratio of the mean particle velocity to the impeller tip speed for a large number of experimental conditions. In close agreement with Fig. 4.10, a trend can be observed where the ratio of the mean tracer particle velocity to the tip speed decreases with an increasing RPM for all tested reactor fill levels. More interestingly, for an increasing rotation speed, the ratio decreases quickly at first but then stabilizes at higher rotation speeds. It should be noted that the supporting data set was acquired for a minimum of 100 agitator rotations per experiment, i.e., a measurement time of 600 s for a rotation speed of 10 RPM and 100 s for a rotation speed of 60 RPM. Due to the reduced measurement time, the supporting data has less statistical confidence, and absolute values may, therefore, also deviate from the 20 min experiments presented throughout this work.

C

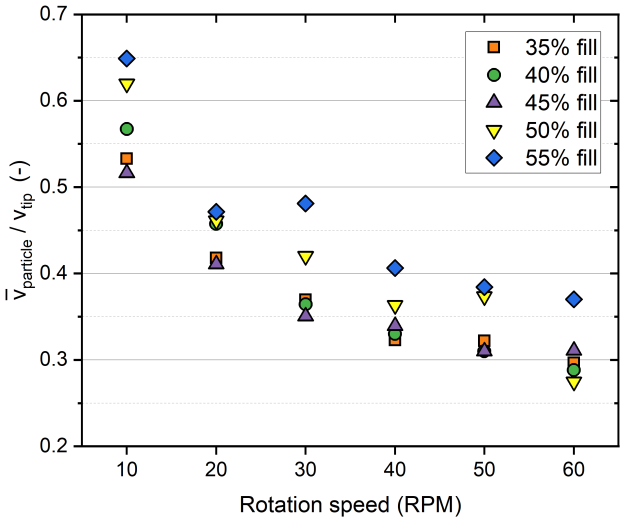

Figure C.4: Supporting information for Section 4.3.2 demonstrating the influence of the fill level and rotation speed on the ratio of the mean particle velocity to the impeller blade tip speed. The data was acquired from an additional extended experimental data set comprising a larger number of experimental conditions.

D

Appendix D

D.1. Supplementary X-ray imaging snapshots

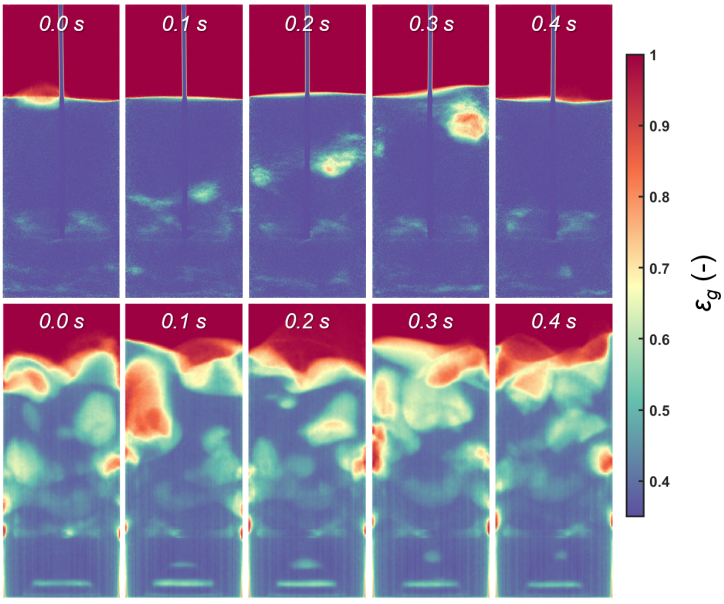

Figure D.1: Typical X-ray imaging snapshots of the flow pattern at a superficial gas velocity of 39.3 cm s^{-1} (top) and 45 cm s^{-1} (bottom) for various stirrer settings.

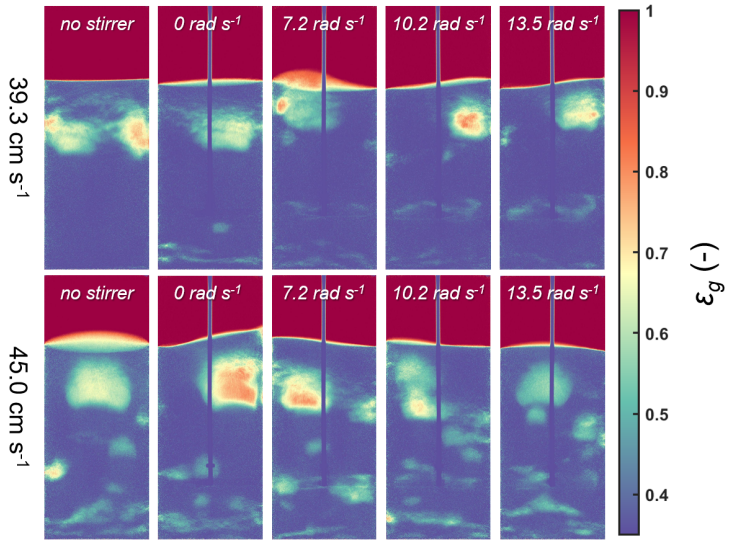

Figure D.2: Temporal evolution of the flow pattern at a superficial gas velocity of 39.3 cm s^{-1} and a rotation speed of 10.2 rad s^{-1} obtained through experimental X-ray imaging (top) and simulation (bottom).

Appendix E

E.1. Supplementary information

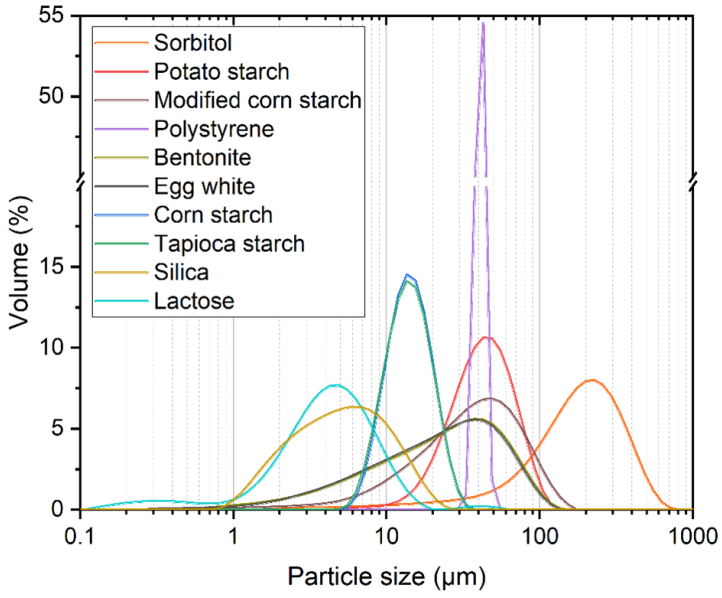

Figure E.1: Volume-based frequency particle size distribution of the powders included in this study.

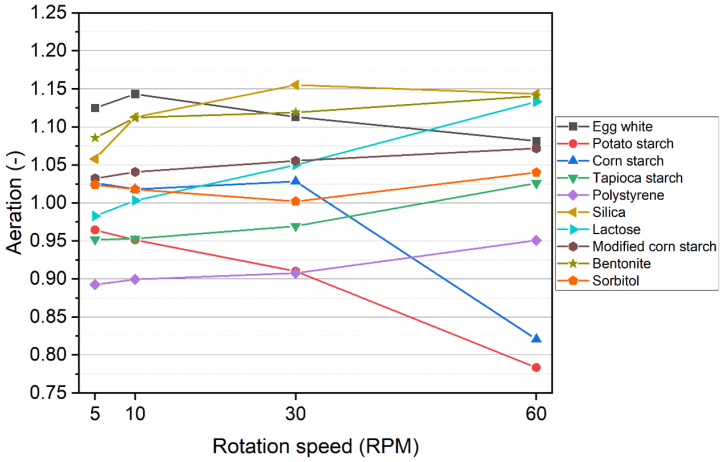

Figure E.2: Aeration of the bed as a function of the rotation speed. The aeration is calculated for each rotation speed relative to the static bed before the experiment using the number of black pixels in the 2D images.

Acknowledgements

This thesis presented and discussed the results of four years of work. During the four years, support was provided from different angles, which ultimately enabled me to compose the thesis you have in front of you.

Reflecting on my journey to this PhD, I am reminded of an important moment some 13 years ago when I was a secondary school student. I participated in a project week at DSM Delft. Having a combination education profile in *Natuur, Techiek en Gezondheid (NT & NG)* and a passion for chemistry, I was part of a group of students appointed to formulate and manufacture tablets with controlled release properties. Our daily supervisor from DSM was... Dr. Gabrie Meesters. Years later, our paths crossed again during my studies at the TU Delft. Gabrie was teaching product design, a core course of the curriculum. After the first lecture, I walked up to him and said, "Interessant college! Ik heb mijn DSM project bij u gedaan toen ik op het CLD zat." We regularly ran into each other in the corridor, which led to an internship at DSM Food Specialties in Sydney, Australia. After completing my internship, Gabrie informed me about a very interesting PhD position in reactor engineering focusing on particle technology in chemical reactors...

During my PhD, I was fortunate enough to have two incredible supervisors who were always there for me during the 4-year trajectory: promotor Ruud van Ommen and co-promotor Gabrie Meesters. Gabrie, je hebt een hele grote bijdrage geleverd aan het pad dat ik heb bewandeld tijdens mijn studies, promotieonderzoek en ook aan het pad dat ik nu bewandel met mijn werkleven buiten academia. Ik heb onwijs veel van je geleerd, zowel op theoretisch als persoonlijk vlak waarvoor ik je heel erg wil bedanken. Met voorbeelden uit de industrie wist je complexe poedertechnologische vraag-stukken altijd concreet en inzichtelijk te maken. Daarnaast heb je heel erg bijgedragen aan het enorm plezierig maken van mijn tijd als promovendus door het samen begeleiden van studenten en onderwijs geven, de werkreizen in binnen- en buitenland, speciaalbiertjes drinken op de beestenmarkt, en het uitwisselen van planten en zaden. We plannen snel een afspraak in om de beloofde portie zelfgebakken kibbeling te proven! Ruud, ik heb enorm veel respect voor jouw kennis, ervaring en toewijding in het vakgebied deeltjestechnologie en reactorkunde. Tijdens mijn promotie kon ik altijd bij je terecht om te brainstormen, je advies te vragen, en mijn voorlopige resultaten te presenteren. Daarnaast heb ik enorm veel respect voor je toewijding als begeleider van promovendi. Er zijn maar weinig

hoogleraren die zo snel feedback, maar toch ook uitgebreid, feedback geven op presentaties, abstracts, of manuscripten. Maar bovenal is het ook erg bijzonder dat je zo benaderbaar bent, wat het uitvoeren van promotieonderzoek onder jou erg plezierig maakt. Bedankt voor alle steun en support gedurende de vier jaar! Ik hoop dat ik in mijn nieuwe functie industriële samenwerkingen met je kan opzetten in de toekomst!

This research involved a lot of (complicated) experimental work, which could not have been performed without Evert Wagner. Evert, van alle mensen die hebben bijgedragen aan de praktische kant van mijn onderzoek ben jij het dichtst betrokken geweest. Samen hebben we heel veel mooie onderzoeken kunnen doen met de X-ray en RPT opstellingen, die jij zelf samen met o.a. prof. Rob Mudde hebt ontwikkeld. We hebben vele uren zonder daglicht doorgebracht in de kelder van het RID, maar dit waren (gekgenoeg) toch altijd de leukste uren van de werkweek. Jouw kennis en kunde hebben een enorme bijdrage geleverd aan de resultaten die we tijdens mijn onderzoek hebben behaald, waar ik je heel erg voor veel bedanken! Ik wens je heel veel succes met de verdere ontwikkelingen aan de opstellingen, en twijfel er niet aan dat er nog heel veel mooie resultaten onder jouw begeleiding behaald gaan worden!

Within our research group, we are extremely lucky to have research technicians capable of designing and constructing advanced laboratory-scale setups. In this work, we used a large variety of setups, from horizontal stirred beds to fluidized beds to rotating drums. You name it, Stefan ten Hagen can design, draw, and (with DEMO) construct it. Stefan, hartelijk dank voor je al je technische support over de jaren. Zonder jou had ik geen experimentele opstellingen gehad om onderzoek mee te doen! Je tekeningen zijn ook veelvuldig terug te vinden in de hoofdstukken. Ik vond het ook erg leuk om elke maandag ochtend even bij te praten over de voetbal van het afgelopen weekend. Duco, je hebt tijdens mijn bachelor, master, en ook tijdens mijn PhD, het altijd mogelijk gemaakt dat ik heel mooie SEM fotos kon schieten. Verder was je altijd beschikbaar om te brainstormen over experimentele aanpak, heb je geholpen met ontwikkelen van opstellingen, en bijgedragen aan het maken van de radioactieve tracers. Bedankt! Hans en Rolf, in het laatste jaar van mijn promotieonderzoek hebben we met jullie hulp mooie technische ontwikkelingen kunnen doorvoeren met de X-ray opstelling. Dit heeft tot bijzonder mooie resultaten geleid in de horizontal geroerde bedreactor, en wordt ook al toegepast op andere systemen nu. Mojgan en Cas, jullie zijn erg belangerijk geweest in het begin en respectievelijk het eind van mijn onderzoek. Bedankt voor alle hulp met de labveiligheid, het maken en verbeteren van opstellingen, en support bij

het begeleiden van studenten in het lab. The radiation-based imaging experiments were performed in the TU Delft Reactor Institute. I thank the Radiation Protection Service for their consults and for ensuring a safe working environment during the experiments. From a non-research point of view, this work could not have been done without Leslie van Leeuwen. Leslie, heel erg bedankt voor al je support gedurende de jaren. Je wist altijd alle administratieve en organisatorische problemen bijzonder snel op te lossen. Daarnaast heb ik enorm veel plezier gehad om de groepsactiviteiten (kerstdiner met pubquiz, uitjes naar het strand, bowlen etc.) samen met jou te organiseren en in goede banen te leiden. Ik ben ook trots dat we allebei een prijs hebben gewonnen voor respectievelijk het beste voorgerecht en het beste nagerecht tijdens het laatste PPE kerstdiner!

The research was part of a larger consortium with three other PhD researchers, Martijn, Raisa, and Sahar. Thank you for the great collaborations, discussions, and for sharing knowledge and experiences. Martijn, bedankt voor de leuke en goede samenwerking, die we hebben kunnen verzilveren met een mooie publicatie in CEJ, en de mooie tijden op nationale en internationale conferenties! Laten we kennis blijven uitwisselen over onze gemeenschappelijke hobby: ambachtelijk ijs maken. Raisa, Sahar, I wish you all the best completing your PhD research! The consortium had a strong oriented focus and industry experts were closely involved in all stages of the research. I thank Erik, Tingwen, Sreekanth, and Christoph for the pleasant collaboration, informative discussions, and suggestions over the four years. I hope that the findings from this research contribute to optimizing the horizontal stirred bed reactors at SABIC.

During my PhD research, I had the opportunity to work together with many talented students: Esgo, Joey, Jack, Amarenske, Michiel, Aleksander, Jan, Yvette, Babette, Aysen, Adil, Sophie, Wendy, Emma, Wout, Wietse, Claris, Yordi, en Lise; het was een eer om met jullie allemaal samen te mogen werken! Daarnaast hebben jullie een enorm belangerijke bijdrage geleverd aan mijn onderzoek, waarvoor ik jullie heel erg wil bedanken! Een groot gedeelte van de bijdrages die jullie hebben geleverd zijn gepubliceerd in wetenschappelijke tijdschriften of gepresenteerd op academische conferenties. Mijn collega PhD's en postdoc's waren altijd jaloers op mij dat ik het geluk had om samen te werken met zulke talentvolle en gezellige studenten! Ik wens jullie al het geluk toe in het afronden van jullie studie en in jullie verdere carrieres!

Together with Rens Kamphorst and Kaiqiao Wu we were the three musketeers from PPE working on particle technology and fluidization. Together, we

embarked on countless adventures in the lab, trying to get challenging powders to fluidize and explain why this could or could not happen. Rens, het was erg leuk om een mede PhD-onderzoeker te hebben die aan een soortgelijk onderwerp werkte als ik. Bedankt voor alle gezelligheid in het kantoor, tijdens de conferenties en werkbezoeken, en tijdens experimenten doen in het lab. Ook wil ik je bedanken voor al je hulp en support in je rol als paranymph! Ik wens je heel veel succes met de laatste loodjes van het schrijven van jouw thesis en tijdens je postdoc binnen de groep! Kaiqiao, it was a great pleasure to work with you. Your experience in particle technology and fluidization catalyzed our research significantly. It was also extremely helpful to always be able to brainstorm with you about experiment setup and processing of X-ray data in Matlab. Thank you for all the great teamwork and I wish you all the best with your professor position in China!

I was fortunate enough to have many other amazing colleagues within the chemical engineering department. Jose, thank you for all the great Basic-Fit gym sessions during which not only we could discuss life, but also get your input in my research from another perspective. I also would like to thank you for your support as paranymph, it is great to have you by my side during the defense! Albert, jij was de eerste die me ontving binnen PPE en mij introduceerde binnen de groep. Het enthousiasme waarmee je dat deed zorgde ervoor dat ik mij meteen welkom heette. Gelukkig heb je dat enthousiasme niet verloren! Bedankt voor de plezierige tijd binnen PPE en daarbuiten! Ik koester goede herinneringen aan alle Indonesische restaurantjes die we hebben bezocht gedurende de vier jaar, dit moeten we zeker blijven doen nu we allebei in het oosten van het land wonen..! Emma, bedankt dat ik altijd bij je terecht kon om jouw kennis, kunde en advies te raadplegen. Ik heb heel veel respect voor je als academicus en persoon. Het was erg leuk om met je samen te werken! Ik zal nu ook regelmatig advies blijven vragen betreft het leven in en rondom de Achterhoek! Lukas, Gao, Nasim, Bhavesh, Ming, Isabell, Tanuj, Dominik, Giacomo, Athina, Peter, Mingliang, it was great to have been able to share the office with you (for some time) during my PhD! I very much appreciate that we belonged to the 'quiet' office, yet always found room for fun and laughter! Also to my non-office colleagues, Ruben, Margherita, Edo, Max, Zaid, Pranav, Marc, Qing, Riccardo, Lena, Ignasi, Ankur, Mahdiyeh, Ida, Simone, Manoj, Damian, Nat, Donato, Gul, Shota, thank you for the great times!

Ik wil ook graag mijn vrienden en (schoon)familie bedanken voor alle support en afleiding door de jaren heen. De ouderwetse avondjes muziek luisteren, speciaalbiertjes drinken, en het jaarlijks weekend weg zorgden er altijd

voor dat ik weer met een opgeladen batterij aan de werkweek kon beginnen. Het is ook heel erg gaaf dat jullie hier vandaag bij aanwezig kunnen zijn! Ik heb altijd heel erg veel steun gehad van mijn schoonouders, schoonzussen, zussen en zwagers, heel erg bedankt daarvoor! Pap en mam, bedankt dat jullie er altijd voor me zijn geweest! Jullie hebben me altijd heel erg gesteund in alles dat ik deed en daar ben ik jullie heel erg dankbaar voor! Ik ben heel blij dat we dit moment nu samen met elkaar zo mogen vieren! Tot slot, lieve Bente, bedankt dat je er altijd voor me bent, in goede tijden en slechte tijden. Ik kan altijd bij je terecht, al is het voor feedback op mijn artikelen (wat je hebt gegeven vanaf het eerste artikel), tot een knuffel als ik die nodig heb. Ik ben zo ontzettend dankbaar om jou in mijn leven te hebben!

PhD Portfolio

Completed PhD Training

General courses	Organizer	Year
PhD start-up	TU Delft GS	2020
Interactive online self-presentation	TU Delft GS	2021
Designing Scientific Posters and Covers	TU Delft GS	2021
Research Data Management	TU Delft GS	2021
The Informed Researcher	TU Delft GS	2021
Software Carpentry Workshops	TU Delft GS	2021
Managing Academic Publication Review Process	TU Delft GS	2022
Data visualisation - A Practical Approach	TU Delft GS	2024
Voice Training	TU Delft GS	2024
Deciding Your Next Career Move	TU Delft GS	2024
Preparing For Job Interviews	TU Delft GS	2024
Writing A Dissertation	TU Delft GS	2024
Career Development - Personality Matters	TU Delft GS	2024
Discipline related courses		
RPO Dispersible Radioactive Materials Level D	TU Delft	2020
Pro2Tech Annual event	TU Delft	2020-2023
Product and Process Engineering of Solid Particles	TU Delft	2021
International Conference Fluidized Bed Technology	GLAB	2021
Physics of Cohesive Granular Materials	Granutools	2021
University Course Fluidization Technology	TUHH	2021

Teaching and supervising

Teaching (assistant) activities

Reactors and Kinetics	TU Delft	2020-2023
Onderzoek & Ontwerpen TU Delft Project	CLD	2020-2022
Multiphase Reactor Engineering	TU Delft	2021
State of Art Reactor Science & Design	PAO	2021
Leren Onderzoeken 2	TU Delft	2021-2024
Product Design	TU Delft	2021-2024

Supervising activities

E. Claassen	MSc CE	Flowability analysis of polypropylene	2020
J. Meijdam	BSc MST	Synthesis methods of tracers for RPT	2021
J. de Mooij	MSc CE	Flow behaviour in an HSBR by RPT	2021
A. Vögtlander	MSc CE	Behavior of particles in an HSBR by X-ray	2021
M. van Wijk	BSc MST	De-aeration of starch in packing process	2021
A. Aarouss	MSc CE	Characterizing powder flow in bag-filling	2022
A. van Zanten	BSc MST	Axial mixing in an HSBR	2022
A. Otman	BSc MST	Flowability in a rotating drum	2022
B. Jacobs	BSc MST	A novel way of making a cup of tea	2022
J. de Jonge	BSc MST	Effect of environment on flow	2022
Y. Ziggers	BSc MST	Powder flow in rotating drums	2022
S. Zwartendijk	BSc MST	Flow of polymeric solids	2023
W. de Jong	BSc MST	Axial mixing in an HSBR	2023
W. Saalmink	BSc MST	Correlating fluidization and flow behavior	2024
E. Brockhus	BSc MST	Behavior of powders in chemical reactors	2022
W. Roovers	MSc CE	Behavior of particles in an HSBR by XPTV	2023
C. de Vries	MSc CE	Hydrodynamic insight in an HSBR by X-ray	2023
Y. Beelen	BSc MST	Hydrodynamic study HSBR by XPTV	2023
L. Willighagen	BSc MST	Automating granular flow studies	2024
A. van Zanten	MSc CE	Stickiness measurements in a drum	2024

List of Publications

Journal articles related to this dissertation

5. **P.C. van der Sande**, K. Wu, R. Kamphorst, E.C. Wagner, G.M.H. Meesters, and J.R. van Ommen, *On the inherent correlation between the fluidization and flow properties of cohesive powders*, Accepted for publication in AIChE Journal (2024).

4. **P.C. van der Sande**, M.J.A. de Munck, K. Wu, D.R. Rieder, D.E.A. van den Eertwegh, E.C. Wagner, G.M.H. Meesters, E.A.J.F. Peters, J.A.M. Kuipers, and J.R. van Ommen, *Fluidization behavior of stirred gas-solid fluidized beds: a combined X-ray and CFD-DEM-IBM study*, Chemical Engineering Journal **499**, 155944 (2024).

3. **P.C. van der Sande**, C. de Vries, E.C. Wagner, A.C. Vögtlander G.M.H. Meesters, and J.R. van Ommen, *Flow behavior of polypropylene reactor powder in horizontal stirred bed reactors characterized by X-ray imaging*, Chemical Engineering Journal (2024).

2. **P.C. van der Sande**, E.C. Wagner, J. de Mooij, G.M.H. Meesters, and J.R. van Ommen, *Particle dynamics in horizontal stirred bed reactors characterized by single-photon emission radioactive particle tracking*, Chemical Engineering Journal **482**, 149100 (2024).

1. **P.C. van der Sande**, J. de Mooij, E.C. Wagner, G.M.H. Meesters, and J.R. van Ommen, *Single-photon emission radioactive particle tracking method for hydrodynamic evaluation of multi-phase flows*, Particuology - In Press, (2023).

Journal articles outside the scope of this dissertation

3. K. Wu, R. Kamphorst, **P.C. van der Sande**, E.C. Wagner, G.M.H. Meesters, J.R. van Ommen, *Gas pulsation-assisted fluidization of cohesive micron powder: an X-ray imaging study*, In preparation (2024).

2. S. Pourandi, **P.C. van der Sande**, T. Weinhart, I. Ostanin, *A mathematical model for the dynamic angle of repose of a granular material in the rotating drum*, Powder Technology **446**, 120176 (2024).

1. R. Kamphorst, **P.C. van der Sande**, K. Wu, E.C. Wagner, M.K. David, G.M.H. Meesters, J.R. van Ommen, *The mechanism behind vibration assisted fluidization of cohesive micro-silica*, KONA Powder and Particle Journal **41** (2023).

Conference presentations

6. **P.C van der Sande**, A. Aarouss, and G.M.H. Meesters, *Understanding industrial bag filling of granular materials through powder characterization*, PARTEC, Nurenberg (2023), Oral communication.

5. **P.C van der Sande**, S.E.J Zwartendijk, G.M.H. Meesters, and J.R. van Ommen, *Influence of liquid content and temperature on the flowability of polypropylene solids*, PARTEC, Nurenberg (2023), Poster communication.

4. **P.C van der Sande**, E.C Wagner, J. de Mooij, G.M.H. Meesters, and J.R. van Ommen, *Elucidating particle flows in horizontal stirred bed reactors by radioactive particle tracking*, Fluidization XVII, Edinburgh (2023), Oral communication.

3. **P.C van der Sande**, J. de Mooij, E.C Wagner, G.M.H. Meesters, and J.R. van Ommen, *Characterizing particle dynamics in horizontal stirred bed reactors with radioactive particle tracking*, World Congres Particle Technology 9, Madrid (2022), Oral communication.

2. **P.C van der Sande**, E.C Wagner, G.M.H. Meesters, and J.R. van Ommen, *Characterizing gas-solids distribution in horizontal stirred bed reactors with fast X-ray analysis*, Fluidized Bed Conversion 24, Gotenburg (2022), Poster communication.

1. **P.C van der Sande**, E.C Wagner, G.M.H. Meesters, and J.R. van Ommen, *Characterizing gas-solids distribution in horizontal stirred bed reactors with fast X-ray analysis*, Nederlands Process Symposium 17, Delft (2022), Poster communication.

About the author

Pieter Christian van der Sande was born on 28 February 1995 in Delft. He obtained his 'Gymnasium (VWO)' secondary school certificate at the 'Christelijk Lyceum Delft' in Delft. After graduation, he started a joint-degree Bachelor in Molecular Science and Technology at Delft University of Technology and Leiden University. He completed a minor in sustainable development and carried out his thesis project in the Catalysis Engineering research group working on metal-organic framework (MOF) based catalysts for Fischer-Tropsch synthesis under the supervision of prof.dr.ir. Freek Kapteijn and prof.dr.ir. Jorge Gascon. He then pursued his Master's in Chemical Engineering with a specialization in process engineering from the Delft University of Technology. During his studies, he applied his process engineering knowledge to practice while working as an intern at DSM Food Specialties in Sydney, where he successfully implemented initiatives to optimize a starter culture plant. Christian carried out his M.Sc. thesis research on the development of metal-organic framework membranes for CO_2 removal in clinical medicine under the supervision of prof.dr. Freek Kapteijn. During his studies, Christian has been actively involved as a teaching assistant in undergraduate and graduate courses, such as *Chemical Reactor Engineering* and *Leren onderzoeken 2*.

In August 2020, Christian joined the Product and Process Engineering group from the Department of Chemical Engineering at the Delft University of Technology to pursue a Ph.D. under the supervision of prof.dr.ir Ruud van Ommen and dr.ir. Gabrie Meesters. His research activities involve hydrodynamic studies with advanced nuclear measurement techniques to study gas holdup, flow patterns, and flow velocities inside multiphase reactors. The outcomes of the Ph.D. research are presented in this dissertation.